

AFRL-PR-WP-TR-2006-2039

**TURBINE ENGINE RESEARCH
CENTER (TERC) DATA SYSTEM
ENHANCEMENT AND TEST
ARTICLE EVALUATION**

**Delivery Order 0002: TERC Aeromechanical
Characterization**



Pamela S. Teets, Dr. Walter Obrien, Dr. Vince Capece, and Dr. Choon Tan

**Battelle Memorial Institute
Information Systems Dayton Operations
5100 Springfield Pike, Suite 110
Dayton, OH 45431-1261**

JUNE 2005

Final Report for 13 May 2003 – 30 June 2005

Approved for public release; distribution is unlimited.

STINFO FINAL REPORT

**PROPULSION DIRECTORATE
AIR FORCE MATERIEL COMMAND
AIR FORCE RESEARCH LABORATORY
WRIGHT-PATTERSON AIR FORCE BASE, OH 45433-7251**

NOTICE

Using Government drawings, specifications, or other data included in this document for any purpose other than Government procurement does not in any way obligate the U.S. Government. The fact that the Government formulated or supplied the drawings, specifications, or other data does not license the holder or any other person or corporation; or convey any rights or permission to manufacture, use, or sell any patented invention that may relate to them.

This report was cleared for public release by the Air Force Research Laboratory Wright Site (AFRL/WS) Public Affairs Office (PAO) and is releasable to the National Technical Information Service (NTIS). It will be available to the general public, including foreign nationals.

PAO case number: AFRL/WS 06-0074

Date cleared: 09 Jan 2006

THIS TECHNICAL REPORT IS APPROVED FOR PUBLICATION.

//S//

CARL WILLIAMS
Technology Evaluation Branch
Turbine Engine Division
Propulsion Directorate

//S//

NORMAN POTI, Chief
Technology Evaluation Branch
Turbine Engine Division
Propulsion Directorate

//S//

JEFFREY STRICKER
Chief Engineer
Turbine Engine Division
Propulsion Directorate

This report is published in the interest of scientific and technical information exchange and its publication does not constitute the Government's approval or disapproval of its ideas or findings.

| REPORT DOCUMENTATION PAGE | | | | Form Approved OMB No. 0704-0188 | |
|--|-----------------------------|------------------------------|---------------------------------------|---|--|
| <p>The public reporting burden for this collection of information is estimated to average 1 hour per response, including the time for reviewing instructions, searching existing data sources, gathering and maintaining the data needed, and completing and reviewing the collection of information. Send comments regarding this burden estimate or any other aspect of this collection of information, including suggestions for reducing this burden, to Department of Defense, Washington Headquarters Services, Directorate for Information Operations and Reports (0704-0188), 1215 Jefferson Davis Highway, Suite 1204, Arlington, VA 22202-4302. Respondents should be aware that notwithstanding any other provision of law, no person shall be subject to any penalty for failing to comply with a collection of information if it does not display a currently valid OMB control number. PLEASE DO NOT RETURN YOUR FORM TO THE ABOVE ADDRESS.</p> | | | | | |
| 1. REPORT DATE (DD-MM-YY) June 2005 | | 2. REPORT TYPE Final | | 3. DATES COVERED (From - To) 05/13/2003 – 06/30/2005 | |
| 4. TITLE AND SUBTITLE TURBINE ENGINE RESEARCH CENTER (TERC) DATA SYSTEM ENHANCEMENT AND TEST ARTICLE EVALUATION Delivery Order 0002: TERC Aeromechanical Characterization | | | | 5a. CONTRACT NUMBER F33615-02-D-2223-0002 | |
| | | | | 5b. GRANT NUMBER | |
| | | | | 5c. PROGRAM ELEMENT NUMBER 62203F | |
| 6. AUTHOR(S) Pamela S. Teets, Dr. Walter Obrien, Dr. Vince Capece, and Dr. Choon Tan | | | | 5d. PROJECT NUMBER 3066 | |
| | | | | 5e. TASK NUMBER 17 | |
| | | | | 5f. WORK UNIT NUMBER 2B | |
| 7. PERFORMING ORGANIZATION NAME(S) AND ADDRESS(ES) Battelle Memorial Institute Information Systems Dayton Operations 5100 Springfield Pike, Suite 110 Dayton, OH 45431-1261 | | | | 8. PERFORMING ORGANIZATION REPORT NUMBER | |
| 9. SPONSORING/MONITORING AGENCY NAME(S) AND ADDRESS(ES) Propulsion Directorate Air Force Research Laboratory Air Force Materiel Command Wright-Patterson AFB, OH 45433-7251 | | | | 10. SPONSORING/MONITORING AGENCY ACRONYM(S) AFRL/PRTE | |
| | | | | 11. SPONSORING/MONITORING AGENCY REPORT NUMBER(S) AFRL-PR-WP-TR-2006-2039 | |
| 12. DISTRIBUTION/AVAILABILITY STATEMENT Approved for public release; distribution is unlimited. | | | | | |
| 13. SUPPLEMENTARY NOTES Report contains color. | | | | | |
| 14. ABSTRACT Battelle has supported the Air Force Compressor Research Facility from May 13, 2003 through June 30, 2005 under this Delivery Order. Under this Delivery Order, aeromechanical characterization research was performed in conjunction with testing performed in the Turbine Engine Research Center (TERC). This research involved data analysis to identify new behavior, verify codes and model simulating aeromechanical behavior, and perform aeromechanical test and evaluation of hardware undergoing testing in the TERC. This work was in direct support of the national High-Cycle Fatigue (HCF) program under Integrated High-Performance Turbine Engine Technology (IHPTET). | | | | | |
| 15. SUBJECT TERMS TERC, aeromechanical characterization, HCF, IHPTET | | | | | |
| 16. SECURITY CLASSIFICATION OF: | | | 17. LIMITATION OF ABSTRACT: SAR | 18. NUMBER OF PAGES 378 | 19a. NAME OF RESPONSIBLE PERSON (Monitor) Carl Williams 19b. TELEPHONE NUMBER (Include Area Code) (937) 255-6802 x253 |
| a. REPORT Unclassified | b. ABSTRACT Unclassified | c. THIS PAGE Unclassified | | | |

1.0 Technical Discussion of Approaches

This Delivery Order defined and authorized aeromechanical characterization research in conjunction with testing performed in the Turbine Engine Research Center (TERC). This research involved data analysis to identify new behavior, verify codes and model simulating aeromechanical behavior, and perform aeromechanical test and evaluation of hardware undergoing testing in the TERC. This work was in direct support of the national High-Cycle Fatigue (HCF) program under Integrated High-Performance Turbine Engine Technology (IHPTET).

2.0 Scope

Under this Delivery Order, six aeromechanical characterization research tasks were performed. Each area focused on research objectives of test programs scheduled for the TERC.

Task I Onsite Aeromechanical Research:

Interface support was provided to the University of Kentucky, the Massachusetts Institute of Technology and Virginia Polytechnic Institute to transfer TERC test program data and information required to perform each research effort.

Task II Flutter Precursor Identification in Transonic Compressors:

The University of Kentucky (UK) finalized their investigation into flutter precursor identification in transonic compressors. Based upon data obtained from the Honeywell Engine System (HES) test in the Compressor Research Facility (CRF), the existence of flutter precursor waves was confirmed in a previous effort. This effort concluded this investigation in the flutter precursor region. The actual quantification of the precursor and the warning time that the precursor provides before the actual onset of flutter is delineated in their final report included as Appendix A.

Task III Forced Response Evaluation:

Forced response evaluation was conducted in conjunction with the Massachusetts Institute of Technology (MIT) to provide a detailed evaluation of the development of inlet flow distortion and the influence of specific flow parameters on the response of compressor blades. This work was used to define the appropriate means to evaluate compressors and fans for high-cycle fatigue (HCF) resistance and drew on research performed at the CRF and at General Electric. The work concentrated on comparing flight test results to ground test data to determine appropriate ground test requirements for HCF evaluations. The final report for this work delineating specific guidelines for appropriate HCF ground tests has been included in Appendix B.

Task IV Distortion Transfer Prediction for Multistage Axial Compressors:

Distortion transfer prediction for multistage axial compressors was investigated in conjunction with Virginia Polytechnic Institute and State University (VPI) to determine how a multistage transonic compressor rotor effects inlet flow distortion. Existing CRF test data was used to perform detailed analyses on how a multistage transonic compressor rotor transfers inlet flow distortion to downstream blade rows. The research considered compressor loading, different distortion patterns, and rotor speeds. A third-order model of the distortion transfer that occurs in transonic compressors was developed. Limits and capabilities of this nonlinear model were defined to help develop a better testing procedure for axial compressors. The final report for this work has been included in Appendix C.

Task V Characterization and Management of Transonic Compressor Tip

Clearance and Casing Treatment Flows:

Characterization and management of transonic compressor tip clearance and casing treatment flows were performed in conjunction with MIT. This task concentrated on addressing technical issues that lead to quantification of flow processes defining effective casing treatment operation and design guidelines for casing treatment in high speed (transonic) compressors with

performance representative of current/future designs. There are two aspects: (1) aerodynamic performance as measured in terms of changes in peak efficiency and stall margin, and (2) aeromechanical response associated with resulting flow unsteadiness in the tip region. Two goals were researched. One was to identify, in a quantitative manner, the end wall flow features which are critical in the mechanism of operation of casing treatment in high speed compressors. A second goal was to define the fluid dynamic effects leading to improved casing treatments without the attendant aeromechanical difficulties. A third goal was to use the results to develop design guidelines/criteria for casing treatments that result in compressor pressure rise capability and performance enhancement. Experiments, computations, and analysis/modeling were performed to address the issues necessary for the accomplishment of the stated objectives. The final report for this work delineating recommended casing treatments and the associated design guidelines/criteria is included in Appendix B.

Task VI Prediction of Blade Response from Finite Element Analysis Using Forces Determined from Computational Fluid Dynamics Analysis:

Prediction of blade response from finite element analysis using forces determined from computational fluid dynamics (CFD) analyses was performed in conjunction with VPI. This task investigated the potential for using finite element analysis along with CFD simulation to predict the blade loading on a transonic compressor blade resulting from inlet flow distortion. The predicted non-uniform blade loading was compared to existing experimental data. The final report for this work has been included in Appendix C. An analytical method model that provides a means to predict resonant forcing functions that would be detrimental to the compressor blading was also provided.

APPENDIX A

University of Kentucky Research

An Experimental Investigation of Flutter Precursor in Compression Systems

By

John D. Gill and Vincent R. Capece

Department of Mechanical Engineering

College of Engineering

University of Kentucky

Paducah, KY 42001-7380

May 1, 2004

SUMMARY

In this investigation casing-mounted high-frequency response pressure transducers are used to characterize the part-speed stall flutter response of a single stage unshrouded axial-flow fan. These sensors are distributed around the circumference at a constant axial location upstream of the fan blade leading edge plane. The pre-recorded experimental data at 70% and 85% corrected speed with open and closed clearances are analyzed for the case where the fan is back-pressured into the stall flutter zone. The experimental data is analyzed using two probe and multiprobe techniques; both analysis techniques are presented in detail.

The data was subdivided into a transitional region, a rapid growth region, and a limit amplitude region. Flutter occurred at a frequency of 411 Hz for 70% corrected speed and 456 Hz for 85% corrected speed with closed clearances. The open clearance results showed flutter occurred at frequencies of 411 Hz and 456 Hz for 70% and 85% corrected speeds, respectively. In each case the dominant nodal diameter was 2, with additional nodal diameter responses occurring at smaller amplitudes. Both analysis techniques exhibited excellent agreement with each other.

The multiprobe technique proved to be able to detect flutter activity at a distinct nodal diameter and frequency on each speedline several seconds before the beginning of the rapid growth region, which is typically defined as the flutter initiation point. The dominant nodal diameter within the transitional region was 2 for each speedline with a frequency of 411 Hz for 70% corrected speed and 456 Hz for 85% corrected speed with closed and open clearances.

This case study presents strong support for the existence of a flutter precursor. This research area needs more experiments to be conducted on other fans/compressors to further investigate this phenomenon.

ACKNOWLEDGMENTS

The authors would like to gratefully acknowledge the support of this research by Dr. Douglas Rabe of the Compressor Research Facility at Wright Patterson Air Force Base, Dayton, OH, and the authors thank Honeywell International, Inc. and Dr. A. Sanders for digitizing the data. The authors thank Dr. R.B. Fost, Technical Monitor, Battelle Memorial Institute, Compressor Research Facility at Wright Patterson Air Force Base, for his continuous support. Dr. R.B Fost was a tremendous help in answering the many questions that arose during the course of this work.

TABLE OF CONTENTS

| | |
|--|-----|
| Acknowledgments | iii |
| List of Tables | vi |
| List of Figures | vii |
| Chapter One: Introduction | 1 |
| Background | 1 |
| Literature Review | 3 |
| Objectives | 5 |
| Chapter Two: Facility Description and Instrumentation | 7 |
| Facility | 7 |
| Test Article | 8 |
| Instrumentation | 9 |
| Chapter Three: Data Acquisition and Analysis | 11 |
| Data Acquisition | 11 |
| Data Analysis | 11 |
| Mathematical Analysis | 11 |
| Integration Method | 15 |
| Two Probe Method | 17 |
| Multiprobe Method | 19 |
| Chapter Four: Results | 22 |
| Results for 70% Corrected Speed Data | 22 |
| Pressure Transducers: The Two Probe Method | 22 |
| Pressure Transducers: Integration Method Using the Two Probe Method | 31 |
| Strain Gages: The Two Probe Method | 33 |
| Summary of Two Probe Method | 37 |
| Pressure Transducers: The Multiprobe Method | 38 |
| Pressure Transducers: The Integration Method Using the Multiprobe Method | 45 |
| Strain Gages: The Multiprobe Method | 48 |
| Summary for Multiprobe Method | 50 |
| Open Clearance Data | 51 |
| Results for 85% Corrected Speed Data | 56 |
| Pressure Transducers and Strain Gages: The Two Probe Method | 57 |
| Pressure Transducers: The Multiprobe Method | 64 |
| Pressure Transducers: The Integration Method Using the Multiprobe Method | 67 |
| Strain Gages: The Multiprobe Method | 68 |

| | |
|---|-----|
| Summary | 69 |
| Open Clearance Data | 70 |
| Flutter Precursor | 75 |
| Chapter Five: Summary and Conclusion | 84 |
| Appendices | 88 |
| Appendix A: Nomenclature | 88 |
| Appendix B: Unequally Spaced Fourier Transforms | 89 |
| Appendix C: Least Squares Spectral Analysis | 93 |
| Appendix D: Rotating Frame Analysis | 95 |
| Appendix E: Theoretical Rotating Frame Analysis | 99 |
| References | 101 |
| Grant Publications and Presentations | 103 |

LIST OF TABLES

| | | |
|-----|---|----|
| 4.1 | Nodal diameter frequency for the largest flutter spectral response using pressure transducers 7 and 8 for the Integration Method. | 32 |
| 4.2 | Nodal diameter, wave harmonic, and rotating reference frame frequency for the largest flutter spectral responses in Figure 4.13. | 42 |
| 4.3 | Nodal diameter, wave harmonic, and rotating reference frame frequency for the largest flutter spectral responses in Figure 4.19. | 47 |
| 4.4 | Nodal diameter, wave harmonic, and rotating reference frame frequency for the largest flutter spectral responses in Figure 4.33. | 65 |

LIST OF FIGURES

| | | |
|------|--|----|
| 1.1 | Typical performance map of a fan or compressor showing the possible flutter regimes. | 2 |
| 2.1 | The Honeywell development fan blisk consisting of 22 wide-chord fan blades. | 9 |
| 2.2 | Performance map showing the flutter boundaries of the unshrouded fan. | 9 |
| 2.3 | Schematic diagram of pressure transducer and strain gage locations for the test article. | 10 |
| 3.1 | Sample of recorded signal from casing mounted pressure transducer 7 at 70% corrected speed. | 16 |
| 3.2 | Sample of recorded signal from casing mounted pressure transducer 7 before and after the integration method at 70% corrected speed in the limit amplitude region. | 17 |
| 3.3 | Procedure for calculating cross-power spectra. The top left figure is pressure transducer 8, and the bottom left figure is pressure transducer 7. The Fourier transform for transducer 7 is multiplied by the conjugate of the Fourier transform for transducer 8. | 19 |
| 3.4 | Each casing mounted pressure transducer has an associated θ in the stationary reference frame. | 20 |
| 4.1 | Time dependent pressure and strain gage response for the fan as it is back-pressured into flutter at 70% corrected speed. | 24 |
| 4.2 | Successive Fourier transforms of pressure transducer 11 as the fan is back-pressured into flutter at 70% corrected speed. | 26 |
| 4.3 | Top down view of Figure 4.2 with the major wave harmonics and nodal diameters identified. | 27 |
| 4.4 | Cross-power spectral analysis of pressure transducers 11 and 12 as the fan is back-pressured into flutter for $3.82E$ at 70% corrected speed. | 28 |
| 4.5 | Pressure transducers 11 and 12 cross-power spectral analysis as the fan is back-pressured into flutter for $3.82E$ at 70% corrected speed. | 29 |
| 4.6 | Cross-power spectral analysis of pressure transducers 11 and 12 as the fan is back-pressured into flutter at 70% corrected speed. | 30 |
| 4.7 | Cross-power spectral analysis of pressure transducers 7 and 8 at 20 seconds for the integration method at 70% corrected speed. | 31 |
| 4.8 | Successive Fourier transforms from strain gage 17. The peak response occurs at $1.82E$ as the fan is back-pressured into flutter for 70% corrected speed. | 34 |
| 4.9 | Top down view of Figure 4.8. The peak response occurs at $1.82E$ | 34 |
| 4.10 | Cross-power spectral analysis of strain gages 17 and 18 as the fan is back-pressured into flutter at 70% corrected speed. | 35 |
| 4.11 | Strain gages 17 and 18 cross-power spectral analysis as the fan is back-pressured into flutter at 70% corrected speed. | 36 |

| | | |
|------|--|----|
| 4.12 | Cross-power spectral analysis of strain gages 17 and 18 and pressure transducers 11 and 12 as the fan is back-pressured into flutter at 70% corrected speed. | 37 |
| 4.13 | Two-dimensional Fourier transform of pressure transducer data at 16 seconds using 25 rotor revolutions for 70% corrected speed. | 40 |
| 4.14 | Two-dimensional Fourier transform of pressure transducer data at 16 seconds using 12 rotor revolutions for 70% corrected speed. | 41 |
| 4.15 | Two-dimensional Fourier transform of pressure transducer data using 25 rotor revolutions as the fan is back-pressured into flutter for $n = 2$ and $m = 1$ at 70% corrected speed. | 43 |
| 4.16 | Two-dimensional Fourier transform of pressure transducer data using 12 rotor revolutions as the fan is back-pressured into flutter for $n = 2$ and $m = 1$ at 70% corrected speed. | 43 |
| 4.17 | Two-dimensional Fourier transform of pressure transducer data using 25 rotor revolutions as the fan is back-pressured into flutter for $n = 4$ and $m = 0$ at 70% corrected speed. | 44 |
| 4.18 | Two-dimensional Fourier transform of pressure transducer data using 25 rotor revolutions as the fan is back-pressured into flutter for $n = 5$ and $m = 0$ at 70% corrected speed. | 45 |
| 4.19 | Two-dimensional Fourier transform of pressure transducer data using the integration method at 16 seconds for 70% corrected speed. | 46 |
| 4.20 | Two-dimensional Fourier transform of pressure transducer data using the integration method as the fan is back-pressured into flutter for $n = 2$ at 70% corrected speed. | 48 |
| 4.21 | Two-dimensional Fourier transform of strain gage data at 16 seconds for 70% corrected speed. | 49 |
| 4.22 | Two-dimensional Fourier transform of strain gage data as the fan is back-pressured into flutter for $n = 2$ at 70% corrected speed. | 50 |
| 4.23 | Time dependent data for strain gage 7 as the fan is back-pressured into flutter at 70% corrected speed with open clearances. | 53 |
| 4.24 | Cross-power spectral content for pressure transducers 7 and 8 at 11 seconds at 70% corrected speed with open clearances. | 54 |
| 4.25 | Two-dimensional Fourier transform of pressure transducer data at 10.5 seconds using 25 rotor revolutions for 70% corrected speed with open clearances. | 55 |
| 4.26 | Two-dimensional Fourier transform of pressure transducer data as the fan is back-pressured into flutter for $n = 2$ and $m = 1$ at 70% corrected speed. | 56 |
| 4.27 | Time dependent pressure and strain gage response for the fan as it is back-pressured into flutter at 85% corrected speed. | 58 |
| 4.28 | Successive cross-power spectra of pressure transducers 7 and 8 as the fan is back-pressured into flutter at 85% corrected speed. | 59 |
| 4.29 | Top down view of Figure 4.28 with the major wave harmonics and nodal diameters identified. | 60 |
| 4.30 | Successive cross-power spectra for strain gages 17 and 18 as the fan is back-pressured into flutter at 85% corrected speed. | 61 |
| 4.31 | Top down view of Figure 4.30 with the major wave harmonics identified. | 62 |

| | | |
|------|---|----|
| 4.32 | Time dependent data for strain gages. | 63 |
| 4.33 | Two-dimensional Fourier transform of pressure transducer data at 7.1 seconds at 85% corrected speed. | 65 |
| 4.34 | Two-dimensional Fourier transform of pressure transducer data as the fan is back-pressured into flutter for $n = 2$ and $m = 1$ at 85% corrected speed. . | 66 |
| 4.35 | Two-dimensional Fourier transform of pressure transducer data as the fan is back-pressured into flutter for $n = 4$ and $m = 1$ at 85% corrected speed. . | 67 |
| 4.36 | Two-dimensional Fourier transform of pressure transducer data as the fan is back-pressured into flutter for $n = 2$ at 85% corrected speed using the integration method. | 68 |
| 4.37 | Two-dimensional Fourier transform of strain gage data as the fan is back-pressured into flutter at 85% corrected speed. | 69 |
| 4.38 | Time dependent data for strain gage 18 as the fan is back-pressured into flutter at 85% corrected speed with open clearances. | 71 |
| 4.39 | Cross-power spectral content for pressure transducers 7 and 8 at 7.8 seconds for 85% corrected speed with open clearances. | 72 |
| 4.40 | Two-dimensional Fourier transform of pressure transducer data at 7.76 seconds using 25 rotor revolutions for 85% corrected speed with open clearances. | 73 |
| 4.41 | Two-dimensional Fourier transform of pressure transducer data as the fan is back-pressured into flutter for $n = 2$ and $m = 1$ at 85% corrected speed. . | 74 |
| 4.42 | Time dependent pressure and strain gage response for the fan as it is back-pressured into flutter at 70% corrected speed with closed clearances. | 77 |
| 4.43 | Two-dimensional Fourier transform of pressure transducer data using 25 rotor revolutions as the fan is back-pressured into flutter for $n = 2$ at 70% corrected speed with closed clearances. | 78 |
| 4.44 | Time dependent pressure and strain gage response for the fan as it is back-pressured into flutter at 85% corrected speed with closed clearances. | 80 |
| 4.45 | Two-dimensional Fourier transforms as the fan is back-pressured into flutter for $n = 2$ at 85% corrected speed with closed clearances. | 81 |
| 4.46 | Two-dimensional Fourier transform of pressure transducer data as the fan is back-pressured into flutter for $n = 2$ and $m = 1$ at 70% corrected speed with open clearances. | 82 |
| 4.47 | Two-dimensional Fourier transform of pressure transducer data as the fan is back-pressured into flutter for $n = 2$ and $m = 1$ at 85% corrected speed with open clearances. | 82 |

CHAPTER ONE

INTRODUCTION

Background

The necessity to understand the fundamental problems associated with the design and operation of turbomachines becomes increasingly important as engineers strive to enhance their performance. One of the challenges often encountered in the design and operation of fans and compressors for both commercial and military aircraft gas turbine engines is flutter. Current design trends of thinner blades and higher pressure ratio per stage make fan and compressor blades more susceptible to flutter. When flutter is encountered in the design and development of a fan or compressor, an expensive redesign and retest program results.

As schematically depicted in Figure 1.1 on a compressor performance map, there are many different types of flutter that can be encountered in the fan and compressor sections of the engine. Supersonic unstalled flutter occurs near the design point where the incidence angles are nominal and the Mach number relative to the blade is supersonic. As the pressure ratio increases at high corrected speeds supersonic stall flutter is encountered near the stall line. At off-design conditions where the corrected speeds are low, choke flutter can be found in the aft stages of high pressure compressors for negative incidence angles, and subsonic/transonic stall flutter in the fan or front stages of the high pressure compressor for positive incidence angles.

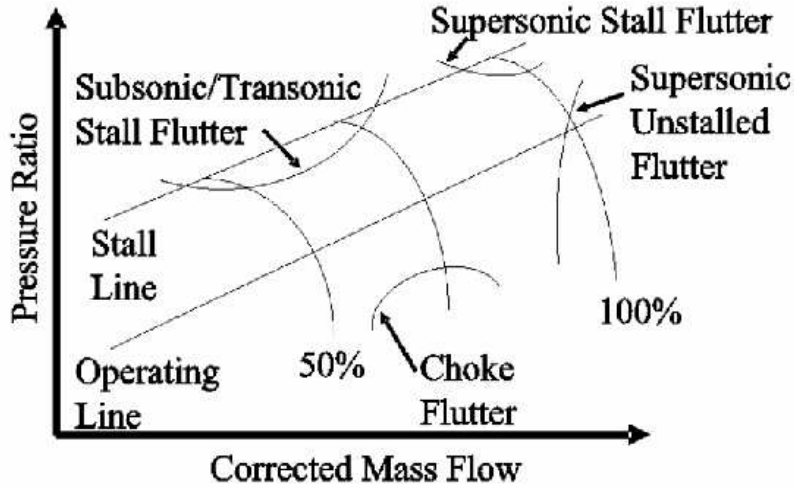


Figure 1.1: Typical performance map of a fan or compressor showing the possible flutter regimes.

Important flutter parameters include the reduced frequency, interblade phase angle, and nodal diameter. Reduced frequency, k , is given by Equation 1.1.

$$k = \frac{2\pi f c}{2V} \quad (1.1)$$

In this relationship f is the oscillation frequency in Hz , c is the blade chord, and V is the inlet velocity. The interblade phase angle, σ , is the phase angle between blades in flutter and depends on the nodal diameter, n , of the flutter response. Due to the circular geometry, the interblade phase angles must sum to a multiple of 2π . Interblade phase angle is given by Equation 1.2

$$\sigma = \frac{2\pi n}{N_b} \quad (1.2)$$

where n is the nodal diameter of the flutter response and N_b is the number of rotor blades. The nodal diameter, n , is equivalent to the number of cycles the flutter wave makes around the circumference of the rotor.

Literature Review

The development of analyses to predict flutter is an area of research interest. Due to the complexity of the flow field and the fluid/structure interaction phenomena, accurate prediction of flutter at all operating conditions has remained elusive. Unsteady aerodynamic analyses with varying degrees of fidelity have been used in fluid/structure interaction calculations. Recently unsteady Reynolds Averaged Navier-Stokes (RANS) models (e.g., Weber and Platzer (2000); Swafford et al. (1994); Ekaterinaris and Platzer (1996); Siden (1991); and Wu et al. (1989)) have been developed to account for viscous effects. The calculation of separated flow phenomena is a general weakness of computational fluid dynamic predictions.

Hence, flutter testing is an important component in the design and development of fan and compressor blades. To measure the dynamic response of the blades during flutter rotating frame and/or stationary frame sensors can be employed. Strain gages are typically used as the rotating frame sensors. These sensors are bonded to the blades with the lead wires routed through a slip-ring to the stationary frame for display of signals during testing. Additionally, the strain gage signals are recorded for post-test analysis. The advantage of strain gage sensors is the direct assessment of the stress during flutter. However, there are some disadvantages to the use of strain gages.

The strain gage sensors and lead wires, albeit thin, disrupt the flow over the surface of the blade, which has an effect on blade aerodynamic performance. Moreover, the sensors and lead wires can influence the vibration characteristics of the blades. Due to this negative impact on the blade performance and structural dynamic characteristics it is desirable to

minimize the number of strain gages and still provide adequate coverage of the possible vibration modes of the blade (see for example Mignolet and Choi (2002)). A major concern with this approach is not having a strain gage on a blade that has the highest stress response. Furthermore, due to the harsh engine operating environment the failure rates of strain gages during testing can be high.

To overcome some of these difficulties blade vibration measurements using stationary frame sensors has been pursued. Stationary sensors mounted in the casing of the fan or compressor have the advantage of being non-intrusive. High frequency response pressure transducers and optical probes have been used to detect blade vibration from the casing above the rotating blades.

Optical displacement probes have received considerable attention. Optical displacement sensors direct a light beam (typically generated by a laser) onto the tips of the blades as they rotate beneath the sensor. The reflected light from the blade tip is measured using a photomultiplier each time a blade passes by the probe. This measurement is compared to a reference pulse generated for the number of rotor blades to establish the blade instantaneous position. During flutter the time of arrival of the blade would be different than the reference pulse indicating blade vibration. Using the measured deflections the frequency of vibration of the blades in flutter can be quantified. Moreover, from these deflections and knowledge of the dynamic structural response of the blade, the blade stress can be inferred.

There are also challenges concerning the use of the optical displacement system. This system requires optical access that is susceptible to fouling from the inlet flow field. Additionally, the blade tips must have a high degree of reflectivity.

Optical measurements to detect flutter have been used by many investigators. Hohenberg (1967) used laser probes to measure the blade tip displacement and shaft mounted rod magnetics to measure zero displacement at the root of the blades during flutter. Zablotskiy et al. (1974) used a cathode ray amplitude register to study vibrations that are non-multiples or multiples of the rotational frequency, for which electrical impulses at the base of the

blades near the rotor shaft and electrical impulses at the tip of the blades are generated and combined on a cathode-ray tube to measure the displacement of the blades during the vibration. Stargardter (1977) used small mirrors mounted on fan blades at different span locations to quantify blade displacement during flutter using the reflections of laser light. Jutras et al. (1981) and Kurkov (1984b) used laser probes to measure the deflection of the fan blades during subsonic/transonic stall flutter. Additionally, Kurkov (1989) and Kurkov and Mehmed (1991) have used this technique for flutter detection of unducted fans.

Stationary reference frame high frequency response pressure transducers have also been used to determine whether a rotor blade was in flutter. An advantage of this method is that commercially available pressure sensors can be used to measure the time-variant pressure during flutter. From the dynamic pressure measurements the vibration frequency and nodal diameter pattern of the rotor blades in flutter can be determined.

Pressure transducers were also used by Jutras et al. (1981) to measure the time-variant pressure during subsonic/transonic stall flutter. Kurkov (1983) used pressure and displacement measurements to determine the unsteady aerodynamic work during flutter.

Objectives

Typically, flutter detection using either pressure transducers or optical sensors employs two sensors mounted in the casing above the rotor. By using two sensors at the same axial location with different circumferential locations, the flutter frequency and nodal diameter (interblade phase angle) can be quantified.

In this investigation the flutter characteristics of an unshrouded fan blade are quantified using casing mounted high frequency response pressure transducers. The configuration employed in this investigation consists of multiple high frequency response pressure transducers mounted evenly around the casing circumference in the tip region of the rotor blades.

The overall objective of this research is to use this instrumentation configuration to investigate flutter initiation of the unshrouded transonic axial flow fan. The specific objectives are to utilize the detailed measurements of the time-variant pressure flow field in the rotor casing region while the rotor is operating in the transitional and flutter modes to quantify the features of flutter initiation. Experimental data is investigated for open and closed rotor tip clearances.

CHAPTER TWO

FACILITY DESCRIPTION AND INSTRUMENTATION

Facility

This experimental program was conducted in the Compressor Research Facility (CRF), which is one of four test facilities in the Turbine Engine Research Center (TERC) at Wright Patterson Air Force Base. The CRF is capable of experimentally evaluating aerodynamic performance and aeromechanics (flow induced vibrations) of full-scale fans or high pressure compressors used in aircraft gas turbine engines.

Air enters the facility test chamber through a set of inlet filters and pressure regulating valves. These valves allow the inlet pressure to be varied from 2 *psia* (13.79 *kPa*) to ambient. From the 20 *ft* (6.1 *m*) diameter by 65 *ft* (19.81 *m*) long test chamber the air flows through flow conditioning elements and enters the fan or compressor. A 30,000 horsepower motor drives a low speed and high speed gearbox that provides accurate speed control for rotational speeds up to 30,000 *RPM*. The air exits the fan or compressor through a throttling valve. Downstream of the throttling valve a venturi meter is used to quantify the mass flow rate. Additionally, there is also a second set of ducts available for compression systems that require a bypass stream. This second flow path is also equipped with a separate throttling valve to control the bypass stream flow and a venturi meter to measure the mass flow rate.

Conventional instrumentation coupled with a state-of-the-art data acquisition system provide high quality aerodynamic performance data for the fan or compressor component. Temperature and pressure measurements at the inlet and exit of the test article quantify the overall performance of the fan or compressor. To resolve stage performance, pressure and

temperature measurements are made at the entrance to each stationary (nonrotating) blade row.

Time-variant data from strain gages and high frequency response pressure transducers are acquired with a wide bandwidth analog data acquisition system (see Fost and Teets (1998)). During testing time-variant data is displayed on a combination of oscilloscopes and spectral analyzers. All analog data is also recorded on high fidelity tape for future review and post-test analysis.

This facility has all the capabilities necessary to experimentally investigate flutter.

Test Article

In this study stall flutter of a single stage unshrouded axial flow fan was considered. The Honeywell development fan blisk consists of 22 wide-chord fan blades, Figure 2.1. The blades and disk were fabricated from a single piece of material (integrally bladed disk). This creates low structural damping for the bladed-disk system. Stall flutter was generated by back-pressuring the fan while holding the rotational speed constant. This reduced the mass flow rate and increased the incidence angle moving the fan operating point towards the stall line. Figure 2.2 shows that stall flutter was encountered over a range of constant speedlines. For this investigation flutter development along the 70% and 85% corrected speedlines was considered.

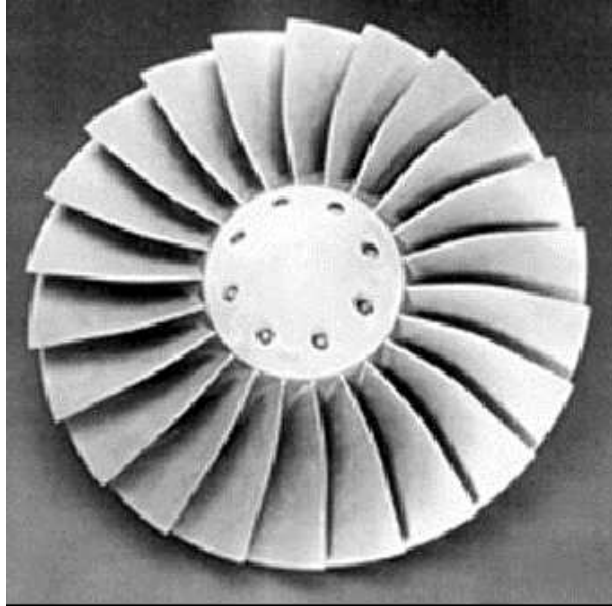


Figure 2.1: The Honeywell development fan blisk consisting of 22 wide-chord fan blades.

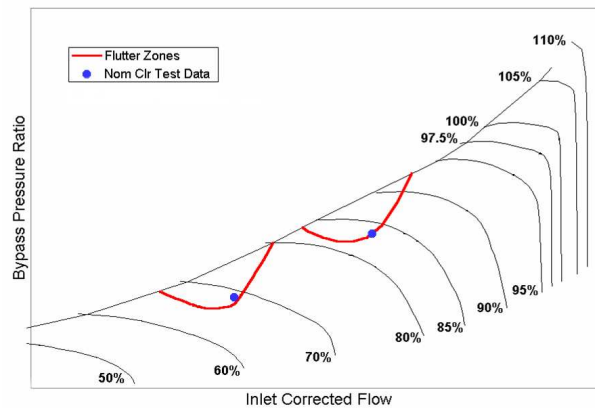


Figure 2.2: Performance map showing the flutter boundaries of the unshrouded fan.

Instrumentation

The time-variant instrumentation consisted of 1) blade mounted high frequency response pressure transducers (Kulite XCQ-062-20A) and strain gages, 2) casing mounted high frequency response pressure transducers located over the rotor blades, and 3) casing

mounted laser light probes. The blade mounted strain gages and high frequency response pressure transducers were transferred from the rotating to the stationary reference frame through a forward mounted 100 channel slip-ring (Sanders et al. (2003)).

This investigation focuses on the casing mounted high frequency response pressure transducers near the leading edge of the fan blades, see Figure 2.3. Pressure transducers two and four through thirteen were flush mounted approximately 1 inch (2.54 *cm*) upstream of the rotor blade leading edge plane and equally spaced around the circumference of the casing. Transducer three was positioned at the midpoint between transducers four and five. Transducer one, which is not shown in Figure 2.3, was mounted in the casing and $\frac{1}{4}$ inch (0.635 *cm*) forward of transducer two. Figure 2.3 shows the relative positions of six of the original eight blade mounted strain gages.

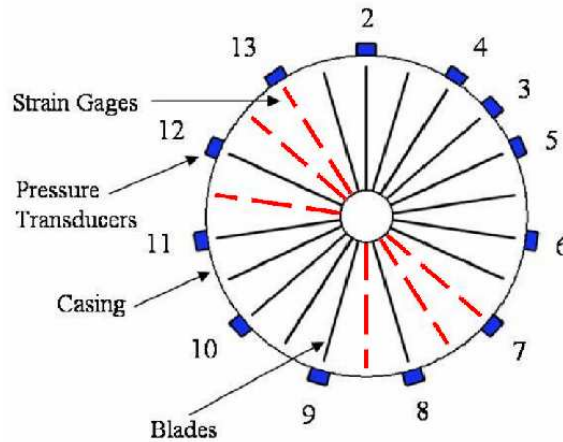


Figure 2.3: Schematic diagram of pressure transducer and strain gage locations for the test article.

CHAPTER THREE

DATA ACQUISITION AND ANALYSIS

Data Acquisition

Data from 12 casing mounted high frequency response pressure transducers and 6 blade mounted strain gages were recorded, along with laser light probes and blade mounted high frequency response pressure transducers. As mentioned previously, the rotating reference frame instrumentation were transferred to the stationary reference frame through a forward mounted 100 channel slip-ring (Sanders et al. (2003)). The data from the strain gages and the high frequency response pressure transducers were recorded on analog tape. A once-per-revolution signal was also recorded onto the analog tape.

Data Analysis

Mathematical Analysis

Turbomachinery flutter is a self-induced vibration due to an instability of the fluid, blade, and disk system, and is usually associated with one of the system's fundamental modes (bending or torsion) with a frequency close to one of the natural frequencies since the blade-to-air density ratio of turbomachine blades is large, unlike aircraft wings. Flutter is comprised of one or more circumferential traveling waves, in the rotating reference frame, each with a distinct nodal diameter. The nodal diameter of the wave is equivalent to the number of cycles the wave makes around the circumference of the rotor, i.e. the spatial frequency of the wave. Each of these waves will have an associated traveling pressure wave. Due to the periodicity condition imposed by having a circular geometry, the phase angle between neighboring blades must sum to a multiple of 2π . This interblade phase

angle is expressed as

$$\sigma = \frac{2\pi n}{N_b} \quad (3.1)$$

where the integer n is the nodal diameter and N_b is the number of blades. Because the casing mounted transducers are in the stationary reference frame, it is necessary to construct a mathematical transformation of the pressure waves from the rotating reference frame to the stationary reference frame to properly interpret a spectral analysis of the pressure transducer data.

Consider an isolated rotor that is vibrating at frequency ω and a constant nodal diameter n . The vibration pattern of the blades in the rotating reference frame can be represented mathematically as

$$e^{i(\omega t + n\theta_r)}$$

where θ_r is the angle in the circumferential direction. The flow field will also respond in this fashion and any flow variable can be expressed as

$$Ae^{i(\omega t + n\theta_r)} \quad (3.2)$$

where A is the amplitude. The amplitude is a function of θ_r and is periodic with a period of $\frac{2\pi}{N_b}$, where N_b is the number of blades. Hence, the amplitude can be expressed as the Fourier series given below.

$$A(\theta_r) = \sum_{m=-\infty}^{\infty} A_m e^{im\theta_r N_b} \quad (3.3)$$

Note that A_m is the coefficient of the m th Fourier spatial harmonic. Combining these last two relations yields the variation of any flow variable due to the rotor blades vibrating at frequency ω with a constant nodal diameter n . Thus, the unsteady pressure wave for each nodal diameter can be represented by the Fourier series

$$p_n = \sum_{m=-\infty}^{\infty} A_{mn} e^{i[\omega t + (n+mN_b)\theta_r]} \quad (3.4)$$

where

- A_{mn} = pressure amplitude of m th harmonic wave
- ω = flutter frequency in the rotating system
- m = wave harmonic number
- n = nodal diameter
- N_b = number of blades
- θ_r = angular position in the rotating reference frame measured positive in the direction opposite of rotation.

Equation 3.4 was also presented previously by Jutras et al. (1981). To transform θ_r to the stationary reference frame, the following equation is used

$$\theta_r = \theta + \Omega t - \beta \quad (3.5)$$

where θ is the transformed angular position, Ω is the rotor speed (rad/sec), and β is the angle between the rotating and stationary reference frames at time $t = 0$, which is taken as 0. Substituting Equation 3.5 into Equation 3.4 gives the stationary reference frame representation of the flutter wave associated with nodal diameter n as

$$p_n = \sum_{m=-\infty}^{\infty} A_{mn} e^{i(\omega_{mn}t + k_{mn}\theta)} \quad (3.6)$$

where

$$\omega_{mn} = \omega + k_{mn}\Omega \quad (3.7)$$

$$k_{mn} = n + mN_b$$

The nodal diameter will be an integer value such that $-\frac{N_b}{2} \leq n \leq \frac{N_b}{2}$, for an even number

of blades, which is the case in this investigation. For an odd number of blades, the range of nodal diameters is $\frac{-(N_b-1)}{2} \leq n \leq \frac{N_b-1}{2}$. The total unsteady pressure in the stationary reference frame is given in Equation 3.8.

$$p = \sum_{n=-\frac{N_b}{2}}^{\frac{N_b}{2}} p_n \quad (3.8)$$

For a pressure wave having a frequency, ω , and nodal diameter, n , in the rotating reference frame, Equation 3.6 shows that the pressure wave will be comprised of several frequencies, ω_{mn} , in the stationary reference frame.

To help formulate the physical interpretation of Equation 3.4, it is necessary to rearrange Equation 3.4 into the form of Equation 3.9.

$$\begin{aligned} p_n &= \sum_{m=-\infty}^{\infty} A_n e^{i[\omega t + n\theta_r]} A_m e^{i[mN_b\theta_r]} \\ p_n &= A_n e^{i[\omega t + n\theta_r]} \sum_{m=-\infty}^{\infty} A_m e^{i[mN_b\theta_r]} \end{aligned} \quad (3.9)$$

Equation 3.10 represents the total unsteady pressure in rotating reference frame coordinates after summing over all nodal diameters.

$$p = \sum_{n=-\frac{N_b}{2}}^{\frac{N_b}{2}} \left[A_n e^{i[\omega t + n\theta_r]} \sum_{m=-\infty}^{\infty} A_m e^{i[mN_b\theta_r]} \right] \quad (3.10)$$

Using Equation 3.5 to transform Equation 3.10 results in Equation 3.11.

$$p = \sum_{n=-\frac{N_b}{2}}^{\frac{N_b}{2}} \left[A_n e^{i[(\omega+n\Omega)t+n\theta]} \sum_{m=-\infty}^{\infty} A_m e^{i[mN_b\Omega t+mN_b\theta]} \right] \quad (3.11)$$

The unsteady pressure distribution given by $\sum_{m=-\infty}^{\infty} A_m e^{i[mN_b\Omega t+mN_b\theta]}$ and the wave components given by $A_n e^{i[(\omega+n\Omega)t+n\theta]}$ are an integral part of each other. Equation 3.10 is used

for transducers located in the rotating reference frame, i.e. blade mounted, and Equation 3.11 is used for transducers located in the stationary reference frame.

These relations will be applied to the case where there are two or more probes mounted in the casing at the same axial location, but at different circumferential locations.

Integration Method

The casing mounted pressure transducers were equally spaced around the circumference of the casing. Given the blades are also equally spaced around the rotor and assuming the rotor blades are identical, the pressure transducers see the beginning and ending of complete blade passings at the same time. However, there will be minor differences, but these differences will be random for no vibration. If there were no vibrations in the blades, each pressure transducer would see identical pressure distributions for each blade passing and, therefore, the integration of the area below each blade passing would have the same numerical value. In practice random vibrations of the blades do exist. When the blades experience vibration due to flutter, the integrated areas of blade passing will exhibit a phase angle between each blade.

The beginning and ending of each blade passing in a pressure transducer data set is easily chosen. Figure 3.1 shows an example casing mounted pressure transducer signal. The solid circles represent the recorded data points. The solid squares indicate the beginning and ending of each blade passing period.

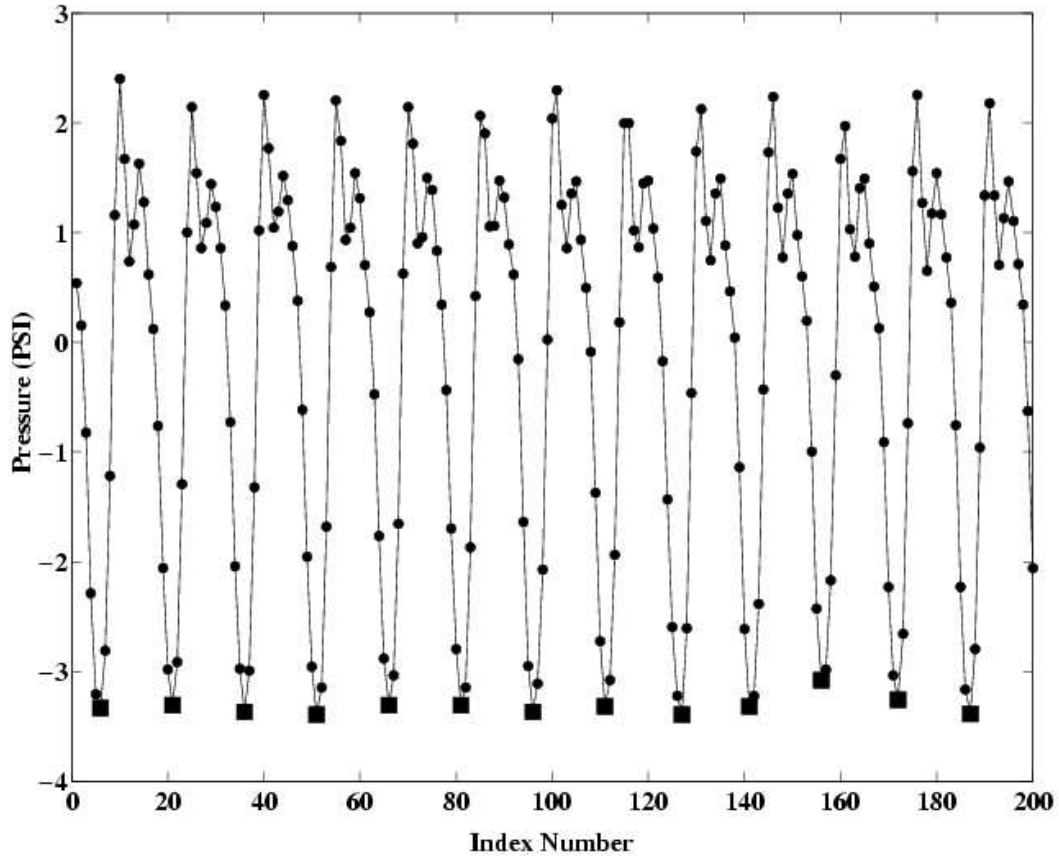


Figure 3.1: Sample of recorded signal from casing mounted pressure transducer 7 at 70% corrected speed.

The area of each blade passing is calculated by numerically integrating the data between two consecutive solid squares. The area of interest lies between the upper and lower boundaries of the data, not what is above and below the zero amplitude line. Figure 3.2 shows a sample of pressure transducer 7 data at 16 seconds (during limit amplitude flutter) before and after the integration method is performed. In addition to the 23 blade passages, a lower frequency of 4 periods can be seen in Figure 3.2(a). This lower frequency signal is associated with the flutter response. After integrating the data the flutter response is easily seen in Figure 3.2(b). The amplitudes in Figure 3.2(b) were divided by the average time of a single blade passage to present the integration results in units of pressure. This integrated data can be analyzed using the two probe and multiprobe methods discussed in the following sections.

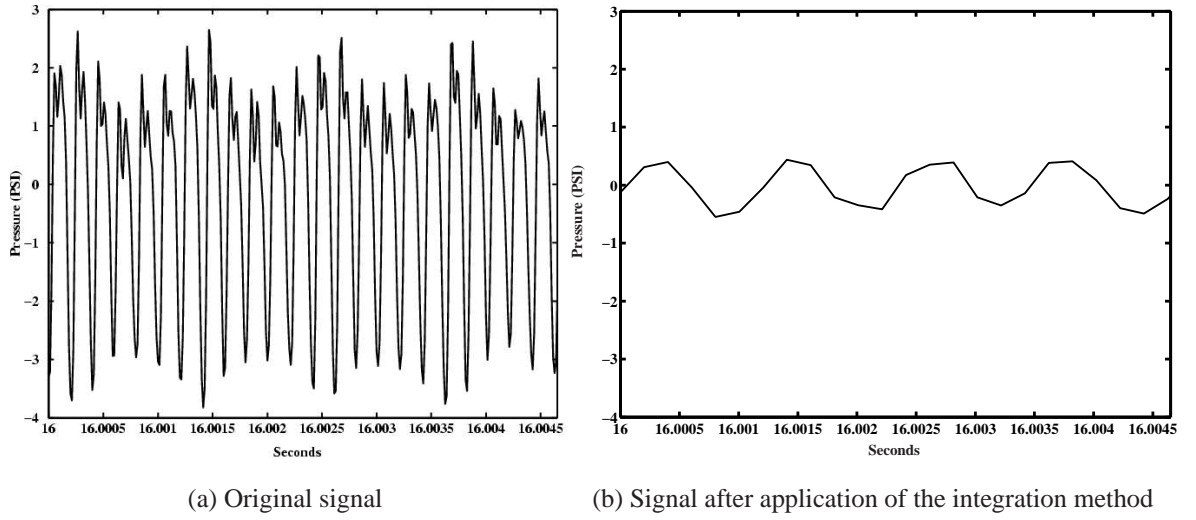


Figure 3.2: Sample of recorded signal from casing mounted pressure transducer 7 before and after the integration method at 70% corrected speed in the limit amplitude region.

Two Probe Method

To determine the nodal diameters associated with the flutter wave, it is necessary to perform a cross-power spectral analysis between two transducers, where both sets of data have the same time index. Figure 3.3 demonstrates calculating a cross-power spectrum between pressure transducers 7 and 8. To compute the nodal diameter at a given frequency in the cross-power spectrum, the phase (ϕ) at that frequency is divided by the angular separation between the two transducers; i.e., there are two sets of data $p_1(t, \theta_1)$ and $p_2(t, \theta_2)$ for which the cross-power spectrum is computed. (The cross-power spectrum is computed by multiplying the Fourier transform of one transducer by the conjugate of the Fourier transform of the other transducer, $FT_1 * conjugate(FT_2)$.)

$$\phi = n\Delta\theta$$

or

$$n = \frac{\phi}{\Delta\theta} \quad (3.12)$$

Moreover, this relation applies to transducer pairs that are in the rotating reference frame as well as those in the stationary reference frame. Once the nodal diameter has been determined, the frequency is calculated using Equation 3.13.

$$\omega_{mn} = \omega + k_{mn}\Omega \quad (3.13)$$

Hence, by using two probes at the same axial location, but different circumferential locations, the frequency and nodal diameter of the flutter instability can be quantified.

In this work, most frequencies have been non-dimensionalized by the once-per-revolution rotational frequency and are represented as engine orders, given by the symbol E .

$$E = \frac{\text{frequency}}{\text{once-per-revolution frequency of the rotor}} \quad (3.14)$$

The case where there are multiple probes mounted in the casing will now be considered.

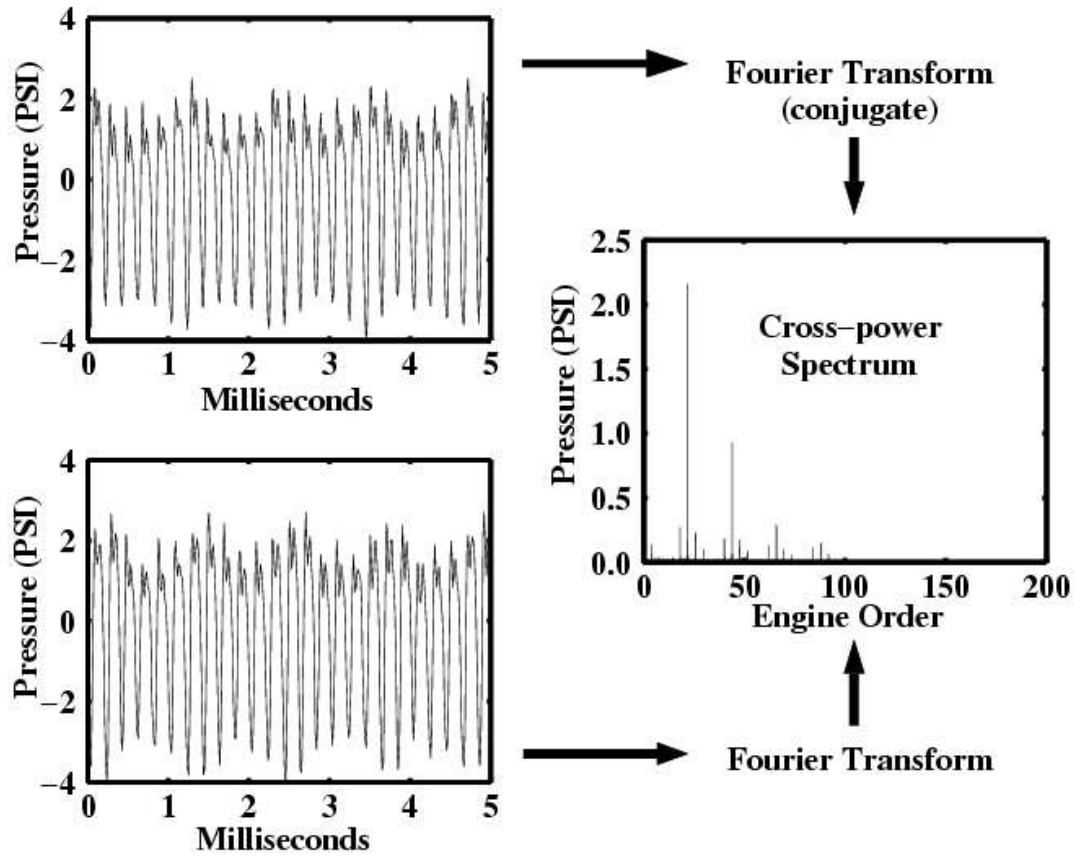


Figure 3.3: Procedure for calculating cross-power spectra. The top left figure is pressure transducer 8, and the bottom left figure is pressure transducer 7. The Fourier transform for transducer 7 is multiplied by the conjugate of the Fourier transform for transducer 8.

Multiprobe Method

Flutter is a traveling wave that extends around the circumference of the entire rotor. However, this may or may not be the case for flutter initiation. As shown by Kurkov (1984a), a single pair of casing mounted pressure transducers provides sufficient detail to study fully developed flutter. To better understand the initiation phase, the circumferential array of transducers at the same axial location upstream of the rotor blade leading edge was used, as illustrated in Figure 2.3. The multiprobe analysis outlined in this section provides the advantage of simultaneously capturing the flutter response about the entire circumference of the rotor. There are 11 casing mounted pressure transducers that are equally spaced around the circumference of the rotor, see Figure 2.3. This type of configuration meets

the requirement of capturing the unsteady pressure field around the entire rotor at each instant in time. Furthermore, this configuration avoids the previously discussed problems associated with blade mounted transducers.

The multiprobe configuration can be used in two ways. The first is to analyze the unsteady pressure field at a given instant of time, where the pressure field is a function of θ , $p(\theta)$. The second is to analyze the unsteady pressure field as a function of angular position and time, $p(\theta, t)$. Figure 3.4 presents the pressure transducer data arranged in the unsteady pressure field. When analyzing the unsteady pressure field as a function of angular position and time, $p(\theta, t)$, two-dimensional sections of the pressure field represented by the shaded region in Figure 3.4 are analyzed. When analyzing the unsteady pressure field at a given instant of time, $p(\theta)$, data is taken from each pressure transducer at the same instant in time. Both of these methods can also be implemented in the rotating reference frame.

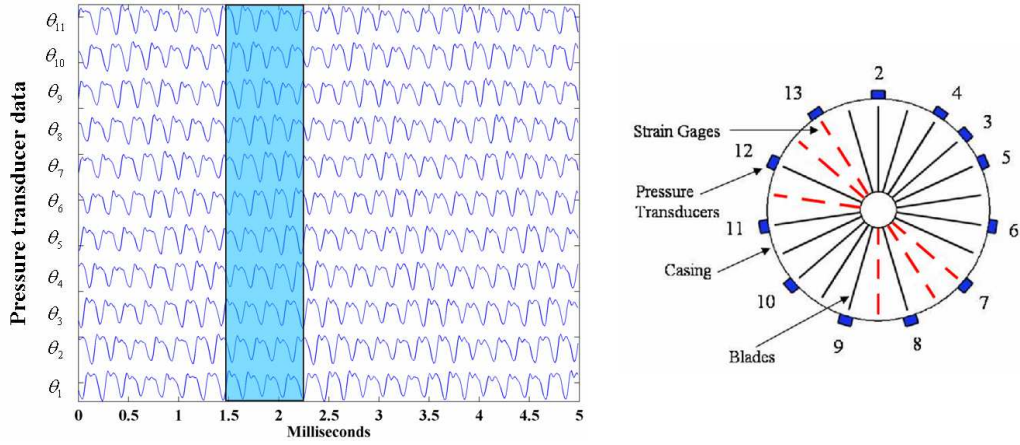


Figure 3.4: Each casing mounted pressure transducer has an associated θ in the stationary reference frame.

In the first method, which will be referred to as the one-dimensional spatial method, a spectral analysis of the unsteady pressure field at fixed time t can be computed for $p(\theta, t)$. Note that the number of data points for this approach is equivalent to the number of casing mounted pressure transducers, 11 in this study. The spectral analysis of the circumferentially distributed transducers yields the spatial frequencies, which are the nodal diameters.

Recall that nodal diameters are integers limited to the range of $-\frac{N_b}{2} \leq n \leq \frac{N_b}{2}$, where N_b is the number of blades. Since the Fourier transform used in this investigation produced only positive frequencies, it is convenient to state the range of nodal diameters as $0 \leq n \leq N_b$. This fan has 22 blades, which means the possible nodal diameters are $0 \leq n \leq 22$. The Nyquist criteria requires 44 data points (i.e. pressure transducers) to avoid aliasing of the spatial frequencies, n . For this study, only 11 pressure transducers were available, meaning that aliasing will occur for any nodal diameter above 5.

For the second method, which will be referred to as the two-dimensional space-time method, a spectral analysis of the unsteady pressure field can be computed for $p(\theta, t)$. For each pressure transducer, there is a recorded signal of pressure versus time, $p(t)$. Additionally, angular position, θ , for each pressure transducer is given by the transducer's angular position on the casing, see Figure 2.3. The data from each of the 11 pressure transducers is combined to form a complete two-dimensional unsteady pressure field, which will be denoted as $\tilde{p}(\theta, t)$. Appendices A and B present an alternative method for the two-dimensional space-time method where the pressure data of the casing mounted pressure transducers is transformed into the rotating reference frame.

From such a set of data a two-dimensional Fourier transform, $FT2$, can be computed. This approach quantifies the frequency and nodal diameter over a given time period simultaneously.

CHAPTER FOUR

RESULTS

Results will now be presented for the fan encountering stall flutter along the 70% and 85% corrected speedlines. The Two Probe Analysis and the Multiprobe Analysis techniques will be presented and compared with each other. Flutter was generated by backpressuring the fan using the core stream and by-pass stream throttling valves. Recording of the pressure transducers was initiated before the flutter boundaries and continued into the flutter zone. The uncertainty in the pressure measurements had a maximum experimental error of $\pm 8\%$. In the limit amplitude region the flutter vibration had reached a steady oscillatory motion of constant amplitude.

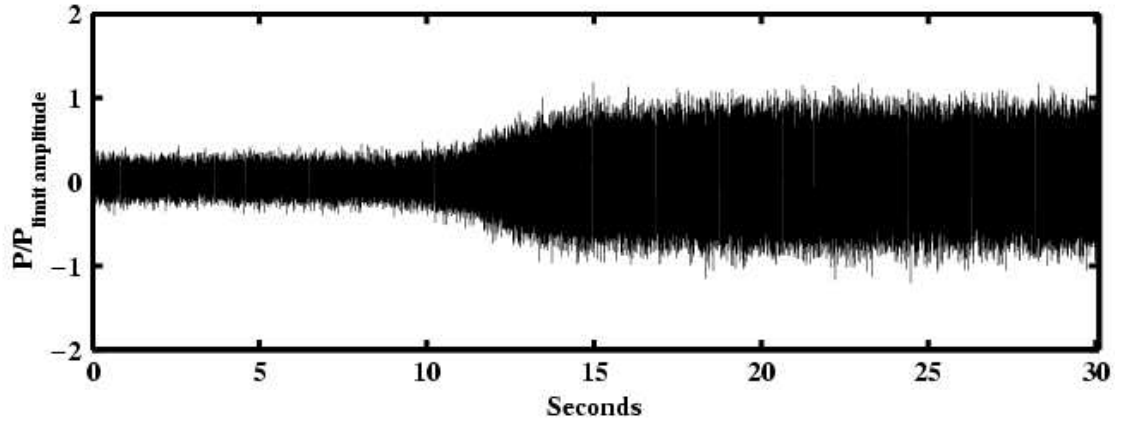
Results for 70% Corrected Speed Data

This section will present the analysis results for 70% corrected speed.

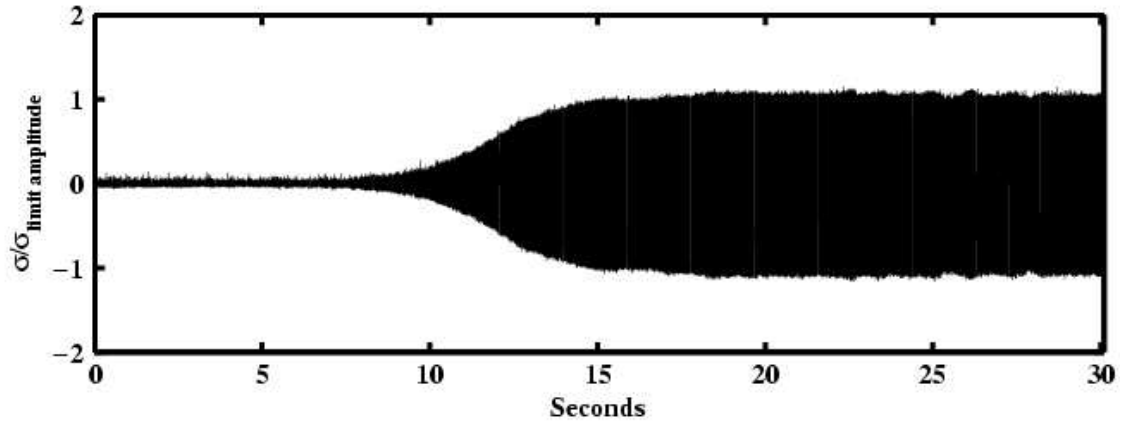
Pressure Transducers: The Two Probe Method

The time variant casing pressure during the transient into flutter along the 70% corrected speedline with closed clearances will now be presented. Figure 4.1 shows the time dependent signals recorded from pressure transducer 11 and strain gage 18. A Butterworth infinite impulse response filter of order 10 and cutoff frequency of 2 kHz has been applied to the pressure transducer signal to remove the pressure component due to blade passing for the purpose of comparing the two signals. Both transducers in Figure 4.1 show a very similar response. Up to 8 seconds the pressure and strain gage signals have nearly constant

amplitude. At approximately 8 seconds there is a distinct change in character of the pressure and strain gage signals. First, there is rapid growth of the pressure and strain, which is the classical response expected for an instability (flutter). At approximately 15 seconds the rapid growth region levels off into a steady oscillating response, which will be referred to as the limit amplitude region. The time dependent pressure measured in the stationary reference frame and the strain gage response measured in the rotating frame exhibit the same characteristics. This indicates that stationary reference frame pressure transducers can be used to quantify flutter initiation and limit amplitude response of blades for flutter monitoring.



(a) Pressure transducer 11



(b) Strain Gage 18

Figure 4.1: Time dependent pressure and strain gage response for the fan as it is back-pressured into flutter at 70% corrected speed.

The pressure transducer and strain gage data were subdivided into smaller blocks. The frequency spectrum of each block was computed using the Fourier transform (FT).

Figure 4.2 presents each of the FT s from pressure transducer 11 successively from the beginning to the end of the recorded data. By displaying the data in this manner the development of flutter can be visualized. The time from the first data point in each 8192-point data block is used for the time axis. The number of rotor rotations for 8192 points is 24. The blade passing frequency and its harmonics, integer multiples of $22E$, have

been reduced in amplitude to allow viewing of the flutter response. The dominant flutter responses occur in pairs about each blade passing harmonic. The primary flutter response frequencies have been labeled in Figure 4.3, a top down view of Figure 4.2.

Consider Equation 3.7 in the form

$$f_{mn} = f + (n + mN_b) f_{rot} \quad (4.1)$$

where f_{rot} is the rotational frequency in Hz . The rotational frequency, f_{rot} , and the number of blades, N_b , are known quantities from the experiment. The frequencies f_{mn} are from the Fourier spectra, such as those in Figure 4.2. The harmonic number m is known by the grouping of the frequencies with the blade passing frequencies/harmonics. Leaving n and f unknown in Equation 4.1. The nodal diameter n can be calculated from cross-power spectra for each frequency f_{mn} , Equation 3.12. The remaining unknown in Equation 4.1 is the flutter frequency f .

The signal-to-noise ratios of the $n = 2$ responses at $m = -1$ and $+1$ are 42 and 47, respectively. The noise level was determined from the Fourier transform at 20 seconds, see Figure 4.2, such that 99% of the random frequencies are below the noise level. The signal-to-noise ratio was calculated by dividing the noise amplitude into the flutter response amplitude.

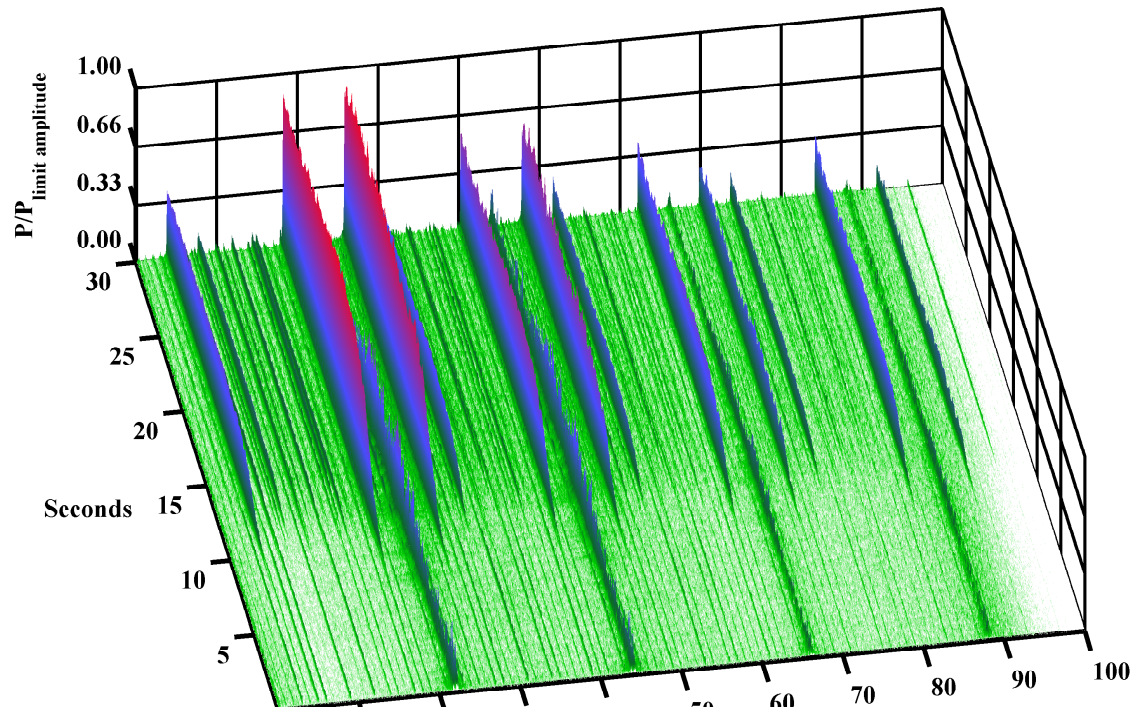
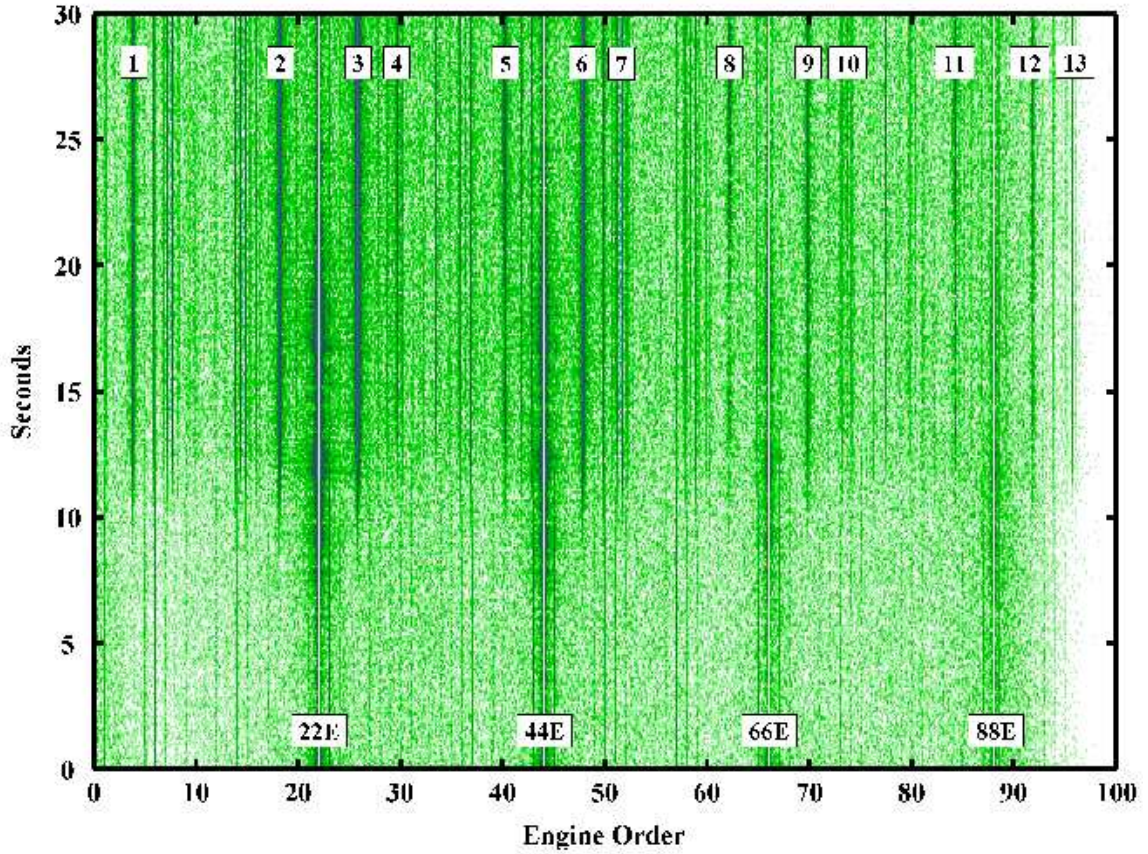


Figure 4.2: Successive Fourier transforms of pressure transducer 11 as the fan is back-pressured into flutter at 70% corrected speed.



| label | m | $f = 411 \text{ Hz}$ | $f = 822 \text{ Hz}$ | label | m | $f = 411 \text{ Hz}$ | $f = 822 \text{ Hz}$ |
|-------|-----|----------------------|----------------------|-------|-----|----------------------|----------------------|
| 1 | 0 | $n = 2$ | | 8 | -3 | $n = 2$ | |
| 2 | -1 | $n = 2$ | | 9 | +3 | $n = 2$ | |
| 3 | +1 | $n = 2$ | | 10 | +3 | | $n = 4$ |
| 4 | +1 | | $n = 4$ | 11 | -4 | $n = 2$ | |
| 5 | -2 | $n = 2$ | | 12 | +4 | $n = 2$ | |
| 6 | +2 | $n = 2$ | | 13 | +4 | | $n = 4$ |
| 7 | +2 | | $n = 4$ | | | | |

Figure 4.3: Top down view of Figure 4.2 with the major wave harmonics and nodal diameters identified.

Cross-power spectra were calculated from casing mounted pressure transducers 11 and 12. Equation 3.12 is used to calculate the nodal diameter for all the frequency responses in the cross-power spectra, except at the rotational frequencies of 22E, 44E, 66E, and 88E. Figures 4.4 and 4.5 show results for the 3.82E frequency line. The cross-power analysis was performed using each of the successive FTs of the individual transducers in pairs from

the beginning to the end of the recorded data. Referring to Figure 4.1, the rapid growth region of the flutter response begins somewhere around 8 seconds and continues through 15 seconds. From the 15 second mark to the end of the recorded data is the limit amplitude region of the flutter response. Figure 4.4 presents the normalized cross-power amplitude in the bottom plot with the corresponding calculated nodal diameter in the upper plot. This figure shows a fully established nodal diameter of 2 by the 8 second mark. It is interesting to note that there are some 2 nodal diameter responses at various points preceding 8 seconds during the transient into flutter. However, the signal-to-noise ratios are poor in this region. At 7.9 seconds the signal-to-noise ratio reaches 1.4.

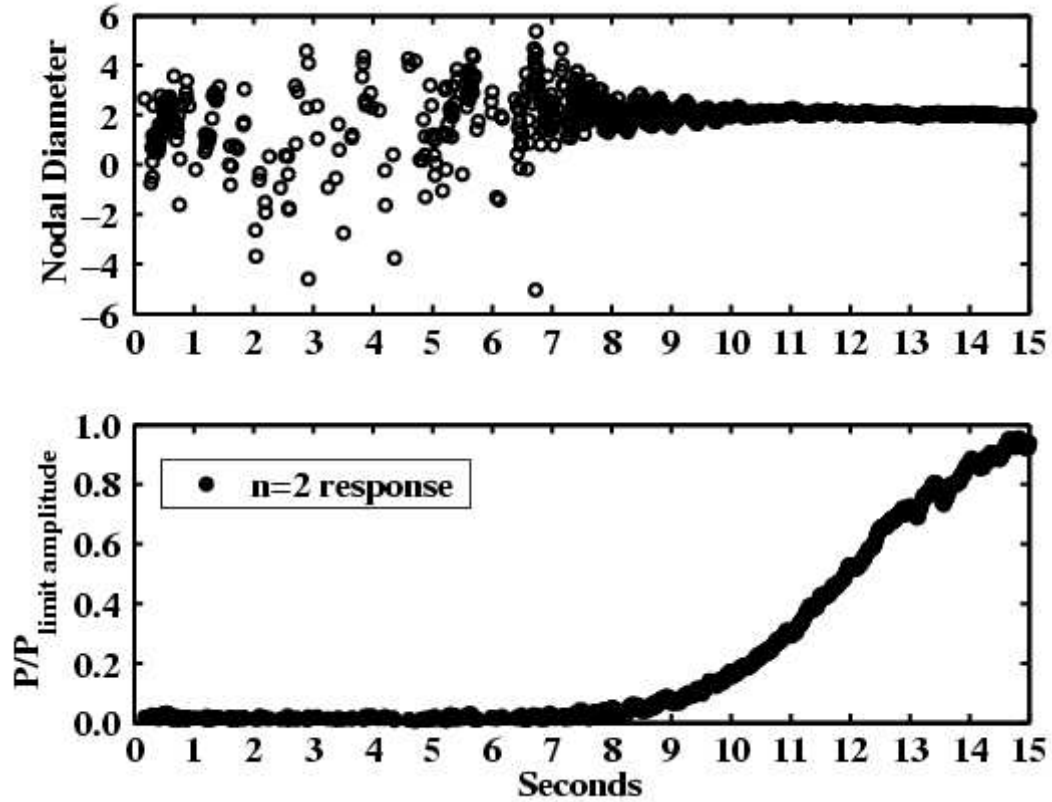


Figure 4.4: Cross-power spectral analysis of pressure transducers 11 and 12 as the fan is back-pressured into flutter for $3.82E$ at 70% corrected speed.

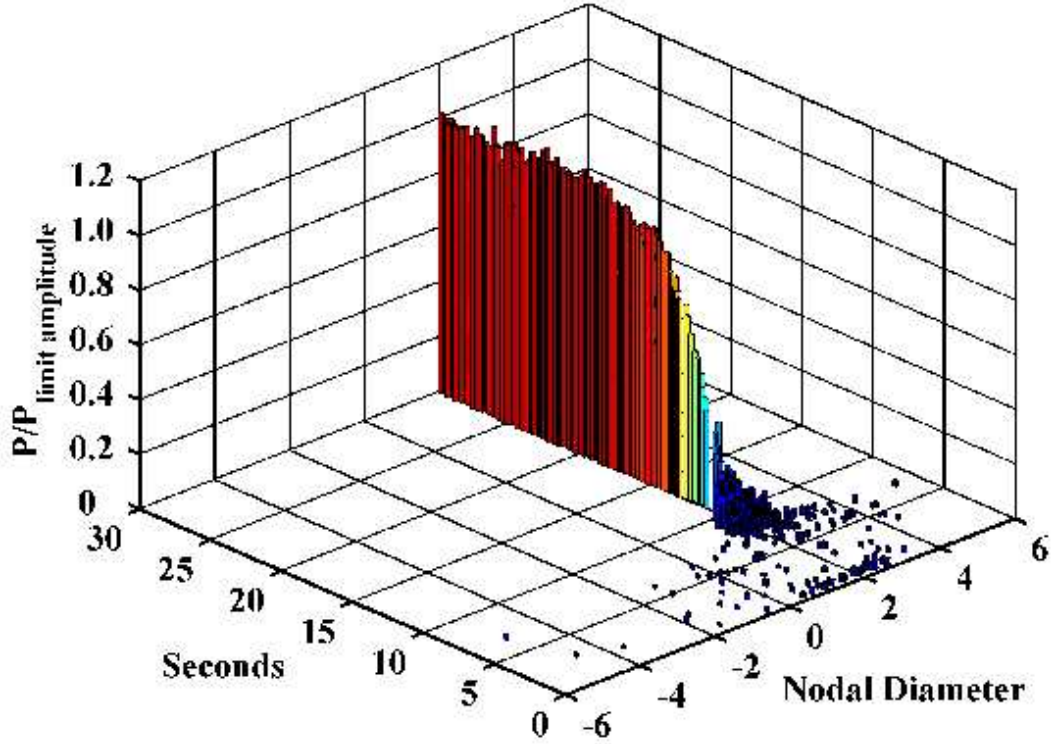


Figure 4.5: Pressure transducers 11 and 12 cross-power spectral analysis as the fan is back-pressured into flutter for $3.82E$ at 70% corrected speed.

Now that the nodal diameter is known for this frequency ($3.82E$) of the cross-power spectrum, the flutter frequency can be quantified using Equation 4.1. The flutter frequency was calculated to be 411 Hz . This procedure was applied to all the frequency responses indicated in the cross-power spectra. Nodal diameters of 2, 4, and 5 were found for the 411 Hz flutter response with $m = 0$ as shown in Figure 4.6. The amplitudes were normalized by the limit amplitude response at $n = 2$. Due to the rapid fall off in the other frequencies, see Figures 4.2 and 4.6, it is believed that aliasing is not a significant issue in this analysis.

The signal-to-noise ratios in the limit amplitude region of the $n = 2, 4$, and 5 responses are 20, 5, and 3, respectively for $m = 0$. Using the previous noise amplitude, the signal-to-noise ratio was calculated by dividing the noise amplitude into the flutter response amplitudes for $n = 2, 4$, and 5 , see Figure 4.6.

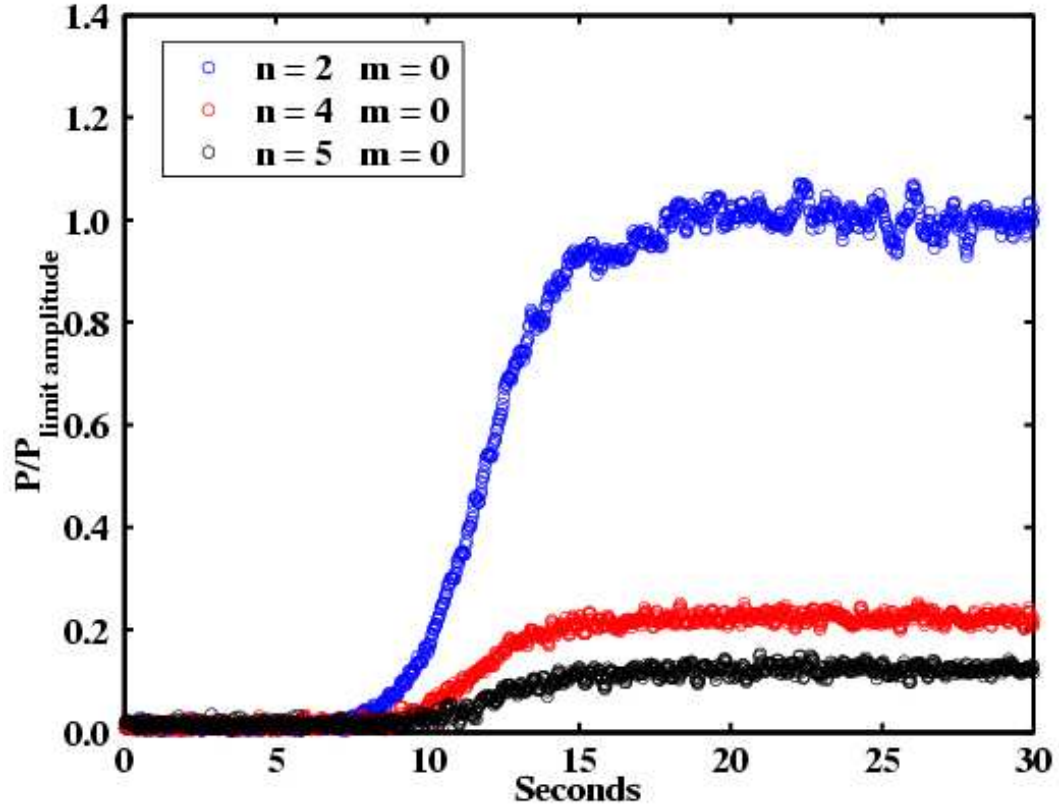


Figure 4.6: Cross-power spectral analysis of pressure transducers 11 and 12 as the fan is back-pressured into flutter at 70% corrected speed.

Interestingly, the second harmonic of the flutter frequency was also identified in both the strain gage response and the pressure transducer response in flutter. Both frequencies are well below the Nyquist frequency of 37.5 kHz for this experiment. At 411 Hz , multiple harmonics of $m = 0, \pm 1, \pm 2, \pm 3, \pm 4$, and ± 5 were active for the nodal diameter of 2. A response was found for a nodal diameter of 4 at 822 Hz and harmonics of $m = 1, 2$, and 3. The largest responses occurred at 411 Hz for $n = 2$ and $m = \pm 1$, followed by $n = 2$ and $m = \pm 2$. Figure 4.3 summarizes the findings.

Integration Method for Pressure Transducers: Integration Method Using the Two Probe Method

The cross-power spectral analysis was also performed on the pressure transducer data using the integration method. Figure 4.7 is a cross-power spectrum between pressure transducers 7 and 8 in the limit amplitude region.

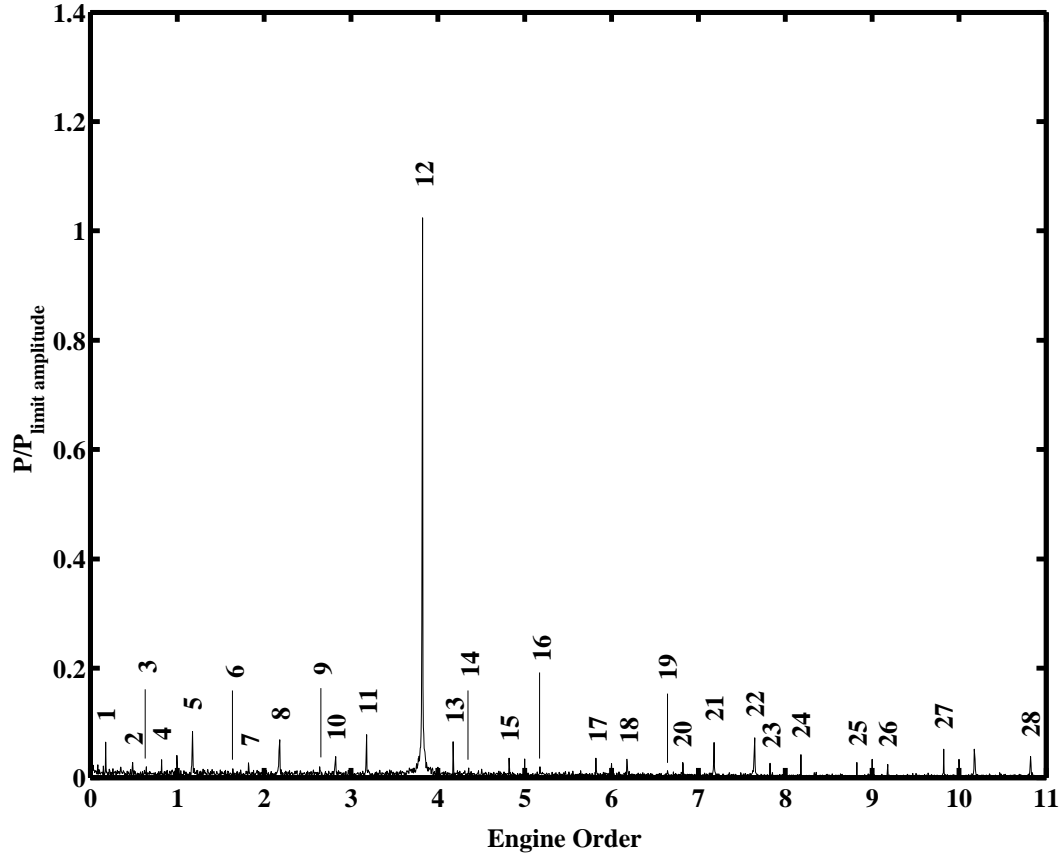


Figure 4.7: Cross-power spectral analysis of pressure transducers 7 and 8 at 20 seconds for the integration method at 70% corrected speed.

The signal to noise ratio for $n = 2$ in the limit amplitude region was improved from 47 ($m = 1$) to 80 with the integration method. Because the data was integrated over individual blade passages, a single numerical value was obtained for each blade passage. The integrated data has an effective sampling rate of 22 times the once-per-revolution rotational speed. Hence, the blade passing harmonics, $m > 0$, are not present in Figure 4.7 as

was seen in the figures of the previous section. The Nyquist frequency is $11E$, hence the Fourier Transform can only resolve frequencies up to $11E$. The flutter response at $3.82E$ is the dominant response. The dominant response along with many additional responses have been labeled in Figure 4.7 and listed in Table 4.1.

Table 4.1: Nodal diameter frequency for the largest flutter spectral response using pressure transducers 7 and 8 for the Integration Method.

| nodal diameter | frequency, (E) | frequency,(Hz) | Figure 4.7 label |
|----------------|----------------|----------------|------------------|
| $n = -2$ | 0.18 | 411 | 1 |
| $n = -5$ | 0.49 | 1233 | 2 |
| $n = -3$ | 0.64 | 822 | 3 |
| $n = -1$ | 0.82 | 411 | 4 |
| $n = -3$ | 1.18 | 411 | 5 |
| $n = -2$ | 1.64 | 822 | 6 |
| $n = -3$ | 1.82 | 411 | 7 |
| $n = 1$ | 2.18 | 411 | 8 |
| $n = -1$ | 2.64 | 411 | 9 |
| $n = 1$ | 2.82 | 411 | 10 |
| $n = -5$ | 3.18 | 411 | 11 |
| $n = 2$ | 3.82 | 411 | 12 |
| $n = -6$ | 4.18 | 411 | 13 |
| $n = -8$ | 4.35 | 822 | 14 |
| $n = 3$ | 4.82 | 411 | 15 |
| $n = -7$ | 5.18 | 411 | 16 |
| $n = 4$ | 5.82 | 411 | 17 |
| $n = -8$ | 6.18 | 411 | 18 |
| $n = 3$ | 6.64 | 822 | 19 |
| $n = 5$ | 6.82 | 411 | 20 |
| $n = -9$ | 7.18 | 411 | 21 |
| $n = 4$ | 7.64 | 822 | 22 |
| $n = 6$ | 7.82 | 411 | 23 |
| $n = -10$ | 8.18 | 411 | 24 |
| $n = 7$ | 8.82 | 411 | 25 |
| $n = -11$ | 9.18 | 411 | 26 |
| $n = 8$ | 9.82 | 411 | 27 |
| $n = 9$ | 10.82 | 411 | 28 |

The flutter response of 411 Hz has nodal diameters of $n = -11...9$. Flutter responses at 822 Hz and 1233 Hz , the second and third harmonics of the flutter frequency 411 Hz , were

present but at significantly lower amplitudes. Nodal diameters of $n = -8, -3, -2, 3, 4$ are seen for the flutter response at 822 Hz . The response at $n = -5$ for 1233 Hz has been labeled in Figure 4.7.

Strain Gages: The Two Probe Method

Data from strain gages 17 and 18 were analyzed in the same manner as the pressure transducer data. Figure 4.8 shows each of the FTs from strain gage 18 in a single waterfall plot. In a top down view of Figure 4.8, individual nodal and harmonic lines are shown in Figure 4.9. Figures 4.8 and 4.9 show a primary frequency line at 1.82 engine orders and a response at 3.64 engine orders with a much smaller amplitude. Cross-power spectra were calculated using strain gages 17 and 18. Figures 4.10 and 4.11 present results from the cross-power analysis applied to the $1.82E$ frequency line. Both figures show an established nodal diameter of approximately 2 by the 8 second mark. In agreement with the pressure transducer analysis, results from the limit amplitude region of the strain gage data show a flutter frequency of 411 Hz ($1.82E$) at approximately 2 nodal diameters with a higher harmonic response at a frequency of 822 Hz ($3.64E$) and approximately 4 nodal diameters at a much smaller amplitude. These results are in agreement with the responses measured with the pressure transducers. Like with the pressure transducers, there are 2 nodal diameter responses at various points preceding 8 seconds during the transient into flutter. The signal-to-noise ratio of the strain gage response in Figure 4.10 is 67 in the limit amplitude region. The noise level was determined from the Fourier transform at 20 seconds, see Figure 4.8.

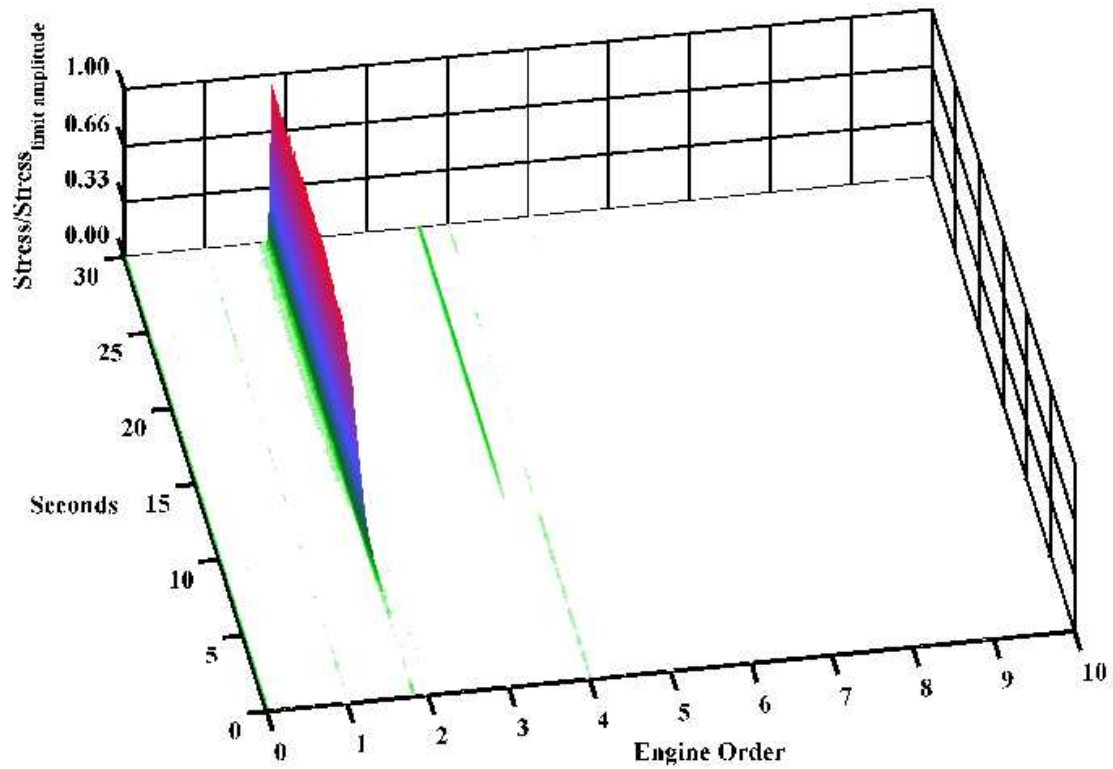


Figure 4.8: Successive Fourier transforms from strain gage 17. The peak response occurs at $1.82E$ as the fan is back-pressured into flutter for 70% corrected speed.

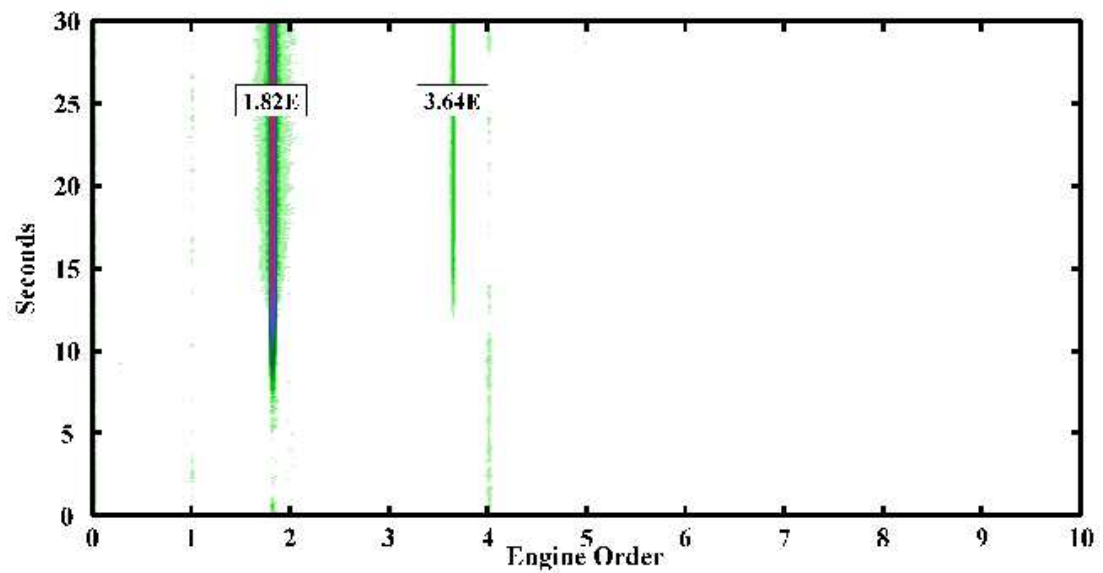


Figure 4.9: Top down view of Figure 4.8. The peak response occurs at $1.82E$.

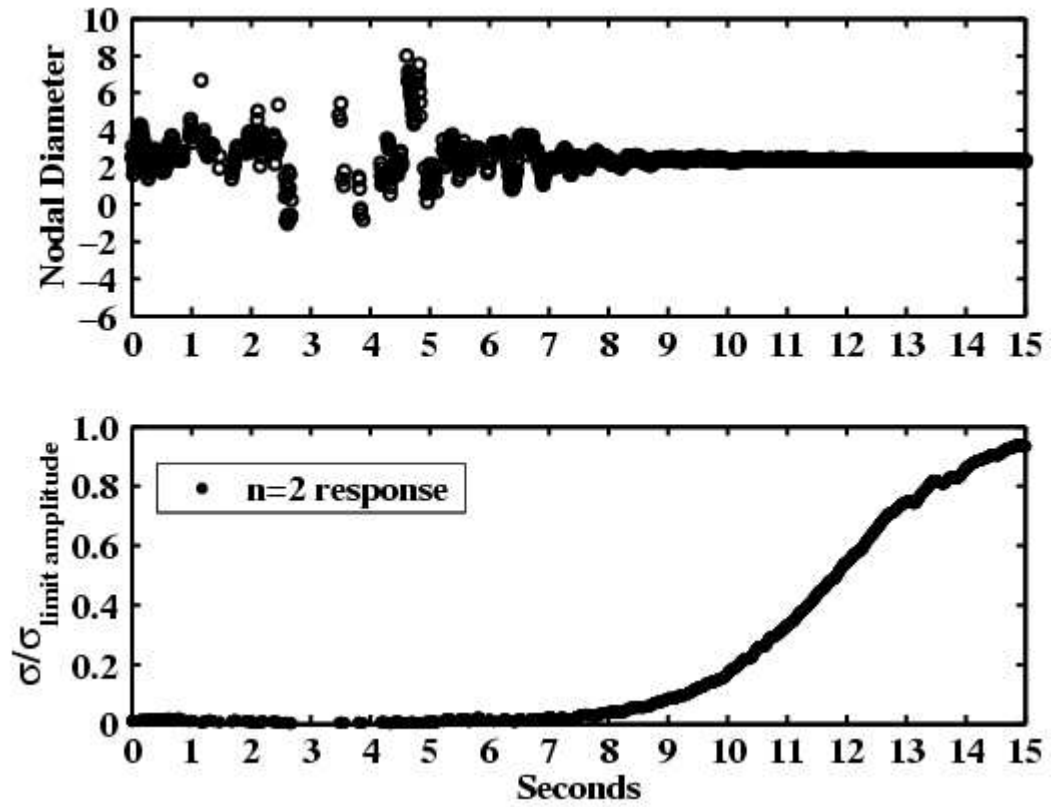


Figure 4.10: Cross-power spectral analysis of strain gages 17 and 18 as the fan is back-pressured into flutter at 70% corrected speed.

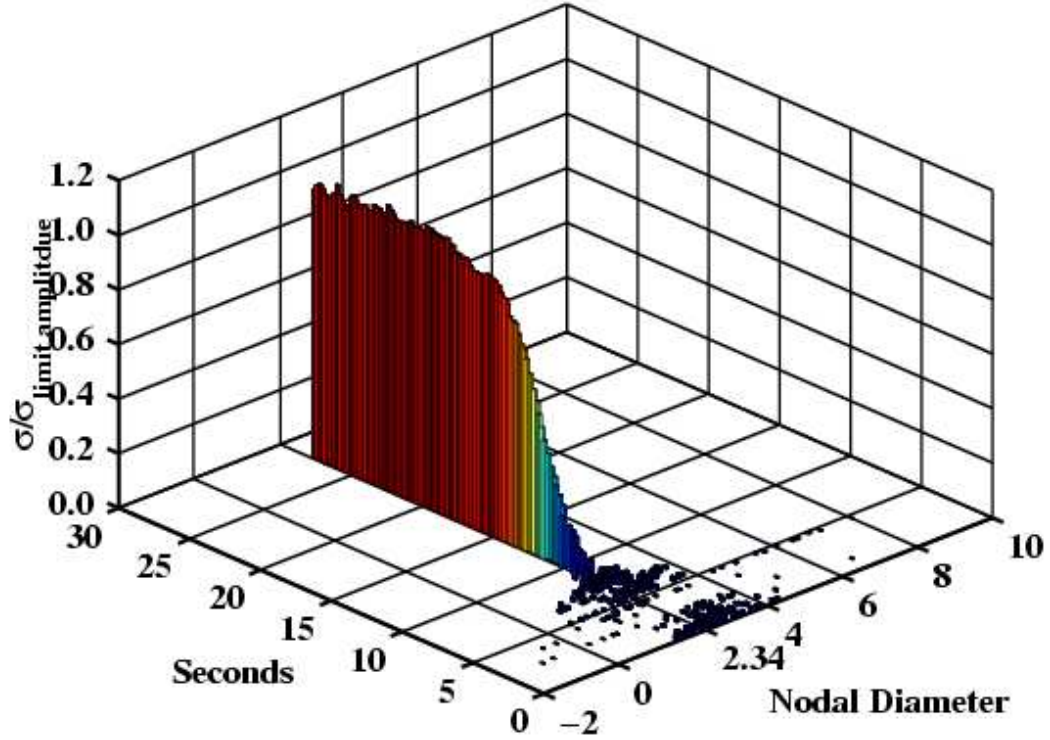


Figure 4.11: Strain gages 17 and 18 cross-power spectral analysis as the fan is back-pressured into flutter at 70% corrected speed.

The nodal diameter determined using the cross-power analysis was 2.34. As shown by the pressure transducers there are other nodal diameters present at the flutter frequency. For the stationary frame pressure transducers the different nodal diameters occur at different frequencies. However, the multiple nodal diameter response for the strain gages is occurring at a single frequency. Hence, the cross-power spectrum for the strain gages is giving a 'weighted average' for the nodal diameter, with a nodal diameter of 2 being the dominant response. Washburn (2002) has also discussed this issue.

Figure 4.12 shows the remarkable similarity between the casing mounted pressure transducer and blade mounted strain gage flutter responses. In this figure, the pressure transducer flutter response is the 411 Hz ($3.82E$) frequency line for a nodal diameter of 2 and $m = 0$ harmonic. The strain gage flutter response is the 411 Hz ($1.82E$) frequency line. The correlation between the pressure transducers and strain gages is excellent.

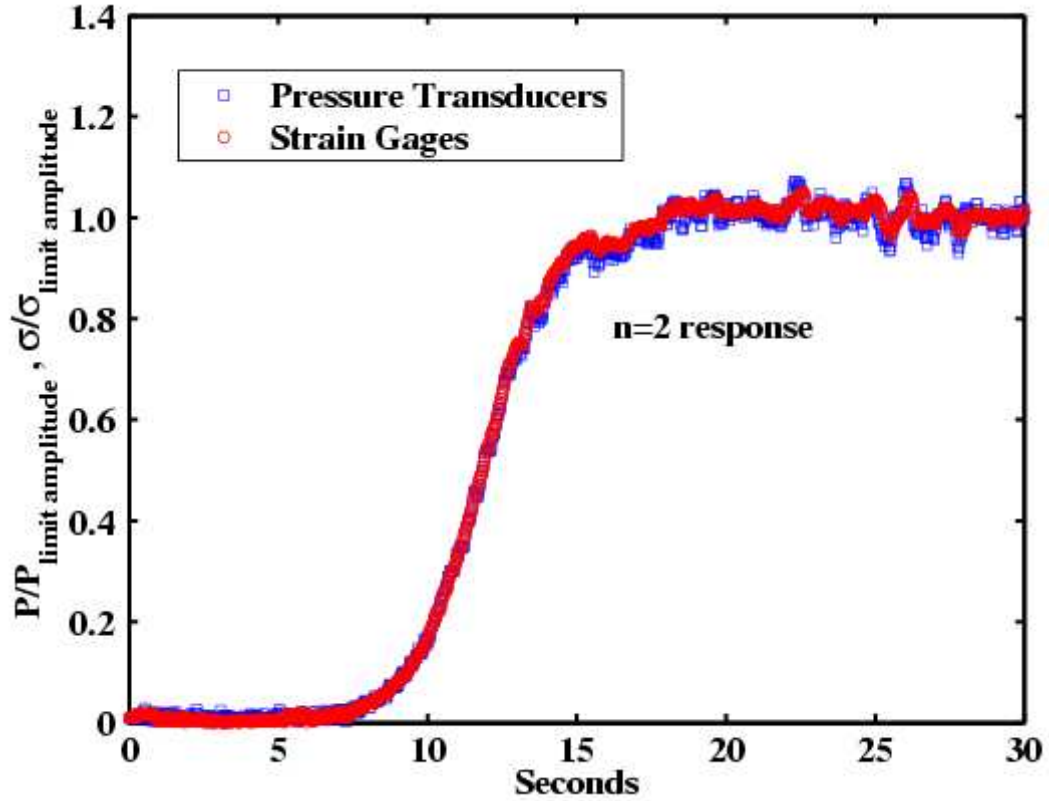


Figure 4.12: Cross-power spectral analysis of strain gages 17 and 18 and pressure transducers 11 and 12 as the fan is back-pressured into flutter at 70% corrected speed.

Summary of Two Probe Method

The two probe method was applied to the casing mounted high frequency response pressure transducer and blade mounted strain gage data at 70% corrected speed. The pressure transducer analysis produced results showing the stall flutter response to have multiple nodal diameter and multiple harmonic content. The flutter frequency of 411 Hz was identified with a dominant nodal diameter of 2. For the zeroth harmonic, $m = 0$, nodal diameters of 2, 4 and 5 were identified for the flutter frequency of 411 Hz . Additionally, the nodal diameter of 2 at 411 Hz showed responses at harmonics of $m = -5 \dots 5$, with the largest amplitudes occurring at $m = \pm 1$. Responses at 822 Hz , the second harmonic of the flutter

frequency, were identified to have a nodal diameter of 4 at harmonics of $m = 1, 2$ and 3, but at a smaller amplitude.

The integration method improved the signal to noise ratio from 47 ($m = 1$) to 80 in the limit amplitude response region. The sampling rate is reduced to 22 times the once-per-revolution rotational frequency, and there are no wave harmonics (m) for this method. However, in addition to the responses observed with the cross-power spectral analysis applied to the signal, nodal diameters for the flutter response at 411 Hz spanned the range of $n = -11 \dots 9$, with the dominant response occurring at $n = 2$. In addition to the nodal diameter of $n = 4$, nodal diameters of $n = -8, -3, -2, 3$ at much smaller amplitudes were also identified at the second harmonic of 822 Hz . Flutter responses at the third harmonic of 1233 Hz were also identifiable, but at a much smaller amplitude.

The two probe method applied to the strain gage data provided results in agreement with the two probe pressure transducer results. Flutter responses at 411 Hz and 822 Hz were identified, where the gross nodal diameters were 2 and 4, respectively.

Although the two probe analysis on the pressure data, pressure data using the integration method, and strain gage data provided excellent results in the rapid growth region and the limit amplitude region, it did not clearly show a flutter signature in the transitional region prior to 8 seconds. As will be shown in the following Multiprobe Method sections, flutter responses can be detected in the transitional region prior to 8 seconds.

Pressure Transducers: The Multiprobe Method

A two-dimensional space-time analysis was performed on the casing mounted pressure transducers. Figure 2.3 shows the relative positions of the casing mounted pressure transducers. For each pressure transducer an angular position, θ , can be assigned in the stationary reference frame. Each pressure transducer has a recorded signal representing $p(t)$. The casing mounted pressure transducers, located at the same axial location, can be

combined to produce a two-dimensional representation of the pressure field, $p(t, \theta)$. In this study there were 12 casing mounted pressure transducers located at the same axial location. Pressure transducer 13 failed early in testing. Pressure transducer 3 is located half way between transducers 4 and 5. With this arrangement of the pressure transducers, the normal two-dimensional Fourier transform can not be used. Instead, an unequally spaced two-dimensional Fourier transform algorithm was used, see Appendix B.

Figure 4.13 is a two-dimensional Fourier transform of the high frequency response pressure transducer data at 16 seconds. The number of data points used was 8303 points, 25 rotor revolutions, from each of the 11 working casing mounted pressure transducers. This number of points was chosen to increase the accuracy of the Fourier transform at the frequency line of $25.82E$. Figure 4.13 appears to have “pyramids.” The pyramid effect is a result of creating a continuous surface even though there exists only 11 discrete data points along the nodal diameter axis. When looking at these types of figures, the true results lie along the nodal diameter lines shown in the figures. The figures are presented in this fashion because it enhances the ability to follow a given frequency line across the nodal diameters. The frequency line of $25.82E$ had the strongest flutter response in the transistional region for the multiprobe analysis. The blade passing frequencies have been removed for easy viewing of the flutter responses. At 16 seconds, the fan has moved into the limit amplitude region of the flutter response. The blade passing frequencies associated with the labeled frequencies in Figure 4.13 are $22E$, $44E$, $66E$ and $88E$. Equation 3.7 can be used to calculate the rotating frame frequency ω . Several frequencies have been labeled in Figure 4.13 and listed in Table 4.2. The dominant rotating reference frame frequency for the flutter response was calculated to be 411 Hz with a nodal diameter of $n = 2$ at wave harmonics of $m = 0, \pm 1, \pm 2, \pm 3, \pm 4$, and ± 5 . Responses for the second harmonic of 411 Hz at 822 Hz occurred at a nodal diameter of $n = 4$ with wave harmonics of $m = 1, 2$, and 3 . These responses are at lower amplitude.

The flutter response could also be resolved with a smaller number of data points. Fig-

ure 4.14 is a two-dimensional Fourier transform of the pressure transducer data at 16 seconds using 3933 points, 12 rotor revolutions.

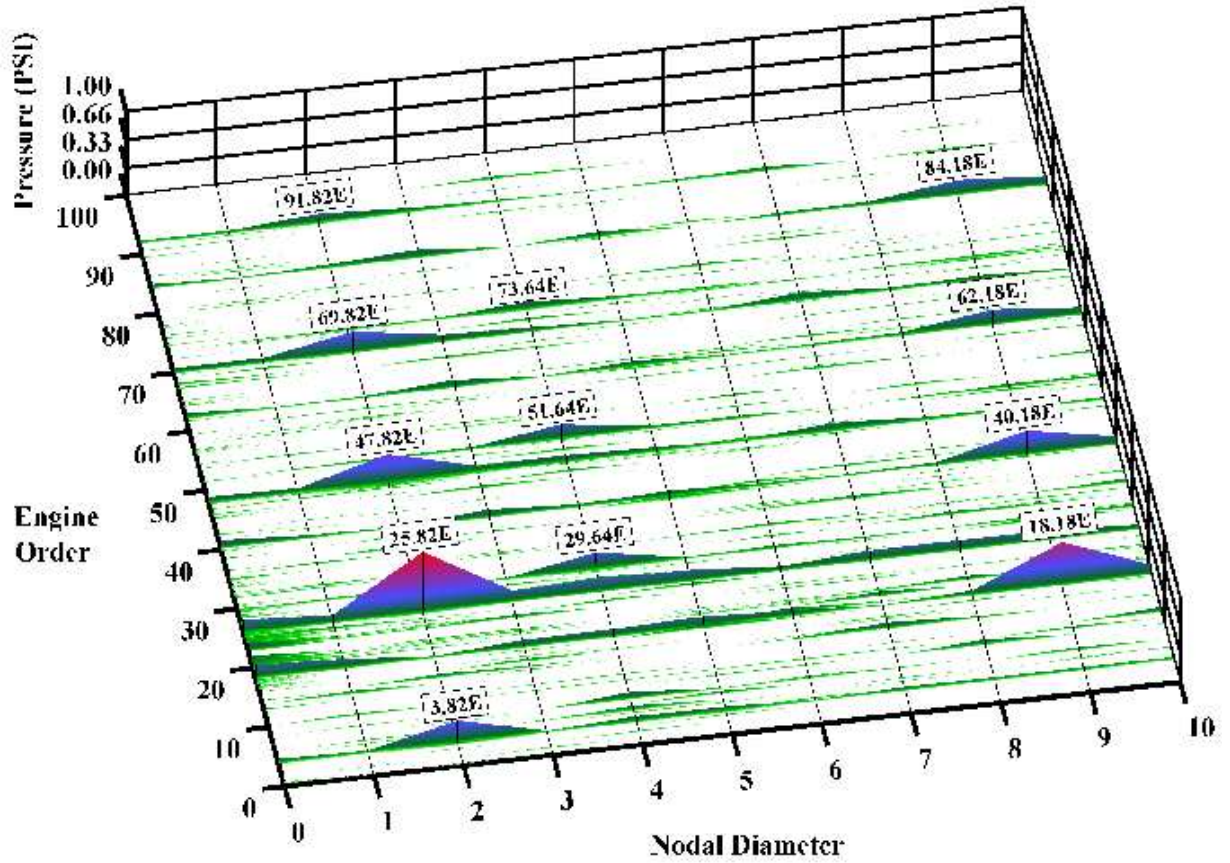


Figure 4.13: Two-dimensional Fourier transform of pressure transducer data at 16 seconds using 25 rotor revolutions for 70% corrected speed.

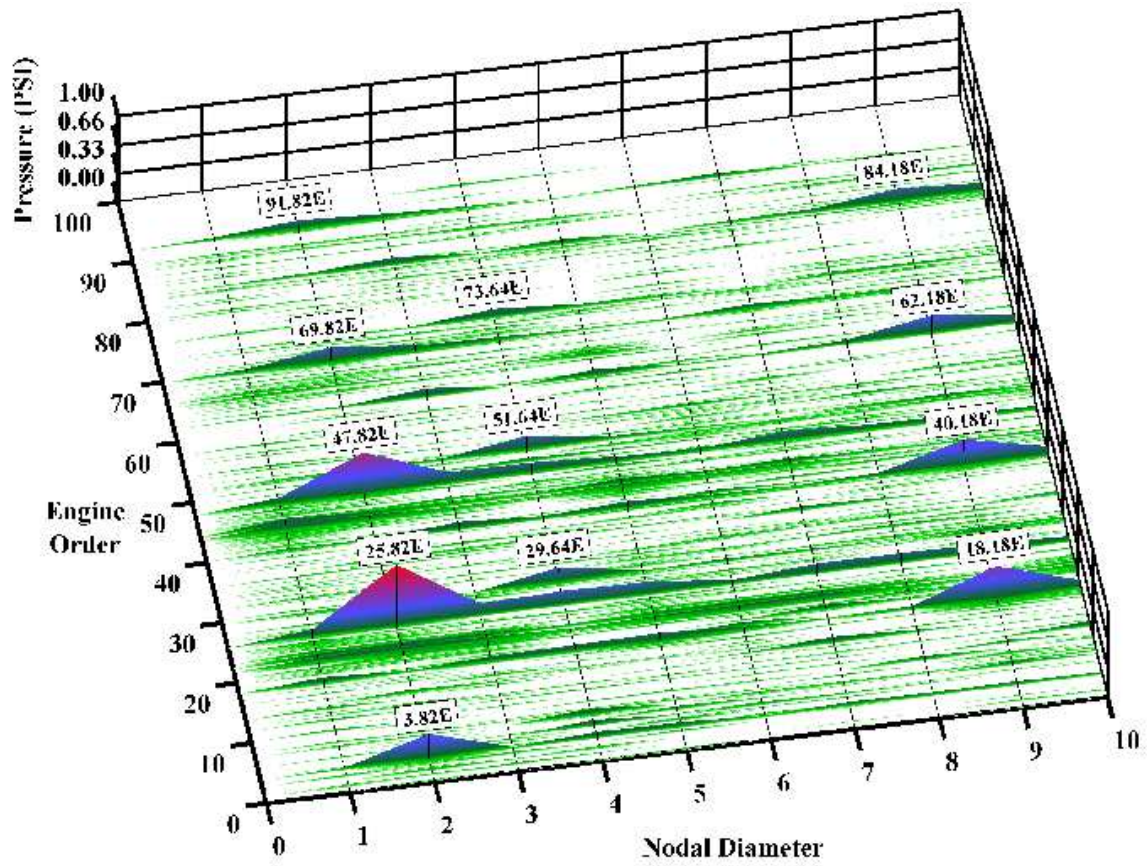


Figure 4.14: Two-dimensional Fourier transform of pressure transducer data at 16 seconds using 12 rotor revolutions for 70% corrected speed.

Table 4.2: Nodal diameter, wave harmonic, and rotating reference frame frequency for the largest flutter spectral responses in Figure 4.13.

| stationary frame frequency, E | nodal diameter, n | wave harmonic, m | rotating frame frequency, Hz |
|---------------------------------|---------------------|--------------------|--------------------------------|
| 3.82 | 2 | 0 | 411 |
| 25.82 | 2 | +1 | 411 |
| 47.82 | 2 | +2 | 411 |
| 69.82 | 2 | +3 | 411 |
| 91.82 | 2 | +4 | 411 |
| 29.64 | 4 | +1 | 822 |
| 51.64 | 4 | +2 | 822 |
| 73.64 | 4 | +3 | 822 |
| 18.18 | 2 | -1 | 411 |
| 40.18 | 2 | -2 | 411 |
| 62.18 | 2 | -3 | 411 |
| 84.18 | 2 | -4 | 411 |

To study the evolution of the stall flutter response, successive two-dimensional Fourier transforms were calculated along the entire length of the pressure transducer data. After calculating the Fourier transforms, results for $n = 2$ were extracted from each transform and combined to form a single surface plot. Figure 4.15 shows the results obtained for $n = 2$ around the flutter response frequency of $25.82E$. These results indicate that a flutter response at $n = 2$ is occurring in the transitional region prior to 8 seconds. After 8 seconds the fan quickly moves into fully developed flutter, as was seen in Figure 4.1. The surface plot in Figure 4.15 is presented from a top-down viewpoint to more clearly show the flutter response. Figure 4.15 shows a strong 2 nodal diameter response for 0 to 1 seconds and between 6.5 and 8 seconds. Figure 4.15 was calculated using 8303 data points in the Fourier transform, 25 rotor revolutions, from each of the pressure transducers. Figure 4.16 was calculated using 3933 data points in the Fourier transform, 12 rotor revolutions, from each pressure transducer. Because the casing mounted pressure transducers were placed 1 inch upstream of the leading edge of the rotor blades, the amplitude of the pressure waves significantly decreased by the time the waves reached the pressure transducers. Hence,

it was necessary to increase the number of data points in the Fourier transforms to help improve the resolution of the flutter response in the transitional region. It is believed that fewer rotor revolutions could have been used if the pressure transducers were placed closer to the rotor leading edge. Nevertheless, the flutter signature is also clearly evident with smaller number of rotor revolutions.

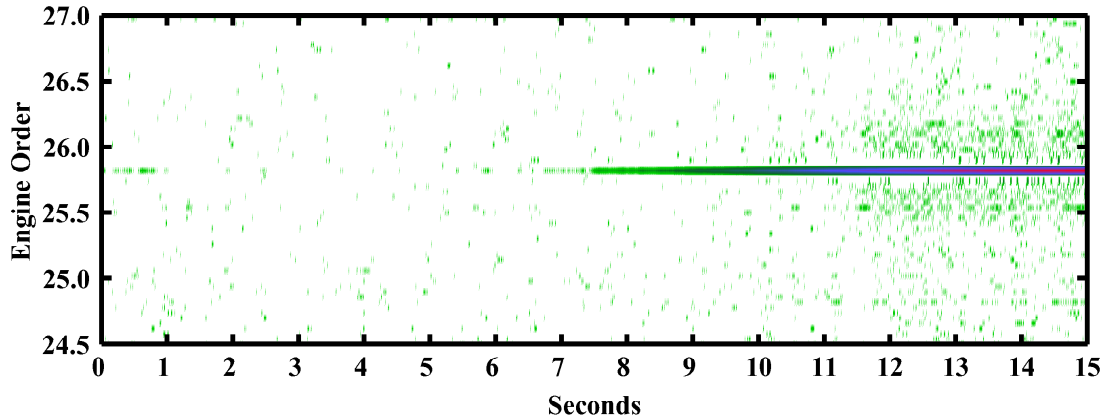


Figure 4.15: Two-dimensional Fourier transform of pressure transducer data using 25 rotor revolutions as the fan is back-pressured into flutter for $n = 2$ and $m = 1$ at 70% corrected speed.

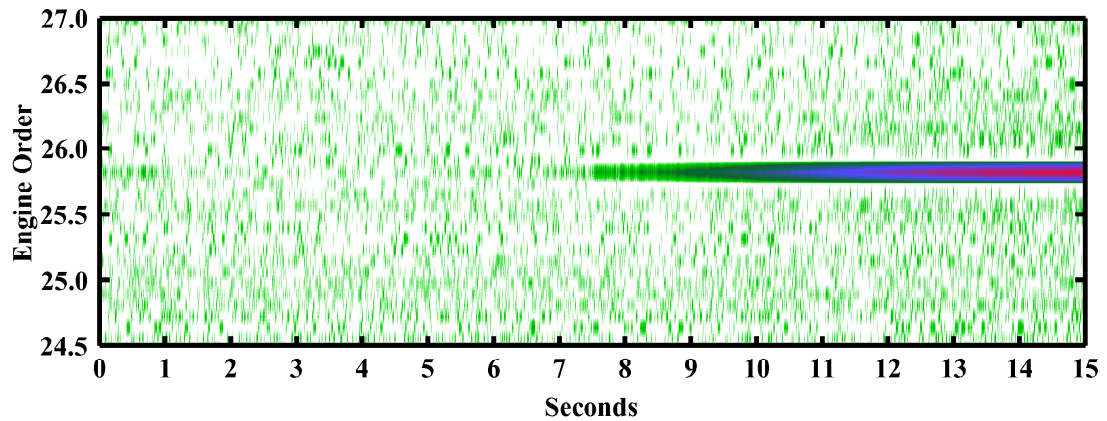


Figure 4.16: Two-dimensional Fourier transform of pressure transducer data using 12 rotor revolutions as the fan is back-pressured into flutter for $n = 2$ and $m = 1$ at 70% corrected speed.

Figures 4.17 and 4.18 represent the results from the two-dimensional space-time anal-

ysis where individual nodal diameters for $n = 4$ and $n = 5$ were extracted from each Fourier transform for the flutter frequency of 411 Hz relative to the rotating reference frame. Figure 4.17 presents results for the stationary frequency of $5.82E$. For $5.82E$, the nodal diameter is $n = 4$ and the wave harmonic is $m = 0$. The flutter response at this frequency becomes fully developed after 9 seconds, whereas the nodal diameter response of $n = 2$ for 411 Hz became fully developed after 8 seconds. Figure 4.17 gives no clear indication of flutter in the transitional region before 8 seconds. Figure 4.18 presents results for the frequency of $6.82E$. For $6.82E$, the nodal diameter is $n = 5$ and the wave harmonic is $m = 0$. Like the $5.82E$ response, the $6.82E$ response becomes fully developed after 9 seconds. This is consistent with the two probe results presented in Figure 4.6.

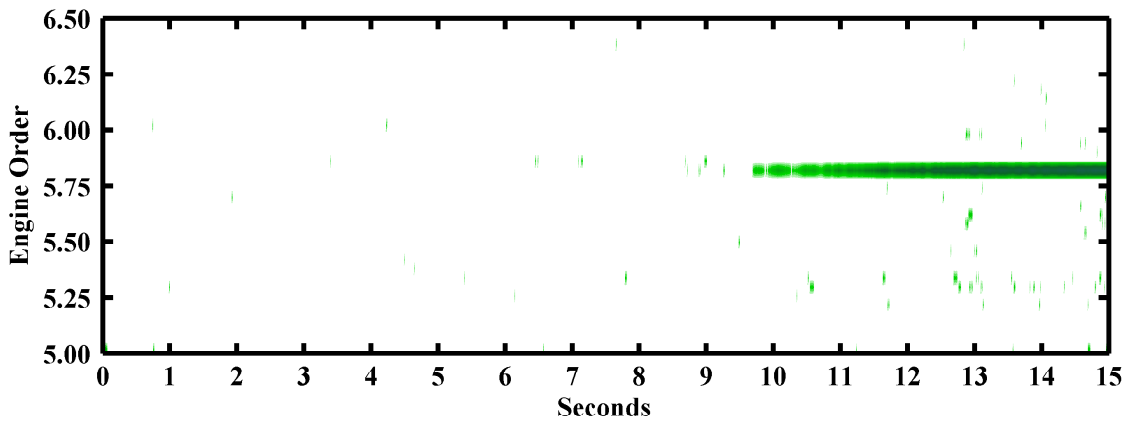


Figure 4.17: Two-dimensional Fourier transform of pressure transducer data using 25 rotor revolutions as the fan is back-pressured into flutter for $n = 4$ and $m = 0$ at 70% corrected speed.

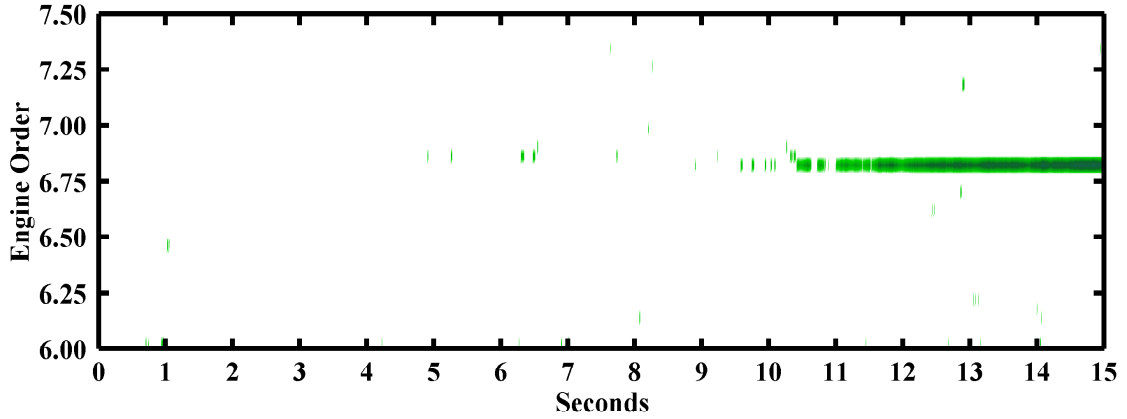


Figure 4.18: Two-dimensional Fourier transform of pressure transducer data using 25 rotor revolutions as the fan is back-pressured into flutter for $n = 5$ and $m = 0$ at 70% corrected speed.

The results presented in Figures 4.17 and 4.18 for nodal diameters of $n = 4$ and $n = 5$, respectively, at a wave harmonic of $m = 0$ reflect what was seen at the other nodal diameters for the flutter response at 411 Hz and 822 Hz . There were no significant responses in the transitional zone for the other nodal diameters at 411 Hz and 822 Hz . Additionally, the flutter response was seen to occur at wave harmonics of 411 Hz with no significant amplitude responses at other frequencies being present in either the transitional region, the rapid growth region, or the limit amplitude region.

Pressure Transducers: The Integration Method Using the Multiprobe Method

Two-dimensional Fourier transforms were applied to pressure transducer data that underwent the integration method. The number of data points used was 1024 points, 47 rotor revolutions, from each of the 11 working casing mounted pressure transducers. This number of points was chosen to decrease the time interval spanned by the Fourier transform. The effective sampling frequency for the integrated data is reduced from 75 kHz to 22 times the once-per-revolution rotational frequency and there are no wave harmonics (m)

for this case. Recall from the previous section the casing mounted pressure transducers can be combined to produce a two-dimensional pressure field, $p(t, \theta)$. Figure 4.19 is a two-dimensional Fourier transform of the pressure transducer data using the integration method at 16 seconds. Several of the stronger responses have been labeled in Figure 4.19. Table 4.3 summarizes the responses labeled in this Figure.

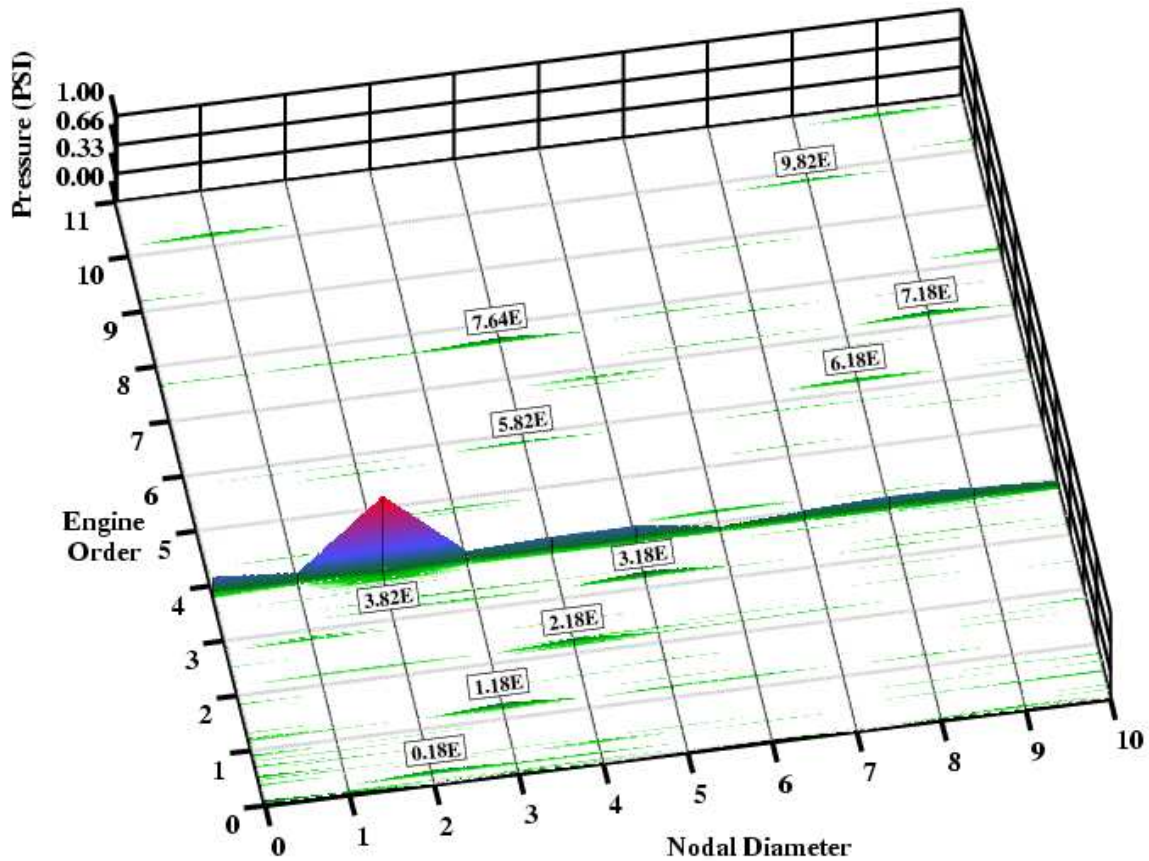


Figure 4.19: Two-dimensional Fourier transform of pressure transducer data using the integration method at 16 seconds for 70% corrected speed.

Table 4.3: Nodal diameter, wave harmonic, and rotating reference frame frequency for the largest flutter spectral responses in Figure 4.19.

| stationary frame frequency, E | nodal diameter, n | rotating frame frequency, Hz |
|------------------------------------|------------------------|-----------------------------------|
| 0.18 | -2 | 411 |
| 1.18 | -3 | 411 |
| 2.18 | 1 | 411 |
| 3.18 | -5 | 411 |
| 3.82 | 2 | 411 |
| 5.82 | 4 | 411 |
| 6.18 | -8 | 411 |
| 7.18 | -9 | 411 |
| 7.64 | 4 | 822 |
| 9.82 | 8 | 411 |

Successive two-dimensional Fourier transforms were calculated along the entire length of the pressure transducer data, using the integration method, to study the evolution of the stall flutter response. The results for the $n = 2$ were extracted from each successive Fourier transform and combined into a single surface plot. Figure 4.20 shows the results for $n = 2$ around the flutter response of $3.82E$.

As with the two probe method, the integration method improved the signal-to-noise ratio significantly. The noise amplitude was established using Figure 4.15, where 99% of the random frequencies are below it. The signal-to-noise ratio for $n = 2$ at $25.82 E$ ($m = 1$) in Figure 4.13 is 58, and the signal-to-noise ratio for $n = 2$ at $3.82 E$ in Figure 4.19 is 71. As was seen in Figure 4.15, Figure 4.20 shows a strong 2 nodal response from 0 to 1 seconds, and between 6.25 and 8 seconds.

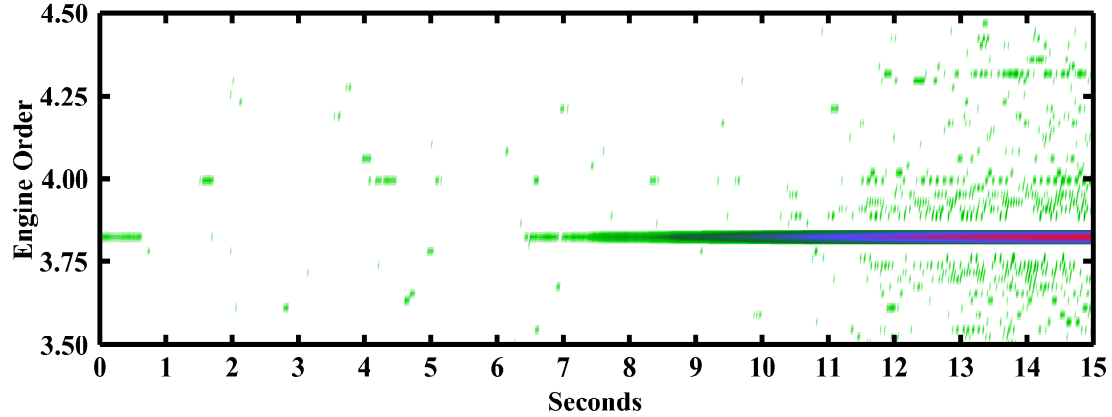


Figure 4.20: Two-dimensional Fourier transform of pressure transducer data using the integration method as the fan is back-pressured into flutter for $n = 2$ at 70% corrected speed.

The integration method enhanced the resolution of the flutter response. Flutter responses were seen before 8 seconds, the beginning of the rapid growth region.

Strain Gages: The Multiprobe Method

There were six working strain gages in this study. Figure 2.3 shows the relative positions of the six blade mounted strain gages. The two-dimensional space-time method using the unequally spaced Fourier transform algorithm was applied to the strain gage data. Figure 4.21 is a two-dimensional Fourier transform of the strain gage data at 16 seconds. The number of data points used in the Fourier transform was 8205, 25 rotor revolutions, to increase the accuracy of the transform along the $1.82E$ frequency line. Unlike the two-probe cross-power spectral analysis, the two-dimensional space-time analysis of the strain gage data is capable of resolving the individual nodal diameters. Unfortunately, the configuration of the strain gages spans approximately 196 degrees around the circumference of the rotor, as seen in Figure 2.3. With this configuration a 2 nodal diameter response will also produce a false 4 nodal diameter response, so this analysis can not be used to definitively prove the existence of the 4 nodal diameter response for the strain gages. However, this analysis is capable of resolving a flutter response for this strain gage configuration. A

strong 2 nodal diameter response can be seen in Figure 4.21 at the frequency of $1.82E$. Although not clearly visible in Figure 4.21, the flutter response at $3.64E$ can be resolved, but it is at a significantly smaller amplitude.

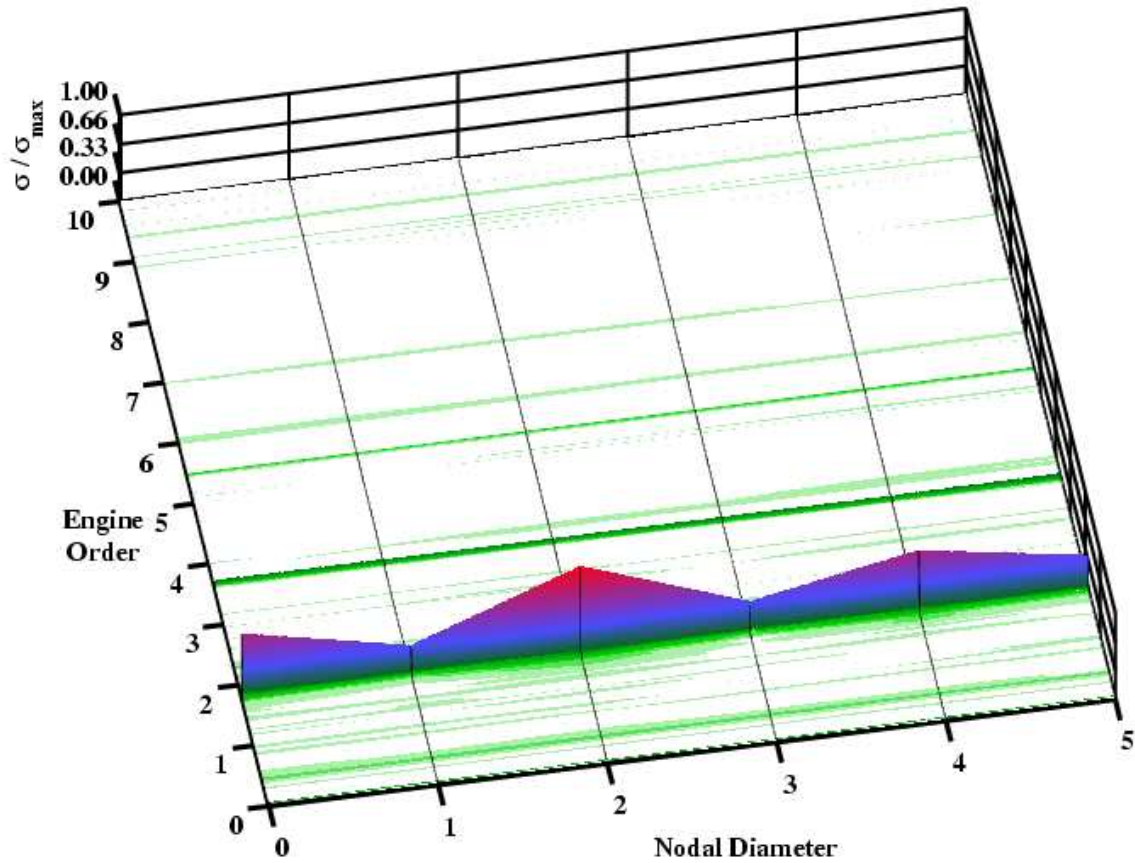


Figure 4.21: Two-dimensional Fourier transform of strain gage data at 16 seconds for 70% corrected speed.

Again, successive two-dimensional Fourier transforms were computed along the entire length of the strain gage data. The results for 2 nodal diameter were extracted from each successive Fourier transform. Figure 4.22 shows the flutter response along the $1.82E$ frequency line. A strong 2 nodal diameter response exist between 0 and 1 seconds and between 5 and 8 seconds in the transitional region before the rapid growth region that starts after 8 seconds. The low level $2E$ response is attributed to two boundary layer probes separated by 180 degrees and located upstream of the rotor (Sanders et al. (2003)).

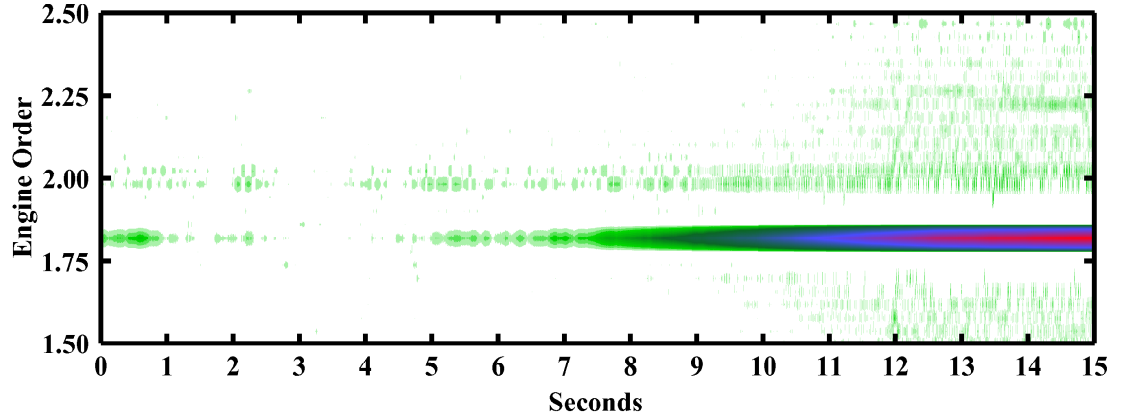


Figure 4.22: Two-dimensional Fourier transform of strain gage data as the fan is back-pressured into flutter for $n = 2$ at 70% corrected speed.

Summary for Multiprobe Method

The two-dimensional space-time analysis established the existence of flutter activity in the transitional region preceding 8 seconds, after which the rapid growth region begins and quickly evolves into a limit amplitude response. The space-time analysis was performed on casing mounted high frequency response pressure transducer data, casing mounted high frequency response pressure transducer data using the integration method, and blade mounted strain gage data. The space-time analysis has advantages over the two probe analysis. The two probe analysis only uses data along the time direction with the only circumferential information being the angular distance between the two transducers. The space-time analysis uses data points from both the time direction and the entire circumferential direction, building a much better view of the pressure field.

The results from the space-time analysis are in excellent agreement with the results of the two probe analysis. The two probe analysis had difficulty resolving flutter activity in the transitional region, but the space-time analysis was a lot more definitive in resolving the existence of an established nodal diameter, i.e. circumferential traveling wave, in the transitional region. A flutter response between 0 and 1 seconds, and 6.5 and 8 seconds

for a nodal diameter of 2 along the $25.82E$ frequency line was resolved from the pressure transducer data. A flutter response between 0 and 1 seconds, and 6.25 and 8 seconds for a nodal diameter of 2 along the $3.82E$ frequency line was resolved from the pressure transducer data with the integration method. The space-time analysis for the strain gage data resolved a flutter response with a strong 2 nodal diameter at $1.82E$ between 0 and 1 seconds, and between 5 and 8 seconds. All the two-dimensional analyses were in excellent agreement with each other.

The pressure transducers were placed 1 inch (2.54 cm) forward of the leading edge of the rotor blades, approximately $\frac{3}{4}$ of an inch (1.905 cm) further than desired, significantly reducing the pressure transducers' ability to detect the flutter signal. Even with this placement of the pressure transducers, the results from the pressure transducers and strain gages were in excellent agreement.

The multiprobe method using the integration method exhibited excellent agreement with the two probe analysis using the integration method within the rapid growth and limit amplitude regions. Multiple nodal diameters were identified as shown in Figure 4.19. The signal-to-noise ratio improved showing stronger flutter activity between 0 and 1 seconds and 6.25 and 8 seconds within the transitional region, see Figure 4.20.

Within the rapid growth and limit amplitude regions, the multiprobe analysis provide results in agreement with the two probe analysis. The multiprobe analysis had the advantage that the two-dimensional Fourier transforms readily provided the nodal diameter and frequencies simultaneously, see Figure 4.13, whereas the two probe method requires a cross-power spectrum to calculate the nodal diameter.

Open Clearance Data

This section will present the analysis results for data recorded with open clearance at 70% corrected speed. Due to the quality of the pressure transducer data, only pressure

transducer results will be presented.

Figure 4.23 presents the time dependent data for strain gage 7. The rapid growth region begins at 4.5 seconds and continues until the fan is moved out of flutter by opening the discharge valves. The fan was moved out of flutter before the limit amplitude response occurred.

In reference to Figure 4.23, a cross-power spectral analysis was performed at the peak amplitude of the flutter response at 11 seconds using pressure transducer data. The spectral content at 11 seconds using pressure transducers 7 and 8 is shown in Figure 4.24. The spectral content of the flutter response is very similar to the spectral content of the flutter response that occurred at 70% corrected speed with closed clearance. The dominant response was at 411 Hz and nodal diameter 2. The secondary response occurred at 822 Hz and nodal diameter 4. Wave harmonics of $m = 0, \pm 1, \pm 2, \pm 3, \pm 4$ for $n = 2$ at 411 Hz are seen in Figure 4.24. The wave harmonics $m = \pm 4$ are more prevalent in the open clearance data than was seen in the closed clearance data.

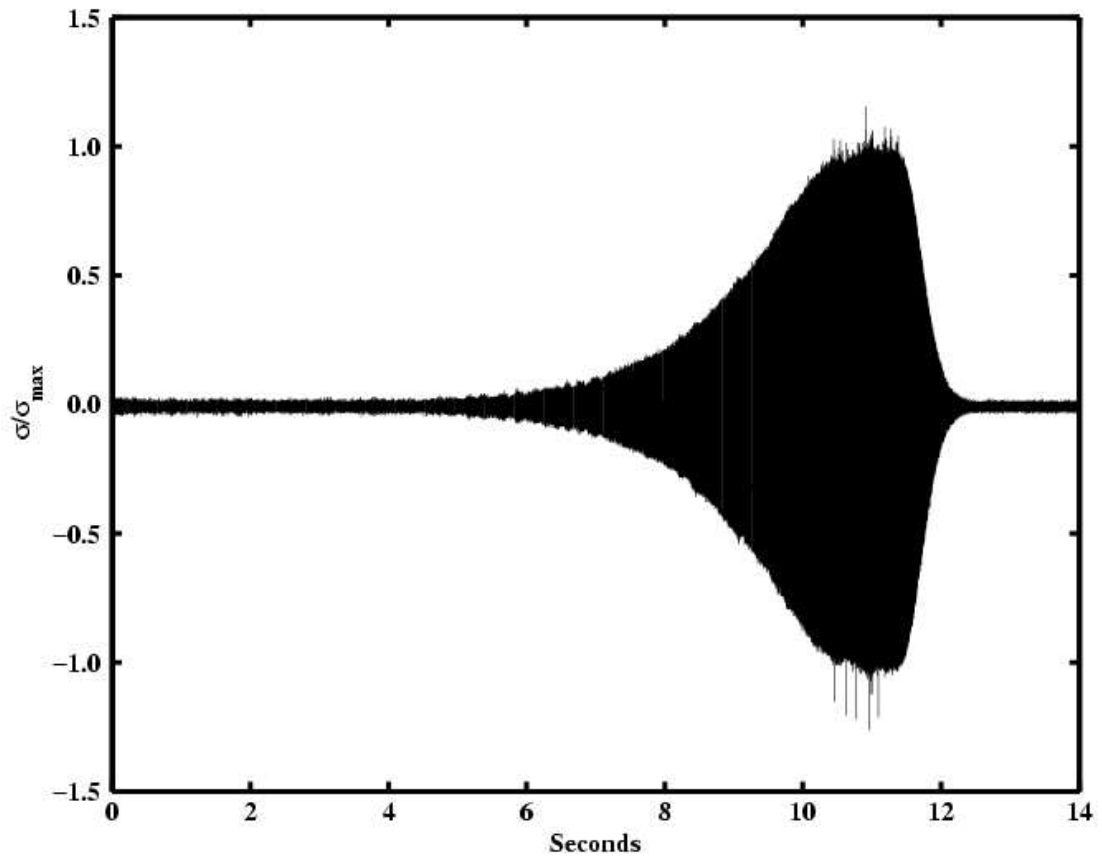


Figure 4.23: Time dependent data for strain gage 7 as the fan is back-pressured into flutter at 70% corrected speed with open clearances.

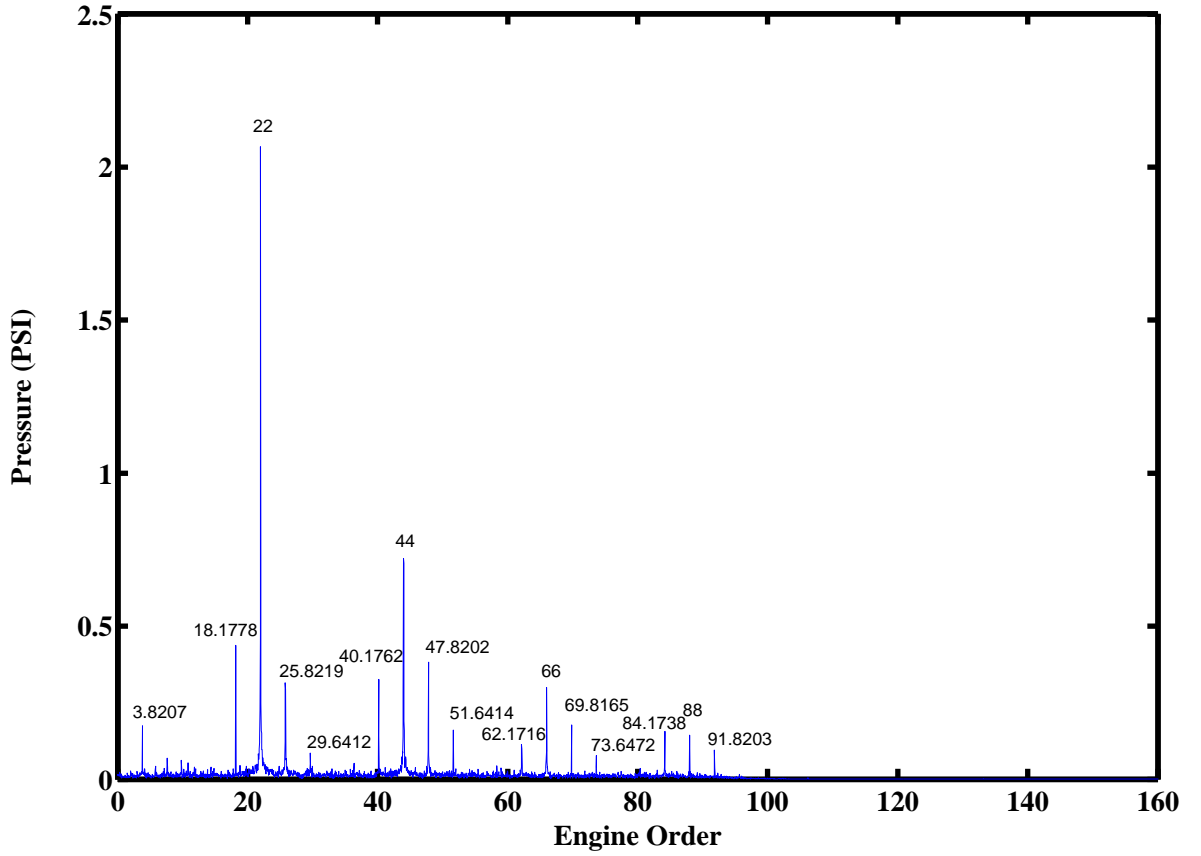


Figure 4.24: Cross-power spectral content for pressure transducers 7 and 8 at 11 seconds at 70% corrected speed with open clearances.

The two-dimensional space-time analysis was performed on the open clearance data. The two-dimensional Fourier transform at 10.5 seconds is presented in Figure 4.25. Figure 4.25 is very similar to Figure 4.13, showing essentially the same flutter response with small differences in the amplitudes. Figure 4.26 presents results from the pressure transducer data as the fan is back-pressured into flutter for nodal diameter 2 and wave harmonic 1. In Figure 4.26 the time axis has been referenced to the point of flutter initiation, hence $t = 0$ is at the beginning of the rapid growth region with the subfigures stopping at this point or proceeding just past it. Like the closed clearance results, flutter activity is seen within the transitional region prior to the rapid growth region for the open clearance results. The initial flutter response occurred between -4.5 and -4 seconds, at the beginning

of the time recorded data or 4.5 seconds prior to the rapid growth region. Additionally, flutter responses occurred between -3.25 and -2.5 seconds and between -0.25 and 0 seconds.

A reference pressure was taken from the two-dimensional Fourier transform results at the time when the strain gage response exceeded 10 KSI peak-to-peak, for both open and closed clearances. For 70% closed clearance, the pressures at -7.39 and -0.1 seconds are respectively 29.8% and 47.5% of the reference pressure. For 70% open clearance, the pressure at -4.45 seconds is 17.3% of the reference pressure.

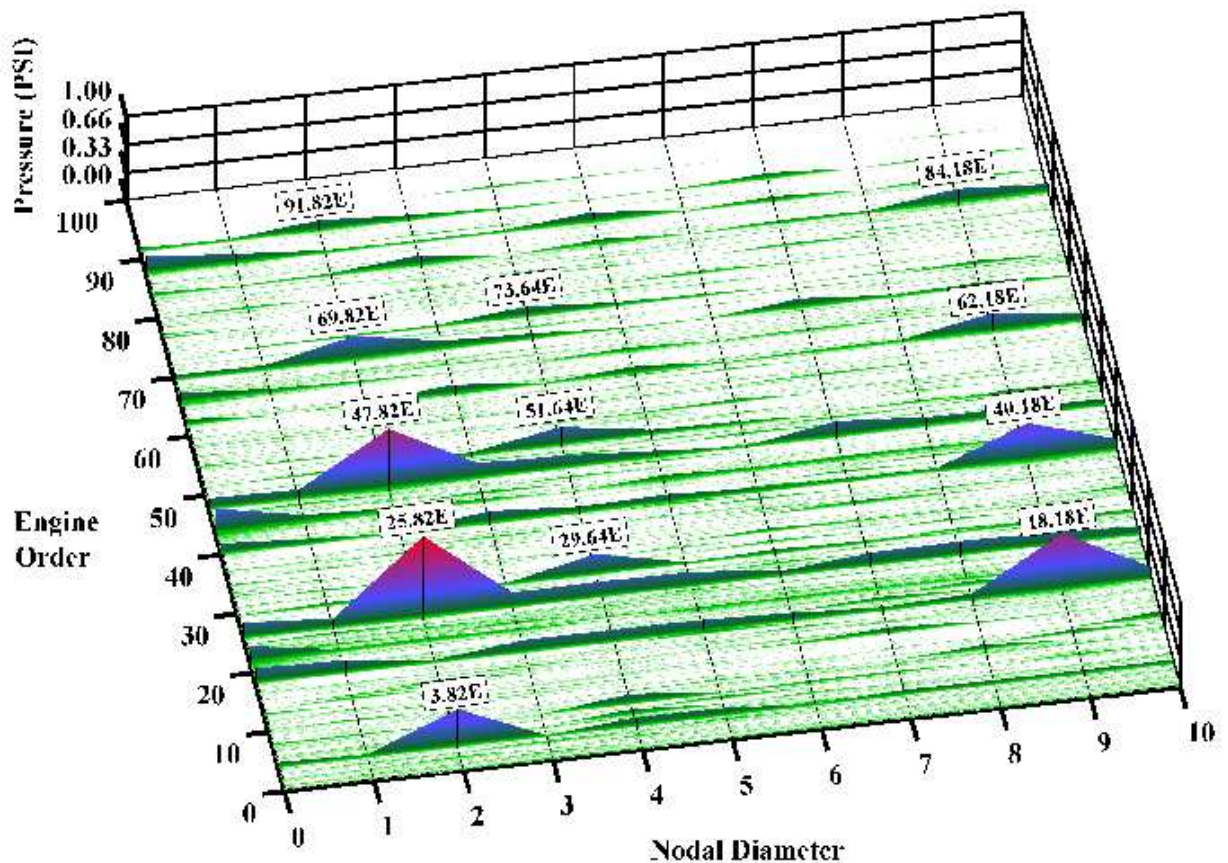
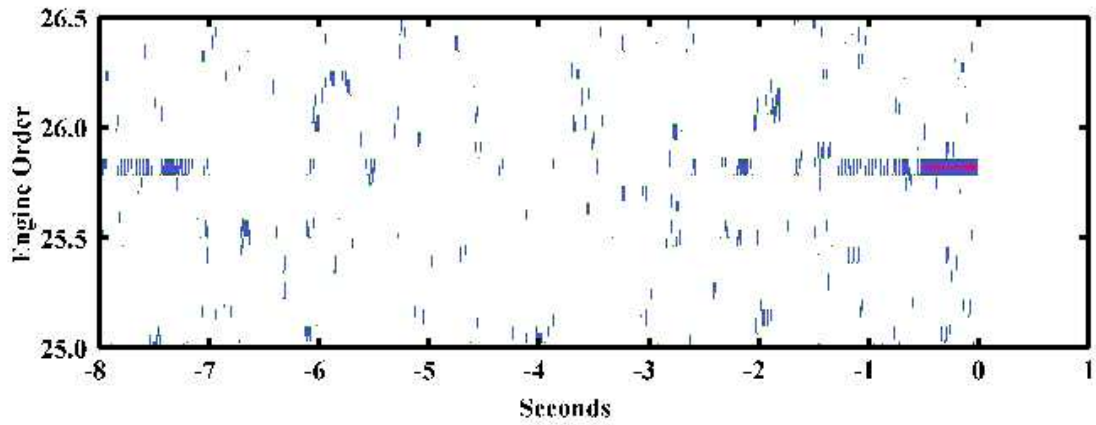
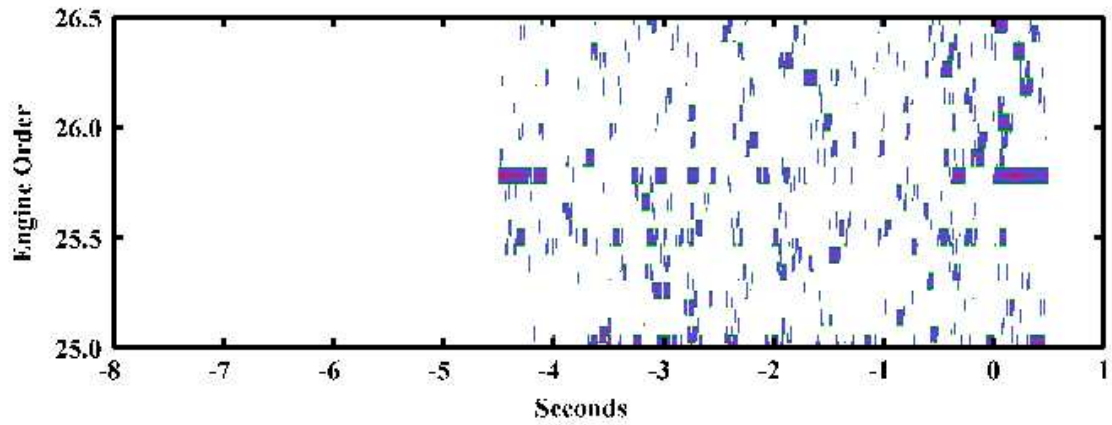


Figure 4.25: Two-dimensional Fourier transform of pressure transducer data at 10.5 seconds using 25 rotor revolutions for 70% corrected speed with open clearances.



(a) Pressure transducer data for 70% corrected speedline with closed clearance



(b) Pressure transducer data for 70% corrected speedline with open clearance

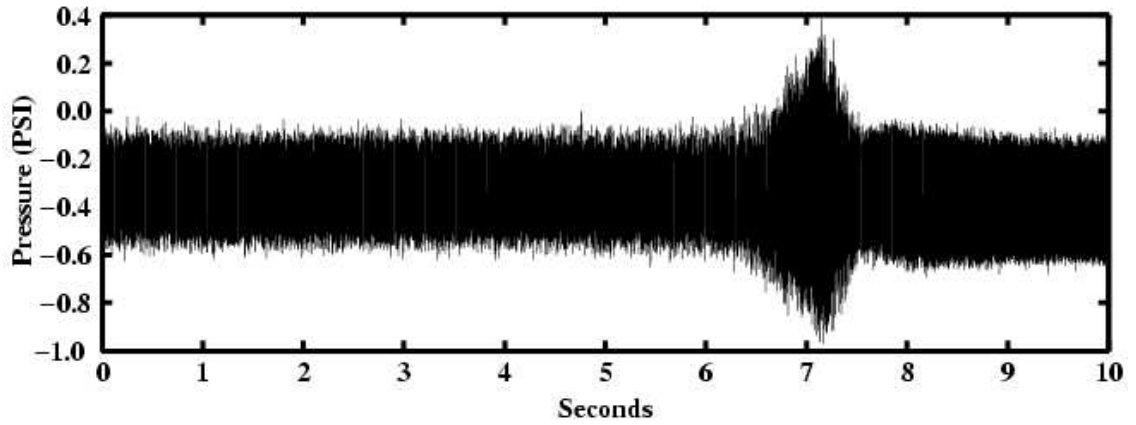
Figure 4.26: Two-dimensional Fourier transform of pressure transducer data as the fan is back-pressured into flutter for $n = 2$ and $m = 1$ at 70% corrected speed.

Results for 85% Corrected Speed Data

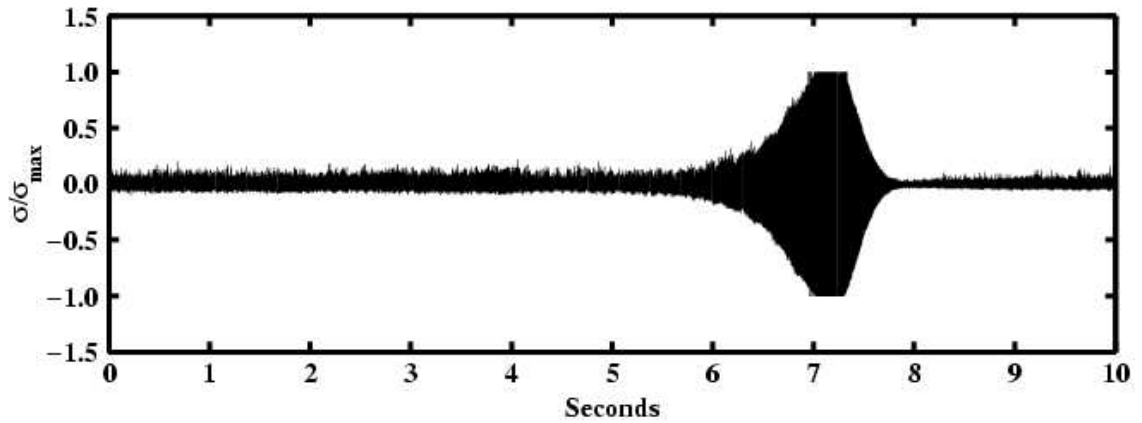
This section will present the analysis results for 85% corrected speed and closed clearances.

Pressure Transducers and Strain Gages: The Two Probe Method

Figure 4.27 shows the time signal from pressure transducer 7 and strain gage 18. A Butterworth infinite impulse response filter of order 10 and cutoff frequency of 2 kHz was applied to the pressure transducer signal to remove the pressure component due to blade passing for the purpose of comparing the two signals. Both transducers in Figure 4.27 show a very similar response. Up to about 5.5 seconds the pressure and strain gage signals have nearly constant amplitude. At approximately 5.5 seconds there is a rapid growth in the pressure and strain gage signals. Before the flutter response was allowed to reach a constant amplitude of oscillation, the back-pressure discharge valves were opened at approximately 7.1 seconds to move the fan out of the flutter region. The strain gage signal is flat at the top and bottom towards the end of the rapid growth region because the amplitude of the flutter response exceeded the cutoff amplitude of the strain gage recording equipment. As was the case for the 70% corrected speed data, the time dependent pressure measured in the stationary reference frame and the strain gage response measured in the rotating frame exhibit the same characteristics.



(a) Pressure transducer 7



(b) Strain gage 18

Figure 4.27: Time dependent pressure and strain gage response for the fan as it is back-pressured into flutter at 85% corrected speed.

The pressure transducer and strain gage data were subdivided into smaller blocks of 8192 points. The number of rotor rotations for 8192 points is 30. The frequency spectrum of each block was computed using the Fourier transform (FTs). A cross-power spectrum was then computed between pressure transducers 7 and 8 and between strain gages 17 and 18 for each time block.

Figure 4.28 presents the cross-power spectra from pressure transducers 7 and 8 successively from the beginning to the end of the recorded data. The blade passing frequency and

its harmonics, integer multiples of $22E$, have been reduced in amplitude to allow viewing of the flutter response. The dominant flutter responses occur in pairs about each blade passing harmonic. The primary flutter response frequencies have been labeled in Figure 4.29. The dominant flutter frequency was 456 Hz (rotating reference frame) with a nodal diameter of 2. A flutter response also occurs for the second flutter harmonic of 912 Hz (rotating reference frame) with a nodal diameter of 4. The nodal diameter pattern and frequency pattern of the 85% corrected speed data is analogous to the 70% corrected speed data.

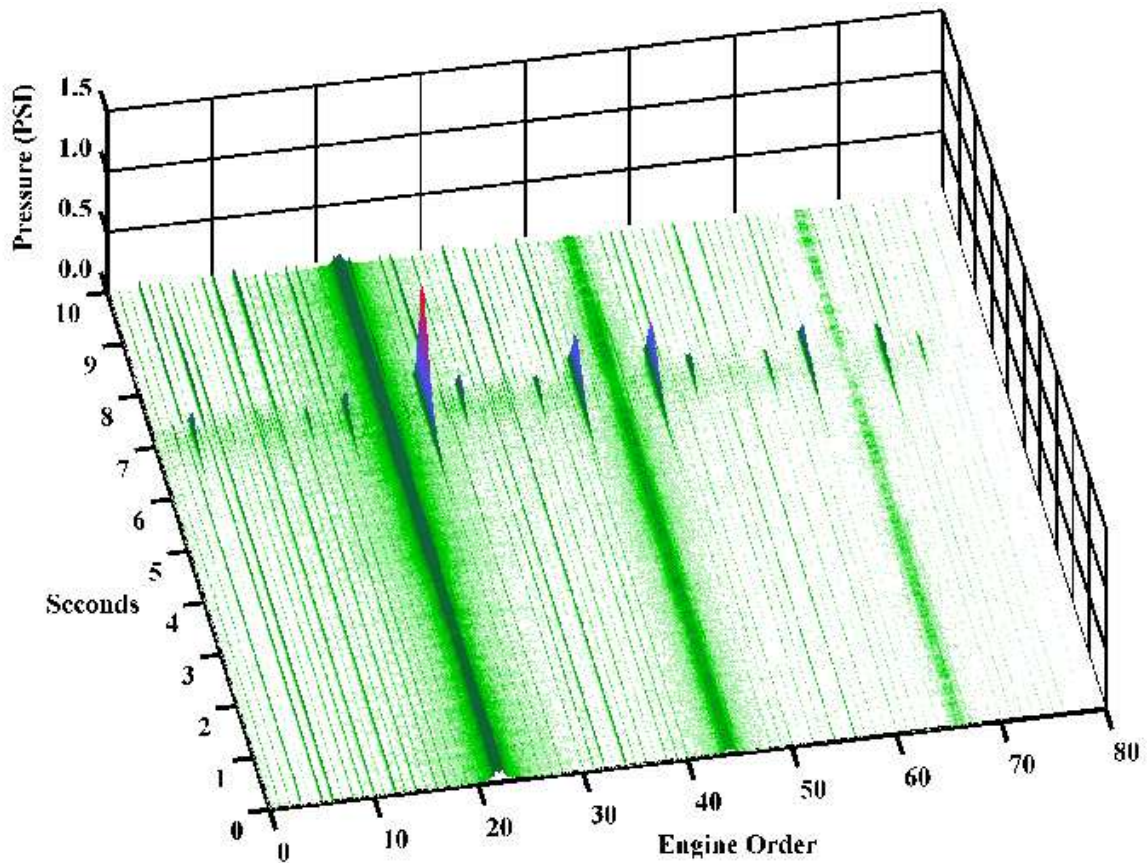
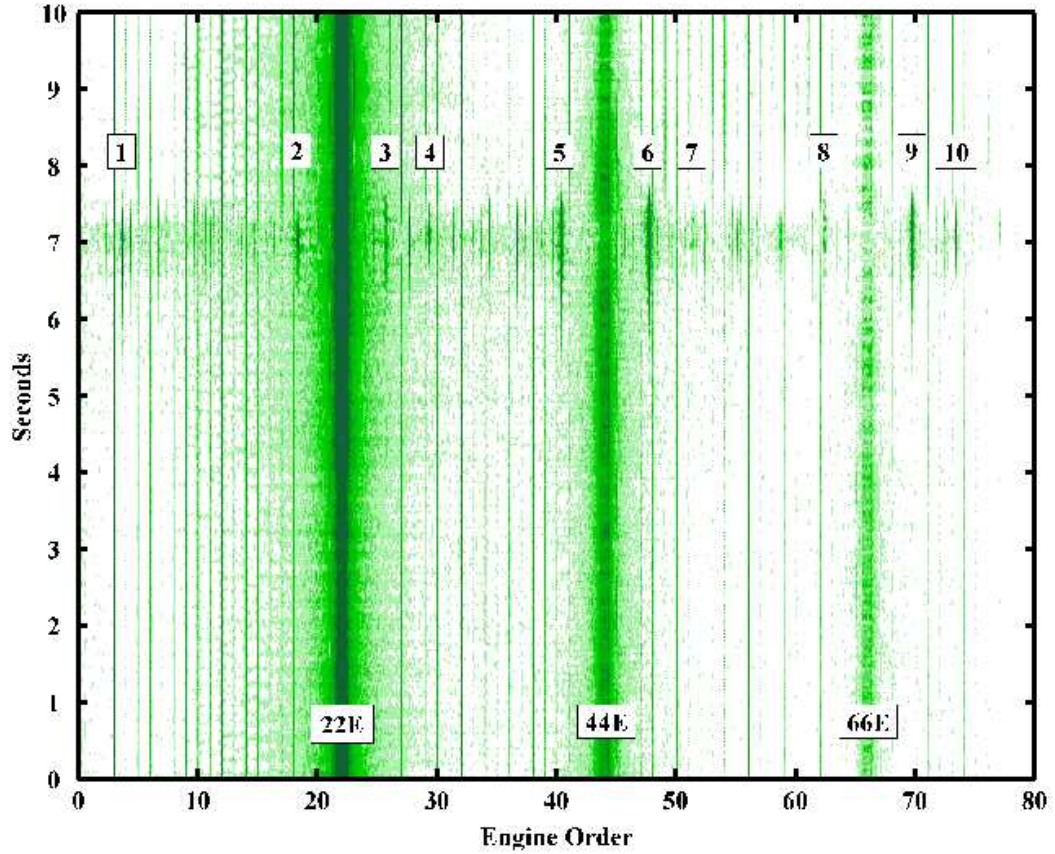


Figure 4.28: Successive cross-power spectra of pressure transducers 7 and 8 as the fan is back-pressured into flutter at 85% corrected speed.



| label | m | $f = 456 \text{ Hz}$ | $f = 912 \text{ Hz}$ | label | m | $f = 456 \text{ Hz}$ | $f = 912 \text{ Hz}$ |
|-------|-----|----------------------|----------------------|-------|-----|----------------------|----------------------|
| 1 | 0 | $n = 2$ | | 6 | +2 | $n = 2$ | |
| 2 | -1 | $n = 2$ | | 7 | +2 | | $n = 4$ |
| 3 | +1 | $n = 2$ | | 8 | -3 | $n = 2$ | |
| 4 | +1 | | $n = 4$ | 9 | +3 | $n = 2$ | |
| 5 | -2 | $n = 2$ | | 10 | +3 | | $n = 4$ |

Figure 4.29: Top down view of Figure 4.28 with the major wave harmonics and nodal diameters identified.

Figure 4.30 presents the cross-power spectra from strain gages 17 and 18 successively from the beginning to the end of the recorded data. The dominant flutter response occurs at a frequency of $1.67E$ (456 Hz in the rotating reference frame) with a nodal diameter of 2. The significant responses have been labeled in Figure 4.31, a top down view of Figure 4.30. Multiple harmonics of the flutter frequency $1.67E$ are seen and are partially attributed to the signal being clipped during recording.

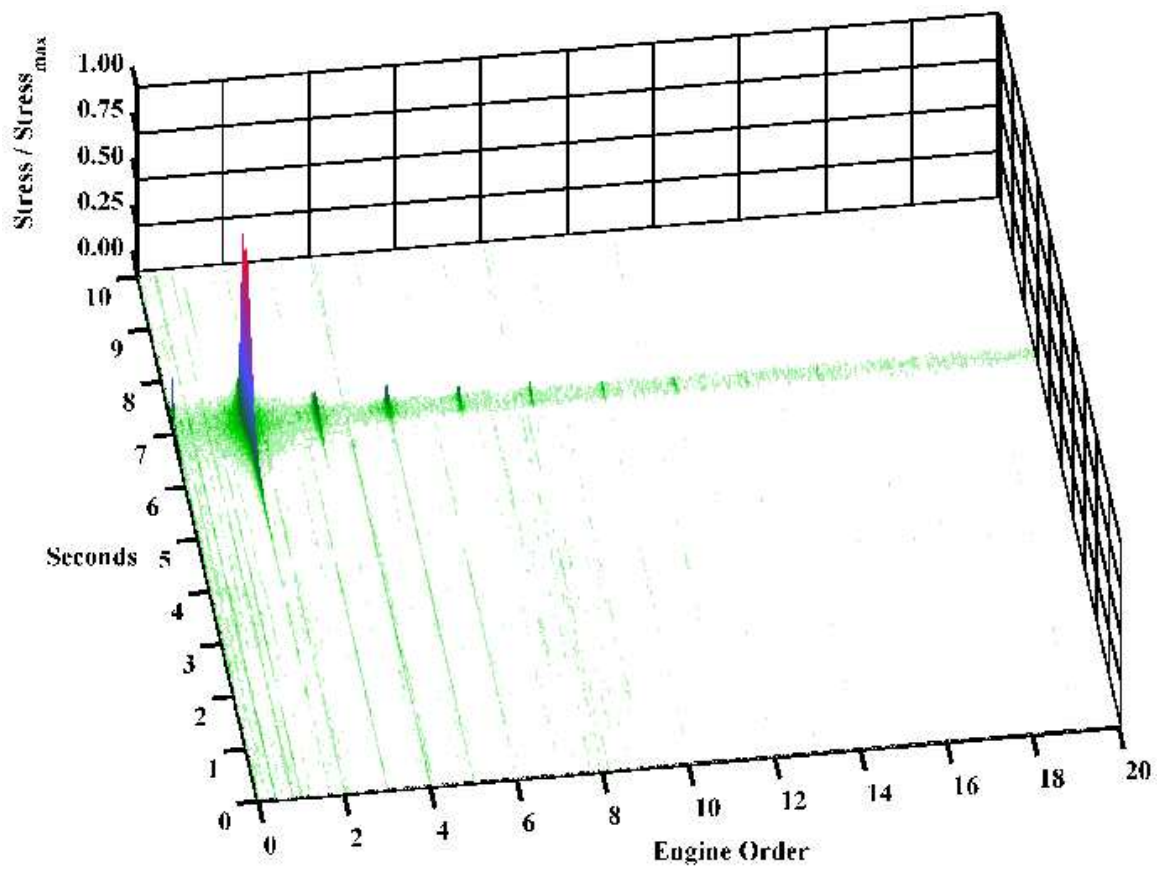


Figure 4.30: Successive cross-power spectra for strain gages 17 and 18 as the fan is back-pressured into flutter at 85% corrected speed.

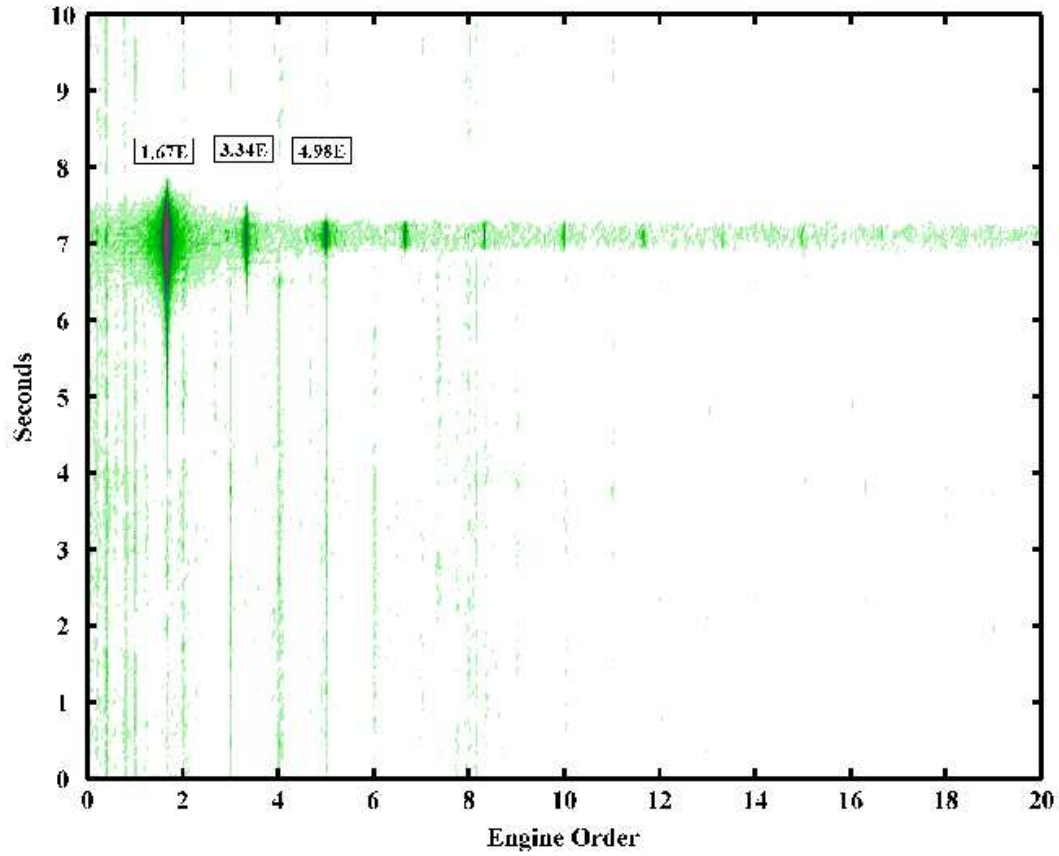
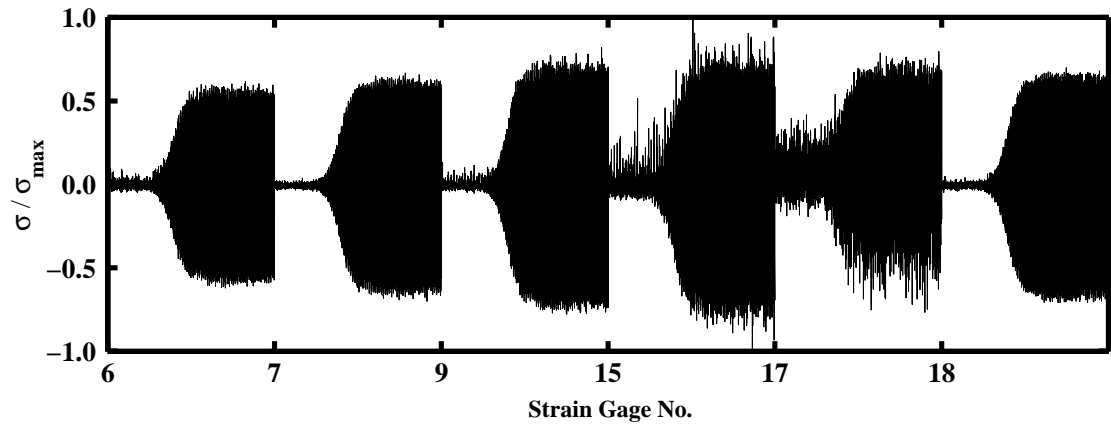
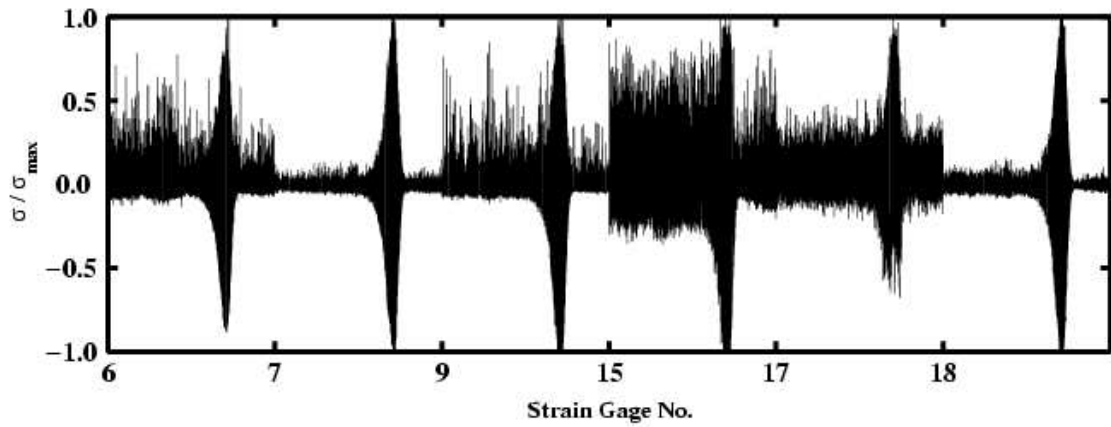


Figure 4.31: Top down view of Figure 4.30 with the major wave harmonics identified.

The pressure transducers that were functional for the 70% corrected speed data remained functional for the 85% corrected speed data. Unlike the strain gages, the casing mounted pressure transducers provided the same quality of data at this point in the experimental tests, see Figure 4.32 for comparison of strain gages during the 70% and 85% speedline experimental tests. The noise level in the strain gage data has increased significantly, further signifying the high failure rate of blade mounted strain gages during extensive testing.



(a) Strain gages for 70% corrected speedline.



(b) Strain gages for 85% corrected speedline.

Figure 4.32: Time dependent data for strain gages.

Due to the success of the multiprobe analysis for the 70% corrected speed data, the two probe analysis is not presented in as much detail as was done for the 70% corrected speed data. The multiprobe analysis technique will now be presented for the 85% corrected speedline.

Pressure Transducers: The Multiprobe Method

A two-dimensional space-time analysis was performed on the casing mounted pressure transducers, see Figure 2.3, in the same manner as was done for the 70% corrected speed data. Figure 4.33 is a two-dimensional Fourier transform of the high frequency response pressure transducer data at 7.1 seconds. The number of data points used was 8128 points, 30 rotor revolutions, from each of the 11 working casing mounted pressure transducers. This number of points was chosen to increase the accuracy of the Fourier transform at the frequency line of $25.66E$. The frequency line of $25.66E$ had the strongest flutter response in the transistional region for both the two probe analysis and the multiprobe analysis. The blade passing frequency, $22E$, and its integer multiples have been removed for easy viewing of the flutter responses. The dominant responses have been labeled in Figure 4.33 and are listed in Table 4.4. The dominant rotating reference frame frequency for the flutter response was calculated to be 456 Hz with a nodal diameter of $n = 2$ at wave harmonics of $m = 0, \pm 1, \pm 2$ and ± 3 . Responses for the second harmonic of 456 Hz at 912 Hz occurred at smaller amplitude for a nodal diameter of $n = 4$ with wave harmonics of $m = 1, 2$, and 3.

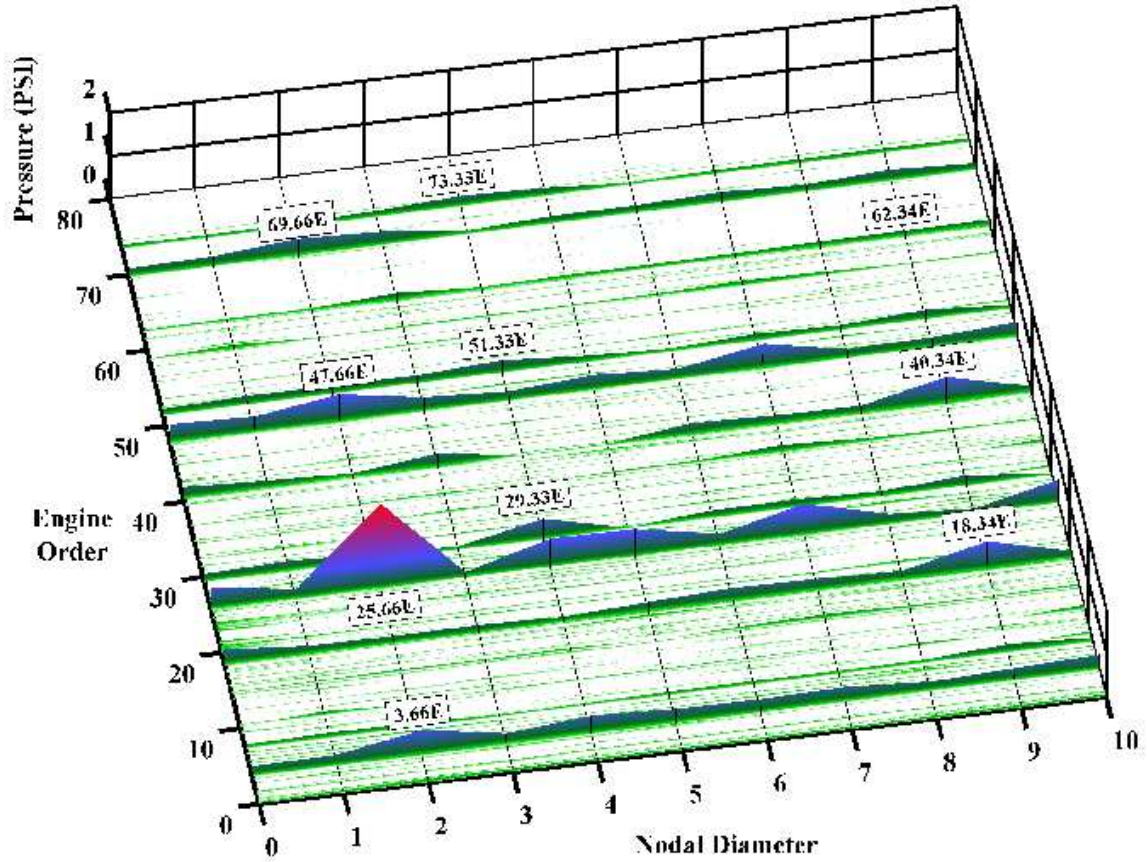


Figure 4.33: Two-dimensional Fourier transform of pressure transducer data at 7.1 seconds at 85% corrected speed.

Table 4.4: Nodal diameter, wave harmonic, and rotating reference frame frequency for the largest flutter spectral responses in Figure 4.33.

| stationary frame frequency, E | nodal diameter, n | wave harmonic, m | rotating frame frequency, Hz |
|---------------------------------|---------------------|--------------------|--------------------------------|
| 3.67 | 2 | 0 | 456 |
| 25.66 | 2 | +1 | 456 |
| 47.66 | 2 | +2 | 456 |
| 69.66 | 2 | +3 | 456 |
| 29.33 | 4 | +1 | 912 |
| 51.33 | 4 | +2 | 912 |
| 73.33 | 4 | +3 | 912 |
| 18.34 | 2 | -1 | 456 |
| 40.34 | 2 | -2 | 456 |
| 62.34 | 2 | -3 | 456 |

Successive two-dimensional Fourier transforms were calculated along the entire length of the pressure transducer data to study the evolution of the stall flutter response. After calculating the Fourier transforms, the results for $n = 2$ were extracted from each transform and combined into a single surface plot. Figure 4.34 shows the results for $n = 2$ around the flutter response of $25.66E$, which is for $m = 1$. Figure 4.34 is presented from a top-down view to visually enhance the flutter response. Transition to flutter occurs prior to 5.5 seconds, after which the fan quickly moves into flutter. A strong flutter response can be seen between 4.5 and 5.5 seconds. The noise amplitude was established using Figure 4.15. For this case the noise level was where 95% of the random frequencies are below it. The signal-to-noise ratio for $n = 2$ at $25.66 E$ in Figure 4.34 is 88. Figure 4.35 shows the results for $n = 4$ around the flutter response of $29.33E$, which is for $m = 1$. This response does not become significant until after 6 seconds.

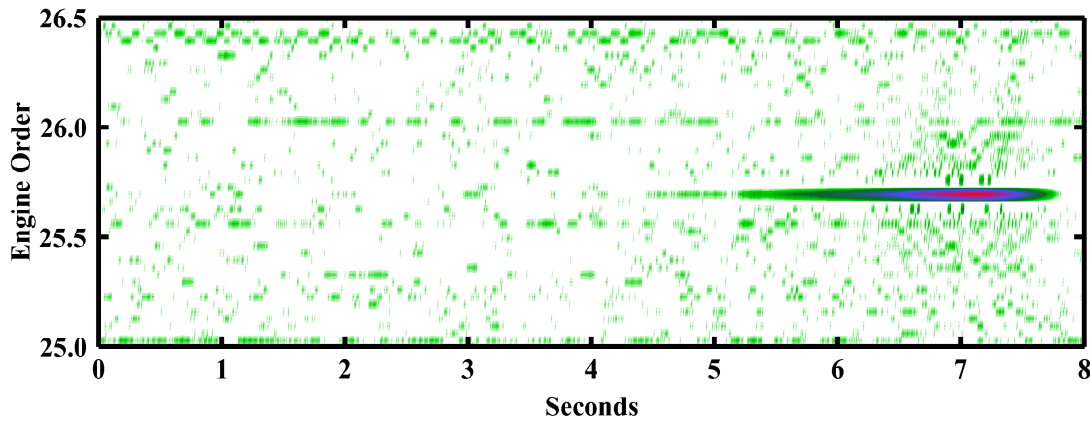


Figure 4.34: Two-dimensional Fourier transform of pressure transducer data as the fan is back-pressured into flutter for $n = 2$ and $m = 1$ at 85% corrected speed.

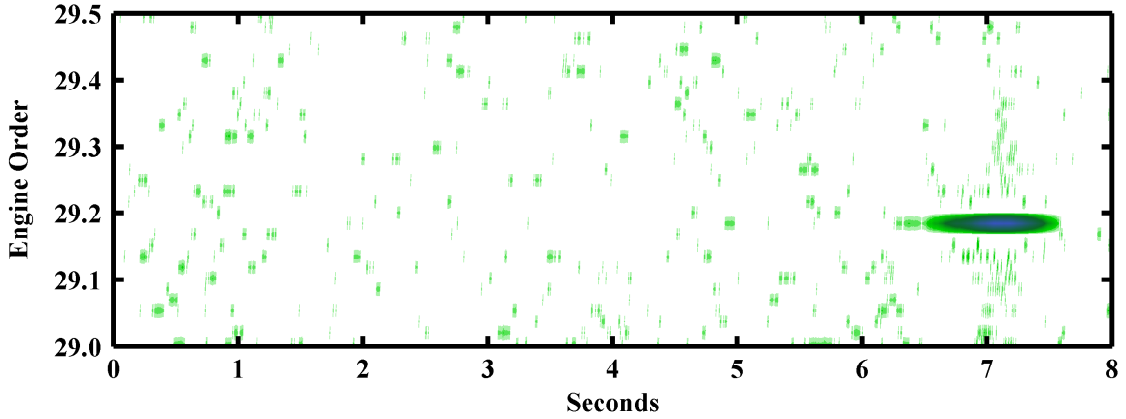


Figure 4.35: Two-dimensional Fourier transform of pressure transducer data as the fan is back-pressured into flutter for $n = 4$ and $m = 1$ at 85% corrected speed.

Pressure Transducers: The Integration Method Using the Multiprobe Method

The integration method was applied to the 85% corrected speed data. Again, successive two-dimensional Fourier transforms were computed along the entire length of the data set. The integration method effectively decreases the sampling frequency to 22 times the once-per-revolution rotational speed. For each two-dimensional Fourier transform, 1043 data points were used for each of the 11 functional transducers. There are 47 rotor revolutions for these 1043 points using the integration method. The results for a nodal diameter of $n = 2$ were extracted from each Fourier transform and are presented in Figure 4.36. The flutter response occurs at $3.66E$. The rapid growth region begins at 5.5 seconds. A strong flutter response occurs at 5.2 seconds, 0.3 seconds prior to the rapid growth region. The noise level used in Figure 4.36 was the same as Figures 4.34 and 4.35, which for this method results in 86% of the random frequencies having a smaller amplitude.

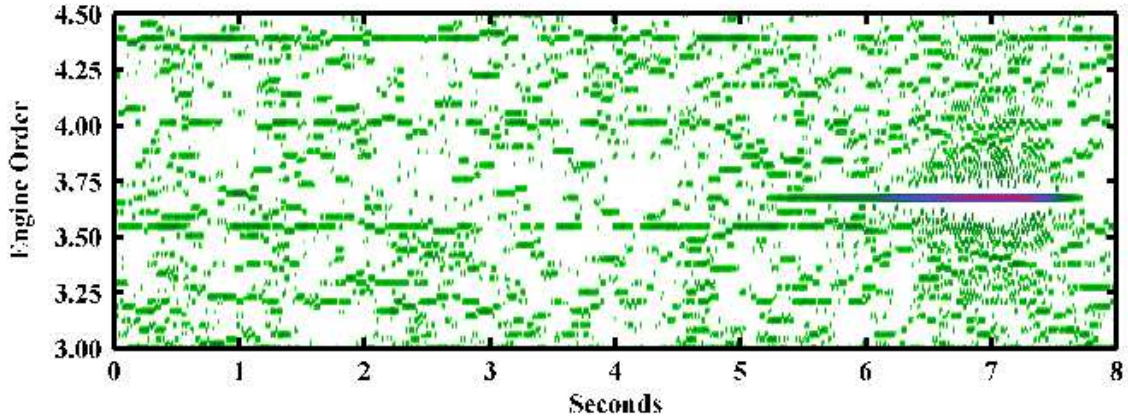


Figure 4.36: Two-dimensional Fourier transform of pressure transducer data as the fan is back-pressured into flutter for $n = 2$ at 85% corrected speed using the integration method.

Strain Gages: The Multiprobe Method

Two-dimensional Fourier transforms were calculated for the strain gages in the same manner as done with the strain gages for the 70% corrected speed data. The dominant strain gage response occurs at a frequency of $1.66E$. The number of data points used was 8313 points, 30 rotor revolutions, from each of the six strain gages. The number of points was chosen to increase the accuracy of the Fourier transforms for the frequency of $1.66E$. After calculating the two-dimensional Fourier transforms along the entire length of the data, the results for $n = 2$ were extracted from each transform and combined into the single surface plot shown in Figure 4.37. At 5.5 seconds the rapid growth region for the flutter response occurs. A $n = 2$ response is seen in Figure 4.37 to begin around 0.5 seconds and continue up to the beginning of the rapid growth region. Again, the low level $2E$ response is attributed to the upstream boundary layer probes.

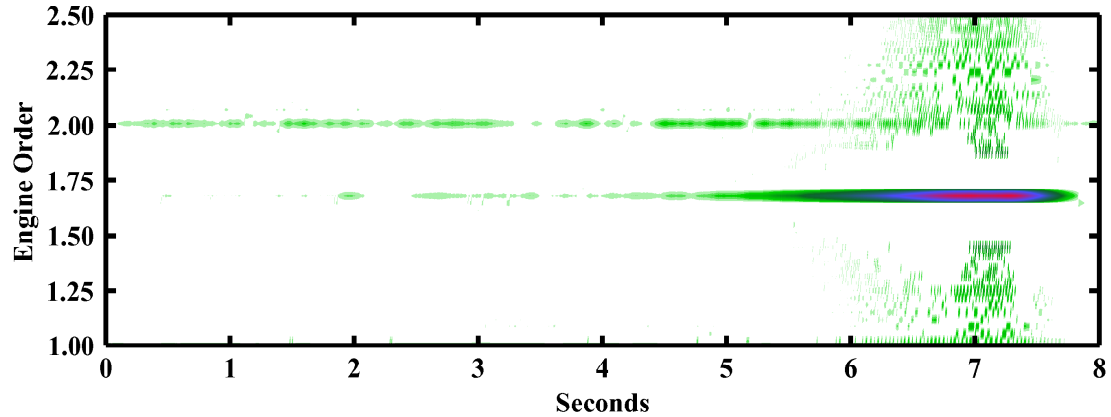


Figure 4.37: Two-dimensional Fourier transform of strain gage data as the fan is back-pressured into flutter at 85% corrected speed.

Summary

The results from the 85% speedline reflect the characteristics found for the 70% speedline results. The rapid growth region occurs at 5.5 seconds for the 85% corrected speed data. Near 7.1 seconds the test article was quickly moved out of the flutter region before a limit amplitude response occurred. Analysis of the high frequency response pressure transducers showed a dominant nodal diameter of $n = 2$ for the primary frequency of 456 Hz in the rapid growth region beginning at 5.5 seconds. The strongest response was at the wave harmonic $m = 1$ for the flutter frequency of 456 Hz and nodal diameter $n = 2$. In addition, there was a response at the second harmonic of 456 Hz at 912 Hz in the rapid growth region. The response at 912 Hz had a dominant response for a nodal diameter of $n = 4$ at the wave harmonic of $m = 1$. The multiprobe analysis of the pressure transducer data showed a flutter response in the transitional region from 4.5 seconds to 5.5 seconds, a full second in advance of the rapid growth region. The multiprobe analysis of the integrated pressure transducer data showed a flutter response in the transitional period starting at 5.25 seconds, $\frac{1}{4}$ of a second prior to the rapid growth region. The multiprobe analysis of the strain gage data shows a flutter response beginning at 0.5 seconds and continuing up to the rapid growth region, for a nodal diameter of $n = 2$. As with the 70% corrected speed

data analysis, the casing mounted pressure transducers were at a disadvantage due to being placed 1 inch (2.54 *cm*) upstream of the leading edge of the rotor blades, as previously discussed.

Unlike the multiprobe analysis using the integration method for the 70% speedline data, the integration method with the 85% speedline data did not extend the region of flutter activity in the transitional region earlier than the 4.5 seconds shown without the integration method, see Figure 4.36. The integration method is based on numerically integrating each blade passage's pressure response. The possible reason for the integration method not showing flutter activity in the transitional period could be related to the rotational speed being faster while the sampling frequency remained the same as with the 70% speedline data. The number of points per blade passage dropped from 15 points to 12 points for the 70% and 85% corrected speedlines respectively. Hence, the waveform in the 85% corrected speed data was not captured as accurately as in the 70% corrected speed data.

Open Clearance Data

This section will present the analysis results for data recorded with open clearance at 85% corrected speed. Only pressure transducer results will be presented due to the quality of the pressure transducer data.

The time dependent data for strain gage 18 is shown in Figure 4.38. The rapid growth region begins at 4.8 seconds and continues until the fan is moved out of flutter by opening the discharge valves. During the rapid growth region, the upper half of the signal was clipped. As with the 70% corrected speed data for open clearance, the fan was moved out of flutter before reaching the limit amplitude response.

A cross-power spectral analysis was performed at the peak amplitude of the flutter response at 7.8 seconds, see Figure 4.38 for location. The spectral content of the analysis for pressure transducers 7 and 8 is shown in Figure 4.39. The spectral content is very

similar to the spectral content of the flutter response that occurred at 85% corrected speed with closed clearance. A nodal diameter of 2 at 456 Hz was the dominant flutter response, with a secondary response of smaller amplitude occurring at 912 Hz and nodal diameter 4, for example 7.32E. Wave harmonics of $m = 0, \pm 1, \pm 2, \pm 3$ for $n = 2$ at 456 Hz are seen in Figure 4.39.

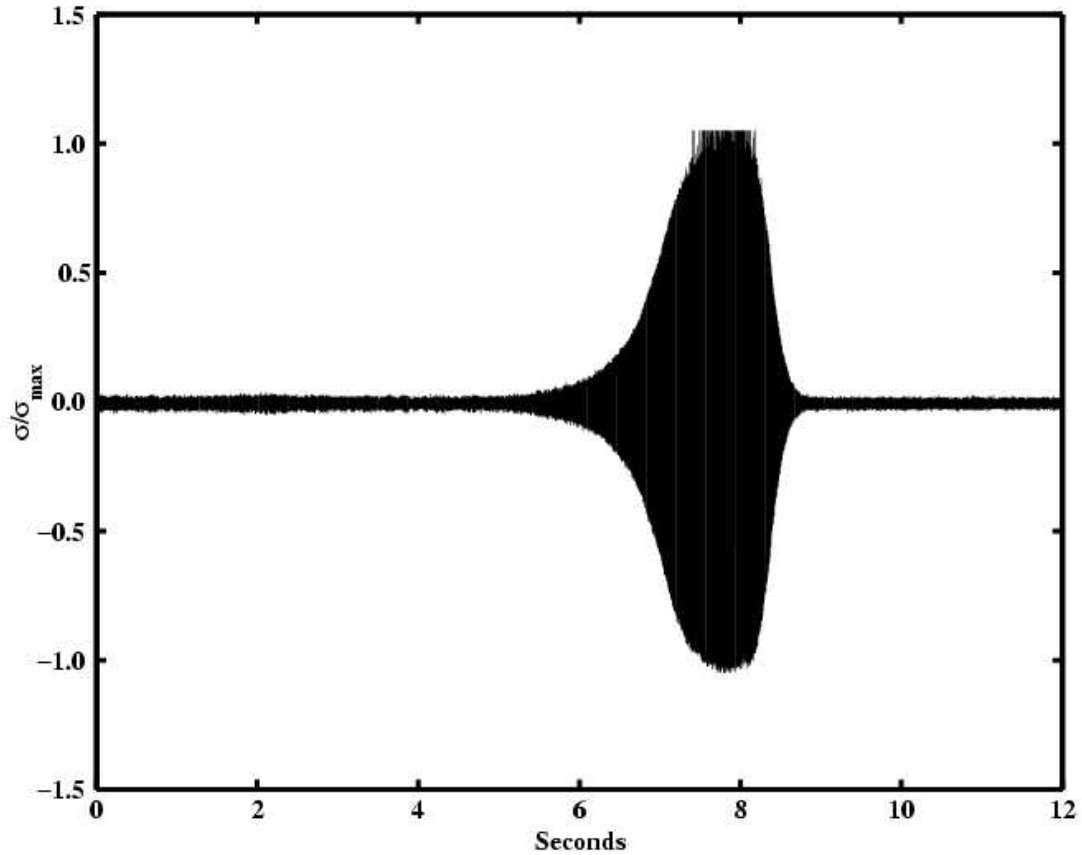


Figure 4.38: Time dependent data for strain gage 18 as the fan is back-pressured into flutter at 85% corrected speed with open clearances.

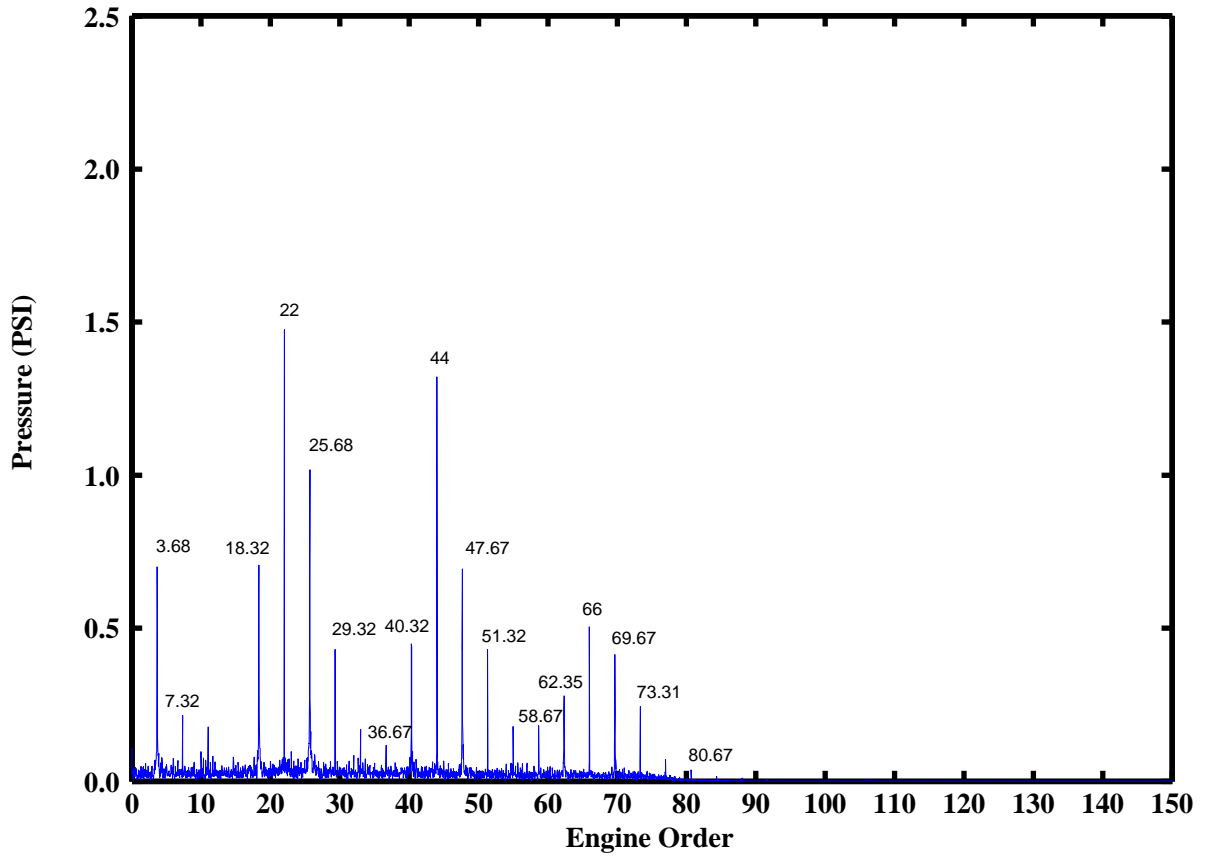


Figure 4.39: Cross-power spectral content for pressure transducers 7 and 8 at 7.8 seconds for 85% corrected speed with open clearances.

The two-dimensional Fourier transform at 7.76 seconds is presented in Figure 4.40. Figures 4.40 and 4.33 show essentially the same flutter response with small differences in the amplitudes. Figure 4.41 presents results from the two-dimensional space-time analysis of the pressure transducer data for nodal diameter 2 and wave harmonic 1 as the fan is back-pressured into flutter. In Figure 4.41, time $t = 0$ is referenced to the beginning of the rapid growth region with the sub-figures stopping at this point or proceeding just past it. Flutter activity is present in the transitional region between -3.3 and -2.3 seconds, see Figure 4.41(a), which is 3.3 seconds in advance of the rapid growth region. The space-time analysis for the 85% correct speed with closed clearance showed a flutter response occurring 1 second in advance of the rapid growth region, see Figure 4.41(b).

Again, a reference pressure was taken from the two-dimensional Fourier transform results at the time when the strain gage response exceeded 10 *KSI* peak-to-peak, for both open and closed clearances. For 85% closed clearance, the pressures at -0.5 and 0 seconds are respectively 29.46% and 56.8% of the reference pressure. For 85% open clearance, the pressure at -2.2 seconds is 25.3% of the reference pressure.

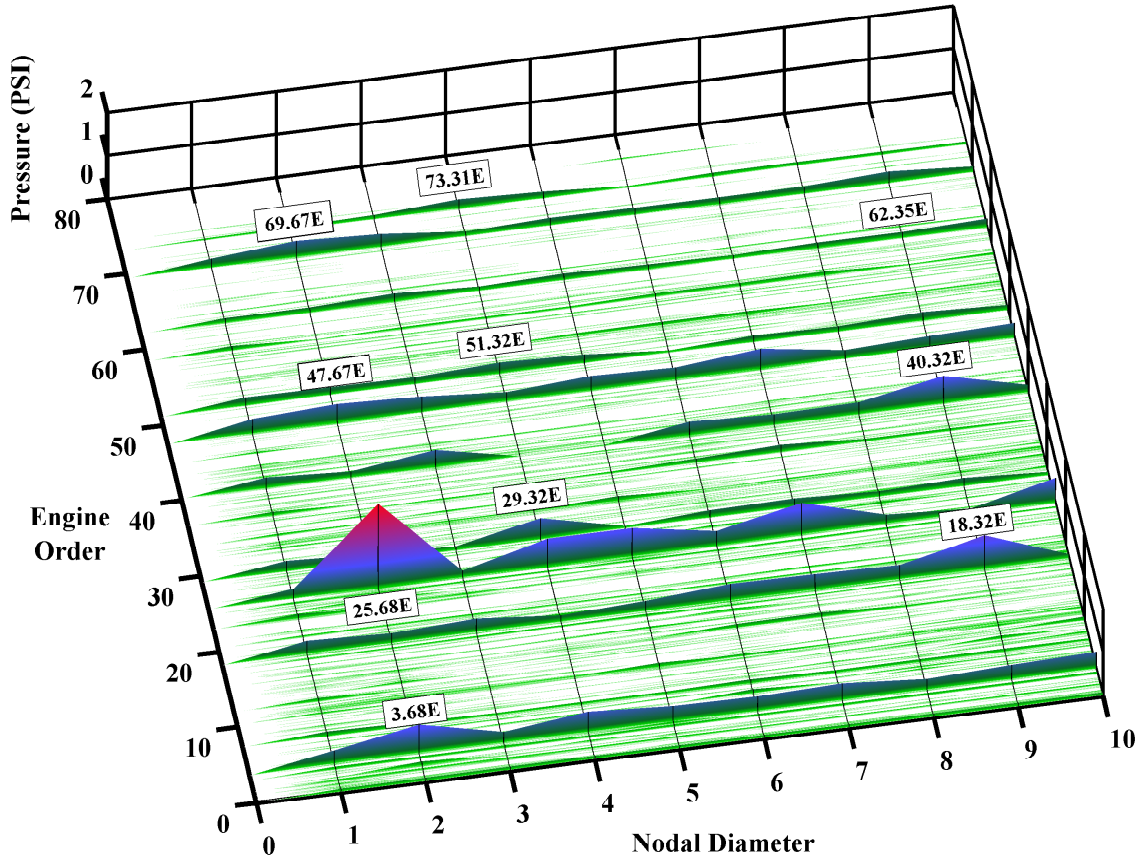
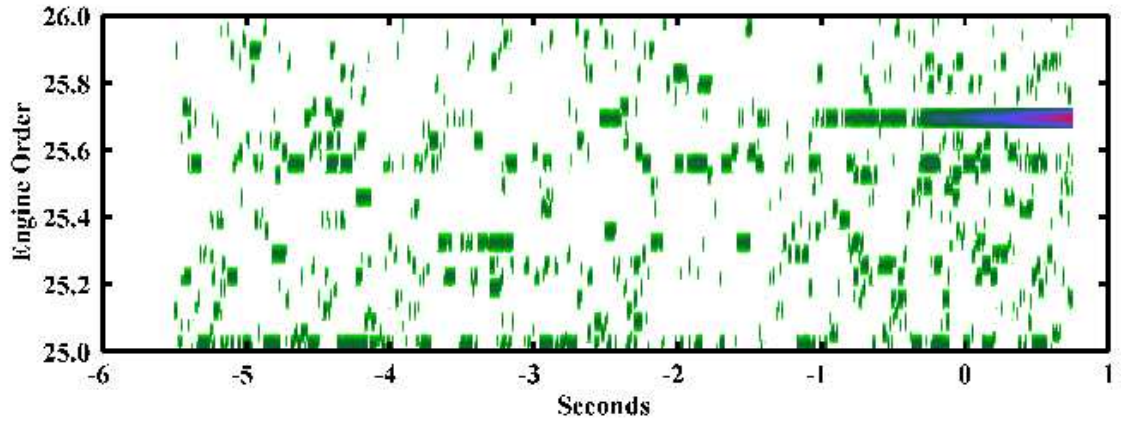
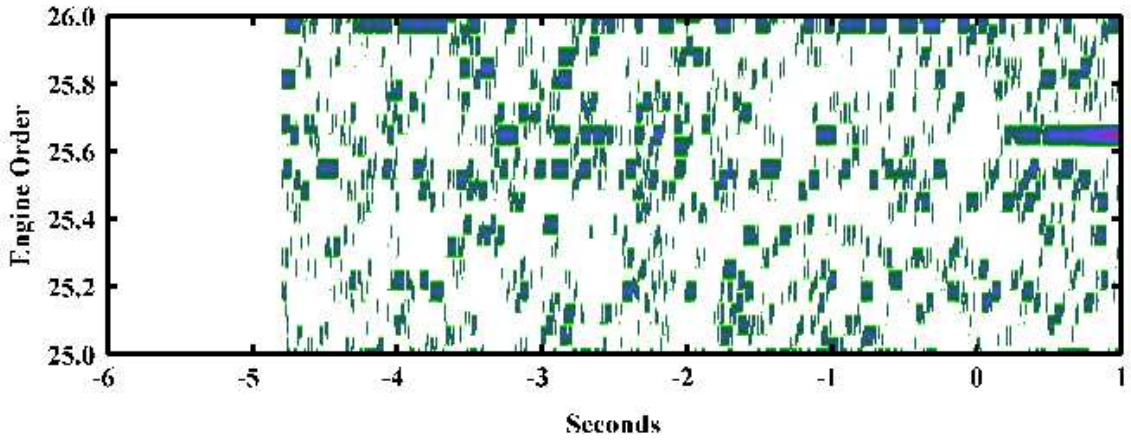


Figure 4.40: Two-dimensional Fourier transform of pressure transducer data at 7.76 seconds using 25 rotor revolutions for 85% corrected speed with open clearances.



(a) Pressure transducer data for 85% corrected speedline and closed clearance



(b) Pressure transducer data for 85% corrected speedline and open clearance

Figure 4.41: Two-dimensional Fourier transform of pressure transducer data as the fan is back-pressured into flutter for $n = 2$ and $m = 1$ at 85% corrected speed.

Summary

The two probe cross-power spectral analysis and the two-dimensional space-time analysis was performed on data at 70% and 85% corrected speed with open clearance. The results for the 70% and 85% corrected speeds were very similar to the results of the closed clearance data at 70% and 85% corrected speed, respectively. The dominant flutter response

at 70% corrected speed had a nodal diameter of 2 at 411 Hz with wave harmonics from 0 to ± 4 . The dominant flutter response at 85% corrected speed had a nodal diameter of 2 at 456 Hz with wave harmonics from 0 to ± 3 . Both the 70% and 85% corrected speed data with closed clearance had a secondary response with nodal diameter of 4 at 822 Hz and 912 Hz , respectively. A flutter response occurred as much as 4.5 seconds and 3.3 seconds in advance of the rapid growth region for the 70% and 85% open clearance data, respectively.

Flutter Precursor

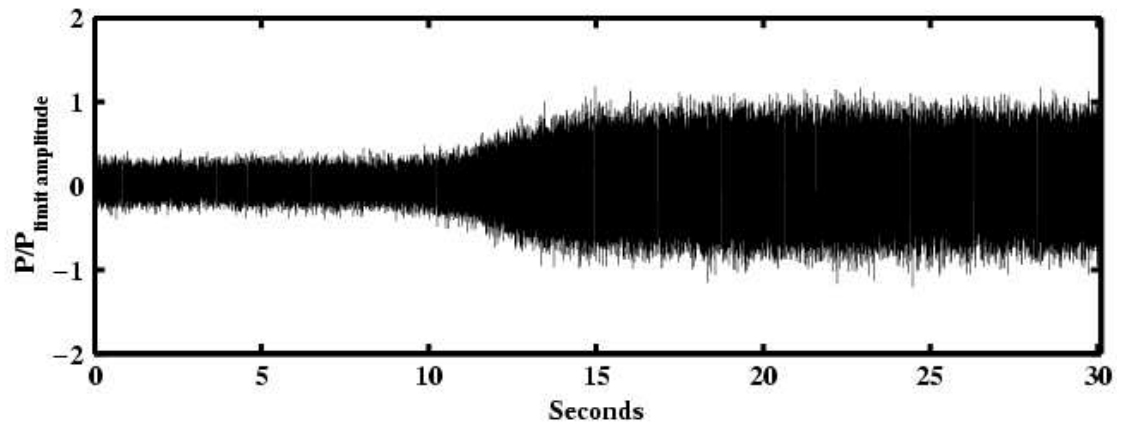
Several types of analysis were performed on two different sets of data, one taken on the 70% corrected speedline and the other taken on the 85% corrected speedline. The two probe methods provided weak evidence of flutter activity prior to the rapid growth region. The multiprobe analysis was in excellent agreement with the proven two probe analysis within the rapid growth and limit amplitude regions. However, the multiprobe analysis was found to produce a stronger indication of flutter activity than the two probe analysis in the transitional region. The multiprobe method has more spectral content than the two probe method to better resolve the flutter frequency and nodal diameter, providing a better signal-to-noise ratio as a result.

70% Corrected Speed Results: Closed Clearances

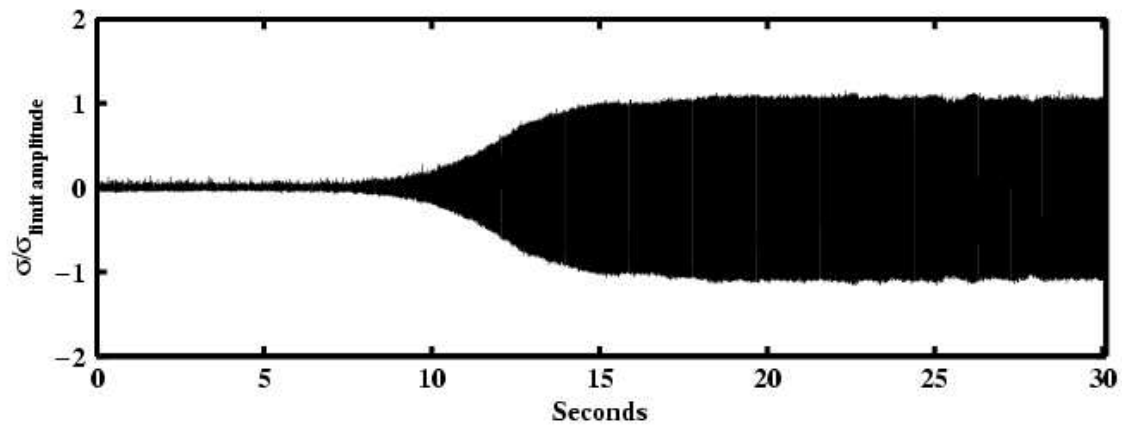
Figure 4.42 shows the time dependent data for pressure transducer 11 and strain gage 18. The transition into flutter begins before 0 seconds and continues to 8 seconds. At 8 seconds the rapid growth region begins, where the amplitude of the blade oscillations grows rapidly until a limit amplitude is reached. Once the blades reach a limit amplitude they continue to oscillate at a constant amplitude for the remainder of the data set. These different regions are easily recognized in both the casing mounted pressure transducer data

and the strain gage data.

The two-dimensional space-time analysis was very valuable in analyzing the transitional region for flutter activity. Figure 4.43(a) presents the space-time results obtained from the casing mounted pressure transducers at the frequency $25.82E$ for a nodal diameter of 2 and wave harmonic $m = 1$. Between 0 and 1 seconds, and 6.5 and 8 seconds, a traveling wave with a strong frequency and nodal diameter response is clearly present. The flutter activity within the transitional region is occurring at the flutter frequency of 411 Hz , respective to the rotating reference frame. The multiprobe analysis was applied to the strain gage data. Figure 4.43(b) shows the strain gage results at the frequency $1.82E$ for a nodal diameter of 2. Like the pressure transducer results, the strain gage results show the existence of a traveling wave with a strong frequency and nodal diameter response within the transitional region. The strain gages show strong flutter activity occurring between 0 and 1 seconds and between 5 and 8 seconds. The pressure transducers and strain gages agree on the existence of flutter activity in the transitional region. The resolution of the pressure transducers were not as strong as the strain gages due to the pressure transducers placement, as noted previously.

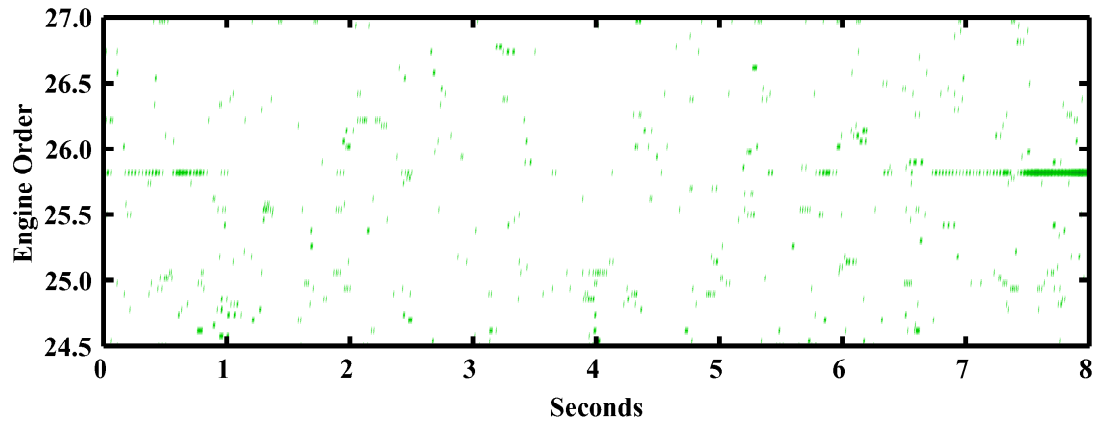


(a) Pressure transducer 11

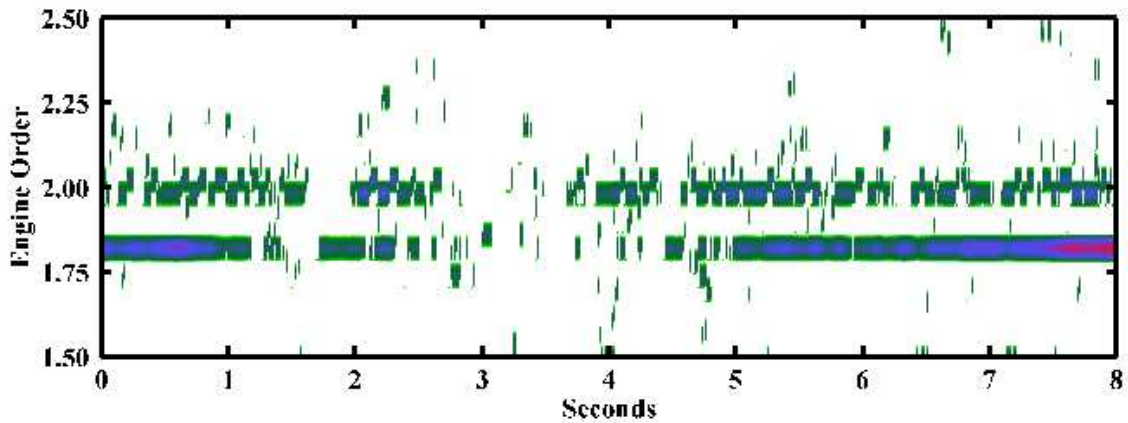


(b) Strain Gage 18

Figure 4.42: Time dependent pressure and strain gage response for the fan as it is back-pressured into flutter at 70% corrected speed with closed clearances.



(a) Pressure Transducers ($m=1$)



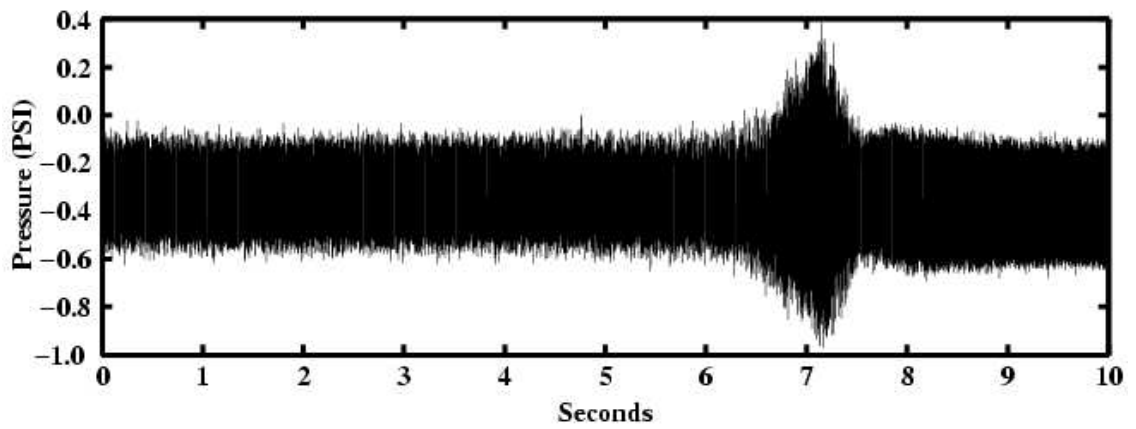
(b) Strain Gages

Figure 4.43: Two-dimensional Fourier transform of pressure transducer data using 25 rotor revolutions as the fan is back-pressured into flutter for $n = 2$ at 70% corrected speed with closed clearances.

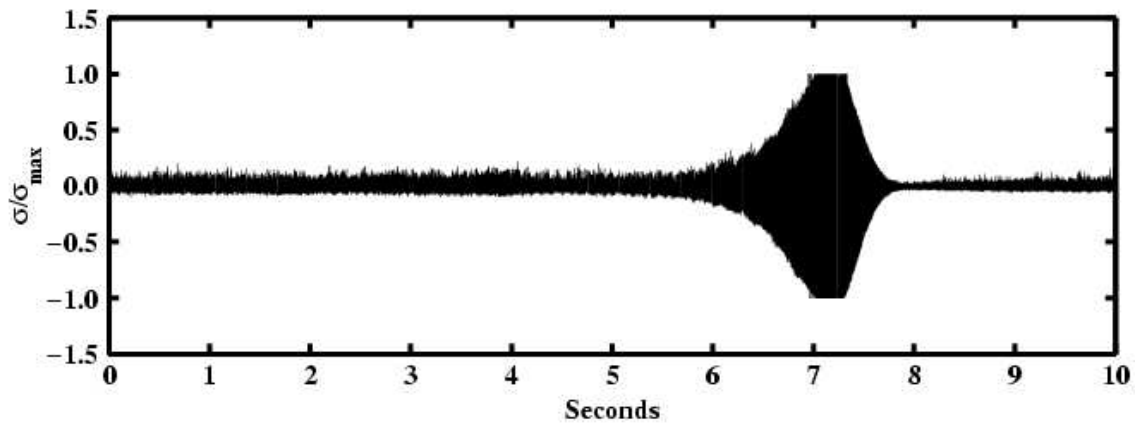
85% Corrected Speed Results: Closed Clearances

Figure 4.44 shows the time dependent data for pressure transducer 7 and strain gage 18. The transition into flutter begins before 0 seconds and continues to 5.5 seconds. At 5.5 seconds the rapid growth region begins. Unlike the 70% corrected speed data, the 85% data does not reach a limit amplitude. After 7 seconds, the fan is quickly moved out of flutter.

As with the 70% corrected speed data, the two-dimensional space-time analysis provided strong support for flutter activity within the transitional region. Figure 4.45 shows the results calculated for the pressure transducers at the frequency $25.66E$ for a nodal diameter of 2 and wave harmonic $m = 1$. The strong frequency and nodal diameter response indicates the existence of a travelling wave between 4.5 and 5.5 seconds. The flutter activity within the transitional region is occurring at the flutter frequency of 456 Hz , relative to the rotating reference frame. Figure 4.45 presents the results calculated for the strain gages at the frequency $1.66E$ for a nodal diameter of 2. The strain gage results show the existence of a traveling wave with a strong frequency and nodal diameter response within the transitional region. The strain gages show flutter activity occurring between 0.5 and 5.5 seconds. Again the pressure transducers and strain gages agree on the existence of flutter activity in the transitional region. The pressure transducer resolution was influenced by the pressure transducers placement, as discussed previously.

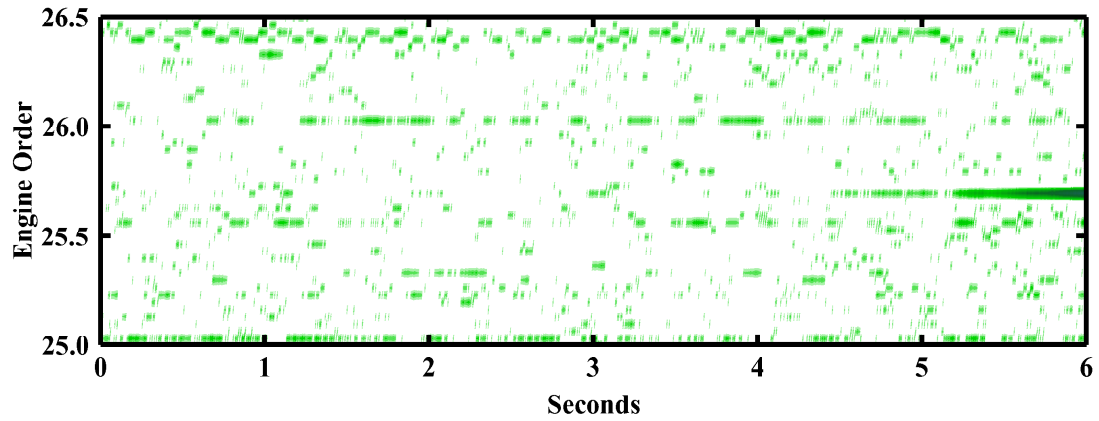


(a) Pressure transducer 7

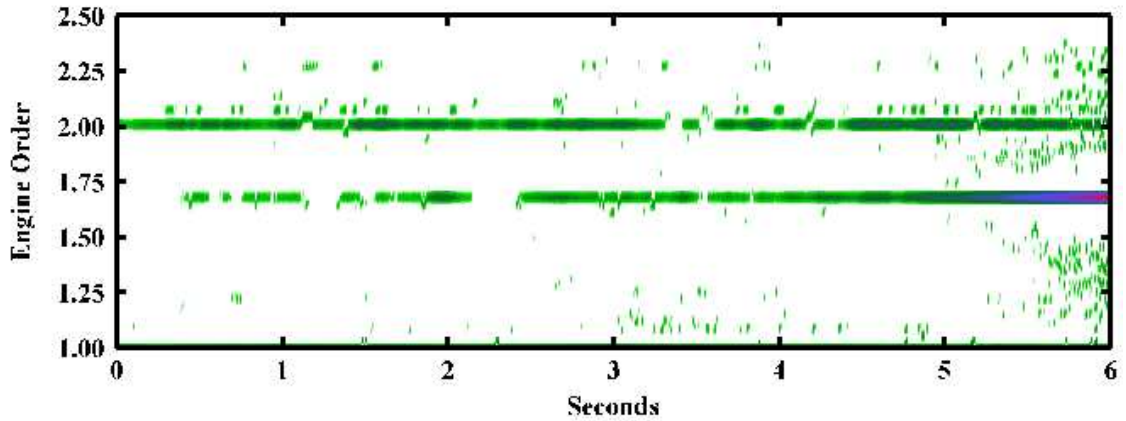


(b) Strain gage 18

Figure 4.44: Time dependent pressure and strain gage response for the fan as it is back-pressured into flutter at 85% corrected speed with closed clearances.



(a) Pressure transducers (m=1)



(b) Strain gages

Figure 4.45: Two-dimensional Fourier transforms as the fan is back-pressured into flutter for $n = 2$ at 85% corrected speed with closed clearances.

Open Clearance Results

The space-time analysis for the open clearance data provided results similar to the closed clearance data results. Flutter activity is seen within the transitional region prior to the rapid growth region.

For the 70% corrected speed data in Figure 4.46, the initial flutter response occurred

between -4.5 and -4 seconds, at the beginning of the time recorded data or 4.5 seconds prior to the rapid growth region. Additional flutter responses occurred between -3.25 and -2.5 seconds and between -0.25 and 0 seconds. Figure 4.47 shows flutter activity is present in the transitional region between -3.3 and -2.3 seconds for 85% corrected speed data, which is 3.3 seconds in advance of the rapid growth region.

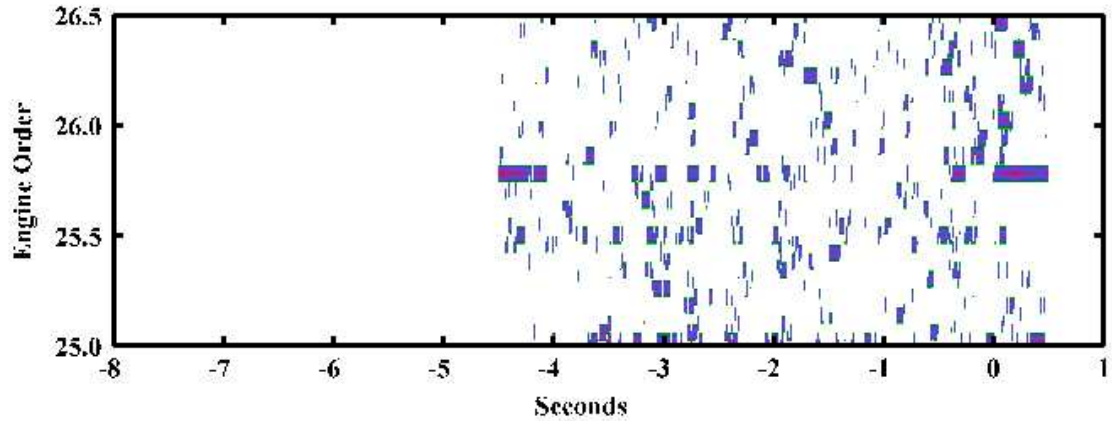


Figure 4.46: Two-dimensional Fourier transform of pressure transducer data as the fan is back-pressured into flutter for $n = 2$ and $m = 1$ at 70% corrected speed with open clearances.

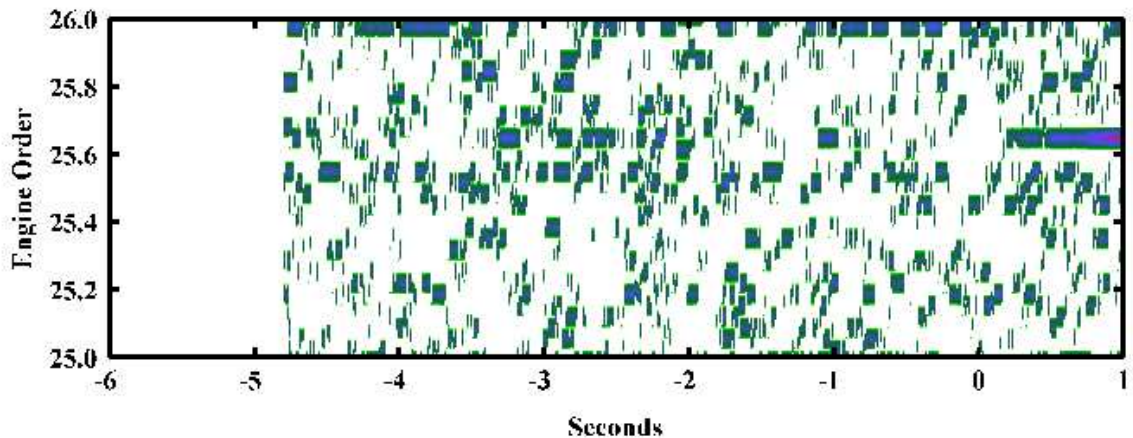


Figure 4.47: Two-dimensional Fourier transform of pressure transducer data as the fan is back-pressured into flutter for $n = 2$ and $m = 1$ at 85% corrected speed with open clearances.

Summary

Investigation of the transitional region with the multiprobe techniques clearly showed flutter activity with an established frequency and nodal diameter occurring several seconds in advance of the rapid growth region. Although the strain gages appear to provide a better analysis of the transitional period, it is important to remember the pressure transducers were placed $\frac{3}{4}$ of an inch (1.905 cm) further upstream of the leading edge than was desired. It is believed that if the pressure transducers had been placed significantly closer to the leading edge they would have provided results as strong and clear as the strain gages did. Furthermore, the functionality of the pressure transducers did not deteriorate as the experimental testing proceeded, unlike the strain gages which show clear signs of deterioration as the test proceeded.

For the 70% corrected speed data with closed clearances, flutter was detected 8 seconds in advance of the rapid growth region. Results from the open clearance data at 70% corrected speed showed a flutter response 4.5 seconds in advance of the rapid growth region. In both cases, flutter activity was detected at the beginning of the recorded data indicating flutter could be occurring sooner than the 8 seconds and 4.5 seconds for the closed and open clearances respectively.

Flutter was detected 1 second in advance of the rapid growth region for the 85% corrected speed with closed clearances. The open clearance results at 85% corrected speed showed flutter activity 3.3 seconds in advance of the rapid growth region.

Flutter activity in the transitional region supports the existence of a flutter precursor. Being able to detect flutter before the onset of flutter has many benefits to the design and maintenance of aircraft gas turbine engines. One such benefit of detecting a flutter precursor is active flutter control. Active flutter control could help extend the life of gas turbine engines and help push their performance envelope to higher levels.

CHAPTER FIVE

SUMMARY AND CONCLUSION

The flutter characteristics of an unshrouded fan blade were quantified when operating in the transitional and flutter regions. The fan was a single stage consisting of a set of rotor blades with a downstream set of stator vanes. The experimental program was conducted at the Compressor Research Facility at Wright Patterson Air Force Base. The time-variant instrumentation consisted of blade mounted and casing mounted high frequency response pressure transducers, blade mounted strain gages, and casing mounted laser light probes. This investigation concentrated on the casing mounted high frequency response pressure transducers and the blade mounted strain gages.

A mathematical model of the unsteady pressure field was developed. The unsteady pressure field was mathematically defined in the rotating reference frame and, using a coordinate transformation, was transformed to the stationary reference frame. This analysis shows the unsteady pressure field is a function of the flutter frequency, nodal diameter, and rotor speed. The data analysis techniques employed consisted of two probe and multiprobe methods. The two probe method uses the time dependent data from two transducers and requires the angular distance between the two transducers. The multiprobe method uses the time dependent data from all the transducers. Unlike the two probe method, the multiprobe method takes advantage of having the transducers located around the entire circumference of the rotor as well as having the time dependent data at each of those locations, providing a two-dimensional pressure field.

Strain gage data from the rotating reference frame and high frequency response pressure transducer data from the stationary reference frame were analyzed. The stationary reference frame analysis technique involving the two probe method provides detailed spectral

content about the nodal diameter and harmonic makeup of the flutter instability. Likewise, it was shown that the typical two probe method applied to strain gage data provides a gross nodal diameter. The multiprobe method is applicable to both casing mounted transducers and blade mounted transducers. The stationary, or casing mounted, transducers include high frequency response pressure transducers and light probes. The rotating, or blade mounted, transducers include strain gages and high frequency response pressure transducers. The multiprobe method depends on the transducers being equally spaced around the circumference of the casing or rotor. In this study, one of the equally spaced pressure transducers failed and strain gage placement was less than ideal. Unequally spaced Fourier transforms, the two-dimensional space-time method, were used to compensate for the missing pressure transducers and strain gage placement. The casing mounted pressure transducers were flush mounted approximately 1 inch (2.54 *cm*) upstream of the rotor blade leading edge plane and equally spaced around the circumference of the rotor. The six strain gages spanned approximately 196 degrees around the rotor circumference.

The two probe and multiprobe analysis were applied to four sets of data. Two sets were taken along the 70% corrected speedline with closed and open clearance and the other two were taken along the 85% corrected speedline with closed and open clearances. Flutter was encountered along all speedlines. Casing mounted high frequency response pressure transducers and rotor blade mounted strain gages were both analyzed for each set of data. The quality of the casing mounted pressure transducer data remained consistent throughout the experimental testing while the quality of the strain gage data degraded significantly, which is typical during engine testing.

The two probe and multiprobe analysis of the casing mounted pressure transducer data provide a detailed analysis of the nodal diameter and frequency content of the flutter response. The two probe analysis with blade mounted strain gages can only provide a gross nodal diameter for each of the frequency harmonics of the flutter response, while a multiprobe analysis with the strain gages is capable of providing more detailed information

about the nodal diameter content. Because the multiple nodal diameter response for the strain gages is occurring at a single frequency, the cross-power spectrum for the strain gages gives a 'weighted average' for the nodal diameter.

The flutter responses for the 70% speedline data with closed and open clearance were found to consist of multiple nodal diameters at multiple frequencies within the rapid growth and limit amplitude regions. The primary frequency was 411 Hz , in the rotating reference frame, with a dominant nodal diameter of $n = 2$, along with other nodal diameters of smaller amplitude. The second harmonic of 411 Hz at 822 Hz was the second strongest response at a nodal diameter of $n = 4$. The strongest flutter responses in the Fourier transforms for both the 411 Hz and 822 Hz frequencies were at the wave harmonics of $m = \pm 1$. The two probe and multiprobe techniques gave consistent results in the rapid growth and limit amplitude regions.

Like the 70% corrected speedline, higher harmonics of the flutter frequency were detected for the 85% corrected speedline with closed and open clearance and developed midway through the rapid growth region. The primary flutter frequency was 456 Hz in the rotating reference frame for both closed and open clearances, with a dominant nodal diameter of $n = 2$. Nodal diameters with smaller response amplitudes also existed at this frequency. The second harmonics of 456 Hz at 912 Hz was the second strongest response at a nodal diameter of $n = 4$. Again, the strongest flutter responses in the Fourier transforms were at the wave harmonic of $m = +1$, noting the response at wave harmonic $m = -1$ with closed clearance was significantly weaker than was seen in the 70% corrected speedline data with closed clearance.

Flutter activity was detected in the transitional region several seconds prior to the rapid growth region in the 70% corrected speedline data with closed clearance. The flutter activity had a distinct frequency of 411 Hz and a nodal diameter of $n = 2$ and occurred at the wave harmonic of $m = 1$. The 85% corrected speedline data with closed clearance also showed flutter activity prior to the rapid growth region; it had a distinct frequency of

456 Hz and a nodal diameter of $n = 2$. The strain gages show a flutter response almost through the entire recorded data, for both the 70% and 85% corrected speedline data. It is believed the pressure transducers would have done the same had they been located closer to the leading edge of the rotor blades.

The open clearance results were very similar to the closed clearance results for both 70% and 85% corrected speedlines. Flutter activity at a frequency of 411 Hz and nodal diameter of $n = 2$ was found several seconds prior to the rapid growth region for the 70% corrected speedline. The transitional region of the 85% corrected speedline had flutter activity at a frequency of 456 Hz and nodal diameter of $n = 2$.

Being able to detect this flutter signature prior to flutter occurring is important to the development and continued use of gas turbine engines. Greater control and understanding of flutter can significantly reduce cost in the design and development of turbomachines. Active flutter control could help push gas turbine engines to new levels of performance as well as extend the gas turbine's life cycle by reducing the stress on the blades.

A single case study has been presented with strong support for the existence of a flutter precursor, however more tests need to be conducted on other fans/compressors to further study the flutter precursor.

APPENDICES

Appendix A: Nomenclature

| | |
|-------------|--|
| A_{mn} | Pressure amplitude of mth harmonic and nth nodal diameter |
| E | Engine order |
| f | Flutter frequency in rotating system (Hz) |
| f_{mn} | Flutter frequency for mth harmonic and nth nodal diameter in the stationary reference frame (Hz) |
| k_{mn} | Stationary reference frame mode number for mth harmonic and nth nodal diameter |
| m | Wave harmonic number |
| N_b | Number of blades |
| N_c | Corrected speed |
| n | Nodal diameter |
| p | Unsteady pressure |
| p_n | Unsteady pressure for nth nodal diameter |
| \tilde{p} | Two-dimensional unsteady pressure field |
| \hat{p} | Interpolated two-dimensional unsteady pressure field |
| β | Initial angle between rotating and stationary reference frames |
| θ | Angular position in stationary reference frame |
| θ_r | Angular position in rotating reference frame positive opposite rotation direction |
| σ | Interblade phase angle |
| ϕ | Cross-power phase angle |
| Ω | Rotor speed ($radians/second$) |

| | |
|---------------|---|
| ω | Flutter frequency in rotating system (<i>radians/second</i>) |
| ω_{mn} | Flutter frequency for <i>mth</i> harmonic and <i>nth</i> nodal diameter in the stationary reference frame (<i>radians/second</i>) |
| FT | Fourier transform |
| $FT2$ | Two dimensional Fourier transform |

Appendix B: Unequally Spaced Fourier Transforms

Let $y(t)$ be the sampled data consisting of N samples taken at times

$$t_k = \{t_0, t_1, t_2, t_3, \dots, t_N\}$$

for a period of time T . The complex coefficients, $Y(\omega)$, are given by the matrix form of the discrete Fourier transform defined according to Equation B.1, where $\omega_k = \frac{2\pi k}{T}$.

$$Y = \exp \left\{ -i \begin{bmatrix} \omega_1 \\ \omega_2 \\ \dots \\ \omega_N \end{bmatrix} \begin{bmatrix} t_1 & t_2 & \dots & t_N \end{bmatrix} \right\} \begin{bmatrix} y_1 \\ y_2 \\ \dots \\ y_N \end{bmatrix} \quad (\text{B.1})$$

Under the conditions that $\Delta t = \text{constant}$, then Equation B.1 can be reduced to the Discrete Fourier Transform algorithm (*DFT*) or the Fast Fourier Transform algorithm (*FFT*) when N satisfies $N = 2^m$. The definition of the FFT or DFT can be found in many different mathematical texts. For data with $\Delta t \neq \text{constant}$, Equation B.1 can be used directly. Equation B.1 can be written in a more compact form shown in Equation B.2.

$$Y = Wy \quad (\text{B.2})$$

The two-dimensional Fourier transform is an extension of the one-dimensional Fourier

transform. Equation B.2 can be extended to two dimensions. The two-dimensional Fourier transform in matrix form is given by Equation B.3.

$$Y = W_1 y W_2 \quad (\text{B.3})$$

In this relation,

$$W_1 = \exp \left\{ -i \begin{bmatrix} \omega_1 \\ \omega_2 \\ \dots \\ \omega_{N_1} \end{bmatrix} \begin{bmatrix} t_1 & t_2 & \dots & t_{N_1} \end{bmatrix} \right\}$$

and

$$W_2 = \exp \left\{ -i \begin{bmatrix} \eta_1 \\ \eta_2 \\ \dots \\ \eta_{N_2} \end{bmatrix} \begin{bmatrix} x_1 & x_2 & \dots & x_{N_2} \end{bmatrix} \right\}$$

For W_2 , x would represent the spatial position of the sample and η represents the spatial frequency. If $\Delta t = \text{constant}$ and $\Delta x = \text{constant}$, Equation B.3 can be reduced to the familiar two-dimensional *FFT* or *DFT*. Equation B.3 can be directly used with unequally sampled data, with any of the following conditions.

$$\left\{ \begin{array}{l} \Delta t = \text{constant} \\ \Delta x \neq \text{constant} \end{array} \right\} \text{ or } \left\{ \begin{array}{l} \Delta t \neq \text{constant} \\ \Delta x = \text{constant} \end{array} \right\} \text{ or } \left\{ \begin{array}{l} \Delta t \neq \text{constant} \\ \Delta x \neq \text{constant} \end{array} \right\}$$

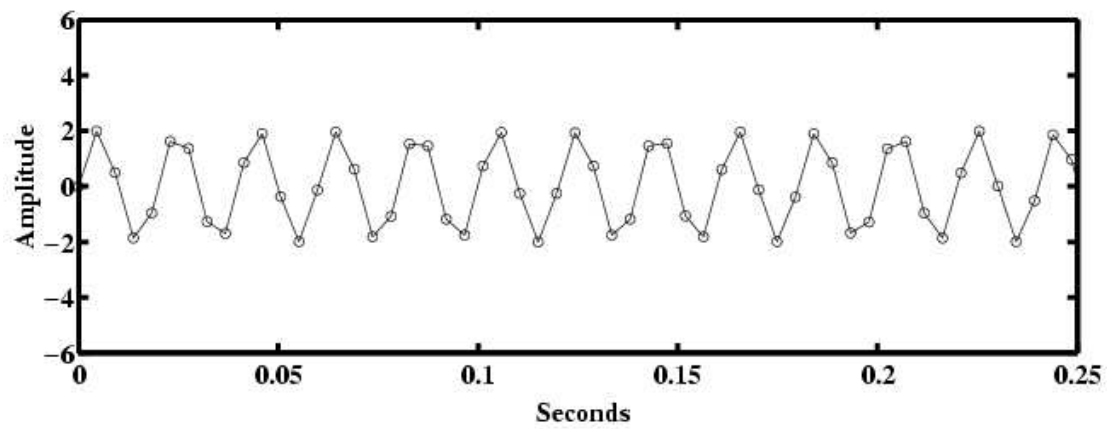
A theoretical signal was generated using Equation B.4. The amplitude, A , was 2.0 and the frequency, f , was 50.0 Hz .

$$y = A \sin(2\pi ft) \quad (\text{B.4})$$

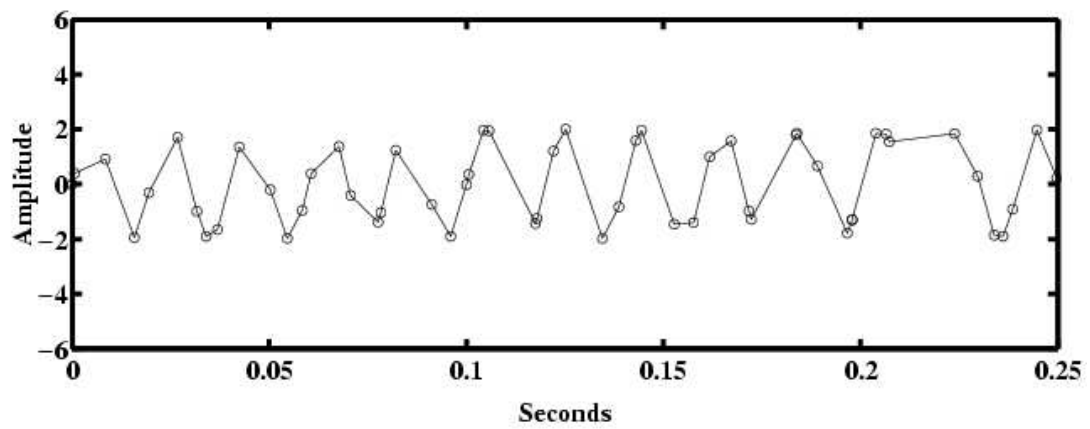
The number of data points, $y_i(t_i)$, sampled was 4096 with a period of $T = 6\pi$. The Fourier transform was computed from the set $\{y_i\}$ where Δt was constant. The unequally spaced

Fourier transform was computed from the set $\{y_i\}$ where Δt was not constant between each sample. Figure B.1 shows a portion of the sampled data for the equally spaced data and unequally spaced data. Figure B.2 shows the Fourier transforms when the data is equally spaced and unequally spaced, using the unequally spaced Fourier transform program for each data set.

The amplitude and phase computed for the equally spaced data was 2.00 and -90.0 deg., respectively. The amplitude and phase computed for the unequally spaced data was 2.0 and -89.1 deg., respectively. Because the theoretical signal was a *sine* wave, the phase angle from the Fourier transform should be -90 deg. The Fourier transforms for the equally spaced and unequally spaced data are in agreement with the theoretical signal.

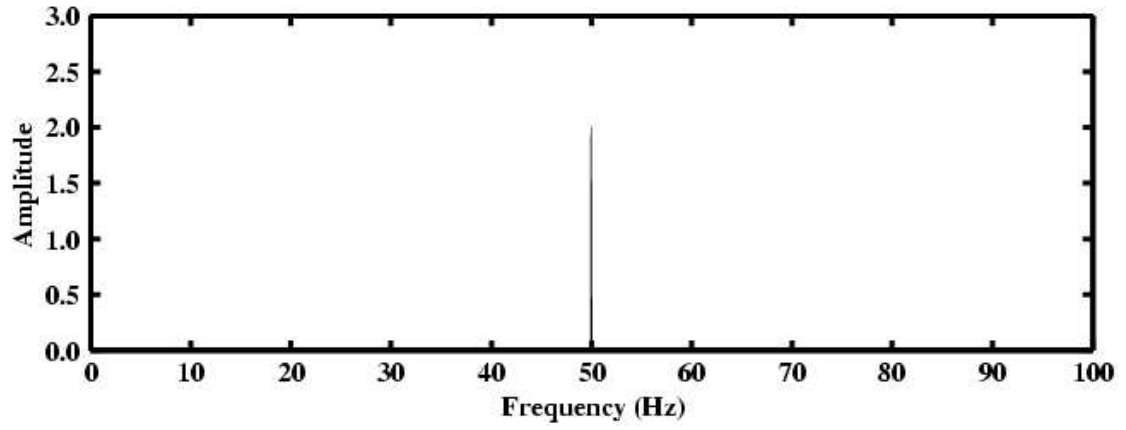


(a) Equally spaced data

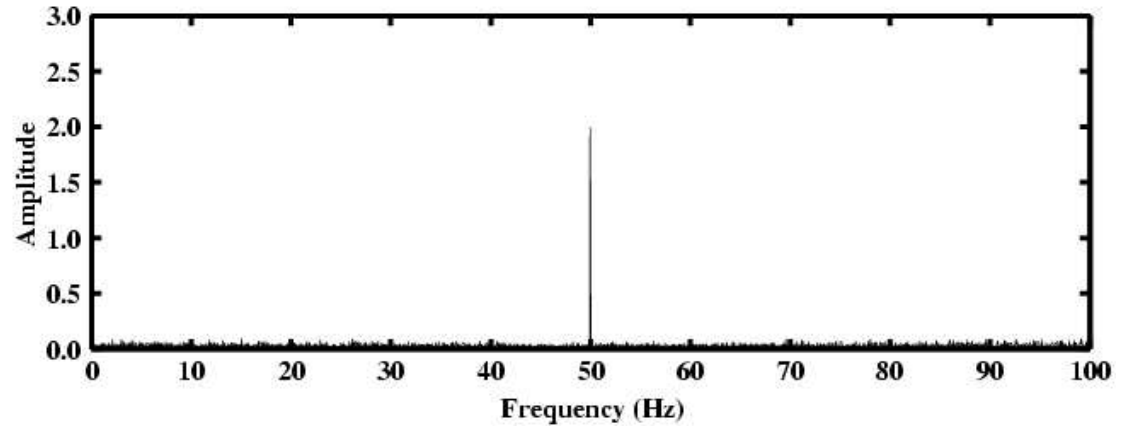


(b) Unequally spaced data

Figure B.1: Equally spaced versus unequally spaced data.



(a) Equally spaced data



(b) Unequally spaced data

Figure B.2: Fourier transform of equally spaced data and unequally spaced data.

Appendix C: Least Squares Spectral Analysis

An alternative method of spectral analysis was developed by Lomb (1976). Let $\{p_i\}$ be the set of data sampled at time t_i , where Δt between t_i and t_{i+1} is not constant throughout

$\{t_i\}$. The mean and variance of $p_i = p(t_i)$ are given by

$$\bar{p} \equiv \frac{1}{N} \sum_i^N p_i \quad \sigma^2 \equiv \frac{1}{N-1} \sum_i^N (p_i - \bar{p})^2$$

where N is the number of samples in $\{p_i\}$. Lomb defines the normalized spectral power as a function of angular frequency.

$$P_N(\omega) = \frac{1}{2\sigma^2} \left\{ \frac{[\sum_i (p_i - \bar{p}) \cos \omega(t_i - \tau)]^2}{\sum_i \cos^2 \omega(t_i - \tau)} + \frac{[\sum_i (p_i - \bar{p}) \sin \omega(t_i - \tau)]^2}{\sum_i \sin^2 \omega(t_i - \tau)} \right\} \quad (\text{C.1})$$

For Equation C.1, τ is an offset defined such that $\sum_i \cos \omega(t_i - \tau) \sin \omega(t_i - \tau)$ terms do not appear in Equation C.1. The coefficients for $p(\omega)$ are calculated as follows.

$$p_i(\omega) = \left[2\sigma^2 \frac{2}{N} P_N(\omega) \right]$$

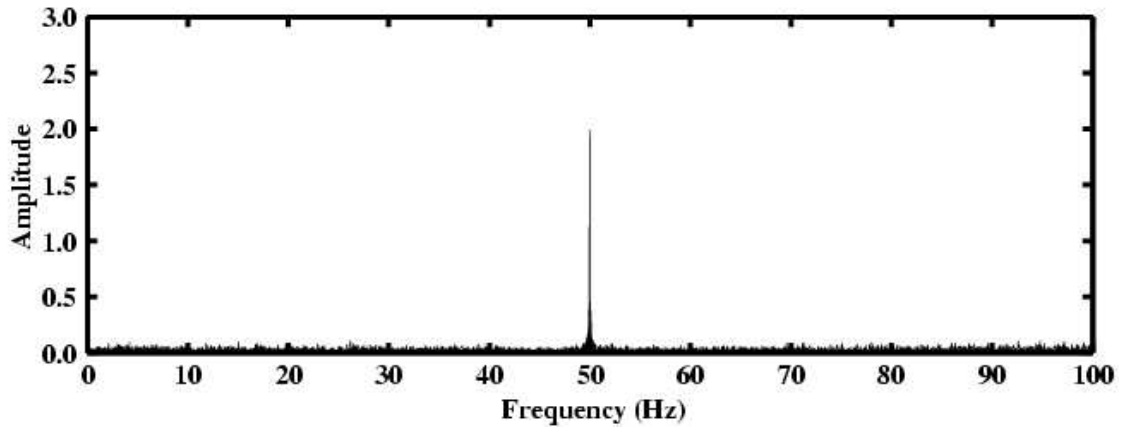
A comparison of the unequally spaced Fourier transform method used in this research and Lomb's method was made for the theoretical signal defined by

$$p(t) = A \sin(2\pi f t) \quad (\text{C.2})$$

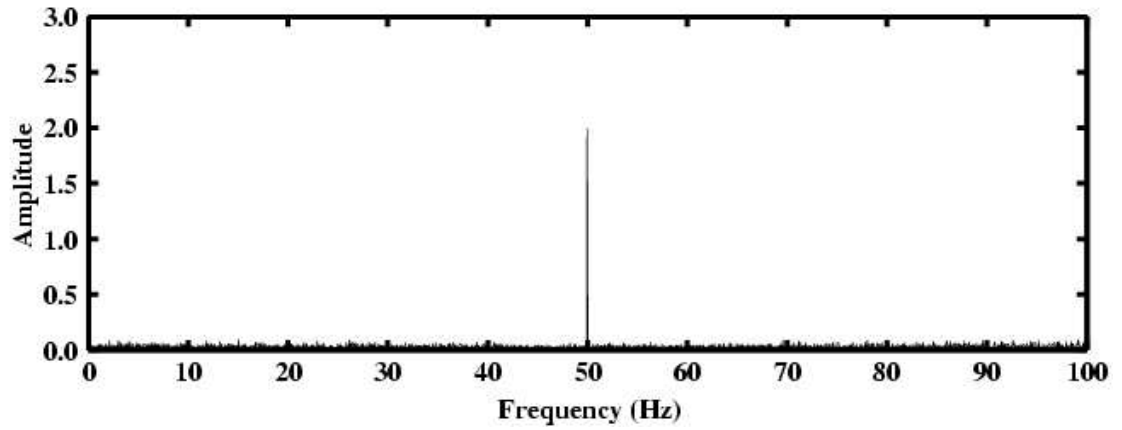
where $A = 2.0$ and $f = 50.0 \text{ Hz}$. The number of sample points is 4096 and the sampling period is 6π .

Figure C.1 presents the results from the least squares method and the unequally spaced Fourier transform method. The amplitude, A , using the least squares method is 2.0, and the amplitude using the unequally spaced Fourier transform method is 2.0. The two methods are in excellent agreement with each other, providing further confirmation the unequally spaced Fourier transform method works. Note that even though both methods agree on amplitude and frequency, the least squares method does not provide information about the phase relationship between the frequency responses, which is an important part of this

work.



(a) Least squares spectral method



(b) Unequally spaced Fourier transform method

Figure C.1: Spectral content for the theoretical signal defined by Equation C.2.

Appendix D: Rotating Frame Analysis

The circumferential distribution of the unsteady pressure field around the rotor allows the data to be investigated as if recorded in the rotating reference frame. For each pressure transducer, there is a recorded signal of pressure versus time, $p(t)$. Additionally, angular position versus time, $\theta_r(t)$, for each pressure transducer can be calculated using Equa-

tion 3.5. Hence, for each pressure transducer, $p(\theta_r, t)$ can be calculated. Due to the circular geometry of the fan, $\theta_r(t)$ must be between 0 and 2π for each sample. When the data from each of the 11 equally spaced pressure transducers is combined correctly, a complete two-dimensional unsteady pressure field, which will be denoted as $\tilde{p}(\theta_r, t)$, is calculated. Note that for any given time $t = t_o$, $\tilde{p}(\theta_r, t)$ will have 11 pressure samples at angular positions between 0 and 2π . If the sampling frequency, F_s , is such that the time between samples is equal to the time it takes the blades to move from one pressure transducer to the next, the set of angular positions in $\theta_r(t_o)$ will be the same for all t , as illustrated in Table D.2.

Table D.2: Location of rotating coordinate system ($\theta_r(t_o)$) with respect to stationary pressure transducer positions.

| Time | Pressure Transducer # | | | | |
|--------------------|-----------------------|----------------|-----|-----------------|-----------------|
| | 1 | 2 | ... | 10 | 11 |
| $t = 0$ | $\theta_{r,1}$ | $\theta_{r,2}$ | ... | $\theta_{r,10}$ | $\theta_{r,11}$ |
| $t = \Delta t$ | $\theta_{r,2}$ | $\theta_{r,3}$ | ... | $\theta_{r,11}$ | $\theta_{r,1}$ |
| $t = \Delta t * 2$ | $\theta_{r,3}$ | $\theta_{r,4}$ | ... | $\theta_{r,1}$ | $\theta_{r,2}$ |
| ... | ... | ... | ... | ... | ... |

Ideally all transducers, pressure or strain gages, function properly and the data has been recorded under optimal conditions, such as low noise. Unfortunately, in this investigation pressure transducer 13 malfunctioned at the start of testing, and pressure transducer 6 has considerable noise, see Figure D.1 which presents each pressure transducer's time dependent data during the transient into flutter. Without all the equally spaced pressure transducer data, the two-dimensional space-time method can not be easily employed. The two-dimensional space-time method was still effective for analyzing the data. To compensate, Lagrange interpolation was used to estimate the missing data for pressure transducers 6 and 13, see Appendix E.

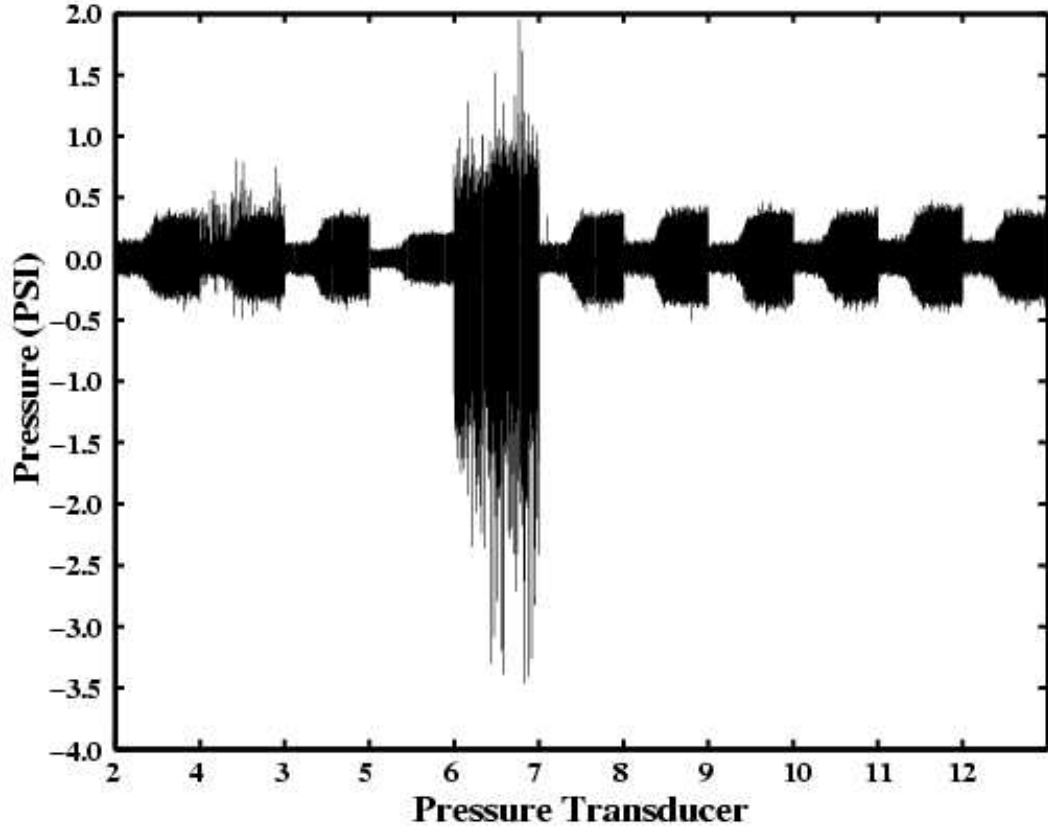


Figure D.1: A comparison of the pressure transducer data sets for 70% corrected speed as the fan is back-pressured into flutter.

Before the pressure transducer data was transformed from the stationary reference frame to the rotating reference frame, each of the signals were digitally filtered with a Butterworth infinite impulse response filter of order 10 and cutoff frequency of 2 kHz to remove the blade passing frequency, and then re-sampled at the rotational frequency using linear interpolation, see Appendix B. With the nine functional pressure transducers and the two interpolated pressure transducers, the unsteady pressure field $\hat{p}(\theta_r, t)$ was created.

The unsteady pressure field, $\hat{p}(\theta_r, t)$, was divided into smaller time blocks. The dimensions of the unsteady pressure blocks were 1024 points along the time axis, 93 rotor revolutions, by 11 points along the spatial axis for the 70% corrected speedline. Two dimensional Fourier transforms were calculated for each of the blocks. Figure D.2 presents the two-dimensional Fourier transform at 15 seconds. The flutter response at 411 Hz and

2 nodal diameters can easily be seen in Figure D.2. Aside from the flutter frequency, responses at multiples of the rotational frequency are seen in Figure D.2. In addition, the weaker 822 Hz response at a nodal diameter of 4 is evident. These results are in excellent agreement with those of the two probe and multiprobe analyses conducted in the stationary reference frame. The remaining significant responses are believed to be effects of using interpolation to estimate the missing pressure transducers, see Appendix B.

For the two-dimensional space-time analysis conducted in the rotating reference frame, a dominant flutter response at 411 Hz and a nodal diameter of 2 were identified. The secondary response at 822 Hz and nodal diameter of 4 were also identified. The existence of multiple nodal diameters is not strongly indicated in the figures because their relative amplitudes are much smaller than the $n = 2$ response, however there is a response at 411 Hz and nodal diameters of 4 and 5.

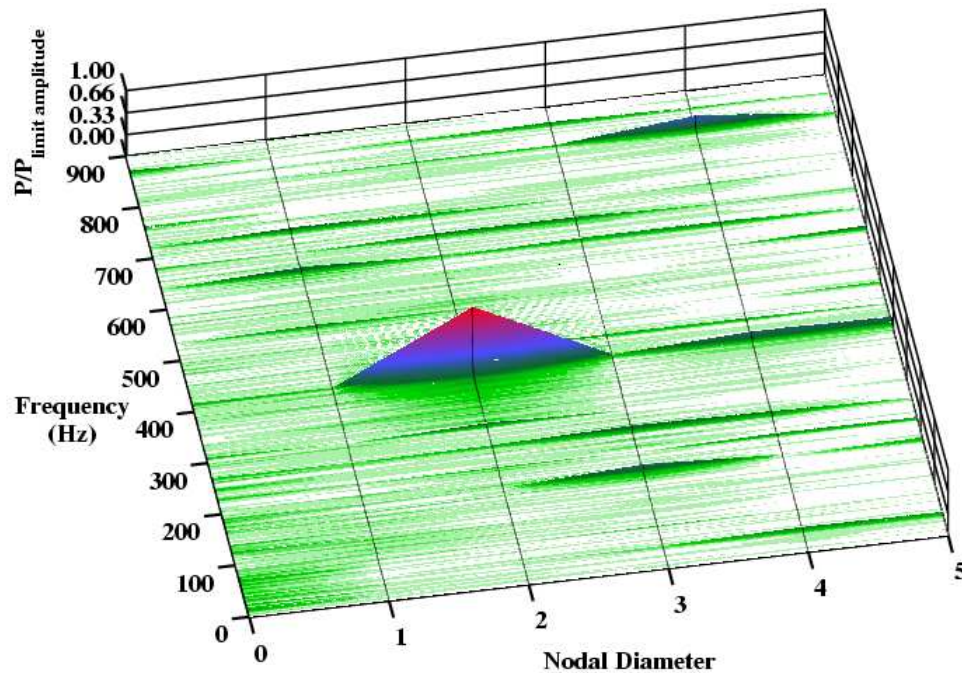


Figure D.2: Two-dimensional Fourier transform of pressure transducer data at 15 seconds at 70% corrected speed.

Appendix E: Theoretical Rotating Frame Analysis

A theoretical analysis was conducted to test the effects produced when Lagrange interpolation is used to estimate the missing data for pressure transducers 6 and 13. Whether or not the interpolation method is acceptable requires a thorough analysis for each case considered. There are many factors to take into account, like the total number of transducers, the circumferential distance between each transducer, the location of the failed transducers, and whether or not they are circumferentially next to each other, etc. To help ensure the interpolation method was valid for the present pressure transducer configuration, numerous tests to understand the effects of the interpolation method were conducted.

The theoretical analysis consisted of simulating the flutter for 11 pressure transducers as used in this experiment. The simulated data points for pressure transducers 6 and 13 were replaced with a constant value, 999,999. Transformation of the 11 pressure transducers is performed next. The transformed data, $\hat{p}(\theta_r, t)$, is then searched for the constant value, 999,999, used for the missing pressure transducers, and then replaced by Lagrange interpolating from the neighboring points using a third order Lagrange polynomial. Figure E.1 shows the results of such a test. The Lagrange interpolation created some random frequencies and nodal diameters. The simulated flutter response had a frequency of 411 Hz with a nodal diameter of 2 and is easily distinguished in the Fourier transform of Figure E.1. Several tests were conducted to add additional characteristics to the simulated data, such as re-sampling at a lower frequency. It was concluded that the two-dimensional space-time method could provide reliable results for data that was re-sampled to a lower frequency and when Lagrange interpolation is used to estimate the missing pressure transducers.

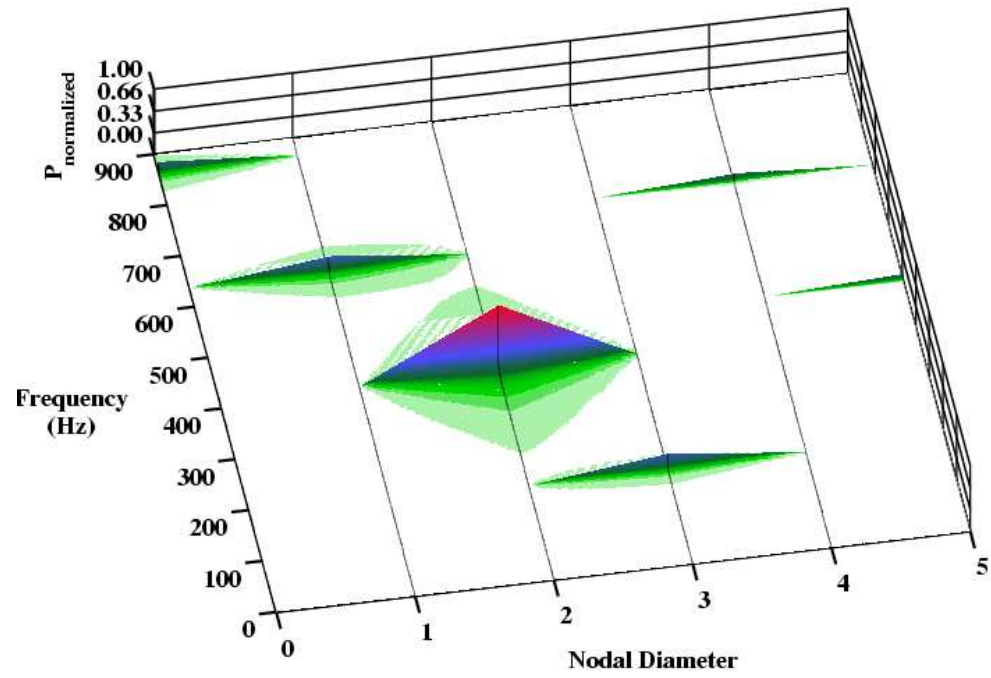


Figure E.1: Theoretical simulation of 2 nodal diameter flutter signal that includes the absence of two pressure transducers.

REFERENCES

- Ekaterinaris, J.A. and Platzer, M.F., 1996, "Numerical Investigation of Stall Flutter," ASME Journal of Turbomachinery, Vol. 118, pp. 197-203.
- Fost, R.B. and Teets, P.S., 1998, "Upgrading the Air Force Turbine Engine Research Center for Enhanced HCF Aeromechanics Evaluations with Light Probes," Third National Turbine Engine High Cycle Fatigue (HCF) Conference, 2-5 February.
- Hohenberg, R., 1967, "Detection and Study of Compressor-blade Vibration," Experimental Mechanics, June 1967.
- Jutras, R.R., Fost, R.B., Chi, R.M., and Beacher, B.F., 1981, "Subsonic/Transonic Stall Flutter Investigation of a Rotating Rig," NASA CR-174625.
- Kurkov, A.P., 1983, "Measurement of Aerodynamic Work During Fan Flutter," Journal of Engineering for Power, Vol. 105, pp.204-211.
- Kurkov, A.P., 1984a, "Formulation of Blade Flutter Spectral Analyses in Stationary Reference Frame," NASA Technical Paper 2296.
- Kurkov, A.P., 1984b, "Measurements of Self-Excited Rotor-Blade Vibrations Using Optical Displacements," Journal of Engineering for Power, Vol. 106, pp. 44-49.
- Kurkov, A.P., 1989, "Optical Measurement of Unducted Fan Blade Deflections," ASME Paper No. 89-GT-298.
- Kurkov, A.P. and Mehmed, O., 1991, "Optical Measurements of Unducted Fan Flutter," ASME Paper No. 91-GT-19.
- Lomb, N.R., 1976, "Least-Squares Frequency Analysis of Unequally Spaced Data," Astrophysics and Space Science, Vol. 39, pp. 447-462.
- Mignolet, M.P. and Choi, B., 2002, "Robust Optimal Positioning of Strain Gauges on Blades," Proceedings of the 7th National Turbine Engine High Cycle Fatigue Conference.
- Sanders, A.J., Hassan, K.K., and Rabe, D.C., 2003, "Experimental and Numerical Study of Stall Flutter in a Transonic Low-Aspect Ratio Fan Blisk," ASME Paper GT2003-38355.
- Siden, L.D.G., 1991, "Numerical Simulation of Unsteady Viscous Compressible Flows Applied to Blade Flutter Analysis," ASME 91-GT-203.
- Stargardt, H., 1977, "Optical Determination of Rotating Fan Blade Deflections," Journal of Engineering for Power, Vol. 99, No. 2, pp. 204-209.
- Swafford, T.W., Loe, D.H., Huff, D.L., Huddleston, D.H., and Reddy, T.S.R., 1994, "The Evolution of NPHASE: Euler/Navier-Stokes Computations of Unsteady Two-Dimensional Cascade Flow Fields," AIAA Paper No. AIAA-94-1834.

Washburn, R.S., 2002, "NSMS Nodal Diameter Analysis for Integral and Non-integral Vibratory Responses," Proceedings of the 7th National Turbine Engine High Cycle Fatigue Conference.

Weber, S. and Platzer, M.F., 2000, "A Navier-Stokes Analysis of the Stall Flutter Characteristics of the Buffum Cascade," ASME Paper 2000-GT-385.

Wu, J., Huff, D.L., and Sankar, L.N., 1989, "Evaluation of Three Turbulence Models for the Prediction of Steady and Unsteady Airloads," NASA Technical Memorandum 101413.

Zablotskiy, I.Ye., Korostelev, Yu.A., and Sviblov, L.B., 1974, "Contactless Measuring of Vibrations in the Rotor Blades of Turbines," FTD-HT-23-673-74.

GRANT PUBLICATIONS AND PRESENTATIONS

This appendix lists the publications and presentations made under the support of this grant.

Archival Journal Publications

Gill, J.D., Capece, V.R., and Fost, R.B., “Experimental Methods Applied in a Study of Stall Flutter in an Axial Flow Fan,” *Journal of Shock and Vibration*, in press.

Conference Publications and Presentations

Gill, J.D., and Capece, V.R., “Experimental Investigation of Flutter in a Single Stage Unshrouded Axial-Flow Fan,” AIAA Paper No. AIAA-2004-0686, January 2004.

Gill, J.D., and Capece, V.R., and Fost, R.B., “Experimental Methods Applied in a Study of Stall Flutter in an Axial Flow Fan,” Proceedings *Eighth National Turbine Engine High Cycle Fatigue Conference*, April 2003, Session 15: Instrumentation II, pp. 71-80. (Also in *Journal of Shock and Vibration*.)

Gill, J.D., and Capece, V.R., “Casing Unsteady Pressure Measurements of an Axial Flow Fan in Stall Flutter,” *Abstracts Twenty-Eighth Annual Dayton-Cincinnati Aerospace Science Symposium*, March 2003. (Abstract)

Gill, J.D., and Capece, V.R., “Unsteady Pressure Response of an Axial Flow Fan in Flutter Using Stationary Reference Frame Sensors,” *Abstracts Twenty-Seventh Annual Dayton-Cincinnati Aerospace Science Symposium*, March 2002. (Abstract)

Gill, J.D., and Capece, V.R., “Flutter Precursor in Turbomachinery,” *Abstracts 26th Annual Dayton-Cincinnati Aerospace Science Symposium*, March 2001. (Abstract)

Thesis

Gill, John D., “Time Dependent Casing Pressure Measurements of an Axial Flow Fan During Transition to Flutter,” MSME, University of Kentucky, May 2004.

Student Awards

John Daniel Gill, Best Technical Presentation, 28th AIAA Dayton-Cincinnati Aerospace Symposium in Fluid/Structures Interaction, March 2003.

APPENDIX B

Massachusetts Institute of Technology Research

*Gas Turbine Laboratory
Department of Aeronautics and Astronautics
Massachusetts Institute of Technology
Cambridge, MA 02139*

FINAL TECHNICAL REPORT

under Subcontract PO #180179

entitled

**EFFECT OF RADIAL TRANSPORT ON COMPRESSOR TIP FLOW
STRUCTURES AND ENHANCEMENT OF STABLE FLOW RANGE**

submitted to

**BATTELLE MEMORIAL INSTITUTE
505 KING AVENUE
COLUMBUS, IN 43201-2693
ATTN: MS. PAMELA TEETS**

DOUGLAS C. RABE, TECHNICAL MONITOR

PREPARED BY: Dr. Choon S. Tan, Principal Investigator
Professor Edward M. Greitzer
Sean P. Nolan, Graduate Research Assistant

PERIOD OF INVESTIGATION: June 2, 2003 - March 31, 2005

May 24, 2005

Effect of Radial Transport on Compressor Tip Flow Structures and Enhancement of Stable Flow Range

by

Sean Nolan

Submitted to the Department of Aeronautics and Astronautics on May 20, 2005 in partial fulfillment of the requirement for the Degree of Master of Science

Abstract

The relation between tip clearance flow structure and axial compressor stall is interrogated via numerical simulations, to determine how casing treatment can result in improved flow range. Both geometry changes and flow field body forces are used as diagnostics to assess the hypothesis that the radial transport of momentum out of the tip region, and the consequent decrease in streamwise momentum in this region, is a key aspect of the flow. The radial velocity responsible for this transport is a result of the flow field set up by the tip clearance vortex. Altering the position of the tip clearance vortex can alter the amount of streamwise momentum lost due to radial transport and hence increase the compressor flow range.

Circumferential grooves improve the flow range in the manner described above. In the presence of such a groove the radial velocity profile along the passage can be altered so that the radial transport of streamwise momentum is decreased. The flow fields associated with grooves at different axial positions, and of different depths, are also examined, along with previous research on circumferential grooves, and it is shown that these are in accord with the hypothesis.

Thesis Supervisor: Edward M. Greitzer

Title: H. N. Slater Professor of Aeronautics and Astronautics

Thesis Supervisor: Douglas C. Rabe

Title: AFRL Turbine Engine Research Center Director

Thesis Supervisor: Choon S. Tan

Title: Senior Research Engineer

Acknowledgements

There are myriad persons I must thank for providing support and guidance in this research. My advisors, Professor E. M. Greitzer and Dr. Choon Tan, have been a great source of technical information regarding thermodynamics and fluid mechanics. More importantly, they have taught me much about the essence of technical research, an activity that is as much an art as it is a science.

Also providing invaluable advice was Dr. Douglas Rabe of the Compressor Research Facility at the Air Force Research Lab. My time working for him at the AFRL gave me much needed experience. There were several other people at AFRL who helped my research progress. They include David Car, Tom McCray, and Carl Williams. Dr. Chunill Hah of NASA Glenn also deserves thanks for his sharing of CFD knowledge and results.

At GTL, Dr. Yifang Gong and Dr. Boris Sirakov helped to greatly ease the learning curve associated with numerical simulation. For their work in providing an environment in which research can be done, Paul Warren, Lori Martinez, Julia Finn, and Holly Anderson also deserve a great deal of recognition.

I am indebted to the students of GTL, with whom ideas were discussed and refined. Parthiv Shah was especially important in this aspect. Apart from the technical help, my fellow students helped to make the atmosphere around the lab enjoyable.

I am grateful towards my roommates Michael Razo, Leilani Roser, and Andrew Wong. Many thanks also to Professor J.P. Clarke, Ben Schmeckpeper, Yuval Mazor, Brian Anderson, and the rest of the MIT track and field and cross country teams.

Most importantly, I want to thank my brother and my mom. My mom, Janice M. Rock-Nolan, has always provided advice and support, and the last two years were no exception.

This work was supported under subcontract from Battelle Columbus Laboratories PO #180179, prime contract #F33615-02-D-2223. Additional backing was provided by AFOSR under grant #FA9550-05-1-0050. This support is greatly appreciated. Fluent was used to perform the numerical experiments.

Disclaimer

The research reported in this document/presentation was performed in connection with contract #F33615-02-D-2223 with the U.S. Air Force. The views and conclusions contained in this document/presentation are those of the authors and should not be interpreted as presenting the official policies or position, either expressed or implied, of the U.S. Air Force or the U.S. government unless so designated by other authorized documents. Citation of manufacturers' or trade names does not constitute an official endorsement or approval of the use thereof. The U.S. Government is authorized to reproduce and distribute reprints notwithstanding any copyright notation hereon.

Table of Contents

| | |
|---|-----------|
| Abstract | 2 |
| Acknowledgements | 3 |
| Table of Contents | 4 |
| List of Figures | 6 |
| List of Table | 9 |
| Nomenclature | 10 |
| 1.0 Introduction and Background | 12 |
| 1.1 Compressor Performance and Use of Casing Treatment..... | 12 |
| 1.2 Research Goals..... | 14 |
| 1.3 Specific Research Contributions..... | 15 |
| 2.0 Previous Research and Hypothesis | 16 |
| 2.1 Previous Research..... | 16 |
| 2.2 Hypothesis..... | 22 |
| 3.0 Technical Approach | 24 |
| 3.1 Use of CFD..... | 24 |
| 3.2 Grid Generation..... | 24 |
| 3.3 Use of Numerical Stall as Flow Range Indicator..... | 26 |
| 4.0 Assessment of the Hypothesis | 27 |
| 4.1 Body Forces as a Diagnostic..... | 27 |
| 4.1.1 Setup..... | 27 |
| 4.1.2 Results..... | 28 |
| 4.1.3 Changes in Radial Transport Term..... | 30 |

| | |
|---|-----------|
| 4.2 Use of a Flat Plate at the Blade Tip as a Diagnostic..... | 37 |
| 4.2.1 Setup..... | 37 |
| 4.2.2 Results..... | 37 |
| 4.2.3 Changes in Radial Transport Term..... | 39 |
| 5.0 Casing treatment..... | 41 |
| 5.1 Setup..... | 41 |
| 5.2 Results..... | 41 |
| 5.3 Changes in Radial Transport Term..... | 45 |
| 5.4 Causal Links..... | 50 |
| 5.5 Mechanism for Induced Radial Velocity..... | 55 |
| 5.6 Vortex Kinematics..... | 61 |
| 5.7 General Guidelines for Circumferential Groove Casing Treatment... | 62 |
| 6.0 Summary and Conclusions..... | 64 |
| 7.0 Suggested Future Work..... | 65 |
| References | 66 |
| Appendix A User-Defined Functions | 68 |
| Appendx B Method of Stall Inception | 71 |
| Appendix C Sensitivity to Turbulence Model | 74 |

List of Figures

| | | |
|-----|--|----|
| 1.1 | Sample compressor map..... | 12 |
| 1.2 | Effect of tip clearance on compressor performance..... | 13 |
| 1.3 | Sample casing treatment..... | 14 |
| 1.4 | Typical effect of casing treatment..... | 14 |
| 2.1 | Non-dimensional blockage vs. loading factor..... | 17 |
| 2.2 | Incidence angle stall criterion | 18 |
| 2.3 | Vo spike stall criteria..... | 19 |
| 2.4 | Losses due to mixing between clearance flow and bulk flow..... | 20 |
| 2.5 | Source of clearance vortex fluid..... | 22 |
| 2.6 | Streamwise momentum balance..... | 23 |
| 3.1 | Radial variation in grid density..... | 25 |
| 4.1 | Sketch of geometric configuration of tip flow region indicating location of body force application..... | 28 |
| 4.2 | Pressure rise coefficient vs. flow coefficient (body force calculation)..... | 39 |
| 4.3 | Adiabatic efficiency vs. flow coefficient (body force calculation)..... | 30 |
| 4.4 | Streamwise velocity contours at 100% span..... | 31 |
| 4.5 | Vortex simplification | 32 |
| 4.6 | Pitchwise-averaged radial velocity vs. axial location..... | 33 |
| 4.7 | Tangential vorticity contours at 100% span..... | 33 |
| 4.8 | Pitchwise-averaged radial velocity vs. axial location (body force calculation)..... | 35 |

| | | |
|------|--|----|
| 4.9 | Pitchwise-averaged radial transport of streamwise momentum vs. axial location (body force calculation)..... | 36 |
| 4.10 | Setup of plate in stream numerical experiment..... | 37 |
| 4.11 | Pressure rise coefficient vs. flow coefficient (plate in stream calculation)... | 38 |
| 4.12 | Adiabatic efficiency vs. flow coefficient (plate in stream calculation)..... | 38 |
| 4.13 | Pitchwise-averaged radial velocity vs. axial location (plate in stream calculation)..... | 40 |
| 4.14 | Pitchwise-averaged radial transport of streamwise momentum vs. axial location (plate in stream calculation) | 40 |
| 5.1 | Views of casing treatment geometry..... | 42 |
| 5.2 | Pressure rise coefficient vs. flow coefficient (casing treatment calculation)..... | 43 |
| 5.3 | Adiabatic efficiency vs. flow coefficient (casing treatment calculation)..... | 43 |
| 5.4 | Total pressure rise coefficient vs. flow coefficient as calculated by Adamczyk and Shabbir, compared with calculations of this research..... | 44 |
| 5.5 | Pitchwise-Averaged streamwise velocity vs. axial location (casing treatment calculation) | 46 |
| 5.6 | Pitchwise-averaged groove-induced radial velocity vs. axial velocity (casing treatment calculation) | 46 |
| 5.7 | Control volume used in momentum balance..... | 47 |
| 5.8 | Flow range extension vs. groove depth..... | 49 |

| | | |
|------|---|----|
| 5.9 | Induced radial velocity vs. axial location (100% groove near baseline design flow coefficient)..... | 49 |
| 5.10 | Change in vortex trajectory with use of casing treatment..... | 50 |
| 5.11 | Illustration of change in radial velocity profile due to shift of clearance vortex..... | 51 |
| 5.12 | Qualitative view of the local beneficial radial transport..... | 53 |
| 5.13 | Block diagram showing causality..... | 54 |
| 5.14 | Mechanism for local radial transport improvement..... | 56 |
| 5.15 | Relative velocity vectors at mid-pitch..... | 57 |
| 5.16 | Groove forward position..... | 58 |
| 5.17 | Total pressure rise coefficient vs. flow coefficient (forward position)..... | 59 |
| 5.18 | Radial velocity contours at the groove entrance..... | 60 |
| 5.19 | Relative velocity vectors at mid-pitch (forward position)..... | 60 |
| 5.20 | Image vortex system for smoothwall case..... | 61 |
| 5.21 | Image vortex system for groove casing treatment..... | 62 |
| B.1 | Comparison of flow fields at blade tip immediately preceding spike and modal stalls..... | 72 |
| B.2 | Entropy contours at 100% span..... | 72 |
| C.1 | Pressure rise coefficient vs. flow coefficient (influence of turbulence model)..... | 75 |
| C.2 | Adiabatic efficiency vs. flow coefficient (influence of turbulence model) | 75 |

List of Tables

| | | |
|---------|--|----|
| Table 1 | Key parameters (body force calculation)..... | 34 |
| Table 2 | Key parameters (plate in stream calculation) | 39 |
| Table 3 | Magnitudes of streamwise momentum terms..... | 47 |
| Table 4 | Incidence angles at blade tip leading edge at the smoothwall stalling flow coefficient..... | 73 |

Nomenclature

Symbols

| | |
|----------|--|
| ρ | density |
| q | dynamic head |
| A_b | blockage area |
| A | area |
| P | pressure |
| P_t | stagnation pressure |
| T | temperature |
| T_t | stagnation temperature |
| η | adiabatic efficiency |
| r | radial position |
| τ | tip clearance gap |
| U_t | blade tip speed |
| V' | Relative Velocity |
| u | velocity |
| μ | viscosity |
| y^+ | non-dimensional distance from wall |
| γ | specific heat ratio |
| ζ | angle between clearance flow and bulk flow |
| ϕ | flow coefficient |

Subscripts

| | |
|----------|--|
| 100 | refers to 100%span (the radial plane level with the blade tip) |
| bp100 | refers to the 100%span region within the blade passage |
| x | axial direction |
| θ | tangential direction |
| s | streamwise direction |
| r | radial direction |
| e | edge of velocity defect |

Chapter 1

Introduction and Background

1.1 Compressor Performance and Use of Casing Treatment

The flow range in which an axial compressor can operate is an important limitation in the operation of a gas turbine. As depicted in Fig. 1.1, if the mass flow becomes too low for a given engine speed, compressor stall or surge will occur. The result of the stall is either rotating stall or surge, two unsteady phenomena which can have serious operational or mechanical consequences [Kerrebrock, 12]. Avoiding stall is thus an important aspect of compressor design and development.

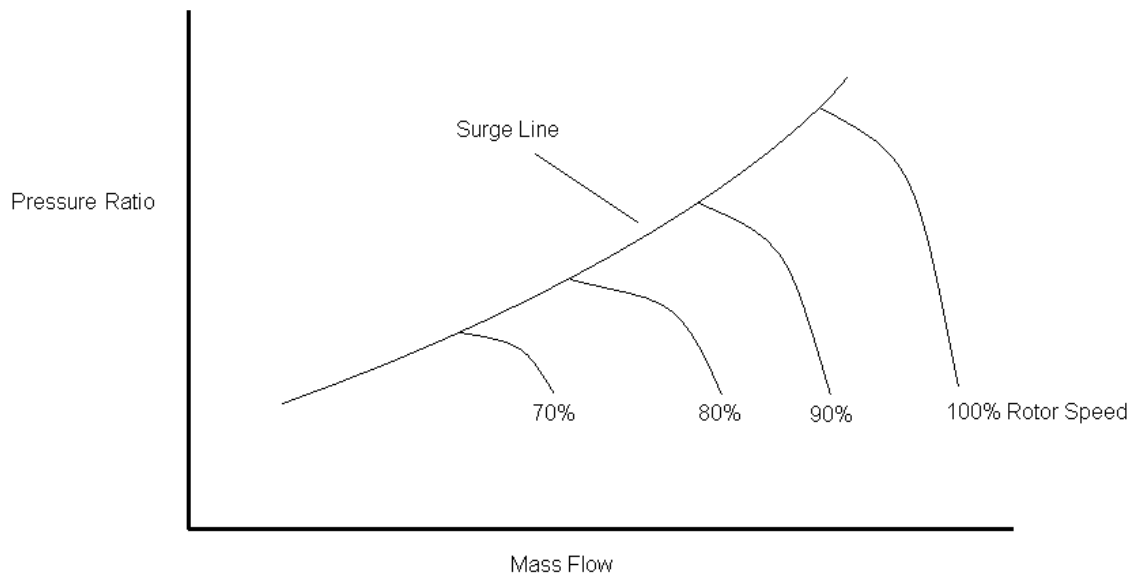


Figure 1.1 Sample compressor map

While stall can be initiated on the blade or in the tip region, for compressors with moderate to high solidities, stall is initiated in the tip region [Koch, 14]. As depicted in figure 1.2 [6], increased tip clearances result in decreased flow range, pressure rise, and efficiency.

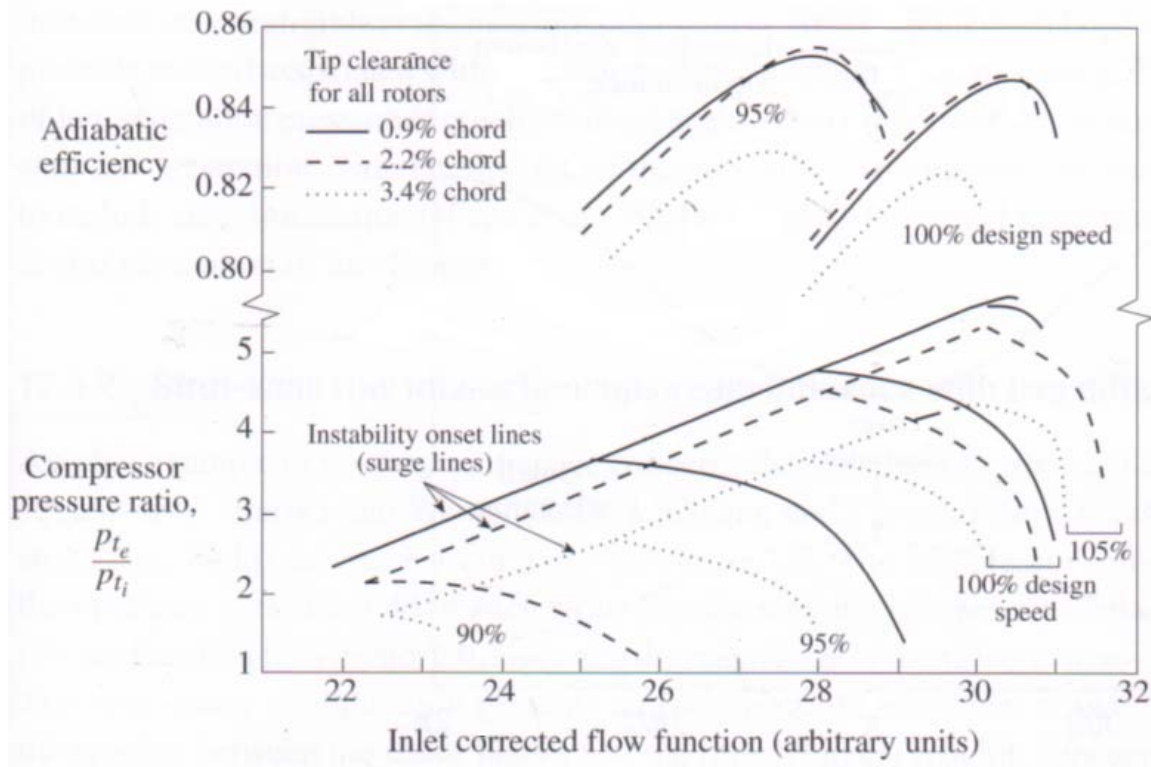


Figure 1.2 Effect of tip clearance on compressor performance. [Cumpsty, 6]

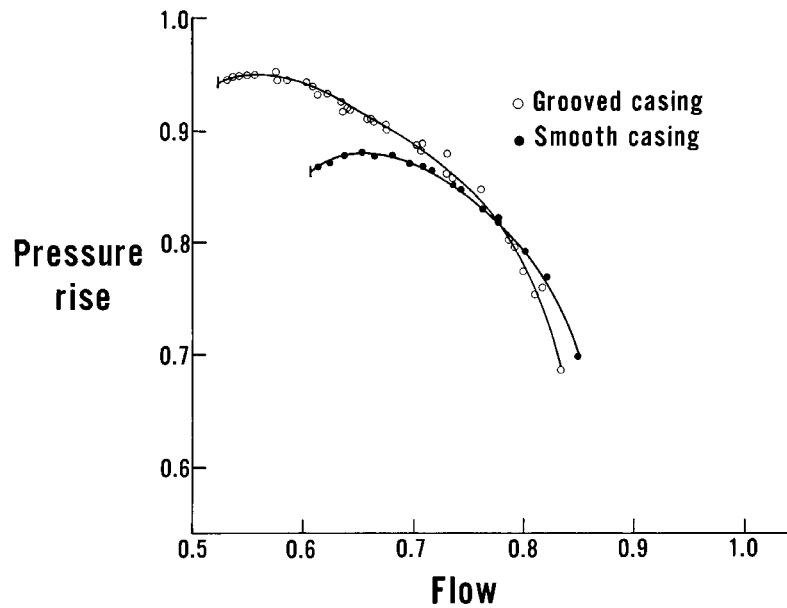
The buffer between the operating line and the stall line is called the stall margin. In spite of the design stall margin, the compressor may approach the stall line during transient operation or if the compressor is deteriorated due to increased tip clearance. If it is determined that stall margin is not adequate, often casing treatment has been incorporated to increase the useful flow range. Casing treatment consists of slots or grooves integrated into the casing above the blade tip (Figure 1.3, which is for a small helicopter engine).

The marked effect that tip casing treatments have indicates the significance of the tip region flow in setting the compressor stall limit. However, much of the knowledge regarding casing treatments and their effectiveness is empirical. Also, the flow range extension obtained through the use of casing treatment is often accompanied by a penalty in pressure rise coefficient and/or efficiency at the design condition (Figure 4). This

thesis addresses the mechanism of compressor stall and flow range enhancement by one type of casing treatment.



Figure 1.3 Sample casing treatment Figure [The Rolls-Royce Magazine]



1.4 Typical effect of casing treatment [Greitzer, et al., 8]

1.2 Research Goals

The objective of this research is to be able to determine the changes in the flow field by which casing treatments improve compressor performance. This would in turn enable a design guideline for casing treatments to be developed. In order to do so, the following specific research questions must be answered:

- What are the critical aspects of tip flow that impact flow range?
- What are the changes that enhance flow range?
- What are the mechanisms of casing treatment which create these flow field changes?

1.3 Specific Research Contributions

- This research identifies a key flow feature (the radial velocity associated with the tip clearance vortex) that results in streamwise momentum being transported radially out of the tip region. Improvement of the radial transport term is shown to improve streamwise momentum at the blade tip and hence improve compressor flow range.
- Demonstration that circumferential groove casing treatments are shown to improve performance by improving radial transport and hence the loss of streamwise momentum in the blade tip region.
- Demonstration that for peak efficiency of circumferential groove treatment, there is an optimum depth, smaller than the tip clearance. If flow range is the sole concern, deeper grooves are better.
- Demonstration that circumferential grooves should be placed so that the tip clearance vortex is roughly parallel to the trailing edge of the groove.
- In-depth discussion of the cause and effect relationship between the use of casing treatment and improvement in flow range. The improvement is linked to repositioning of the tip clearance vortex further towards the trailing edge of the blade passage.
- A unified description including this research and previous research concerning tip clearance flow is presented relating blockage, backflow, streamwise momentum, and the tip clearance vortex.

Chapter 2 Previous Research and Hypothesis

2.1 Previous Research

Much research has been done to show the relation between tip clearance flows and the onset of compressor stall. Key results from previous research relevant to this work are described here.

Lee performed experiments on a stator row with a rotating hub [11]. Both smooth hubs and hubs with casing treatments were examined. It was shown that increasing the streamwise momentum (momentum in the blade-fixed frame projected onto the chordline of the blade) in the tip region resulted in improved performance, most notably the pressure rise at which the blade row stalled. The streamwise momentum increase was achieved through use of the casing treatment with axially skewed slots as well as through suction and blowing.

Crook[5] also found that increased streamwise momentum in the tip clearance improved flow range based on numerical simulations.

Khalid [13] developed a simple analysis for the relationship between tip clearance, loading, and blockage, defined as the momentum deficit calculated on a plane normal to the flow. Stall is closely related to blockage, in that the slope the curve of blockage vs. flow coefficient increases markedly as stall is approached. The definition for blockage proposed by Khalid is given in equation 1.

$$A_b = \iint \left(1 - \frac{\rho u}{\rho_e u_e} \right) dA. \quad (1)$$

In equation 1, the subscript “e” refers to the values at the edge of the momentum defect region. Flow blockage determines the pressure rise possible across the compressor, since

blockage reduces the effective flow area. Khalid found that the primary contributor to blockage is the expansion of the low relative total pressure region in the vortex core. Two key factors that determine blockage generation are thus the pressure rise through the blade passage and the magnitude of the relative total pressure deficit.

Fig. 2.1 shows the relation between nondimensional blockage and loading, computed by Khalid. On the y-axis, A_b represents the absolute blockage, while τ represents the tip clearance. On the x-axis, ΔP_t represents the change in relative total pressure experienced from upstream of the blade passage to the tip clearance vortex core, ΔP is the static pressure rise through the blade passage, and Q is the dynamic head at the inlet. Given a constant static pressure rise and dynamic head, as the total pressure defect in the vortex core becomes more pronounced, the blockage increases.

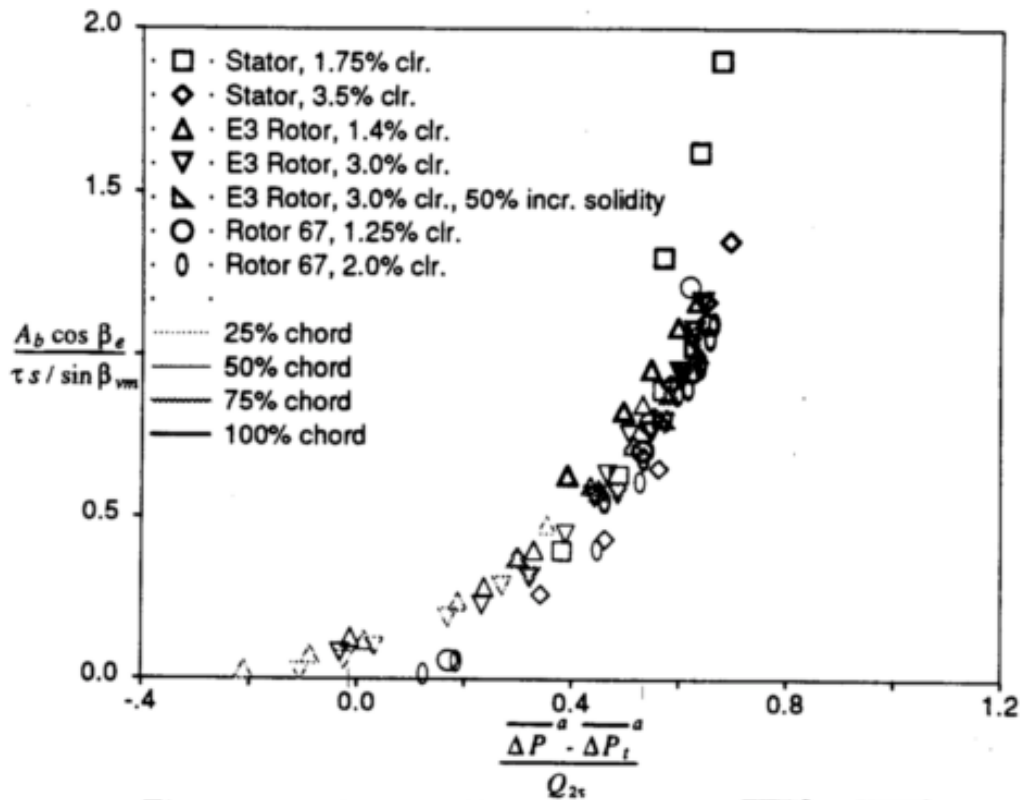


Figure 2.1 Non-Dimensional blockage vs. loading factor[Khalid, 13]

Rabe and Hah [15] studied the effect of a circumferential groove casing on a transonic rotor blade. It was determined that the stall point coincided with a particular incidence angle at the blade tip leading edge. The use of casing treatment lowers the overall flow coefficient at which this incidence angle was achieved, delaying stall. The stalling incidence angle, however, was found to be common between baseline and casing treatment cases, as shown in Fig. 2.2.

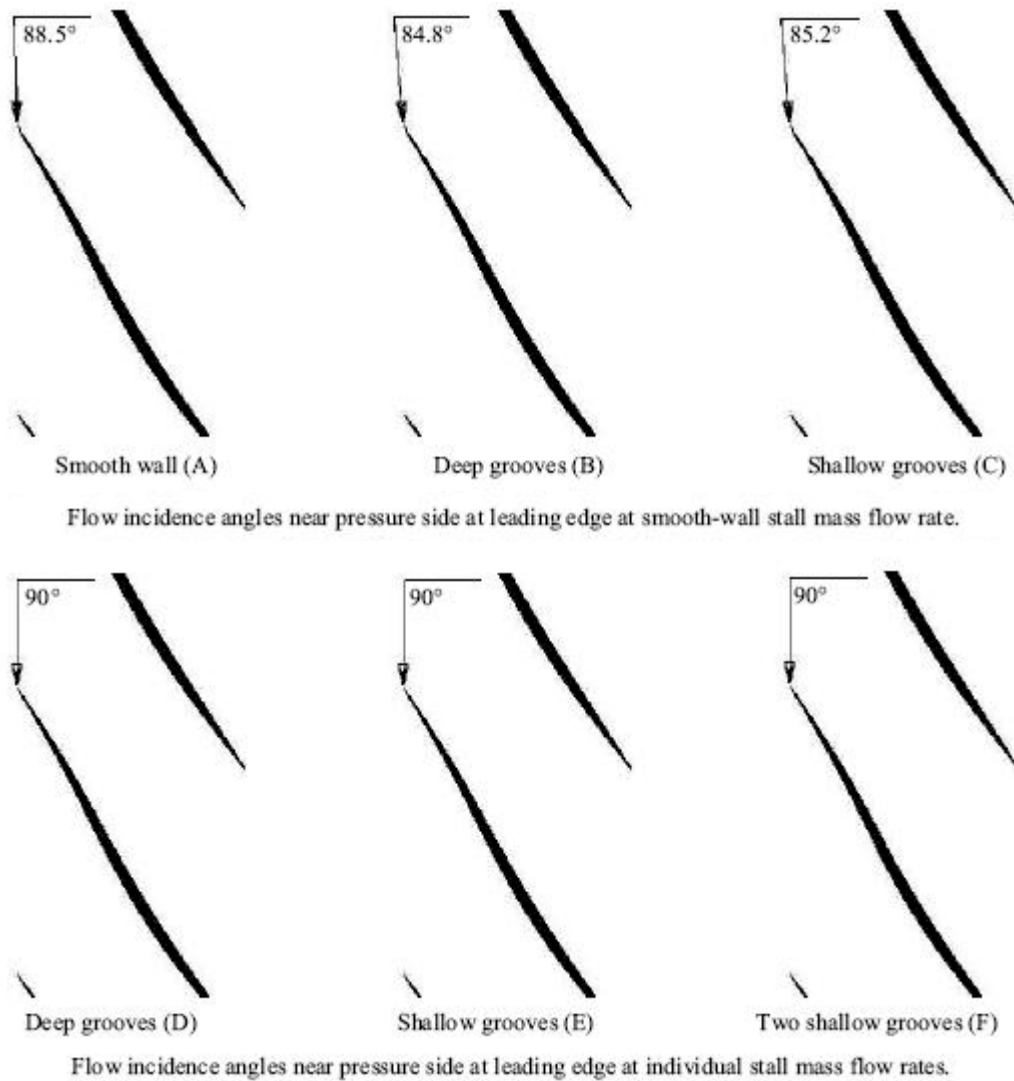


Figure 2.2 Incidence angle stall criterion. Casing treatment lowered the flow coefficient at which the critical incidence angle was reached [Rabe, 15]

It has been found that there are two routes to compressor rotating stall. Spike stall inception develops from a relatively short wavelengthed disturbance of 2-3 blade pitches. In contrast, modal inception occurs from low amplitude, long wavelength disturbances that take longer to develop into full stall [Camp, 3]. More details concerning the different paths of stall inception can be found in Appendix B. Vo [19] concluded that there are two flow features that are necessary and sufficient for spike stall onset to occur. There must be flow into the adjacent passage from around the trailing edge, and from around the leading edge (see figure 2.3) for spike stall to occur. The order in which these phenomena occur depends on the particular compressor configuration, but once they both occur spike stall will occur.

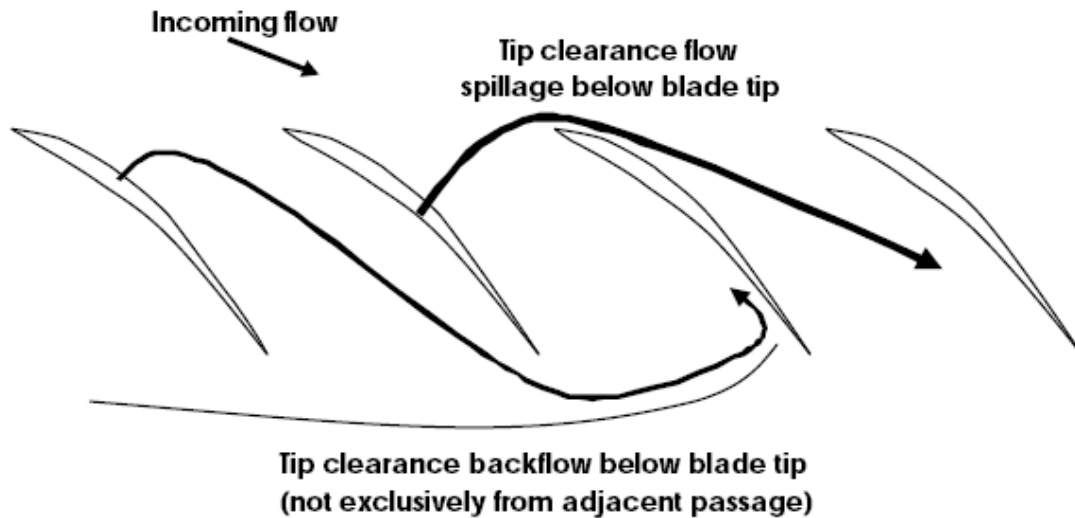
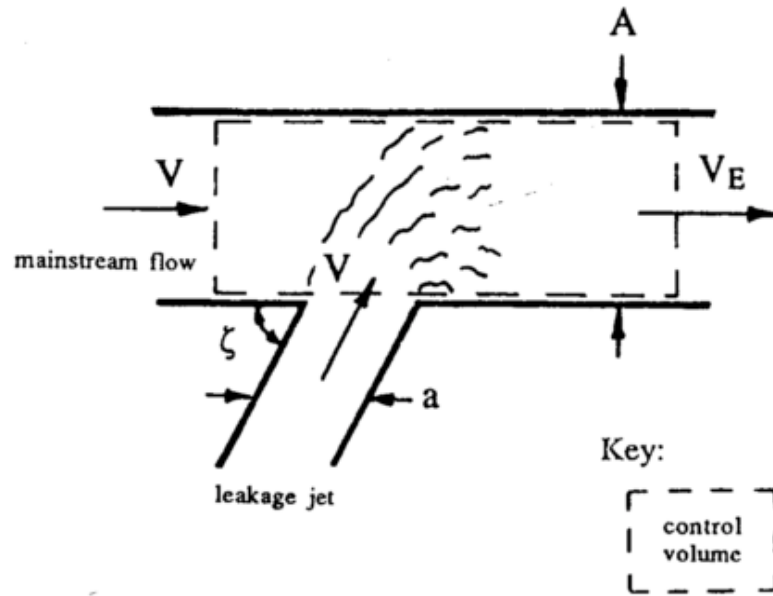


Figure 2.3 Stall criteria of Vo[19]. Flow into the adjacent blade passage around the leading and trailing edges of the blade.

The tip clearance flow also has a large effect on efficiency. Storer and Cumpsty [17], used a control volume approach to show that the loss caused by mixing of the clearance flow with the mainstream flow increases as the angle, ζ , between clearance

and mainstream flows increases. Figure 2.4 shows if the clearance flow's streamwise momentum is increased, the angle will decrease, providing a possibility for loss reduction.



Model for predicting losses due to mixing between clearance and mainstream flows [Storer and Cumpsty, 17]

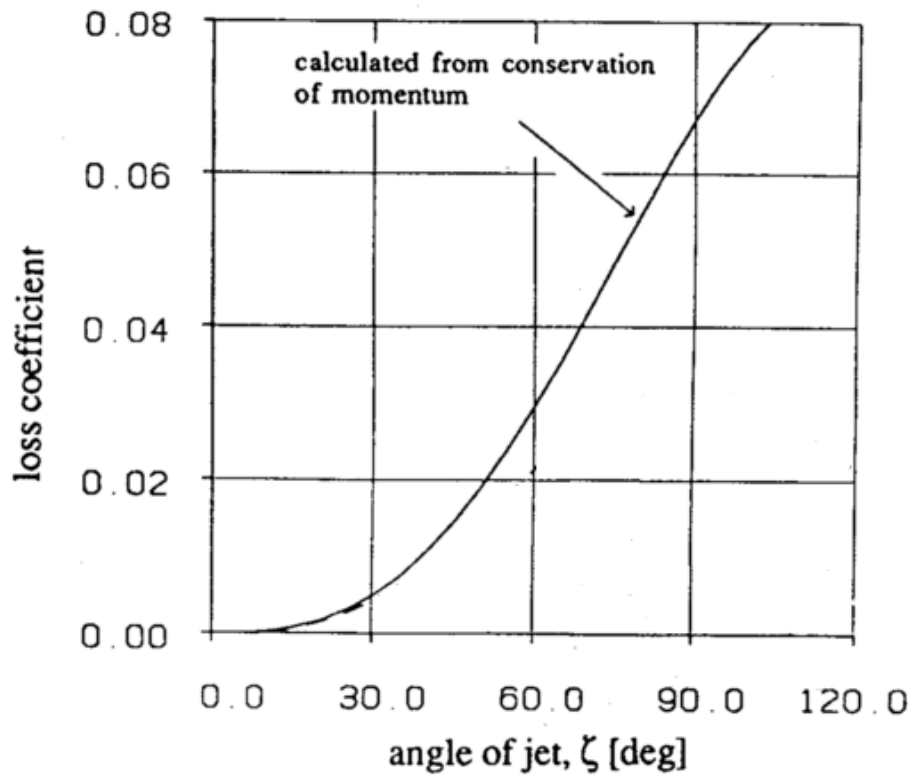


Figure 2.4 Losses due to mixing between clearance flow and bulk flow [Storer and Cumpsty, 17]

The previous research indicates that increased streamwise momentum at the blade tip can improve performance. Another question is how the measure of streamwise momentum relates to the blockage view and to the stall criteria identified by Vo [19] and Rabe and Hah [15]. The connection lies in the location from which the tip clearance fluid is drawn. The clearance flow can come from upstream or from the adjacent blade passage. Ideally, as much of the tip clearance flow as possible should come from upstream of the blade passage, since that is where the relative total pressure is greatest. Even near the design point, however, some fluid that goes into making the tip clearance vortex comes from an adjacent blade passage, and as a result has a total relative pressure deficit before entering the blade clearance. The formation of the clearance vortex further reduces the low total pressure.

As the streamwise momentum decreases, the proportion of reingested fluid increases, and the core of the clearance vortex experiences a severe drop in the relative total pressure. Figure 2.5 shows qualitatively how the source for the core of the clearance vortex changes as the compressor is throttled towards stall. As per Khalid's blockage relationship, this results in greater blockage, and hence a tendency to stall. The stall indicators highlighted by Vo and Rabe and Hah are qualitative measures of the streamwise momentum in certain regions near the tip. A high incidence angle at the leading edge, or backflow around the leading and trailing edges of the blades both indicate the streamwise momentum near the blade tip is low.

Put succinctly, low streamwise momentum can lead to significant regions of backflow, with fluid to from the adjacent passage forming the clearance vortex. This results in a vortex core of very low total pressure, leading to large blockages and stall.

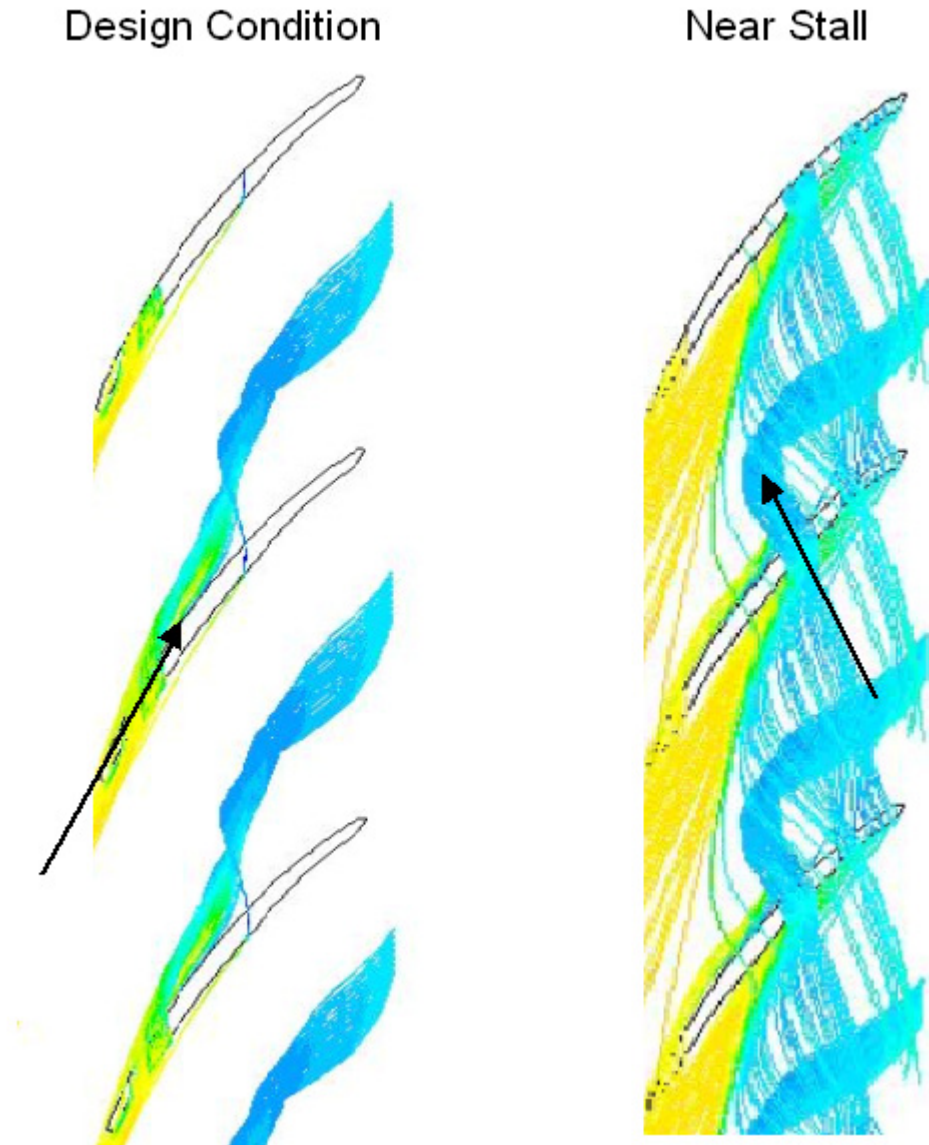


Figure 2.5 Source of Clearance Vortex Fluid. The two plots show fluid path lines of the particles that make up the vortex core. The arrows indicate from where the majority of tip clearance fluid is coming from.

2.2 Hypothesis

As stated, increasing the streamwise momentum near the blade tip has been shown to improve compressor flow range. A cause of the decrease in streamwise momentum through the blade passage is the radial transport away from the tip region. If this radial transport term can be improved, then compressor stall will be delayed. A hypothesis can thus be stated as:

- Increased streamwise momentum at the blade tip can improve compressor flow range. This fact has been highlighted by previous research, but is important in setting up the key elements of the hypothesis which follow.
- Streamwise momentum is diverted out of the blade tip region due to the radial velocity profile set up by the tip clearance vortex.
- A casing treatment geometry that helps to prevent this diversion will thus enhance the stable flow range of the compressor.

Figure 2.6 illustrates the intended effect on the flow.

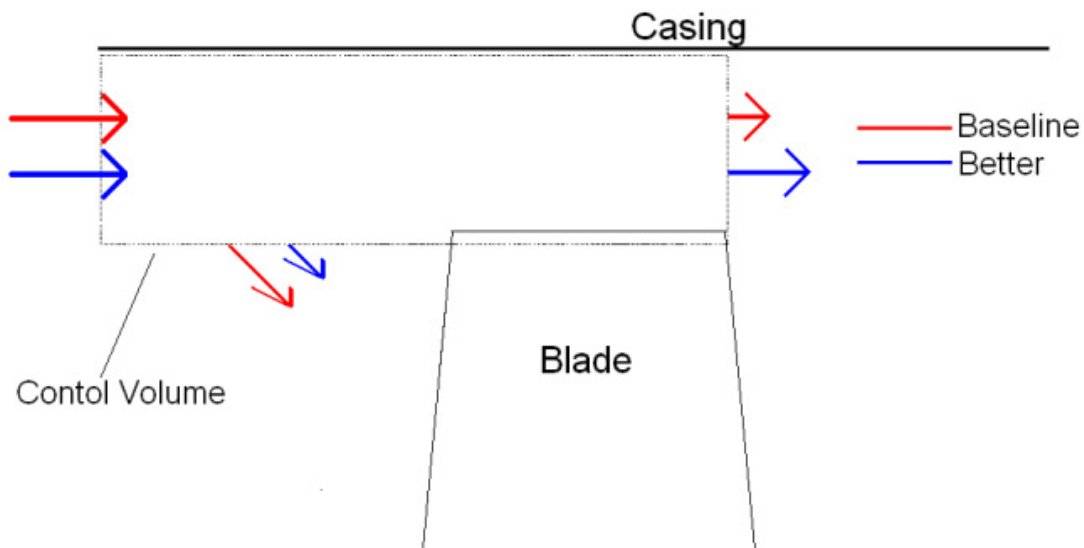


Figure 2.6 Streamwise momentum balance. The streamwise momentum via radial transport in baseline case (shown in red) is greater than with well-designed treatment (shown in blue).

Chapter 3 Technical Approach

3.1 Use of CFD

A computational approach has been used to investigate the tip clearance flow. Computational fluid dynamics (CFD) allows for effective testing and screening of a variety of casing geometries and momentum injection schemes, some of which are difficult to examine in a physical experiment. Furthermore, the flow field parameters are available everywhere in the flow, to aid interrogation. The rotor examined was the E³ rotor B, with a 3% chord tip clearance.

In order to keep the computational cost low, single passage steady state calculations were used with a standard k- ϵ turbulence model. The operating point was set through varying the ratio of inlet stagnation pressure to exit static pressure. Radial equilibrium boundary conditions were applied to the exit plane, and inlet swirl (to simulate the effect of inlet guide vanes) was included as part of the inlet boundary condition.

3.2 Grid Generation

The clearance region was meshed as a separate block (this is not always a necessity, as Khalid was able to achieve accurate tip clearance flows using a periodic boundary condition on each side of the tip gap. However, to ensure capture of the clearance and casing treatment flow features, it was decided that a meshed clearance region would be used. All grids were structured in the radial direction, allowing for precise control of radial distance between cells. This is important in attaining acceptable y^+ values in the

casing region, upon which turbulence modeling depends¹. Wall functions are used so the boundary layer does not need to be fully resolved in detail. For these estimates to be accurate, the cells adjacent to the wall must be within a specific range of y^+ values.

Although the density of cells in the vicinity of the blade surface is not as great as in the tip region (Figure 2.7), this should not affect the results appreciably. This compressor row has been shown by Vo [19] to be tip limited, so the flow over the main portion of the blade surface is healthy and not as crucial to stall onset.

Ideally, the solution should be independent of the grid resolution. Given the number of grids and geometries that were tried, this is difficult. However, solutions from different grids indicate that difference in results (flow range, pressure rise, efficiency) due to grid change is still less than the differences due to the experimental changes (momentum injections, geometry changes) that were being tested.

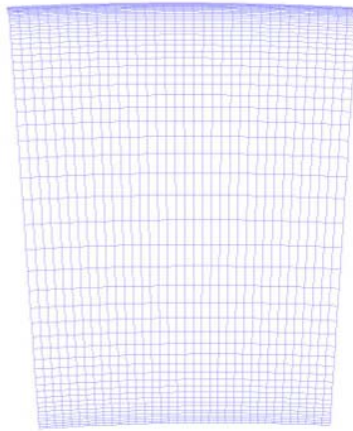


Figure 3.1 Radial variation in grid density, showing high density in the tip region.

¹ This value is simply a non-dimensional distance, defined as

$$y^+ = \frac{\rho u_\tau y}{\mu}. \quad (2)$$

3.3 Use of Numerical Stall as Flow Range Indicator

The relationship between steady-state numerical stall and physical stall is critical to this study. The type of numerical calculations done were single-passage, steady state calculations. The point at which numerical stall occurs in these calculations will be referred to as the equilibrium point. Past the equilibrium point, a solution for the flow conditions specified cannot be found, and the flow field becomes progressively further from a solution, with the residuals showing a sharp increase². More importantly, the equilibrium point coincides with a sharp rise in the production of tip blockage. Physical stall is also associated with a sharp increase in the blockage level in the vicinity of the stall point. While this gives some plausibility to the relationship between the equilibrium point and the physical stall point, it by no means links them clearly.

In his thesis, Vo [19] performed both steady and unsteady calculations to compare the equilibrium point found in steady state calculations with physical stall point found in the unsteady calculation. He found that changes in equilibrium point follow the trend that occurs with physical stall point. In other words, if something is done to the flow field that delays the equilibrium point, evidence indicates that the change will occur for the physical stall.

² The residuals are a measure of how well the calculation satisfies the defining equations (continuity, Navier-Stokes, etc.). Large residuals indicate that computation is not accurate.

Chapter 4.0 Assessment of the Hypothesis

4.1 Body Forces as a Diagnostic

The use of body forces within the flow, or massless momentum injection, provides one way to test the hypothesis put forth in Chapter 2. In the implementation, the direction of the applied force is specified so that it remains perpendicular to the relative velocity and the relative total pressure is unaffected by the force. The local force per unit volume magnitude is scaled with the local relative velocity magnitude, as in equation 3.

$$\text{Force/volume} = C \bullet V' \quad (3)$$

The constant ‘C’ can be changed to vary the strength of the body force. Two cases are described below. In one, the constant was chosen so that the total body force was approximately 0.3 percent of the blade force. This value was chosen because initial casing treatment calculations indicated the magnitude of the force of the grooves on the flow is approximately 0.3 percent of the blade force. This setup will be referred to as “Casing Force (low)”. “Casing Force (high)” refers to the setup when the total body force was approximately 0.9 percent of the blade force.

These specifications of the characteristics of the body forces were implemented through a user-defined function such that the body forces were updated after every iteration. This code for the user-defined function can be found in Appendix A. Fig. 4.1 shows the region in which the force was applied. The momentum injection was applied at different locations, but the following detailed interrogation is associated with only one region of application; this position provides the greatest benefit and insight into the best way to alter the flow in order to improve flow range.

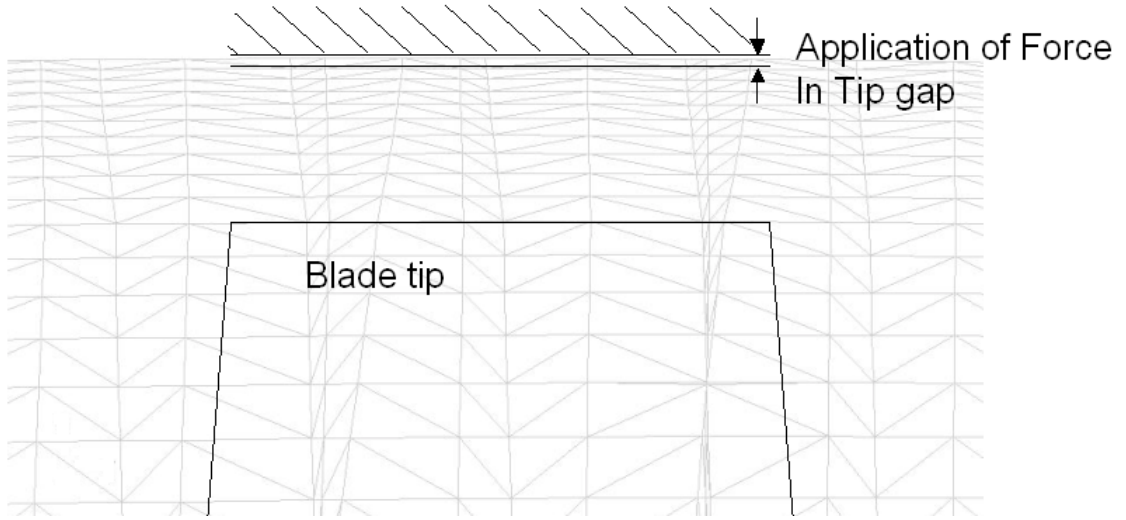


Figure 4.1 Sketch of geometric configuration of tip flow region indicating location of body force application

4.1.2 Results

Figures 4.2 and 4.3 show the results of pressure rise coefficient and efficiency for the baseline (no force), casing force (low), and casing force (high). The pressure rise coefficient used is the total-to-static pressure rise, as shown in equation 4.

$$\text{Pressure Rise Coefficient} = \frac{P_2 - P_{t1}}{0.5\rho U_{tip}^2} \quad (4)$$

Station 1 is a 10% of the blade tip axial chord upstream of the blade passage, and station 2 is 10% downstream of the blade passage. Static pressures are area-averaged, and stagnation pressures and temperatures are mass-averaged. The definition for adiabatic efficiency is shown in equation 5 below.

$$\text{Adiabatic Efficiency} = \frac{\left(\frac{P_{t2}}{P_{t1}}\right)^{\frac{\gamma-1}{\gamma}} - 1}{\left(\frac{T_{t2}}{T_{t1}}\right) - 1} \quad (5)$$

The flow coefficient is the area-averaged axial velocity at the inlet normalized by the blade tip speed.

$$\phi = \frac{u_x}{U_{tip}} \quad (6)$$

Figures 4.2 and 4.3 indicate that the body force has resulted in a flow range extension, an increased peak pressure rise, and increased peak efficiency compared to the baseline case. Furthermore, the improvements increase as the magnitude of the body force increases.

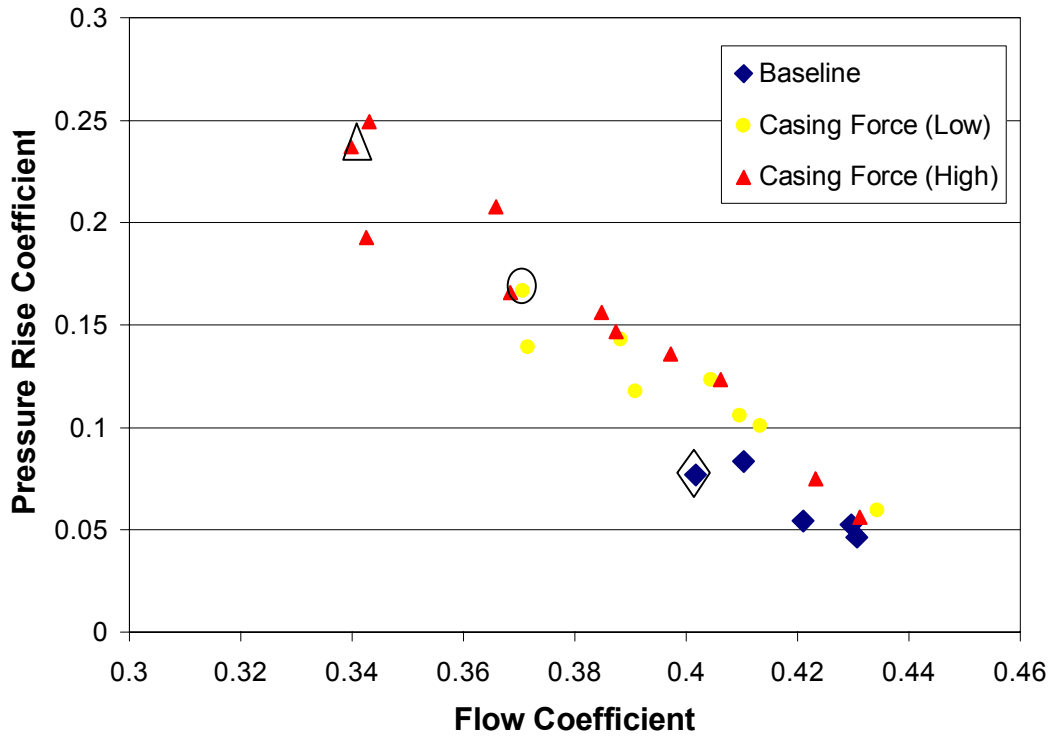


Figure 4.2 Pressure rise coefficient vs. flow coefficient. The equilibrium point of each case is marked with a dark encirclement.

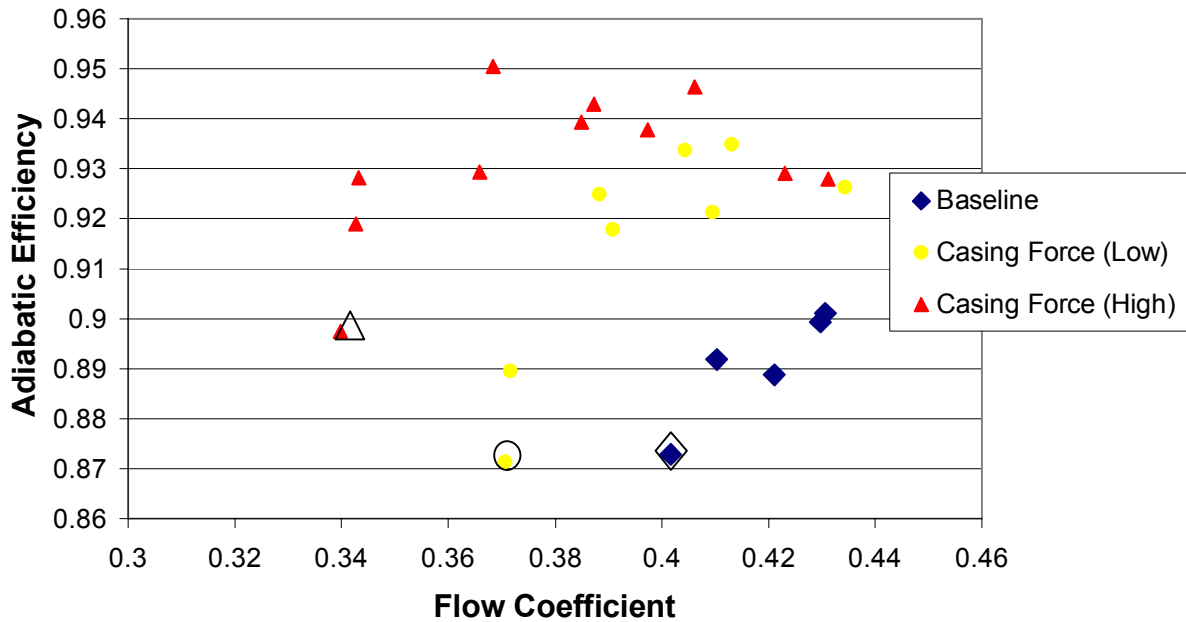


Figure 4.3 Adiabatic efficiency vs. flow coefficient

As discussed in Chapter 2, increased streamwise velocity within the blade passage at the blade tip level results in improved flow range, peak pressure rise, and peak efficiency. One can expect that the streamwise velocity in the tip region is greater with the body force. This is confirmed in the streamwise velocity contours evaluated at the blade tip level, which are shown Figures 4.4.

4.1.3 Changes in Radial Transport

The results show that a small force acting near the casing wall produces a large change close to the blade tip, and improves the flow range. To understand this influence, we first look at the baseline case. We consider the radial flux of streamwise momentum

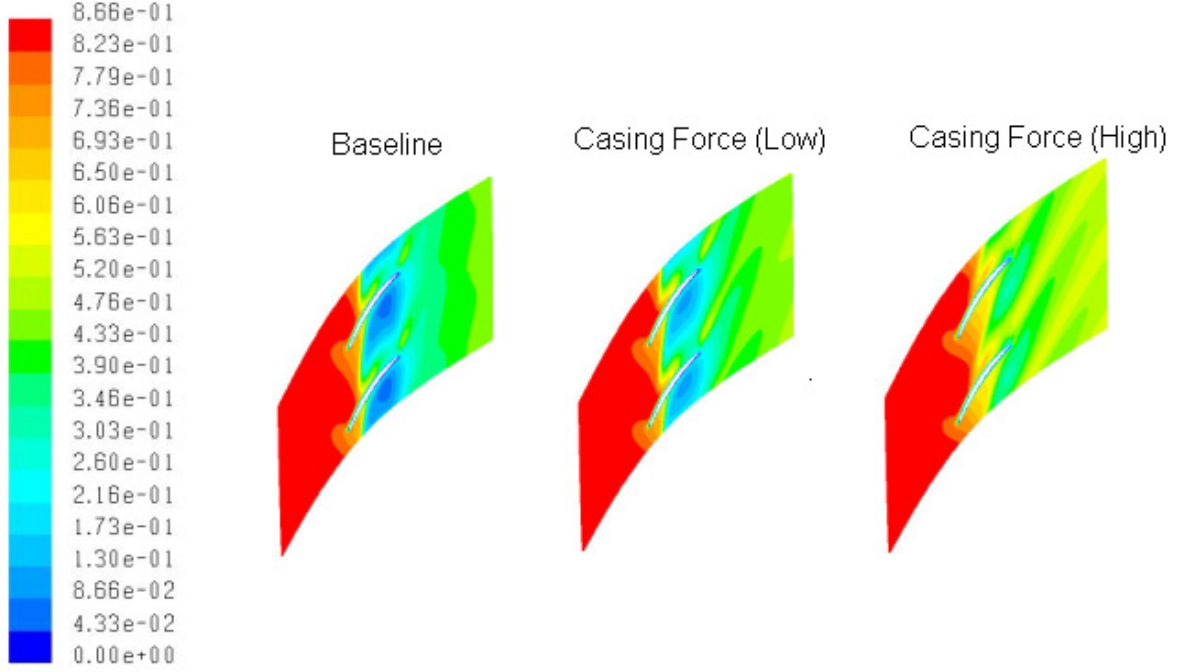


Figure 4.4 Streamwise velocity contours at 100% span. The values shown are streamwise velocities normalized by the blade tip speed.

Evaluated at the tip location, as defined in equation 7. The integration is carried out over one blade passage.

$$\text{Normalized Radial Transport of Streamwise Momentum} = \frac{\frac{\iint_{100\%} \rho u_r u_s dA}{\tau}}{\frac{Force_{blade}}{(r_t - r_h)}} \quad (7)$$

The flux per tip clearance distance is 1.4 times the blade force per unit blade span, which means near the blade tip this flux is of similar importance as the blade force. This is a result of the velocity associated with the tip clearance vortex, as shown by the following.

The radial velocity can be estimated using a potential flow model of the tip clearance vortex. As shown in figure 4.5, the clearance vortex was estimated as a straight line vortex in the tangential direction. The circulation of the model vortex is taken to be equal to the average circulation of the actual vortex.

Figure 4.6 shows the potential theory estimate and the CFD results of the radial velocity at 100% span. The figure shows good agreement in the radial velocity profile, especially in the first half of the blade passage. Towards the trailing edge, the potential theory model diverges from the CFD result because the former does not account for the effects of blockage that occurs near the trailing edge. The main point, however, is that the tip clearance vortex is responsible for the large inward radial velocity near the leading edge.

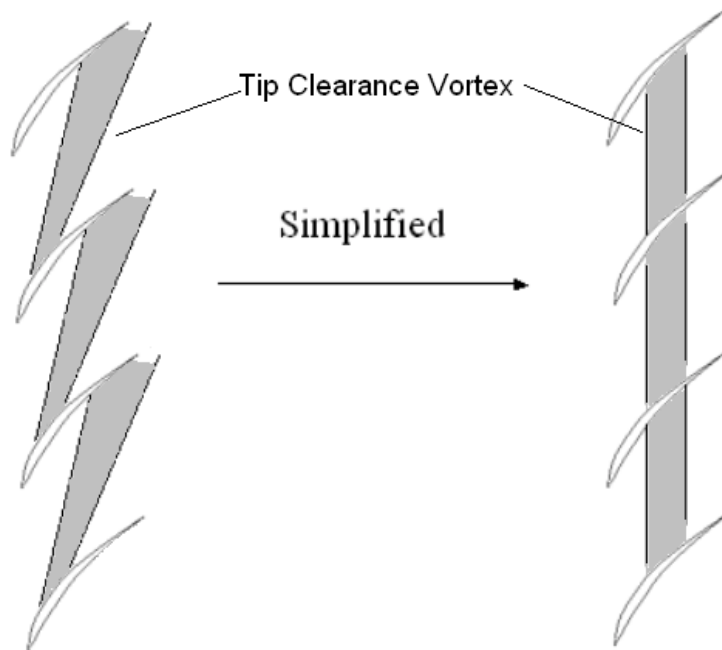


Figure 4.5 Vortex simplification. The complex geometry and trajectory of the tip clearance vortex is modeled as a simple straight vortex in the tangential direction.

The body forces reduce the effect of the tip clearance vortex on the radial velocity profile. The radial transport of streamwise momentum leaving the tip region is thus lessened. This occurs because the non-conservative body force creates a vortex counter to the tip clearance vortex (see Figure 4.7), essentially reducing the strength of the clearance vortex.

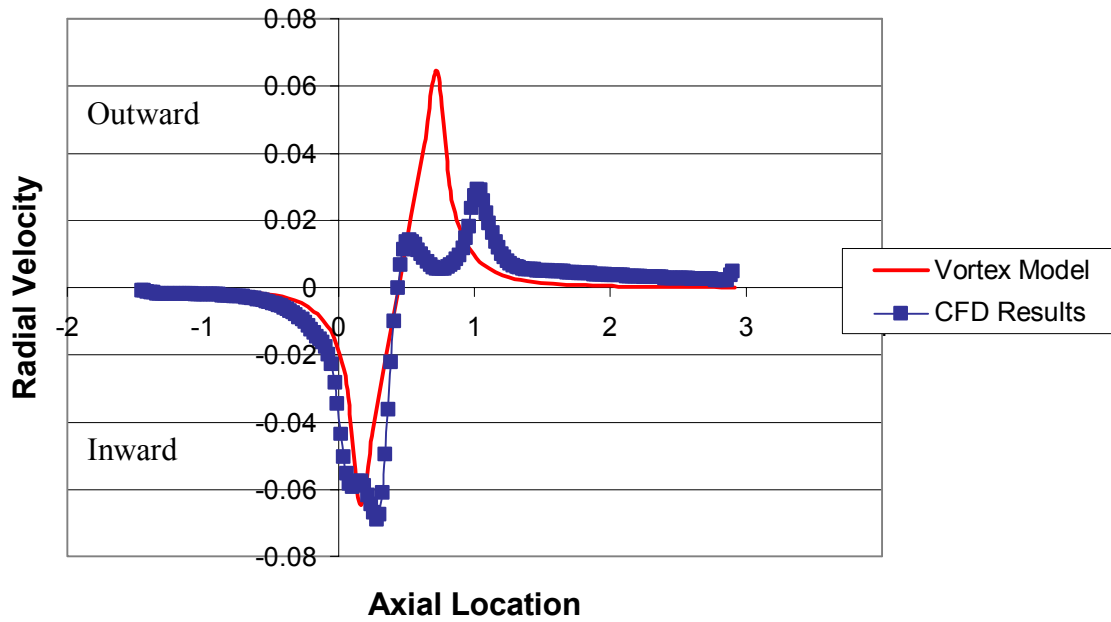


Figure 4.6 Pitchwise-averaged radial velocity vs. axial location, measured at the blade tip. $x=0$ represents the blade tip leading edge and $x=1$ is the trailing edge location

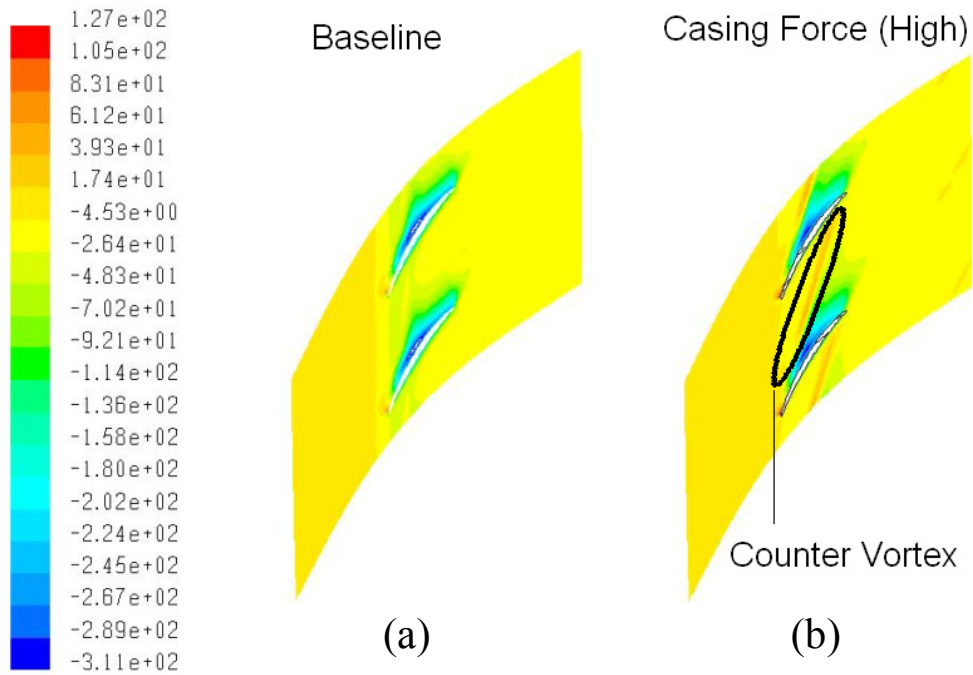


Figure 4.7 Tangential vorticity at 100% span. Values normalized by angular velocity. The presence of the body force generated counter vortex is indicated in (b), compared to the baseline case in (a)

Key properties associated with the use of the body force are shown in Table 1. The change in the radial transport term (as given in equation 7) is the primary factor associated with the improvement of streamwise momentum at the blade tip. Since the measurement is made on a two-dimensional plane at 100% span, streamwise velocity is parameter measured. The streamwise velocity is area-averaged at 100% span within the axial extent of the blade passage and normalized by the blade tip speed (equation 8, below).

$$\text{Streamwise Velocity} = \frac{\left[\left(\frac{1}{A_{BP100\%}} \right) \iint_{BP100\%} u_s dA \right]}{U_{tip}} \quad (8)$$

The flow range extension is defined as the fractional change in the stall flow coefficient, or

$$\text{Flow Range Extension} = \frac{\phi_{s,new} - \phi_{s,baseline}}{\phi_{s,baseline}} \quad (9)$$

The change in streamwise momentum retained in the endwall region through change in radial transport term is about 5 times greater than the body force. The implication is that the direct effect of momentum injection is not as important as the associated changes to the flow field.

Table 1 Key properties at the baseline stalling flow coefficient.

| | Radial Transport Term | Streamwise Velocity | Flow Range Extension |
|---------------------|-----------------------|---------------------|----------------------|
| Baseline | -1.397 | 0.530 | 0 |
| Casing Force (Low) | -0.988 | 0.625 | 0.077 |
| Casing Force (High) | -0.619 | 0.676 | 0.154 |

Pitch-Averaged radial velocity and radial transport profiles show how the streamwise momentum is more effectively retained near the blade tip with the body force than in the baseline situation. With the body force the radial velocity magnitudes are greatly reduced, particularly the large negative spike near the leading edge (see figure 4.8). These radial velocities are linked closely with the radial transport of streamwise momentum, as depicted in figure 4.9.

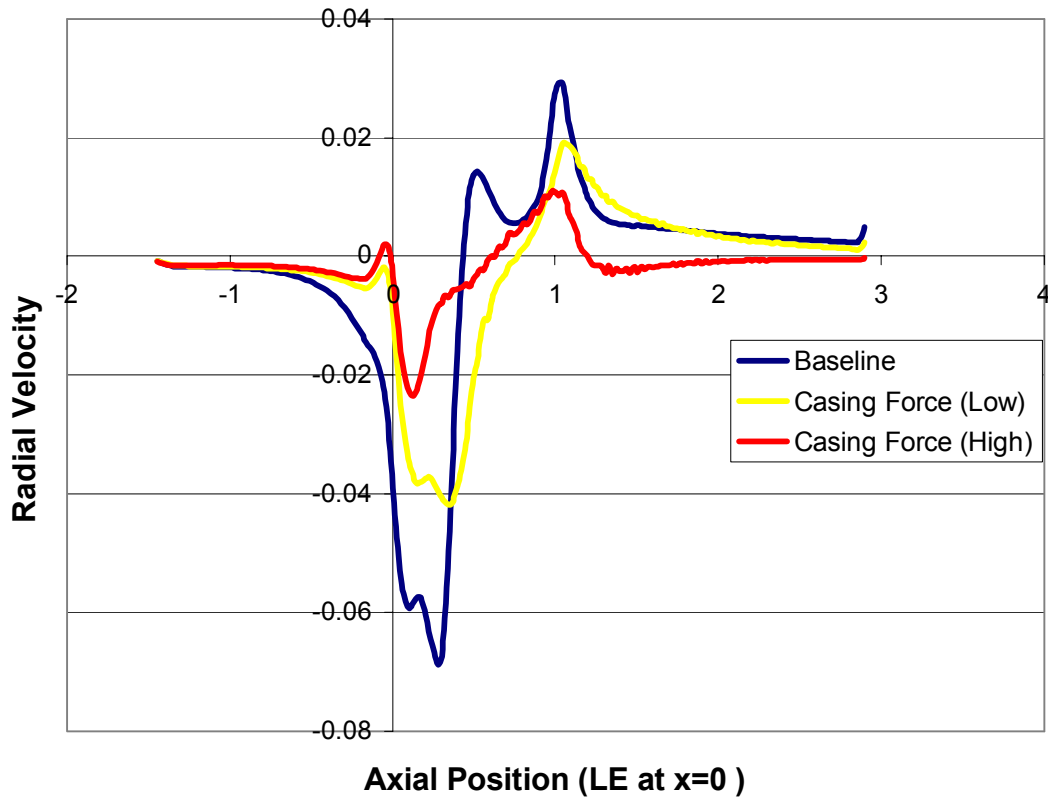


Figure 4.8 Pitchwise-averaged radial velocity vs. axial position. Radial velocity normalized by the blade tip speed. The leading edge of the blade tip is located at $x=0$. The trailing edge is located at $x=1$.

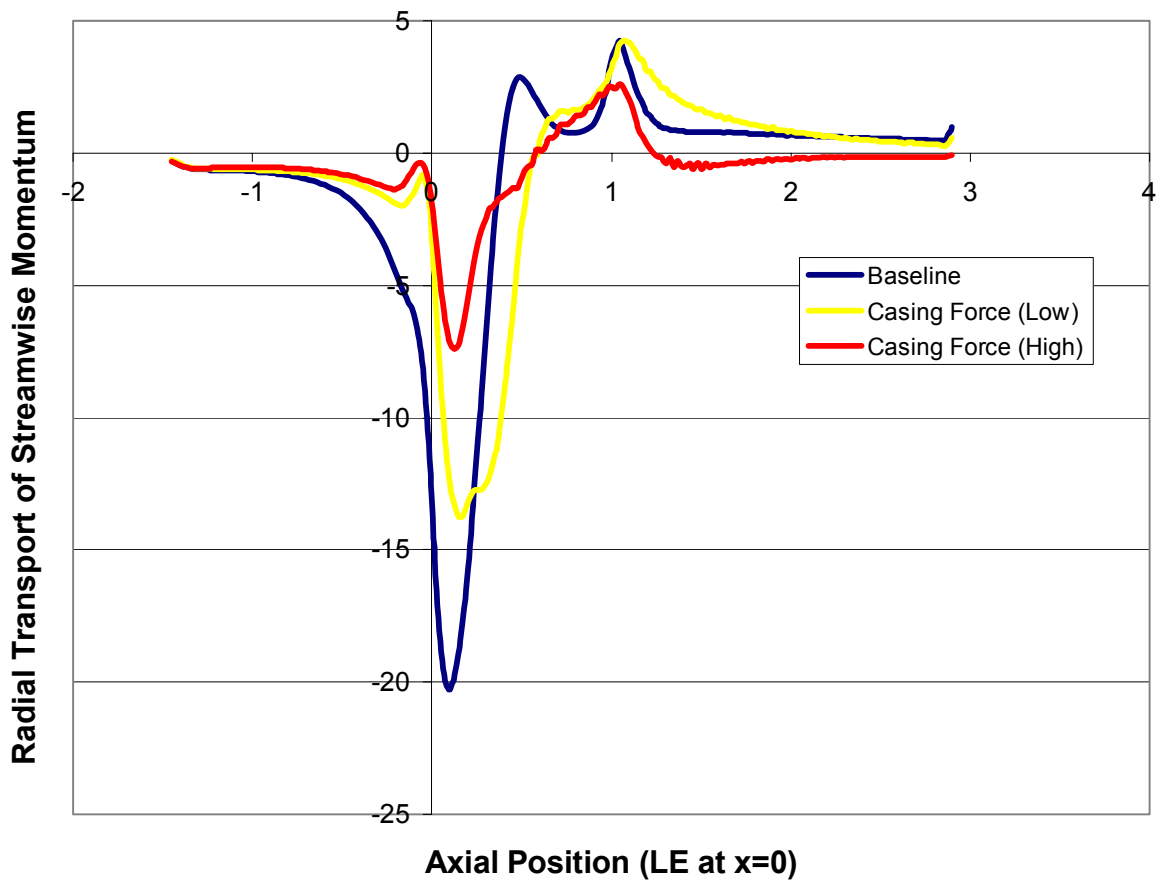


Figure 4.9 Pitchwise-averaged radial transport of streamwise momentum vs. axial position. Radial Transport normalized by the blade force per unit blade area. The leading edge of the blade tip is located at $x=0$. The trailing edge is located at $x=1$.

4.2 Use of a Flat Plate at the Blade Tip as a Diagnostic

Another set of simulations which support the hypothesis is provided by the insertion of a plate into the compressor flow upstream of the blade, as shown in figure 4.10. No flow can pass through the plate. As described below, it is found that more streamwise momentum is retained in the tip region than in the baseline situation.

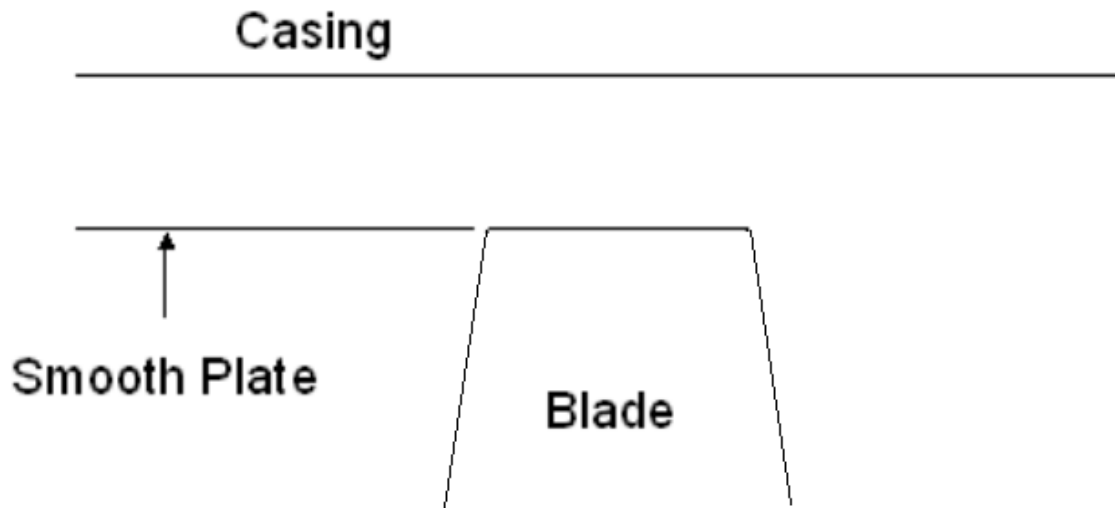


Figure 4.10 Setup of plate in stream experiment

4.2.2 Results

The results of the experiment with the plate can be seen in figures 4.11 and 4.12. The presence of the plate resulted in greater flow range, greater peak pressure rise, and greater efficiency compared with the baseline. The results from the low casing force are also included comparison. The radial transport term, streamwise velocity, and flow range of the experiment can be seen in Table 2. The plate lessens the magnitude of the radial transport term and increases streamwise momentum at the blade tip (relative to the baseline case).

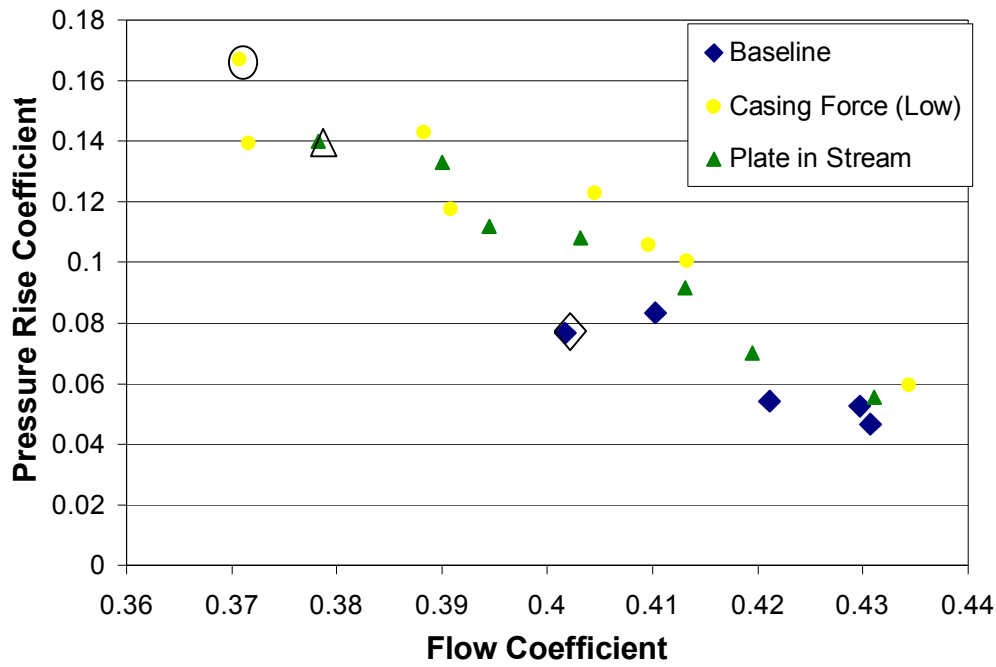


Figure 4.11 Pressure rise coefficient vs. flow coefficient. The presence of the plate improves flow range, peak pressure rise.

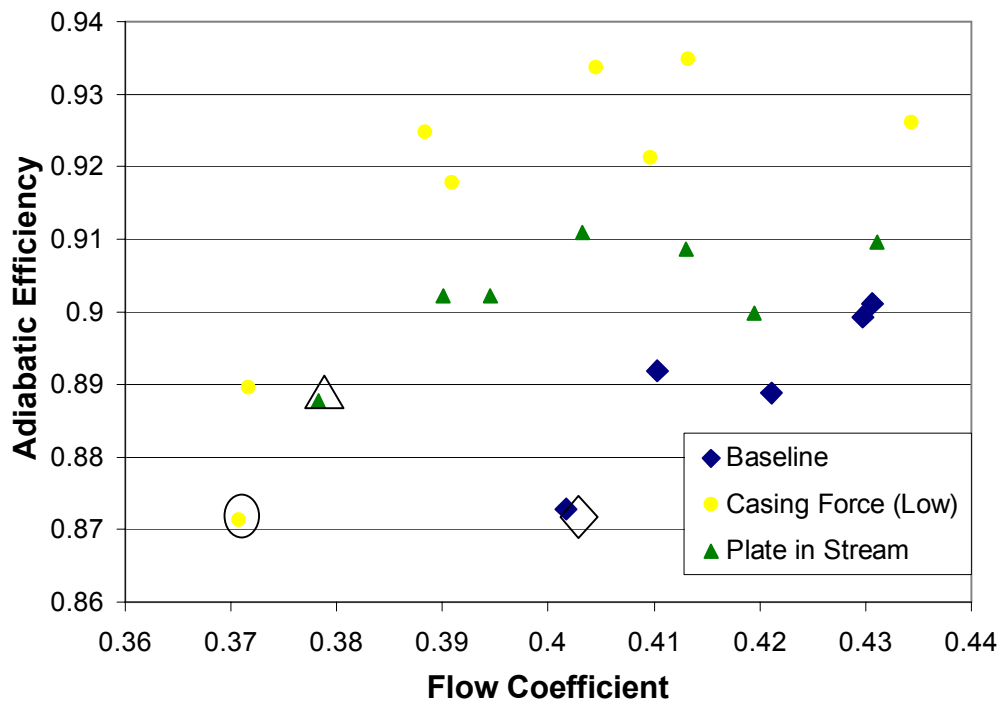


Figure 4.12 Adiabatic efficiency vs. flow coefficient. The presence of the plate increases peak efficiency.

Table 2. Key properties at baseline stalling flow coefficient.

| | Radial Transport Term | Streamwise Velocity | Flow Range Extension |
|--------------------|-----------------------|---------------------|----------------------|
| Baseline | -1.397 | 0.530 | 0 |
| Casing Force (Low) | -0.988 | 0.625 | 0.077 |
| Plate in Stream | -0.984 | 0.591 | 0.059 |

4.2.3 Changes in Radial Transport

Figure 4.13 shows the radial velocity profile at 100% span. The profile is not changed within the blade passage. Only upstream of the blade passage is the radial velocity at 100% span brought to zero. This control of the radial velocity, even within the limited axial extent, leads to greater retainment of streamwise momentum within the tip region, as seen in figure 4.14.

The simulation with the plate shows an improvement in flow range without direct streamwise momentum injection. Rather, it is due to alteration of the radial velocity profile³. These results, which provide support that the improvement is obtained by changing the radial velocity profile, also provide a stepping-stone to understanding of casing treatment.

³ There is a small direct streamwise force by the plate on the flow. In the same way that an axial flow can exert a force on an engine inlet, the streamlines curving around the leading edge of the plate cause a net pressure force to act on the plate [7]. However, this force is more than two orders of magnitude smaller than the total change in the radial transport term seen with the plate. Therefore, it is unlikely that this effect is important.

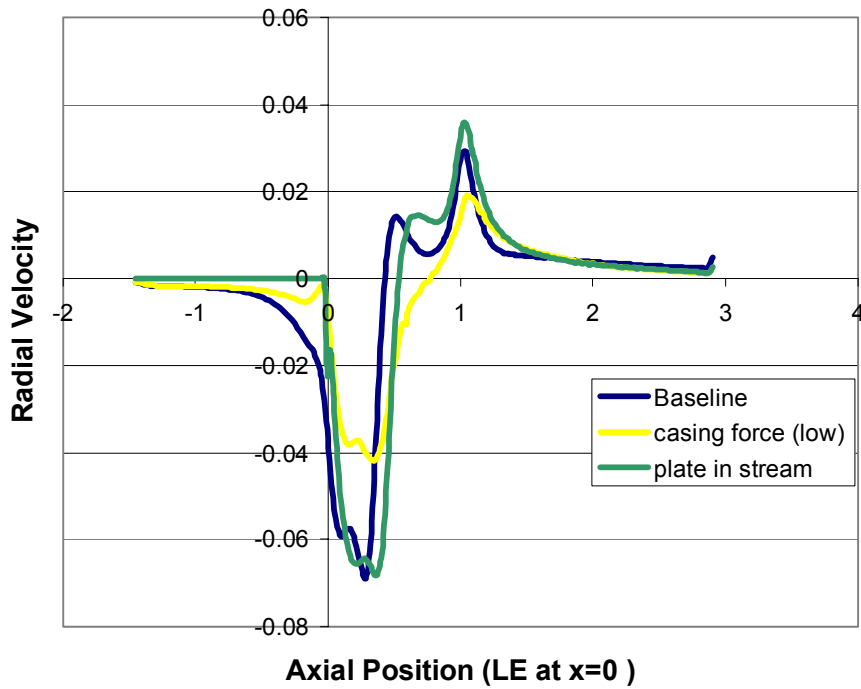


Figure 4.13 Pitchwise-averaged radial velocity vs. axial position. The presence of the plate prevents radial velocity upstream of the blade.

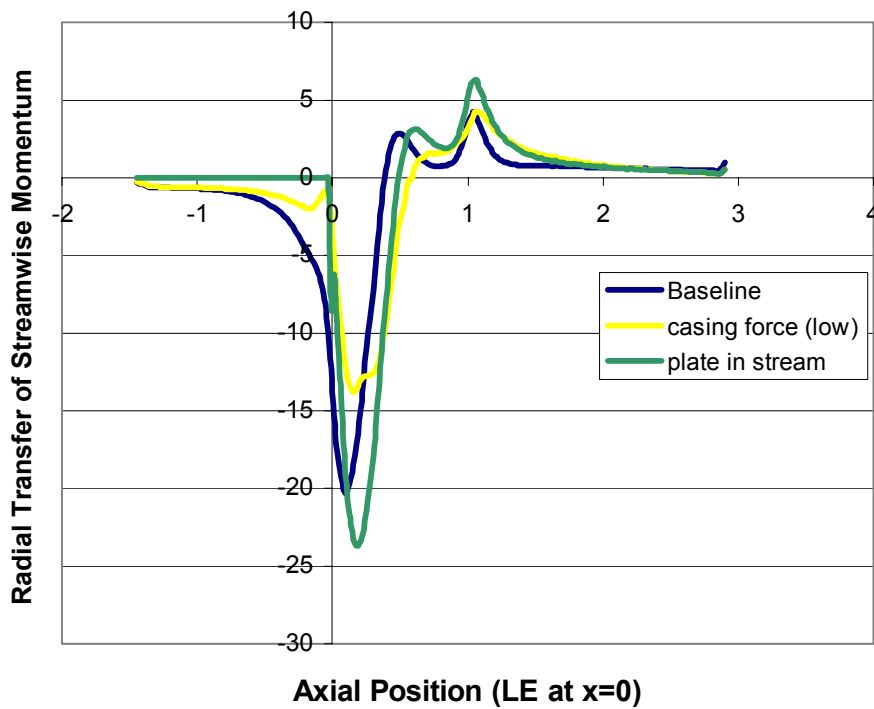


Figure 4.14 Pitchwise-averaged radial transport of streamwise momentum vs. axial position. The presence of the plate prevents radial transport upstream of the blade.

Chapter 5 Casing Treatment

5.1 Setup

One goal of this research is to link flow changes that result in enhanced flow range with practical casing treatment geometry. The casing treatment configuration examined consisted of a single shallow circumferential groove located at the quarter chord of the blade passage. The choice of geometry was made after consideration of previous research pertaining to circumferential grooves. Two major geometrical factors were number and depth of grooves. Adamczyk and Shabbir [2] and Rabe and Hah [15] found that the most benefit is achieved from the grooves near the leading edge. Rabe and Hah tried different groove depths and showed that the groove depth necessary to affect substantial change only needs to be on the order of the clearance gap. For this reason, only one groove near the leading edge was used, and the maximum groove depth was equal to the clearance gap. Shallower groove depths were examined in order to determine how the performance approached the smoothwall performance as the depth approached zero. The geometry of the groove treatment is shown in Fig. 5.1.

5.2 Results

The pressure rise coefficients and efficiencies resulting from the casing treatment numerical experiments are shown in figures 5.2 and 5.3. The percentage given before each data set tells how deep the groove is relative to the tip clearance (i.e. 100% is equal to the tip clearance). Circumferential treatment of groove depths tried resulted in improved flow range, greater pressure rise, and greater efficiency.

The computed results were assessed against those of Adamczyk and Shabbir [2], who also investigated a low speed rotor with circumferential groove type casing treatment. The result from their work is reproduced in Figure 5.4. The change in

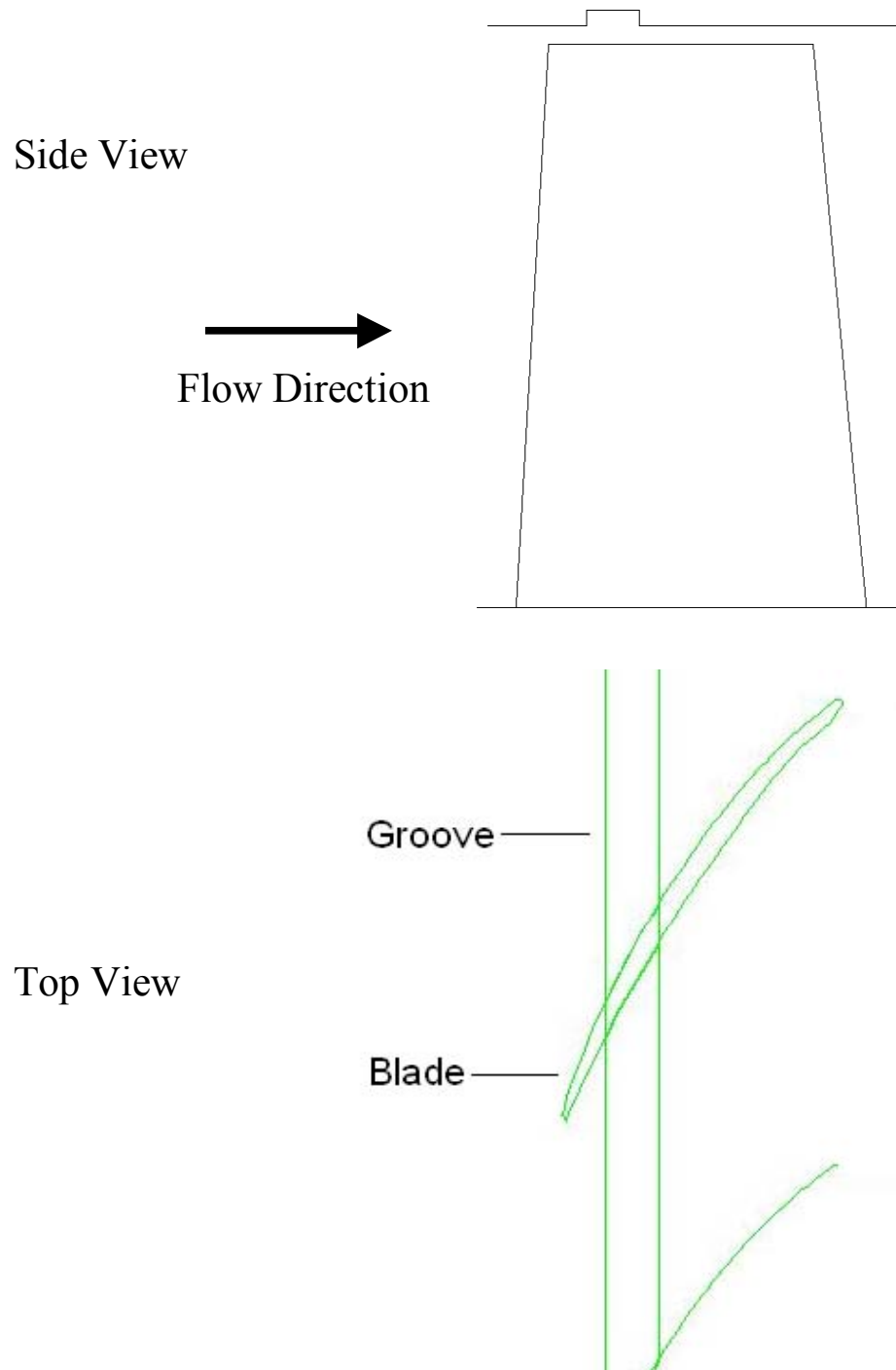


Figure 5.1 Views of the casing treatment geometry

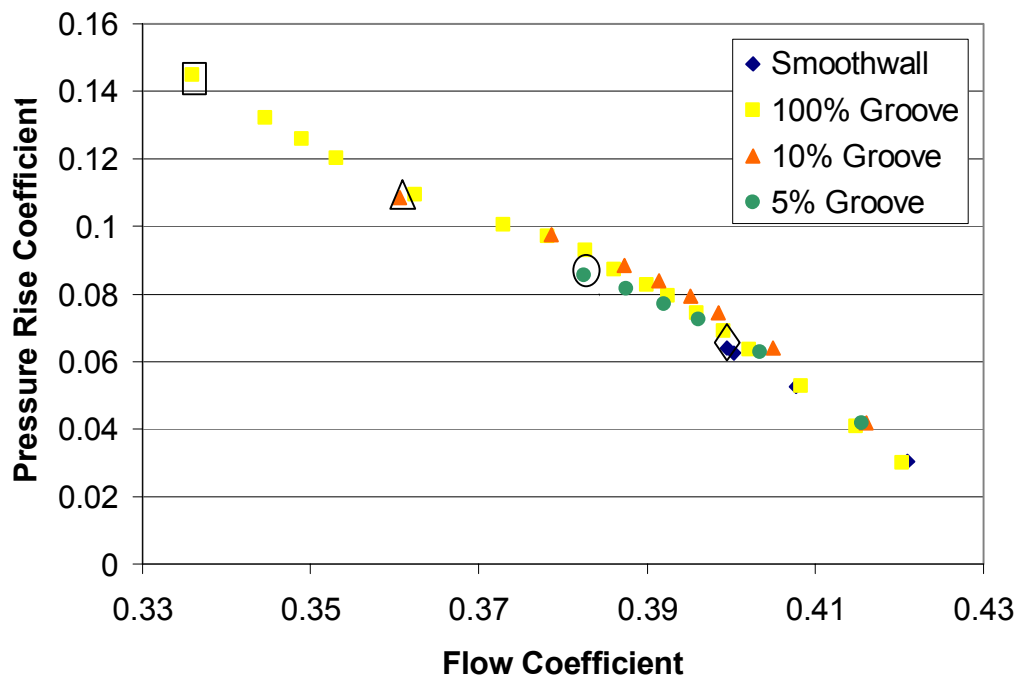


Figure 5.2 Pressure rise coefficient vs. flow coefficient. The casing treatment improves flow range and peak pressure rise.

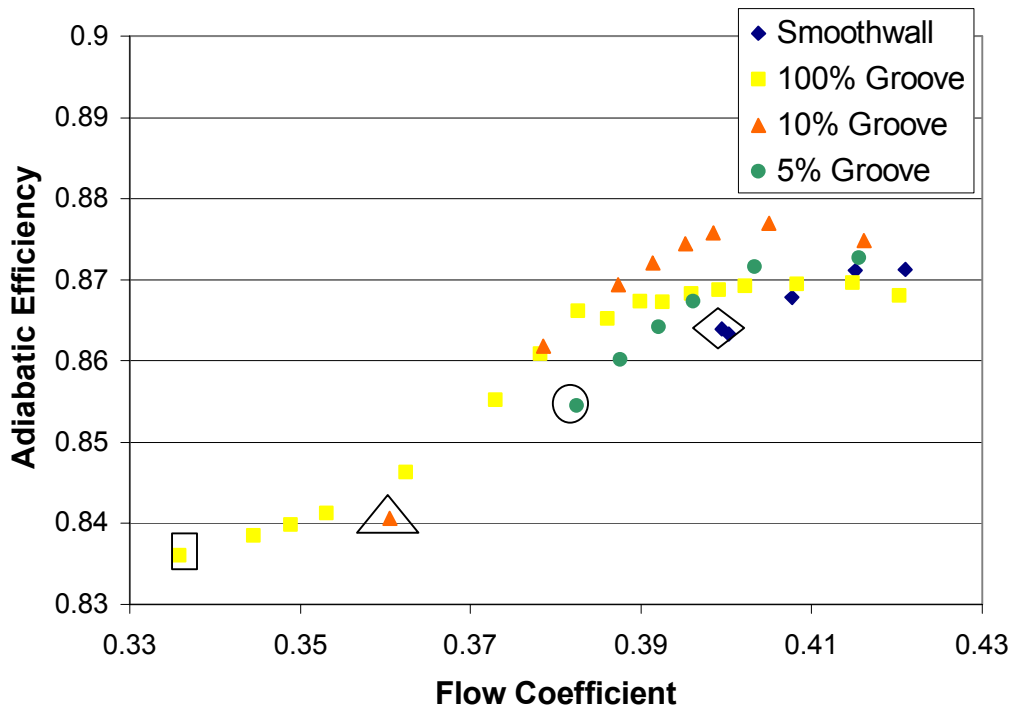


Figure 5.3 Adiabatic efficiency vs. flow coefficient. The casing treatment improves efficiency.

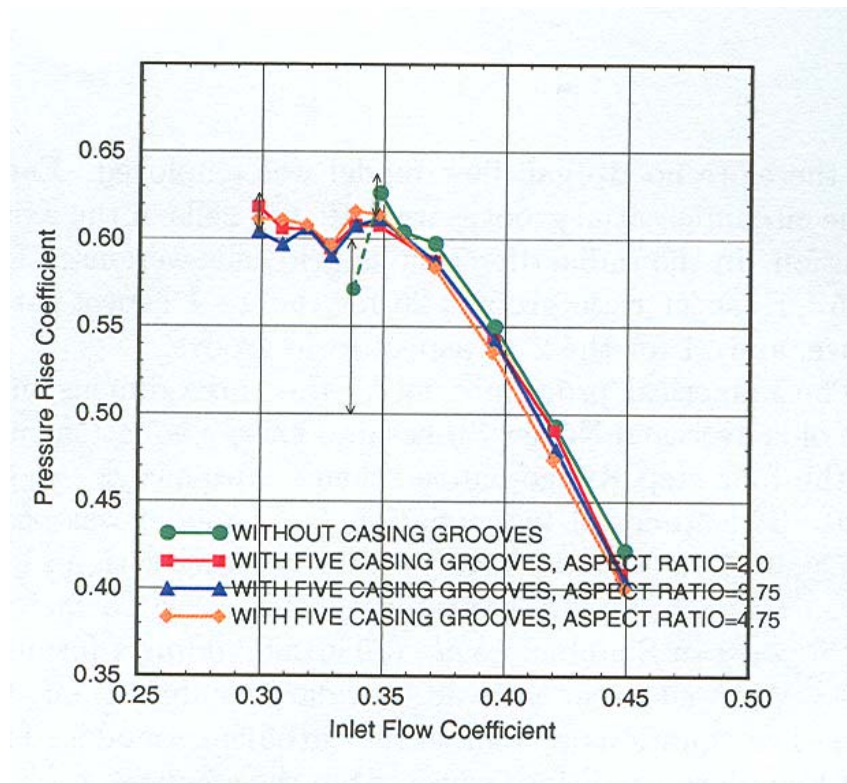
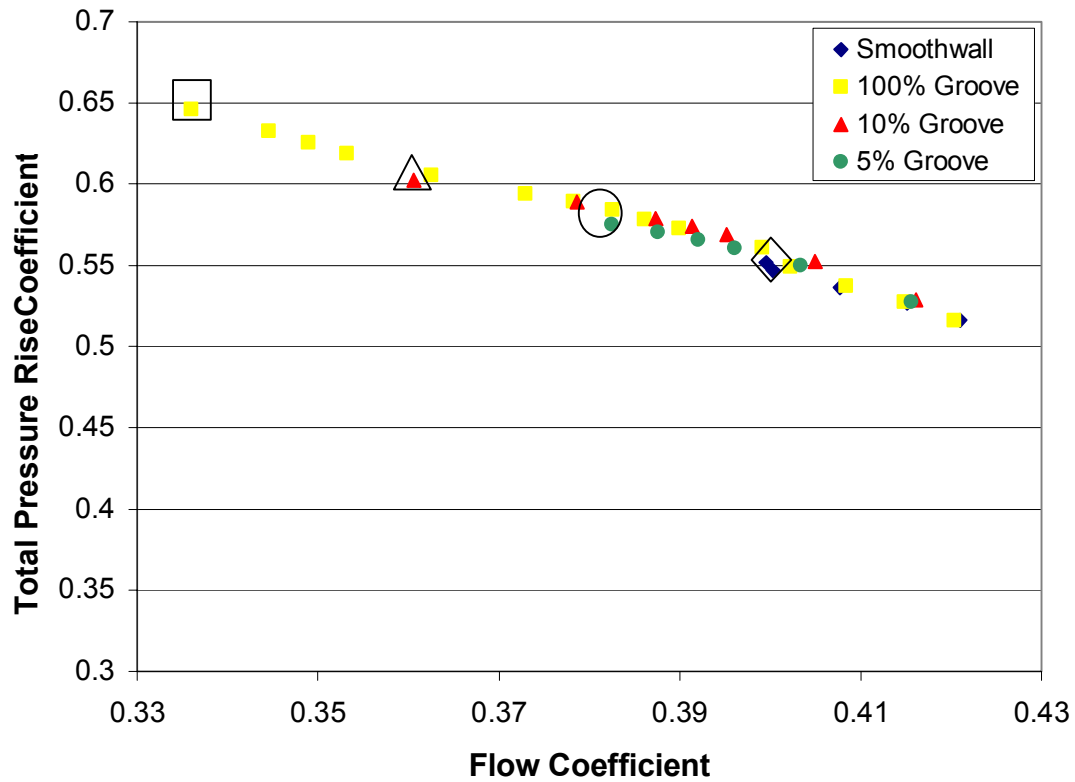


Figure 5.4 Total pressure rise coefficient vs. flow coefficient as calculated by Adamczyk and Shabbir [2] (bottom), compared with calculations of this research (top).

the computed stall flow coefficient achieved by Shabbir, et al. was 14.3%, compared to 16.0% for the case of the 100% groove described here, for similar (not identical rotors). The details of the flow will now be examined to determine how flow range has been extended.

5.3 Changes in Radial Transport Term

As with the previous methods of flow field alteration, the major effect of the casing treatment is seen as mitigating the radial transport of streamwise momentum out of the tip region, especially in the leading edge region. Continuity (for an incompressible flow) dictates that the average radial velocity at the groove entrance is zero. However, the circumferential groove can affect the distribution of radial velocity. This is important because of the distribution of streamwise velocity at the blade tip. Figure 5.5 shows the change in streamwise velocity is a result of radial transport and diffusion. Radial velocities near the leading edge affect the radial transport more than velocity changes at the trailing edge. Therefore, if the radial velocity profile is altered so that there is an increase in radial velocity at the leading edge and a decrease near the trailing edge, the total radial transport of momentum can be reduced, even though the average radial velocity is the same.

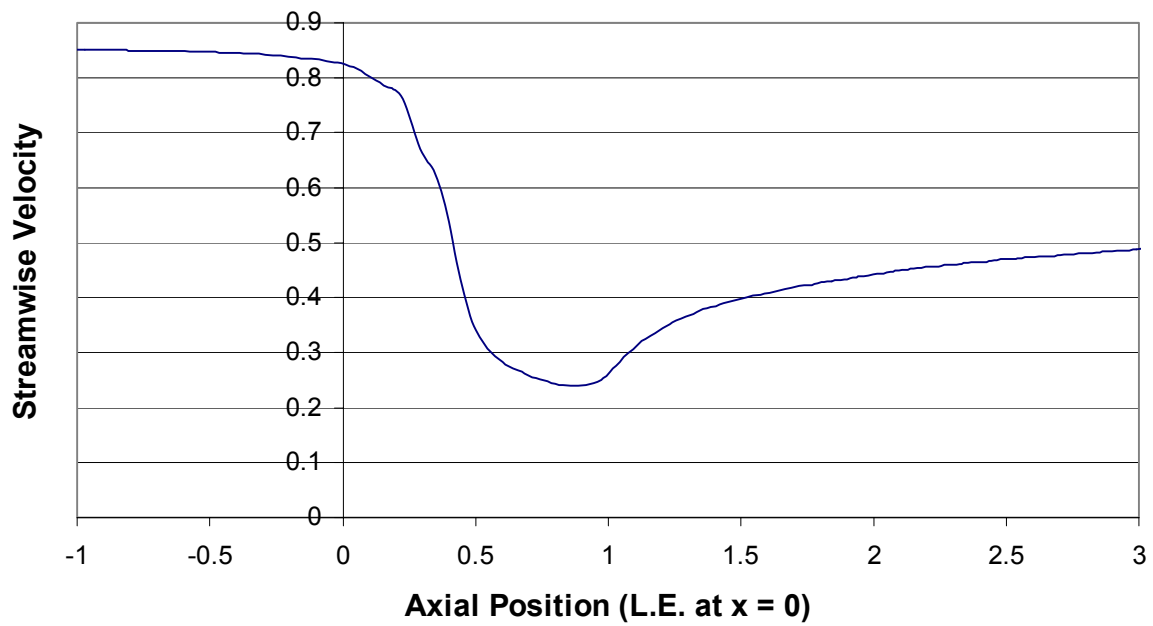


Figure 5.5 Pitchwise-averaged streamwise velocity vs. axial position. Measurement taken from smoothwall case near stall at 100%span. L.E. at x=0. T.E. at x=1.

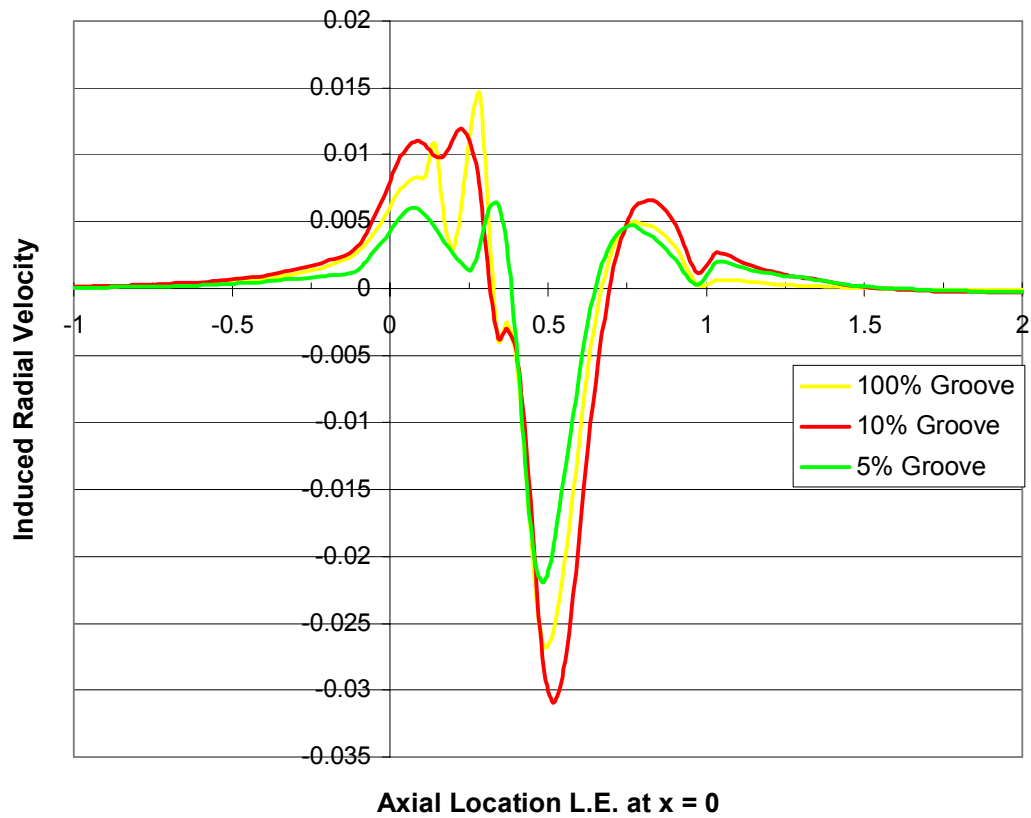


Figure 5.6 Pitchwise-averaged induced radial velocity vs. axial location, measured at 100%span.

The induced radial velocity is defined as the difference in radial velocity between the casing treatment and the smoothwall case. Figure 5.6 shows the induced radial velocity profiles of the circumferential groove casing treatments. There is a large positive induced velocity near the leading edge, which is responsible for the improvement in the radial transport of streamwise momentum.

To isolate the dominant mechanism proposed for the enhancement of streamwise momentum, we can also examine the change in shear force on the flow, the flux of streamwise momentum out of the groove, and the pressure force using the control volume shown in Fig. 5.7. The changes in each term are listed in Table 3. The terms are listed as force per unit span, normalized by the blade force per unit blade span. The radial

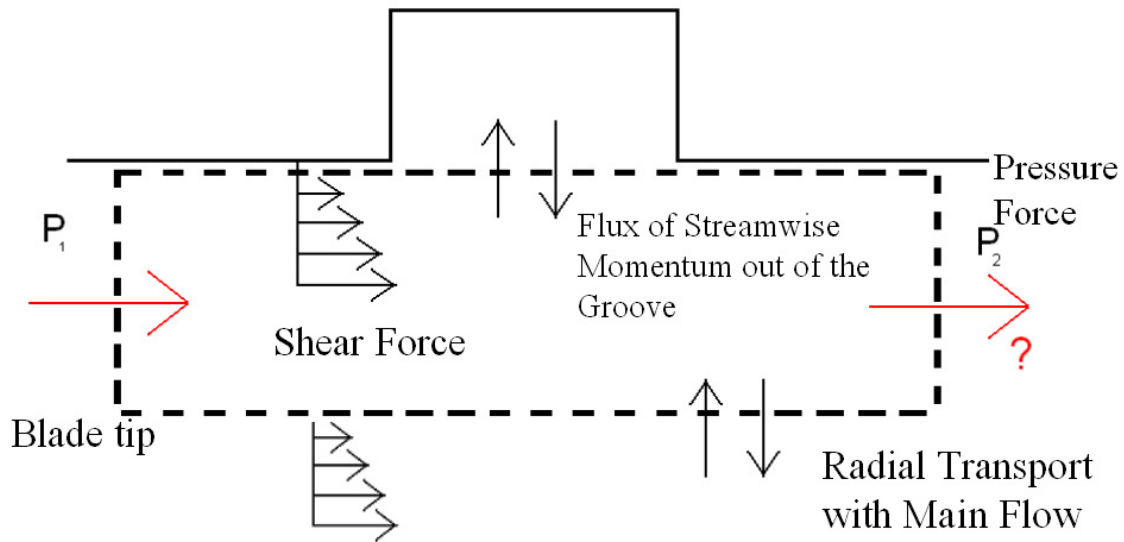


Figure 5.7 Control volume used in momentum balance

Table 3 Magnitudes of streamwise momentum terms

| | Pressure | Shear | Groove Flux | Radial Transport |
|-------------|----------|--------|-------------|------------------|
| 100% Groove | -0.909 | -0.179 | 0.005 | -1.126 |
| Smoothwall | -0.902 | -0.166 | 0 | -1.178 |
| Difference | -0.007 | -0.013 | 0.005 | 0.052 |

transport term constitutes the largest difference. In fact, the pressure force and shear forces on the control volume slightly worsen use of casing treatment. We can infer that the change in streamwise momentum at the blade tip is primarily a result of changes in radial transport. Table 3 confirms the radial transport of streamwise momentum is the dominant term that is altered by the application of circumferential groove type casing treatment.

Calculations with different groove depths show an optimum groove depth for achieving the best peak efficiency, and which is smaller than the clearance gap. In terms of flow range extension and peak pressure rise, however, grooves with greater depth perform better, although a 50% groove showed nearly identical flow range improvement as the 100%. The 50% groove calculations were examined specifically to show that flow range improvement increases with groove depth, but the improvement asymptotically approaches a maximum. These characteristics are illustrated in figure 5.8.

The qualitative effect of the groove changes the flow coefficient. At high flow coefficients, for instance, there is a slight reduction in flow range with the 100% groove (i.e. groove depth = tip clearance) compared to the smoothwall case. The computed groove-induced radial velocity (at flow coefficient near the smoothwall design) shown in figure 5.9 show that velocity profile has not been altered in a manner which improves radial transport.

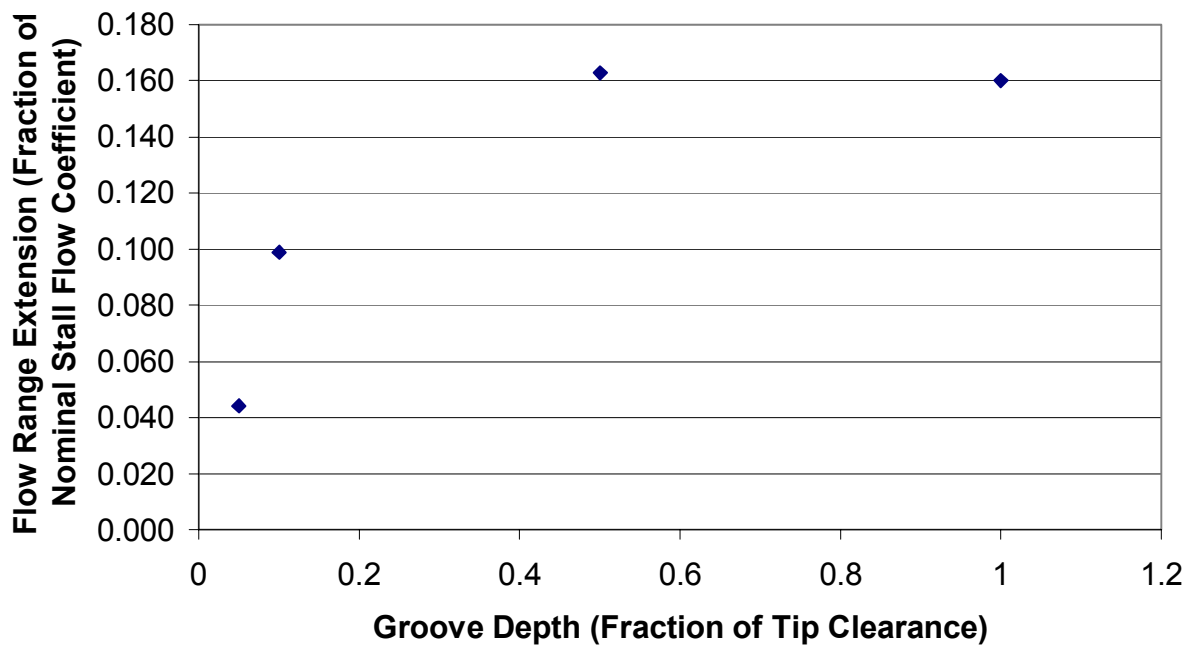


Figure 5.8 Flow range extension vs. groove depth. Flow range improvement asymptotically approaches a maximum as groove depth is increased.

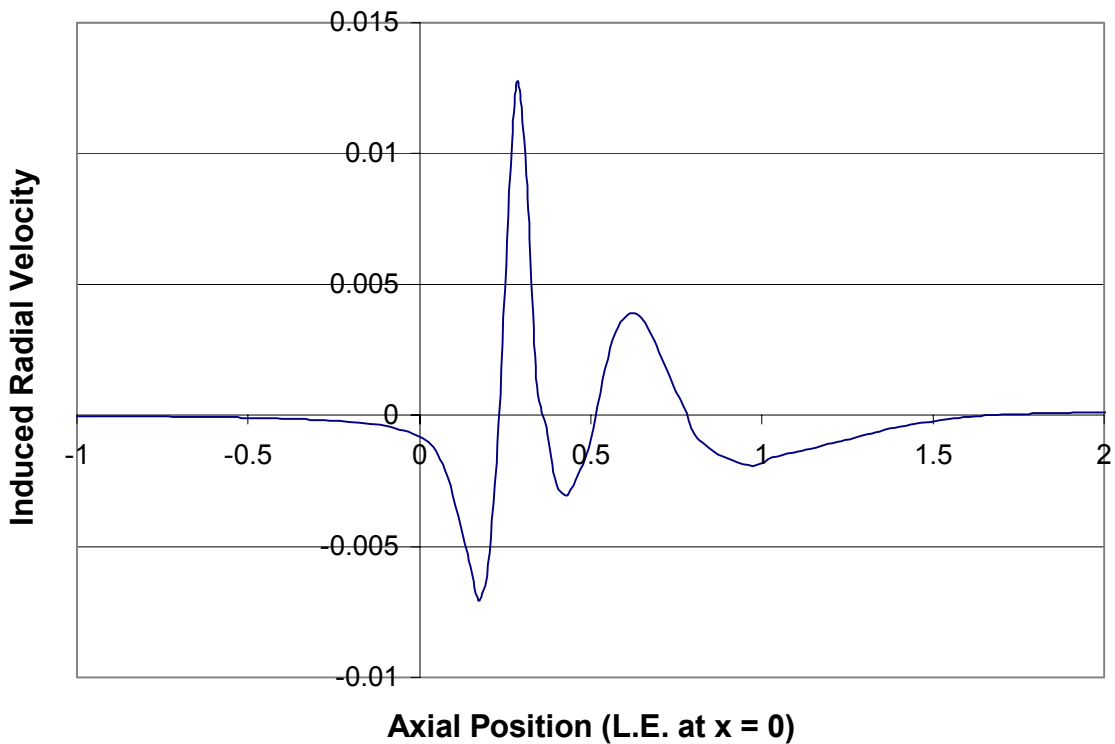


Figure 5.9 Pitchwise-averaged radial velocity vs. axial location. Computed radial velocity for 100% groove at flow coefficient close to smoothwall design flow coefficient.

Fi

5.4 Causal Links

The results have shown that the radial transport term is important in increasing the streamwise momentum in the tip region, but a more detailed examination is necessary to determine causality and mechanisms that cause this change. The calculations show that change in radial transport of streamwise momentum is due to a repositioning of the tip clearance vortex with the groove, as shown in figure 5.10. This is why the change in radial velocity (refer to figure 5.6) exists in a region much larger than the extent of the groove. Figure 5.11 illustrates how a shift of the tip clearance vortex results in the double humped induced velocity profiles shown in figure 5.6.

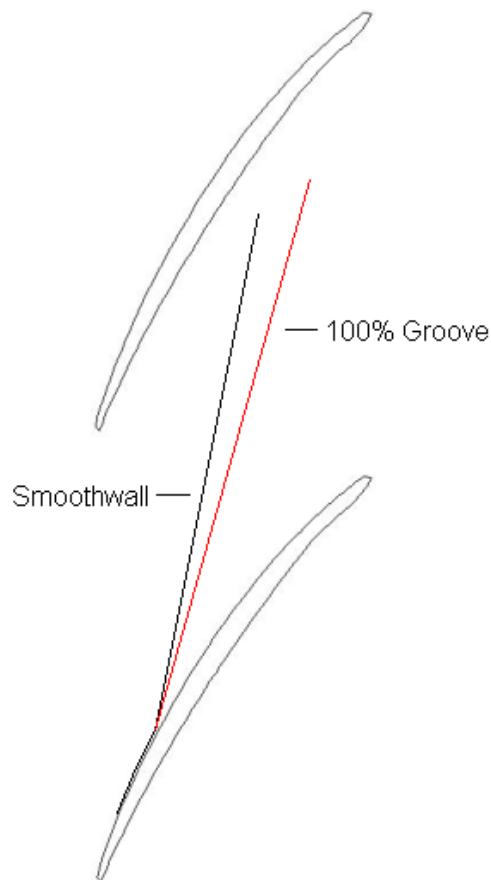


Figure 5.10 Change in vortex trajectory with use of the casing treatment (circumferential groove of depth equal to 100% of tip clearance gap).

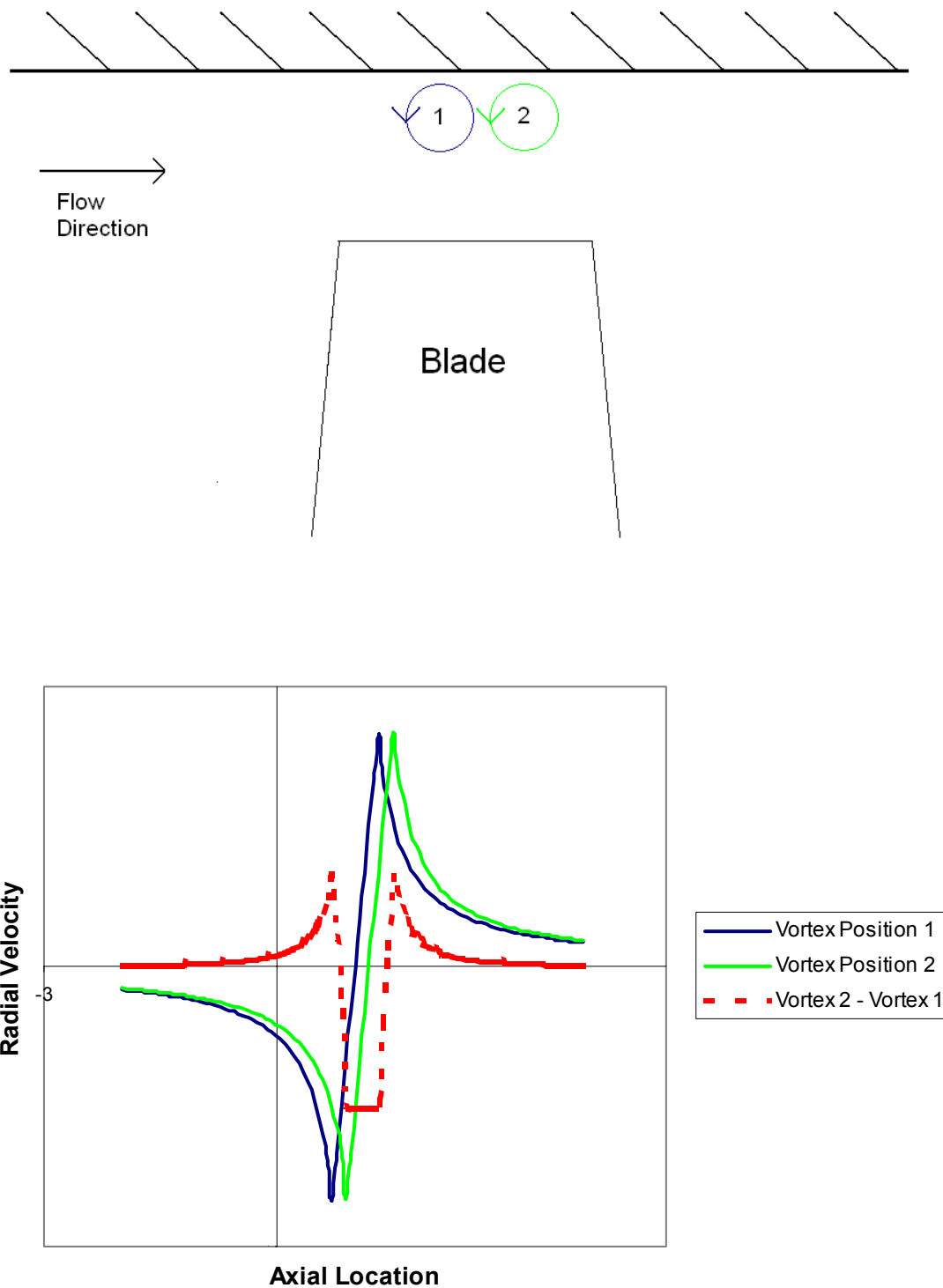


Figure 5.11 Illustration of change in radial velocity profile due to shift of clearance vortex. Two vortex positions are shown in (a). In (b), the velocity profiles that would result from these vortex positions are shown, in addition to the difference between the two profiles.

Since the vortex is now farther away from the leading edge, it is farther from the fluid with the greatest streamwise velocity, and the effect of the of the vortex on the radial transport is therefore reduced.

To change the position of the tip clearance vortex, there must first be some local increase (relative to the smoothwall case) in the streamwise momentum. Circumferential groove type casing treatment supply this increase through two routes:

- Radial exchange between the tip region and the grooves causes some reverse flow to be terminated by the walls of the groove, so there is a positive flux of momentum out of the grooves. This has been shown to be true using a simple integration of radial transport at the groove entrance ('Groove Flux' term in Table 3)
- Induced radial transport between the tip region and the main flow also increases streamwise momentum because outward radial velocity occurs closer to the leading edge, where streamwise velocity is greater. This local effect can be seen qualitatively in figure 5.12. It is a mechanism similar to that described in section 5.3, except on a smaller scale. This feature will be discussed further in sections 5.5 and 5.6.

The block diagram in figure 5.13 summarizes the events that lead to the increase in streamwise momentum at the blade tip relative to the smoothwall. The two routes of increased streamwise momentum result from the use of the casing treatment. As a result of these local events, the clearance vortex is positioned further away from the leading edge compared to the smoothwall case. This new vortex position results in a further reduction of the debit of streamwise momentum from the tip region, which is a more global effect.

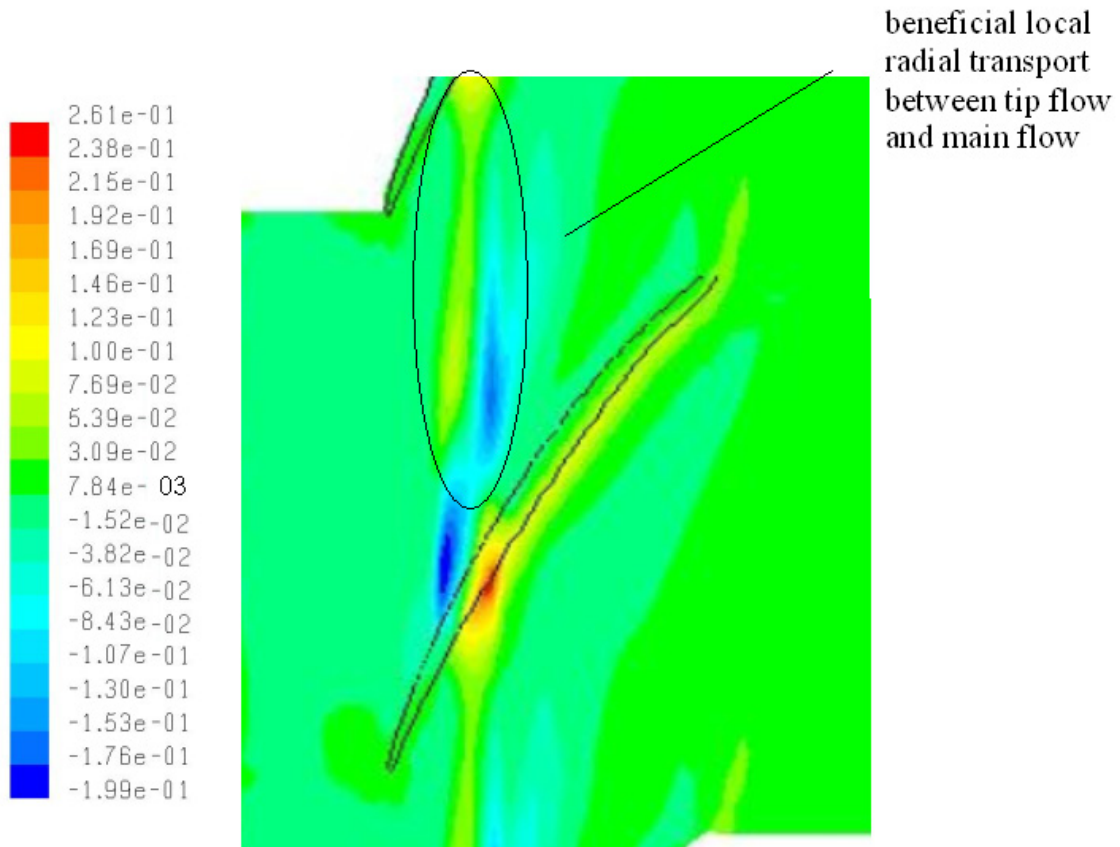


Figure 5.12 Qualitative view in the midgap of the local beneficial radial transport . Radial velocity contours are shown within the tip gap of the 100% groove case. The blue region is the inward radial velocity and marks the leading edge of the clearance vortex. The vortex is clearly pushed downstream by the flow field induced by the casing treatment.

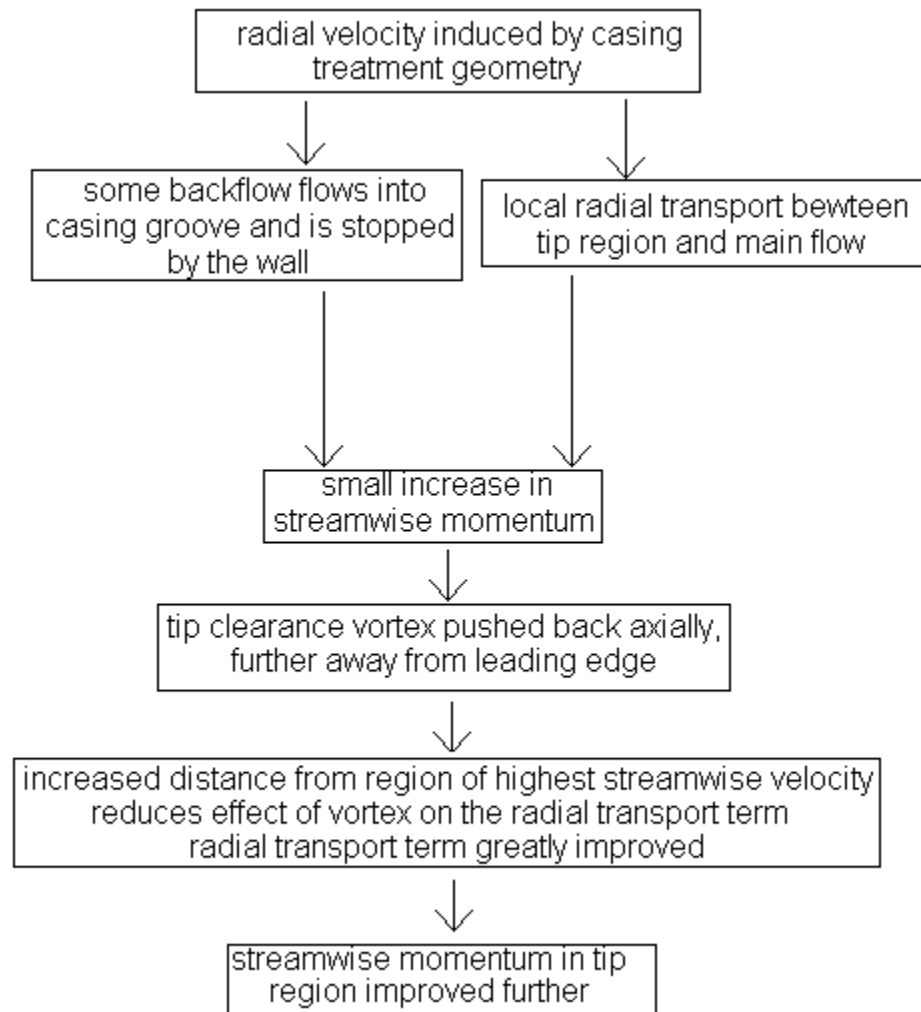


Figure 5.13 Block diagram showing role of casing treatment

5.5 Mechanism for Beneficial Local Radial Transport

The local radial transport mentioned in the previous section and illustrated in figure 5.12 is a result of the local groove-induced radial velocity, which results from the proximity of the tip clearance vortex to the groove. Figure 5.14 illustrates how this flow is produced when the tip clearance vortex is near the downstream edge of the circumferential groove. The flow field near the trailing edge of the groove is dominated by the influence of the clearance vortex, and has a large negative radial velocity. In order to satisfy continuity, there must be a positive radial velocity in the forward region of the groove. Figure 5.15 shows the computed relative velocity vectors (both smoothwall and 100% groove), confirming that this mechanism is responsible for the induced radial velocity. If the vortex is too far from the groove, the beneficial radial velocity will not be induced. Furthermore, if the groove is too shallow, boundary condition (no velocity perpendicular to the wall) on the groove wall will prevent the important changes in radial velocity.

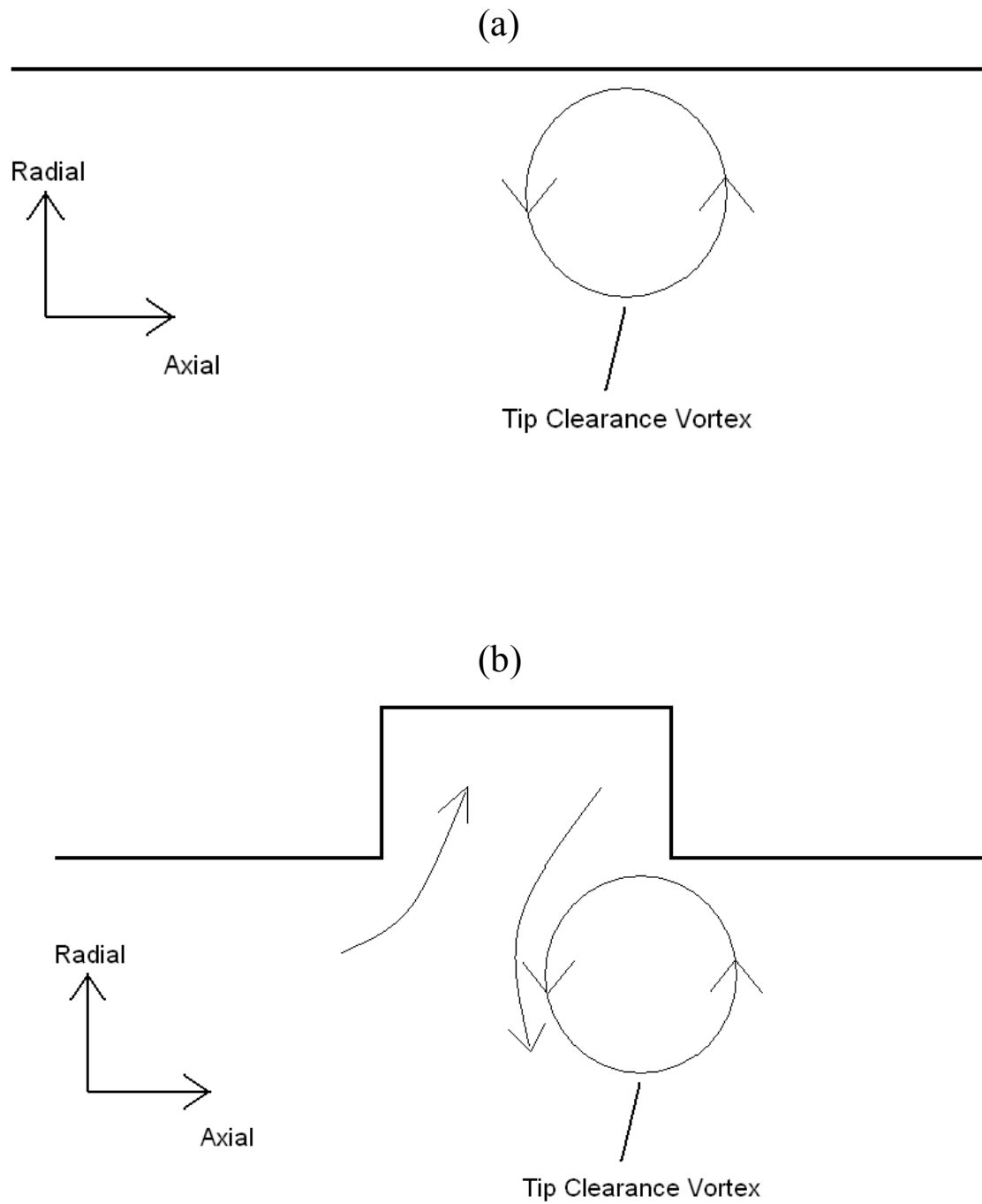


Figure 5.14 Mechanism for local radial transport improvement. Figure(a) shows the smoothwall case. Figure (b) shows the 100% groove case.

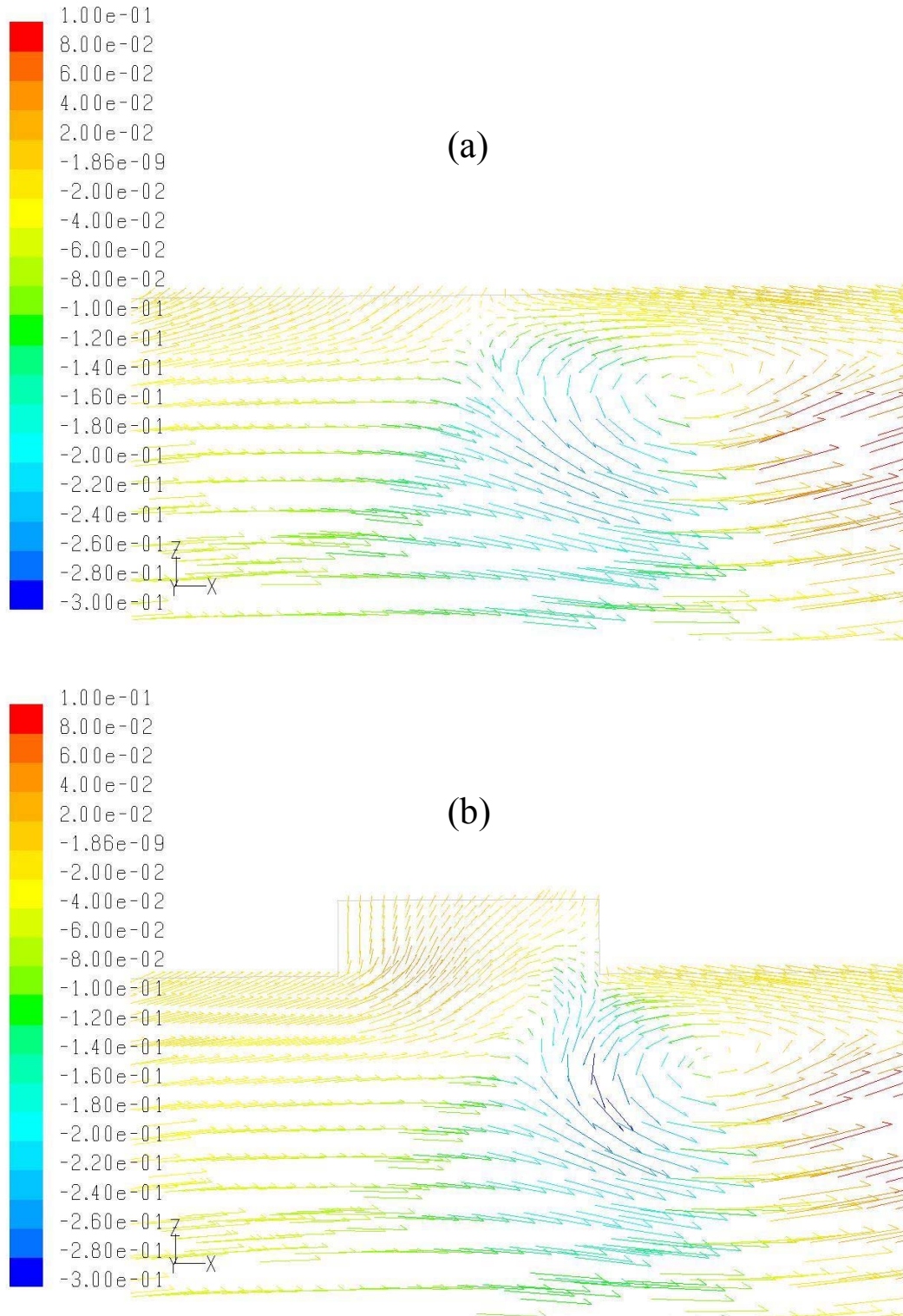


Figure 5.15 Relative velocity vectors at the mid-pitch. The vectors are colored by radial velocity, normalized by the blade tip speed. Both plots show the same axial extent, so direct comparisons can be made. Plot (a) shows the smoothwall case. Plot (b) shows the 100% groove case, illustrating the features sketched in figure 5.14.

To further assess some of the ideas regarding the interaction between the casing treatment and the clearance vortex, the circumferential groove casing geometry was altered. The groove was moved forward and centered at 5% axial chord, rather than at 25% chord position (Figure 5.16). Because the groove is now far ahead of the clearance vortex, this configuration was not effective and flow range was slightly worsened, as depicted in figure 5.17.

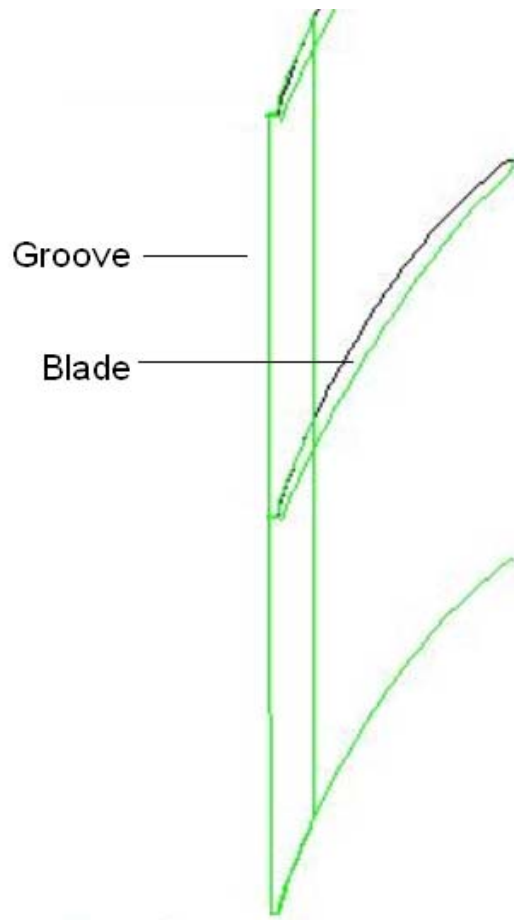


Figure 5.16 Groove forward position. This figure shows the groove axial position when centered at the 5% chord.

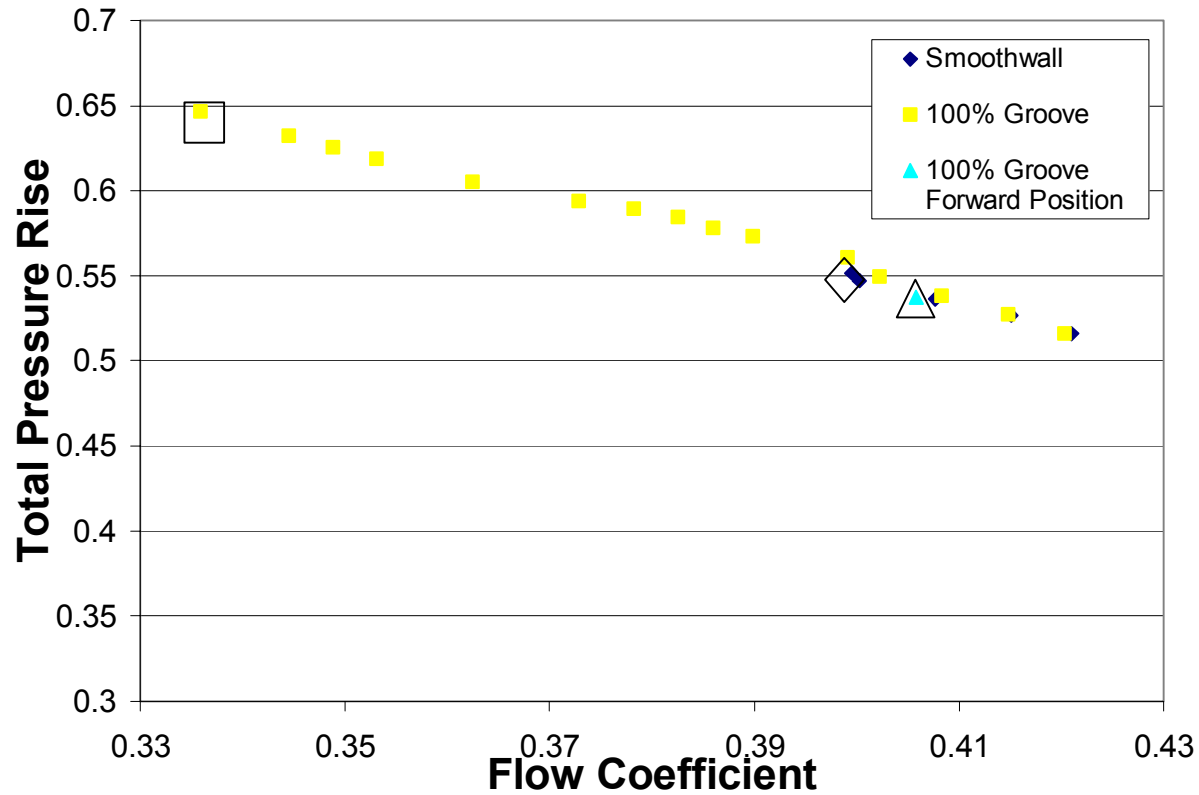
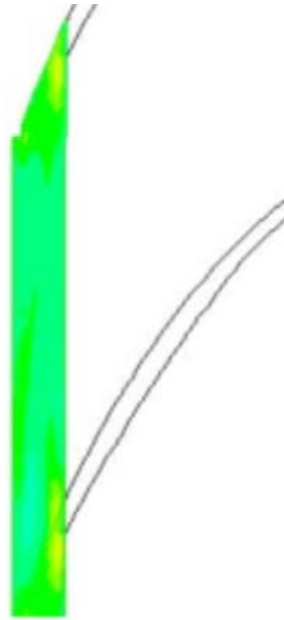


Figure 5.17 Total pressure rise coefficient vs. flow coefficient

The contours of radial velocity for two groove configurations are shown in Figures 5.18(a) and (b). Figure 5.18(a) confirms that the radial velocity associated with the beneficial local radial transport is not present when the groove is in the forward position centered at 5% chord. This is in contrast to the computed contour of radial velocity for the groove centered at 25% axial chord shown in figure 5.18(b), in which there is a region of large positive radial velocity at the mid-pitch of the groove leading edge. The vector plot in figure 5.19 confirms that the groove located at 5% chord is too far ahead of the vortex to induce the beneficial radial velocities.

(a) 5% chord position



(b) 25% chord position

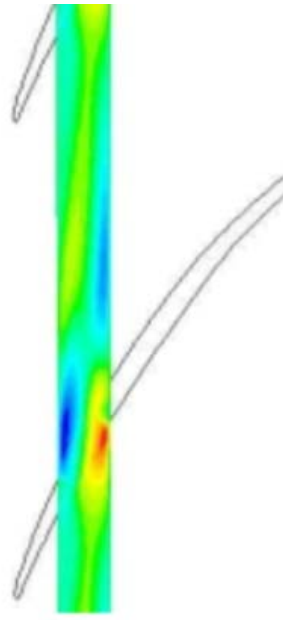


Figure 5.18 Radial velocity contours at the groove entrance, for both the original groove position and the forward groove position.

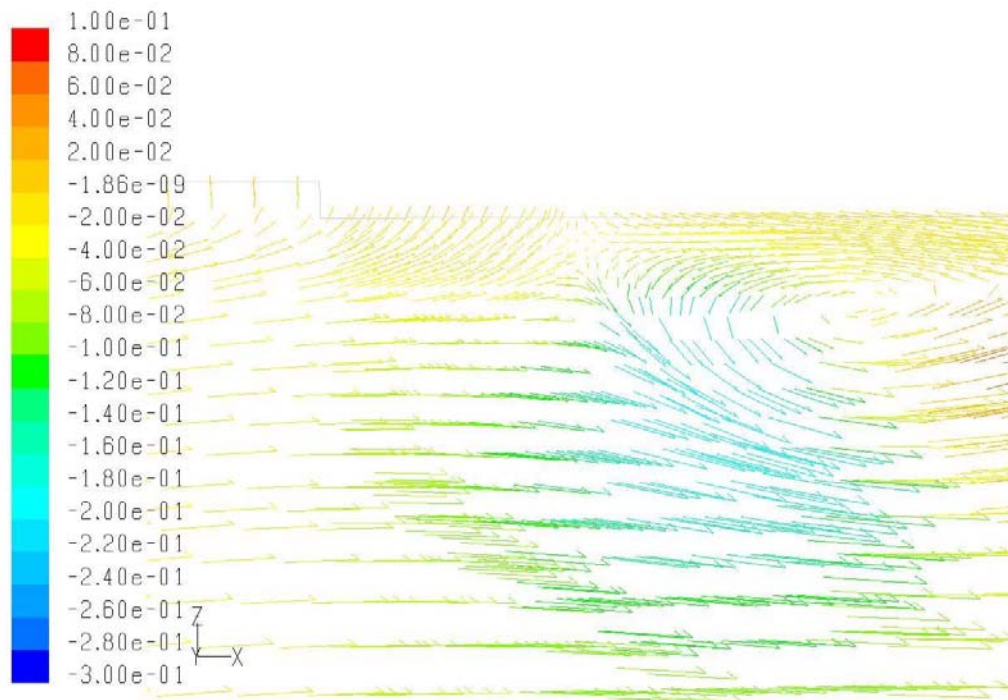


Figure 5.19 Relative velocity vectors measured at the mid-pitch when the groove is centered on the 5% chord. This plot shows a greater axial extent than those in figure 5.15, which was necessary since the groove and vortex are much further apart. This further highlights the fact that the groove is too far ahead of the clearance vortex to induce the beneficial radial velocity.

5.6 Vortex Kinematics

It is possible that vortex kinematics may also be used to explain the shift in position of tip clearance vortex. In potential flow theory, an image vortex is used to satisfy the boundary condition that prevents normal velocity at the casing wall, as shown in figure 5.20. The flow field of the image vortex acts to force the tip clearance vortex upstream.

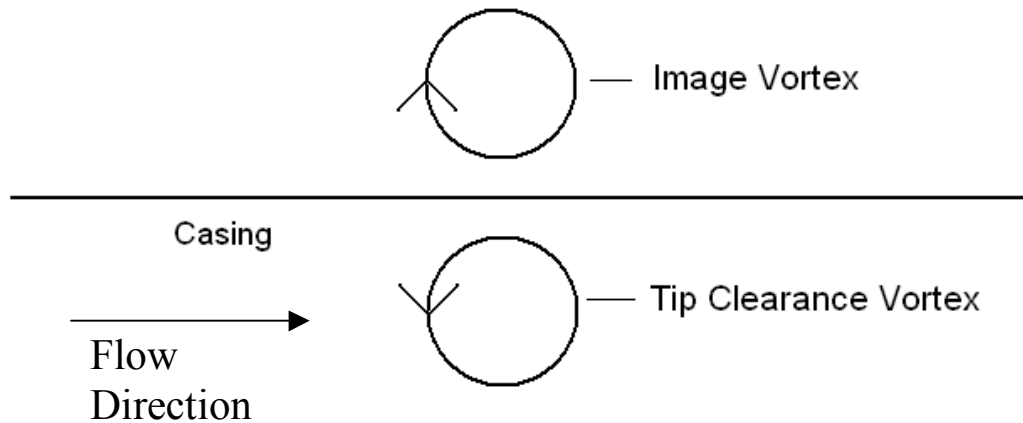


Figure 5.20 Image vortex system for the smoothwall case. The image vortex induces a flow field that tends to force the tip clearance vortex upstream.

The recession of the casing wall associated with the circumferential groove results in the image vortex being positioned further away from the tip clearance vortex, (see figure 5.21) and the upstream force on the clearance vortex is thus lessened. The image vortex system is more complicated than shown in figure 5.21, but the main features are captured by this simple model. If the clearance vortex is not in the vicinity of the groove, the image vortex will not be positioned further away from the clearance vortex when compared to the smoothwall case, and hence no improvement will be seen. This is

the same conclusion reached in the previous section, lending validity to this kinematics view of the circumferential groove action.

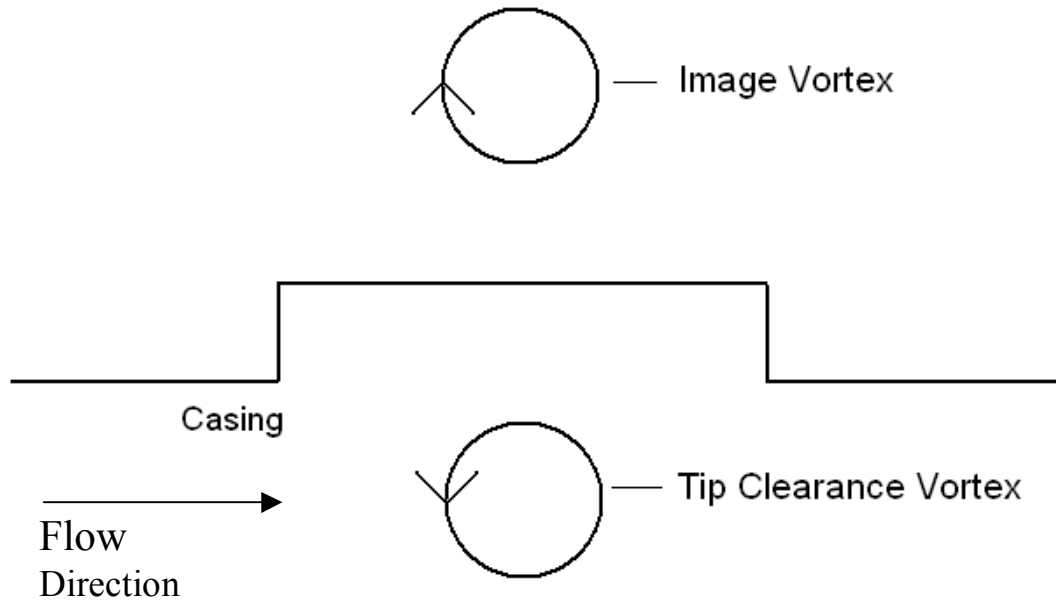


Figure 5.21 Image vortex system for the groove case. The image vortex is further away from the clearance vortex when compared to the smoothwall case.

5.7 General Guidelines for the Design of Groove Casing Treatment

Based upon the results presented in this research, the following design guidelines for circumferential groove casing treatments are suggested:

1) The depth of the groove does not have to be larger than the clearance gap in order to obtain a significant increase in flow range. In fact, nearly all of the flow range extension can be obtained with a groove depth that is half of the tip clearance gap. This is consistent with the work of Rabe and Hah [15] and Adamczyk and Shabbir[2].

2) Positioning the groove in the forward half of the blade passage is effective. It has been shown that the change in the radial transport of streamwise momentum is

dependent on the profile of streamwise velocity at the groove axial location. As most of the diffusion in streamwise velocity occurs only within the first half of the blade passage, the circumferential groove should be located in the first half of the blade passage. This consideration implies the groove should be located at the axial position where variation of streamwise velocity with axial position is the maximum (i.e. the slope of the curve in Fig. 5.5 is the most negative). However, in order for circumferential groove casing treatment to be beneficial and effective, the tip clearance vortex needs to be near the trailing edge of the circumferential groove.

3) One would need to focus on the leading edge region in designing new casing treatment. Any method of improving radial velocity in this region or lessening the impact on this region has the potential to improve the flow range.

4) We have not examined how the axial extent of the groove affects the flow range extension, but based upon the knowledge of how the casing treatment and tip clearance flow interact, some basic considerations can be outlined. The axial extent has to be large enough so that the radial velocity profile is appreciably changed. This sets the minimum axial extent needed to affect a flow range extension. If the extent becomes too large, however, the effective tip clearance gap would increase, thereby making the tip clearance vortex stronger and negating the beneficial effects of the casing treatment.

Chapter 6 Summary and Conclusions

1) Numerical experiments were performed to define the way in which tip clearance flow is altered by casing treatment to improve flow range.

2) This research corroborates previous research in that increased streamwise momentum at the blade tip is found to improve flow range in axial compressors. It extends these views, however, to show that a primary reason for the decrease in streamwise momentum within the tip region is that momentum is diverted inward by radial transport.

3) The radial velocity profile responsible for this transport is a result of the tip clearance vortex.

4) The effect of circumferential casing treatment is to alter the radial velocity profile in a manner that lessens the amount of streamwise momentum diverted out of the blade tip region.

5) To improve the radial transport term, the induced velocity should be towards the casing near the leading edge, and away from the casing near the trailing edge. Using circumferential groove type casing treatment, this is achieved by having the clearance vortex located towards the trailing edge.

6) Changes in the radial velocity very close to the circumferential groove provide the small, local, increase in momentum that affects the clearance vortex, as described in figure 5.14.

Chapter 7 Suggested Future Work

While suggested design guidelines for circumferential grooves and the intended effect of casing treatment have been described, the design process of casing treatment needs to be cast in a more quantitative basis.

Casing treatment should be assessed at different tip clearances. Since the routes to compressor instability (stall) can be dependent on tip clearance size, one should test different clearances to ensure that the findings are universally applicable to both spike and modal stall inceptions. The different stall inception processes are further elaborated in Appendix B.

This research used the geometry of a low-speed machine. Whether the findings described in this research apply to the transonic regime should be addressed. It is the author's opinion that while the shock structure will complicate the tip flow structure, the findings should be applicable to a high-speed compressor.

References

- [1] Adamczyk, J. J., Celestina, M. L., and Greitzer, E. M., 1993, "The Role of Tip Clearance in High-Speed Fan Stall," ASME Journal of Turbomachinery, Transactions of the ASME, Vol. 115, January 1993.
- [2] Adamczyk, J.J. and Shabbir, A., "Flow Mechanism for Stall Margin Improvement due to Circumferential Casing Grooves on Axial Compressors", ASME Turbo Expo 2004, paper GT2004-53903.
- [3] Camp, T.R., and Day, I.J., "A Study of Spike and Modal Stall Phenomena in a Low-Speed Axial Compressor", ASME Journal of Turbomachinery 97-GT-526, June 1997.
- [4] Chen, G. T., Greitzer, E.M., Tan, C.S. and Marble, F.E., "Similarity Analysis of Compressor Tip Clearance Flow Structure", ASME Journal of Turbomachinery, Vol 113, pp 260-271, April 1991.
- [5] Crook, A.J., Greitzer, E.M., Tan, C.S., and Adamczyk, J.J., 1993, "Numerical Simulation of Compressor Endwall and Casing Treatment Flow Phenomena", ASME J. Turbomachinery, Vol. 115, No. 3, 501-512.
- [6] Cumpsty, N.A., Compressor Aerodynamics, Longman Group UK Ltd., London, England, 1989.
- [7] Gong, Y., Tan, C.S., Gordon, K.A., and Greitzer, E.M., "A Computational Model for Short Wavelength Stall Inception and Development in Multi-Stage Compressors", ASME Journal of Turbomachinery, 98-GT-476, June 1998.
- [8] Greitzer, E.M., Nikkanen, J.P., Haddad, D.E., Mazzawy, R.S., Joslyn, H.D., "A Fundamental Criterion for the Application of Rotor Casing Treatment", Journal of Fluids Engineering, Vol. 101, June 1979.
- [9] Greitzer, E.M., Tan, C.S., Graf, M.B., Internal Flow, Concepts and Applications, Cambridge University Press, 2005.
- [10] Hill, P.P. and Peterson, C.R., "Mechanics and Thermodynamics of Propulsion", Addison-Wesley Publishing, 1992.
- [11] Lee, N.K.W. and Greitzer, E.M., "Effects of Endwall Suction and Blowing on Axial Compressor Stability Enhancement", ASME Journal of Turbomachinery, Vol. 112, pp.133-144, January 1990.
- [12] Kerrebrock, J.L. Aircraft Engines and Gas Turbines, 2nd Edition. MIT Press, 1992.

- [13] Khalid, S.A., Khalsa, A.S., Waitz, I.A., Tan, C.S., Greitzer, E.M., Cumpsty, N.A., Adamczyk, J.J. and Marble, F.E., "Endwall Blockage in Axial Compressors", ASME Journal of Turbomachinery, Vol. 121, pp.499-509, July 1999.
- [14] Koch, C. C., "Stalling Pressure Rise Capability of Axial Flow Compressor Stages," ASME J. Eng. Power, 103, pp. 645–656, 1981.
- [15] Rabe, D.C., Hah, C.,2002, "Application of Casing Circumferential Grooves for Improved Stall Margin in a Transonic Axial Compressor", ASME Turbo Expo 2002, paper GT-2002-30641.
- [16] Seitz, P.A. "Casing Treatment for Axial Flow Compressors", Cambridge University Ph.D. dissertation, April 1999.
- [17] Storer, J.A. and Cumpsty, N.A., "Tip Leakage Flow in Axial Compressors", ASME Journal of Turbomachinery, Vol. 113, pp.252-259, April 1991.
- [18] Thompson, D.W., and King, P.I., Hah, C., and Rabe, D.C., "Experimental and Computational Investigation of Stepped Tip Gap Effects on the Flowfield of a Transonic Axial-Flow Compressor Rotor", ASME Journal of Turbomachinery, 98-GT-90, June 1998.
- [19] Vo, H. D., "Role of Tip Clearance Flow on Axial Compressor Stability", Massachusetts Institute of Technology, Ph.D. Thesis, September 2001.

Appendix A User-Defined Function

The custom code that communicates with Fluent to determine the Body Force vectors is shown here. The force per volume distribution (as a function of position and relative velocity field) is the output of the code. The radial extent in which the algorithm is to be applied first needs to be specified within Fluent.

```
#include "udf.h"

DEFINE_ADJUST(v_adjust, domain)
{
    int id = 1;
    cell_t cell;
    Thread *thread = Lookup_Thread(domain, 1);
}

DEFINE_SOURCE(cell_x3_source, cell, thread, dS, eqn)
{
    real x[ND_ND];
    real Fx;
    real Fy;
    real vx;
    real vy;
    real theta;
    real source1;
    real x1, y1, z1, r_local;
    real vmag, Fmag;

    //Variables representing the position of the cells
    C_CENTROID(x, cell, thread);
    x1 = x[0];
    y1 = x[1];
    z1 = x[2];

    //Find the radial position of the cells
    r_local = sqrt(pow(y1, 2) + pow(z1, 2));

    //Find the relative axial and circumferential velocities
    vx = C_U(cell, thread);
    vy = C_V(cell, thread) + 223*r_local;

    //Calculate the total relative velocity
    vmag = sqrt(pow(vx, 2) + pow(vy, 2));
    //Scale the body force proportionally with the relative velocity
```

```

//7163 is the factor for Casing Force(high); 2000 for Casing Force(Low)
Fmag = 7163*vmag;
//The radial extent of the force can easily be specified in Fluent, but
//it is easier to express the axial extent here. Only within the axial
//extent of the blade tip will the body force be applied

if(x1 < -0.02313)
Fmag = 0;

if(x1 > 0.02938)
Fmag = 0;

//Calculate the relative velocity angle
theta = atan(vy/vx);

//Calculate the axial component of the Body Force
Fx = Fmag*sin(theta);

//The x-component of the body force should always be pointed downstream
if(Fx < 0)
Fx = -Fx;

source1 = Fx;

//C_UDMI(cell,thread,0) = source1;

dS[eqn] = 0;

return source1;
}

//The determination of the tangential component of the body force is
//done in the same manner as the axial component. Much of the code
//could be combined, but it worked as shown, so it was left in this
//form
DEFINE_SOURCE(cell_y3_source, cell, thread, dS, eqn)
{

real x[ND_ND];
real Fx;
real Fy;
real vx;
real vy;
real theta;
real source2;
real x1,y1,z1,r_local;
real vmag, Fmag;

C_CENTROID(x,cell,thread);
x1 = x[0];
y1 = x[1];
z1 = x[2];

r_local = sqrt(pow(y1,2)+pow(z1,2));

vx = C_U(cell,thread);

```

```

vy = C_V(cell,thread) + 223*r_local;

vmag = sqrt(pow(vx,2)+pow(vy,2));
Fmag = 7163*vmag;

if(x1 < -0.02313)
Fmag = 0;

if(x1 > 0.02938)
Fmag = 0;

theta = atan(vy/vx);

Fy = -Fmag*cos(theta);

//The axial component is made to point downstream, and the tangential
//component direction is fixed by this decision.
if(vx*vy < 0. && Fy < 0.)
Fy = -Fy;

if(vx*vy > 0. && Fy > 0.)
Fy = -Fy;

source2 = Fy;

dS[eqn] = 0;

return source2;
}

```

Appendix B Method of Stall Inception

There are two stall inception methods: modal stall and spike stall [Day and Camp, 3]. Modal stall occur when a long-wavelength disturbance (one the order or of the annulus distance) grows slowly into fully developed stall cells. Spike stall, on the other hand, occurs when a short-wavelength (2-3 blade passages) triggers a stall within a few rotor revolutions [Day and Camp, 3]. Vo [16] outlined the flow field characteristics that accompany spike stall. If the last converged solution does not exhibit the limit of stable flow according to the spike stall criteria, then it is modal stall that is responsible for the inception.

Figure A.1, from Vo [16] compares the flow field characteristic immediately preceding the different types of stall. When spike stall is the limiter, the high entropy gradient at the blade tip is aligned with the blade passage entrance. When modal stall is the inception route, the interface remains well within the blade passage. Vo achieved the two different types of characteristics in the same blade geometry by varying the tip clearance gap. From the entropy contours of the present calculation (shown in Fig. A.2), one can see that the interface is located well within the blade passage, suggesting that this geometry has a flow range limited by modal stall. Vo also found that an E^3 Rotor with 3% chord tip clearance gap, which is the geometry used in the present research, is characterized by modal stall inception.

This work focuses on the physics behind the beneficial effects of casing treatments, so the inception route may not be of primary importance. We note that the mechanisms here were for a compressor with modal type of stall, and some features of casing treatment may change if the type of stall changes.

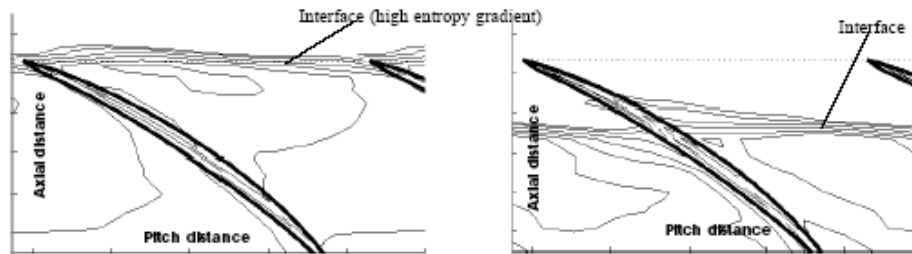


Figure B.1 Comparison of flow fields at blade tip immediately preceding spike and modal stalls

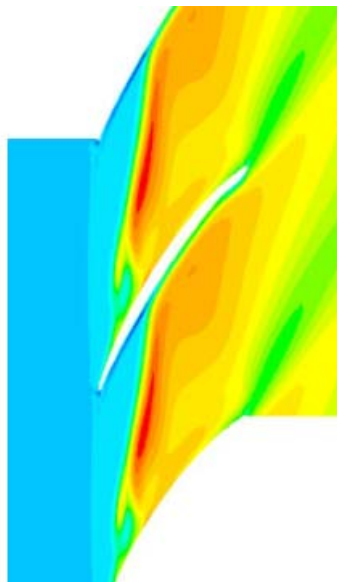


Figure B.2 Entropy contours at 100% span. The high-entropy interface is well within the blade passage.

When the relative flow angle at the leading edge in a spike-limited compressor reaches a critical angle, stall occurs. As the compressor is pushed further towards stall, the incidence increases until this limit is reached (assuming modal stall does not occur first). Table 4, however, shows that because the casing treatment reduces the incidence angle at a given flow coefficient, it is likely the treatment is also effective if spike disturbance is the stall inception method

Table 4 Flow angle at blade tip leading edge at the smoothwall stall flow coefficient. Note that the presence of the casing treatment reduces the flow angle at the blade tip leading edge.

| Geometry | Relative Flow Angle |
|-----------------|----------------------------|
| Smoothwall | 75.6 degrees |
| 5% Groove | 74.4 |
| 10% Groove | 73.5 |
| 100% Groove | 73.8 |

Appendix C Sensitivity to Turbulence Model

In the current research, one of the most surprising results was the ability of the 5% groove to affect a substantial change in the flow range over the smoothwall case. This prompted a study to ensure that the results were indicative of changes in the flow field, and not due to poor modeling by the CFD calculation.

First the grid was examined to determine if the cell density was high enough. Standard wall functions are used on every solid surface in order to reduce the number of cells needed to run the calculation. Wall functions estimate the effect of the viscous boundary layer without actually fully resolving the boundary layer. For wall functions to operate correctly, the cell size adjacent to wall in question must be a particular size. The distance of importance is called the y^+ value, described by the equation,

$$y^+ = \frac{\rho u_\tau y}{\mu} \quad (C.1)$$

The y^+ values present in these calculations are between 30 and 80, which is within the acceptable range.

After confirming the adequacy of cell density, the turbulence model was tested. The wall functions were changed from standard to non-equilibrium wall functions. As another test, the entire turbulence model was changed from standard k-epsilon to Spalart-Allmaras. Using these different tools of turbulence models, a few points were calculated for both the smoothwall and the 5% Groove. The results from these calculations are shown in Fig. C.1 and Fig C.2. Although the absolute values of the pressure rise, stalling flow coefficients, and efficiencies change as a result of the different turbulence models, the relative changes are comparable. These interrogations of the grid and alterations of

the turbulence models show that the conclusions are relatively independent to turbulence model.

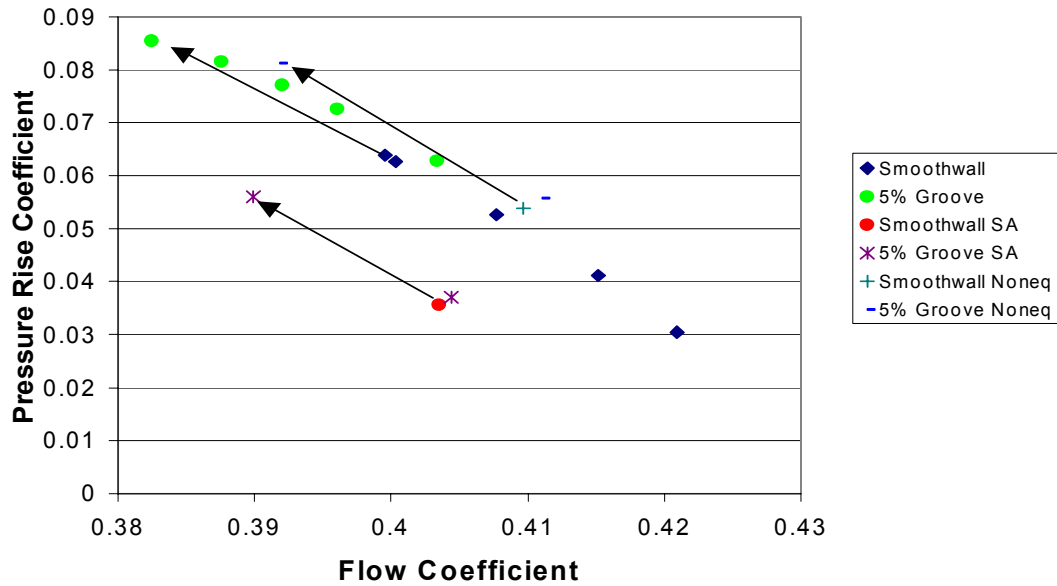


Figure C.1 Pressure rise coefficient vs. flow coefficient. Results using Spalart-Allmaras and non-equilibrium wall functions are shown. The arrows show the change in stall point between the smoothwall and the 5% groove. The change is similar for all three turbulence model setups.

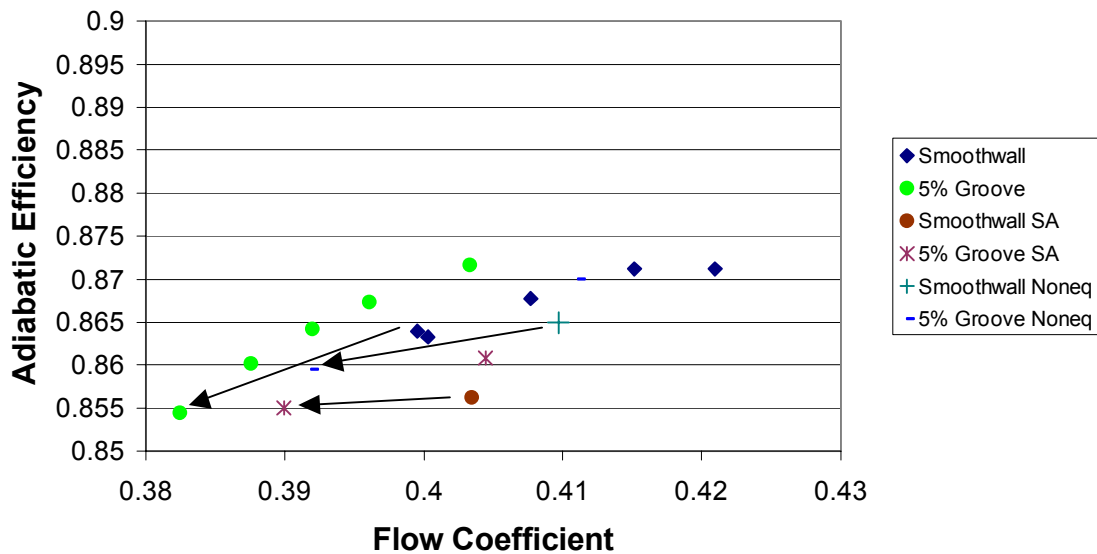


Figure C.2 Adiabatic efficiency vs. flow coefficient. The arrows show the change in stall point using the 5% groove. Once again, the change is similar regardless of the turbulence model.

APPENDIX C

Virginia Polytechnic Institute Research

Final Report

Virginia Tech Project Number 414720
Battelle Purchase Order 180206

**Distortion Transfer Prediction through the
Blade Rows in an Axial Compressor, and
Prediction of Blade Response from Finite
Element Analysis**

**Part A: Prediction of Inlet Distortion Transfer through the Blade Rows in a
Transonic Axial Compressor**

Author: John F. Ryman, Research Assistant

**Part B: Modal Response of a Transonic Fan Blade to Periodic Inlet
Pressure Distortion**

Author: Robert M. Wallace, Research Assistant

**Principal Investigator: Walter F. O'Brien
J. Bernard Jones Professor of Mechanical Engineering**

**Technical Monitor: Douglas C. Rabe
Director, Turbine Engine Research Center
AFRL-PRTE**

**Turbomachinery Laboratory
Center for Turbomachinery and Propulsion Research
Mechanical Engineering Department
Virginia Tech
Blacksburg, VA 24061**

Sponsor

**AFRL-PRTE, Battelle Corporation
Attn: Ms. Pamela Teets
Building 71B, Area B
Wright-Patterson AFB, OH, 45433
June 2005**

Abstract

Part A: Distortion Transfer Prediction Through the Blade Rows in an Axial Compressor **John F. Ryman**

Inlet total pressure non-uniformities in axial flow fans and compressors can contribute to the loss of component structural integrity through high cycle fatigue (HCF) induced by the excitation of blade vibratory modes. As previous research has shown total pressure distortion to be the dominant HCF driver in aero engines [Manwaring et al, 1997], an understanding of its transfer through, and impact on, subsequent turbomachine stages and engine components is an important topic for assessment. Since current modeling techniques allow for total pressure distortion magnitudes to be directly related to blade vibratory response, the prediction of downstream distortion patterns from an upstream measurement would allow for the inference of the vibratory response of downstream blade rows to an inlet total pressure distortion.

Several mathematical techniques can be considered for the prediction of the transfer of distortion patterns through compressor rotors. This report covers an investigation of nonlinear Volterra theory for the purpose, which can be used to model any periodic nonlinear system as an infinite sum of multidimensional convolution integrals. A semi-empirical model has been developed using this theory by assuming that a distortion waveform is a periodic signal that is being presented to a nonlinear system, the compressor being the system. The use of Volterra theory in nonlinear system modeling relies on the proper identification of the Volterra kernels, which make up the transfer function that defines the system's impulse response characteristics. Once the kernels of a system are properly identified, the system's response can be calculated for any arbitrary input. This model extracts these kernels from upstream and downstream total pressure distortion measurements of a transonic rotor of modern design. The resulting transfer function is then applied to predict distortion transfer at new operating points on the same rotor and compared with the measured data.

The judicious choice of distortion measurement data allows predictions of the downstream distortion content based on a measured non-uniform inlet flow at conditions different from those at which the transfer function was derived. This allows for the determination of downstream total pressure distortion that has the potential to excite blade vibratory modes that could lead to HCF under operating conditions other than those at which the data was taken, such as varying inlet distortion patterns, mass flow settings, rotational speeds, and inlet geometry.

This report presents the creation of a Volterra model in order to predict distortion transfer in axial flow fans and compressors. This model, in three variations, is applied to a variety of distortions and compressor operating conditions as measured in the ADLARF tests at the Compressor Research Facility. Predictions are compared with data from the test and final results are also compared with two previous studies conducted at Virginia Tech using the same experimental data. Using the Volterra model it is shown that, with appropriate limitations, distortion transfer can be predicted for flow conditions different from those used for calibration. The model is considered useful for both performance and HCF investigations.

**Part B: Modal Response of a Transonic Fan Blade to Periodic Inlet
Pressure Distortion
Robert M. Wallace**

A new method for predicting forced vibratory blade response to total pressure distortion has been developed using modal and harmonic analysis. Total pressure distortions occur in gas turbine engines when the incoming airflow is partially blocked or disturbed. Distorted inlet conditions can have varying effects on engine performance and engine life. Short-term effects are often in the form of performance degradation where the distorted airflow causes a loss in pressure rise, and a reduction in mass flow and stall margin. Long-term effects are a result of vibratory blade response that can ultimately lead to high cycle fatigue (HCF), which in turn can quickly cause partial damage to a single blade or complete destruction of an entire compressor blade row, leading to

catastrophic failure of the gas turbine engine. A better understanding and prediction of vibratory blade response is critical to extending engine life and reducing HCF-induced engine failures.

This work covers the use of finite element modeling coupled with computational fluid dynamics-generated pressure fields to create a generalized forcing function. The first three modes of a low-aspect-ratio, transonic, first stage blade of a two-stage fan were examined. The generalized forcing function was decomposed to the frequency domain to identify the dominant harmonic magnitude present, as well as other contributing harmonics. A method to define the relationship between modal force with varying total pressure distortion levels produced a sensitivity factor that describes the relationship in the form of a simple multiplier. A generalized force was applied to the blade and varied harmonically across a frequency range known to contain the first natural frequency. The mean rotor stress variation was recorded and compared to experimental results to validate the accuracy of the model and verify its ability to predict vibratory blade response accurately.

Part A: Prediction of Inlet Distortion Transfer Through the Blade Rows in a Transonic Axial Compressor

John F. Ryman

Table of Contents

| | | |
|-----|--|----|
| 1 | Introduction | 16 |
| 2 | Literature Review | 20 |
| 2.1 | Inlet Distortion Effects on Compressor Performance and Blade Response..... | 20 |
| 2.2 | Aerodynamic Performance Modeling Techniques | 24 |
| 2.3 | Conclusions from Literature Review | 31 |
| 3 | Nonlinear Volterra Theory Modeling | 34 |
| 3.1 | Nonlinear Volterra Theory | 34 |
| 3.2 | Volterra Kernels | 38 |
| 3.3 | System Requirements for Volterra Series Modeling..... | 38 |
| 4 | Identification of Volterra Kernels | 40 |
| 4.1 | Volterra Kernel Identification Methods..... | 41 |
| 4.2 | Indirect Extraction Technique | 42 |
| 4.3 | Choice of Basis Functions | 46 |
| 4.4 | Number of Basis Functions..... | 50 |
| 5 | Experimental Data | 52 |
| 5.1 | Experimental Facility..... | 52 |
| 5.2 | Experimental Procedure | 55 |
| 5.3 | Data Reduction..... | 59 |
| 5.4 | Data Characteristics | 60 |
| 6 | Solution Technique | 66 |
| 6.1 | System Identification..... | 66 |
| 6.2 | Data Set Expansion | 67 |
| 6.3 | Data Conditioning | 69 |
| 6.4 | Training and Prediction Data Sets..... | 70 |

| | | |
|-----|---|-----|
| 6.5 | Modeling Method Variations | 71 |
| 7 | Prediction Results of Nonlinear Volterra Series Model | 73 |
| 7.1 | Validation of Model | 74 |
| 7.2 | Same Speed Predictions | 77 |
| 7.3 | Different Speed Predictions..... | 88 |
| 7.4 | Higher-Order Effects | 97 |
| 7.5 | Comparison with Previous Models..... | 99 |
| 8 | Summary and Conclusions..... | 101 |
| 9 | Recommendations..... | 104 |
| 10 | Postscript..... | 106 |
| 11 | Works Cited | 108 |

Table of Tables

| | |
|--|----|
| Table 5-1: First stage blisk geometry characteristics [Rabe et al., 1999]. | 54 |
| Table 5-2: Radial locations of inlet total pressure probes [Morrow, 1993]. | 56 |
| Table 5-3: First stage stator probe locations [Morrow, 1993]. | 57 |
| Table 5-4: Second stage stator probe locations [Morrow, 1993]. | 57 |
| Table 7-1: Prediction results when replicating the same data used in kernel calculation (9100NOL) in the time and frequency domain of each model. Best prediction is highlighted in blue in the frequency domain and red in the time domain. | 82 |
| Table 7-2: Prediction results of compressor output at 9500WOD from 9500NOL, NS, and PE in the time and frequency domain are shown. | 87 |
| Table 7-3: Prediction results made at 9500NOL after kernel calculation with 9100 and 13200-rpm data. | 94 |
| Table 7-4: Summary of results obtained with Model 2 when predicting compressor output at 9500NOL after calculating the kernels with 9100rpm data. | 96 |
| Table 7-5: Comparison of Model 2 with previous modeling methods. The percent error of the dominant frequency magnitude is shown. | 99 |

Table of Figures

| | |
|---|----|
| Figure 1-1: Capabilities of modern day aircraft increase the potential that the inlet flow to their engines is non-uniform [www.airforce.com]. | 16 |
| Figure 1-2: F117 Nighthawk has an 'S' shaped or stealth inlet, increasing the potential for the inlet flow to its engines to be non-uniform [www.aladdinsoft.com]. | 17 |
| Figure 1-3: The AV-8B Harrier. The ingestion and subsequent mixing of the hot exhaust gases with the cooler atmospheric air could cause the inlet pressure profile to the aircraft's engine to be non-uniform [www.globalsecurity.org]. | 17 |
| Figure 1-4: Compressor map showing the loss in surge limit caused by a distorted inlet flow [ARP-1420, 2002]. | 18 |
| Figure 2-1: The effect on surge delivery static pressure of spoiled sector width and of sub-dividing the spoiled area [Reid, 1968]. | 21 |
| Figure 2-2: Campbell Diagram [Manwaring et al., 1997] and the variation of blade vibration amplitude with the intensity of the distortion [Danforth, 1975]. | 22 |
| Figure 2-3: Pictorial representation of parallel compressor theory [Reid, 1969]. | 25 |
| Figure 2-4: Deviation of flow from predicted square-wave pressure pattern [Roberts et al., 1968]. | 26 |
| Figure 2-5: Multiple stream-tube model versus parallel compressor theory [Mazzawy, 1977]. | 27 |
| Figure 2-6: Exponential decay transfer function [Lecht, 1986]. | 28 |
| Figure 2-7: Actuator disk total exit pressure predictions compared with experimental measurements [Colpin and Kool, 1978]. | 29 |
| Figure 2-8: TEACC methodology [Davis et al., 2000]: (a) three-dimensional grid built from the conservation equations (b) streamline curvature code calculates mass flow, blade forces, and shaft work (c) digital computer | |

| | |
|--|----|
| combines a & b to solve the conservation equations and (d) model distortion in steady-state conditions. | 31 |
| Figure 2-9: Distortion screen designs to generate total pressure non-uniformities [Datko et al., 1987]..... | 32 |
| Figure 3-1: Third order system representation [Bendat, 1998]..... | 35 |
| Figure 4-1: Linear kernel calculated from experimental data obtained at 9500rpm, RI3. | 48 |
| Figure 4-2: Second-order kernel calculated from experimental data obtained at 9500rpm, RI3. | 49 |
| Figure 4-3: Three-dimensional view of the second-order kernel calculated from experimental data obtained at 9500rpm, RI3. | 50 |
| Figure 4-4: Convergence of the linear kernel as the number of basis functions increases. | 51 |
| Figure 5-1: Test facility at the Compressor Research Facility, Wright-Patterson AFB [Morrow, 1993]. | 53 |
| Figure 5-2: First stage blisk mounted on test rig [Morrow, 1993]..... | 54 |
| Figure 5-3: Second stage rotor [Morrow, 1993]..... | 55 |
| Figure 5-4: Experimental setup [Morrow, 1993]..... | 56 |
| Figure 5-5: Instrumented stator vane [Morrow, 1993]..... | 56 |
| Figure 5-6: Example of a 3 per rev distortion screen [Morrow, 1993]. | 58 |
| Figure 5-7: SLC computed streamline positions though the compressor [Small, 2001]. | 60 |
| Figure 5-8: Compressor operating map, including clean and distorted inlet conditions [Small, 2001]. | 61 |
| Figure 5-9: Time-series inlet and outlet dynamic total pressure profiles at 9100 NOL RI3..... | 62 |
| Figure 5-10: Frequency content of 9100 NOL RI3. | 62 |
| Figure 5-11: Time-series inlet and outlet dynamic total pressure profiles at 9500 NOL RI1..... | 63 |

| | |
|---|----|
| Figure 5-12: Frequency content of 9500 NOL RI1. | 63 |
| Figure 5-13: First stage dynamic total pressure at 9100 rpm, mid-span, inlet, and outlet. | 64 |
| Figure 5-14: First stage distortion magnitude gain as a function of blade position and rotational speed. | 65 |
| Figure 6-1: Data set before and after being run through spline code. Final data set of 720 points directly overlays the original, which consisted of 360 data points. | 68 |
| Figure 7-1: Prediction result from kernels calculated with input of $\sin(x)$ and output of $\sin^2(x)$. Prediction directly overlays the actual data set analytically calculated from sine squared..... | 76 |
| Figure 7-2: Prediction result from kernels calculated with input of $\sin(x)$ and output of $\sin^3(x)$. Prediction directly overlays the actual data set analytically calculated from sine cubed. | 76 |
| Figure 7-3: Prediction result from kernels calculated with input of $\sin(x)$ and output of $\sin(x) + \sin(2x)$. Prediction directly overlays the actual data set analytically calculated from the addition of $\sin(x)$ and $\sin(2x)$ | 77 |
| Figure 7-4: Time domain prediction obtained with Model 3 of the output variation in total pressure at 9100NOL, RI5 after calculating the system kernels with the same data. | 78 |
| Figure 7-5: Time domain prediction obtained with Model 3 of the output variation in total pressure at 9100NOL, RI4 after calculating the system kernels with the same data. | 78 |
| Figure 7-6: Time domain predictions obtained with Model 3 of the output variation in total pressure at 9100NOL, RI3 after calculating the system kernels with the same data. | 78 |
| Figure 7-7: Time domain predictions obtained with Model 3 of the output variation in total pressure at 9100NOL, RI2 after calculating the system kernels with the same data. | 79 |

| | |
|---|----|
| Figure 7-8: Time domain predictions obtained with Model 3 of the output variation in total pressure at 9100NOL, RI1(near tip) after calculating the system kernels with the same data..... | 79 |
| Figure 7-9: Magnitude plot in the frequency domain of the output variation in total pressure corresponding to the prediction shown in Figure 7-4 that was made with Model 3. | 79 |
| Figure 7-10: Magnitude plot in the frequency domain of the output variation in total pressure corresponding to the prediction shown in Figure 7-5 that was made with Model 3. | 80 |
| Figure 7-11: Magnitude plot in the frequency domain of the output variation in total pressure corresponding to the prediction shown in Figure 7-6 that was made with Model 3. | 80 |
| Figure 7-12: Magnitude plot in the frequency domain of the output variation in total pressure corresponding to the predictions shown in Figure 7-7 that was made with Model 3. | 80 |
| Figure 7-13: Magnitude plot in the frequency domain of the output variation in total pressure corresponding to the prediction shown in Figure 7-8 that was made with Model 3. | 81 |
| Figure 7-14: Prediction of Model 1 of the output variation in total pressure at 9500WOD, RI5 after calculating the system kernels with the other data sets at that same rotational speed..... | 83 |
| Figure 7-15: Prediction of Model 1 of the output variation in total pressure at 9500WOD, RI4 after calculating the system kernels with the other data sets at that same rotational speed..... | 84 |
| Figure 7-16: Prediction of Model 1 of the output variation in total pressure at 9500WOD, RI3 after calculating the system kernels with the other data sets at that same rotational speed..... | 84 |

| | |
|--|----|
| Figure 7-17: Prediction of Model 1 of the output variation in total pressure at 9500WOD, RI2 after calculating the system kernels with the other data sets at that same rotational speed..... | 84 |
| Figure 7-18: Prediction of Model 1 of the output variation in total pressure at 9500WOD, RI1 after calculating the system kernels with the other data sets at that same rotational speed..... | 85 |
| Figure 7-19: Magnitude plot in the frequency domain of the output variation in total pressure corresponding to Figure 7-14 that was made with Model 1... | 85 |
| Figure 7-20: Magnitude plot in the frequency domain of the output variation in total pressure corresponding to Figure 7-15 that was made with Model 1... | 85 |
| Figure 7-21: Magnitude plot in the frequency domain of the output variations in total pressure corresponding to the prediction shown in Figure 7-16 that was made with Model 1..... | 86 |
| Figure 7-22: Magnitude plot in the frequency domain of the output variations in total pressure corresponding to the prediction shown in Figure 7-17 that was made with Model 1..... | 86 |
| Figure 7-23: Magnitude plot in the frequency domain of the output variations in total pressure corresponding to the prediction shown in Figure 7-18 that was made with Model 1..... | 86 |
| Figure 7-24: Prediction of Model 2 of the output variation in total pressure at 9500NOL, RI5 after calculating the system kernels with the data sets from the other two rotational speeds..... | 89 |
| Figure 7-25: Prediction of Model 2 of the output variation in total pressure at 9500NOL, RI4 after calculating the system kernels with the data sets from the other two rotational speeds..... | 89 |
| Figure 7-26: Prediction of Model 2 of the output variation in total pressure at 9500NOL, RI3 after calculating the system kernels with the data sets from the other two rotational speeds..... | 89 |

| | |
|--|----|
| Figure 7-27: Prediction of Model 2 of the output variation in total pressure at 9500NOL, RI2 after calculating the system kernels with the data sets from the other two rotational speeds..... | 90 |
| Figure 7-28: Prediction of Model 2 of the output variation in total pressure at 9500NOL, RI2 after calculating the system kernels with the data sets from the other two rotational speeds..... | 90 |
| Figure 7-29: Magnitude plot in the frequency domain of the output variation in total pressure corresponding to the prediction shown in Figure 7-24 that was made with Model 2. | 90 |
| Figure 7-30: Magnitude plot in the frequency domain of the output variation in total pressure corresponding to the prediction shown in Figure 7-25 that was made with Model 2. | 91 |
| Figure 7-31: Magnitude plot in the frequency domain of the output variation in total pressure corresponding to the prediction shown in Figure 7-25 that was made with Model 2. | 91 |
| Figure 7-32: Magnitude plot in the frequency domain of the output variation in total pressure corresponding to the prediction shown in Figure 7-26 that was made with Model 2. | 91 |
| Figure 7-33: Magnitude plot in the frequency domain of the output variation in total pressure corresponding to the prediction shown in Figure 7-27 that was made with Model 2. | 92 |
| Figure 7-34: Prediction of Model 1 of the output variation in total pressure at 9500NOL RI3, after calculating the system kernels with the data sets measured at 9100 and 13200rpm. | 93 |
| Figure 7-35: Magnitude plot in the frequency domain of the output total pressure prediction shown in Figure 7-34. | 93 |
| Figure 7-36: Same scenario as in Figure 7-34, only data sets were further normalized with the non-dimensional stage work. | 93 |

| | |
|---|----|
| Figure 7-37: Magnitude plot in the frequency domain of the output total pressure prediction shown in Figure 7-36. | 94 |
| Figure 7-38: Example of the output in Matlab of a prediction of the variation in total pressure at 9500rpm, NOL mass flow, RI3 (mid span). Blue coloring corresponds to the actual experimental data and red the prediction. | 97 |
| Figure 7-39: Graphical display of the 1 st , 2 nd , and 3 rd order terms and their combination to form the final response prediction using Model 2. | 98 |

Table of Equations

| | |
|---------------------|----|
| Equation 3-1 | 34 |
| Equation 4-1 | 43 |
| Equation 4-2 | 43 |
| Equation 4-3 | 43 |
| Equation 4-4 | 43 |
| Equation 4-5 | 44 |
| Equation 4-6 | 44 |
| Equation 4-7 | 44 |
| Equation 4-8 | 44 |
| Equation 4-9 | 44 |
| Equation 4-10 | 45 |
| Equation 4-11 | 45 |
| Equation 4-12 | 46 |
| Equation 4-13 | 46 |
| Equation 4-14 | 47 |
| Equation 4-15 | 48 |
| Equation 4-16 | 48 |
| Equation 6-1 | 69 |
| Equation 6-2 | 69 |
| Equation 6-3 | 70 |

1 Introduction

Historically, the assumption has been made that the airflow through axial compressors in aircraft engines is uniform. As the performance continues to increase in modern aero engines, the capabilities of the aircraft that they are put in also increase. It is these capabilities that cause the inlet flow to the engines of these aircraft to often be non-uniform. Extreme flight maneuvers, operating within the wake of other aircraft, and firing wing-mounted weapons are some of the operational causes of non-uniform inlet flow (see Figure 1.1).



Figure 1-1: Capabilities of modern day aircraft increase the potential that the inlet flow to their engines is non-uniform [www.airforce.com].

Another possible cause of non-uniform inlet flow to modern aircraft engines is advanced inlet configurations such as the serpentine inlets used on stealth aircraft. Additionally, when vertical take-off and landing aircraft (VTOL) are hovering, the ingestion and mixing of hot exhaust gases with the cooler atmospheric air could also cause the inlet pressure profile to the plane's engines to be non-uniform (see Figures 1.2 and 1.3).



Figure 1-2: F117 Nighthawk has an ‘S’ shaped or stealth inlet, increasing the potential for the inlet flow to its engines to be non-uniform [www.aladdinsoft.com].



Figure 1-3: The AV-8B Harrier. The ingestion and subsequent mixing of the hot exhaust gases with the cooler atmospheric air could cause the inlet pressure profile to the aircraft’s engine to be non-uniform [www.globalsecurity.org].

Non-uniform inlet flow, also known as inlet distortion, has negative short term and long-term effects on a compressor. The short-term effects are most easily seen on a compressor map as a loss in pressure rise, reduction in mass flow, and/or a reduction of stall margin (see Figure 1.4). A great deal has been done and is known about the effects of non-uniform inlet flow on performance in order to prevent compressor stall and surge.

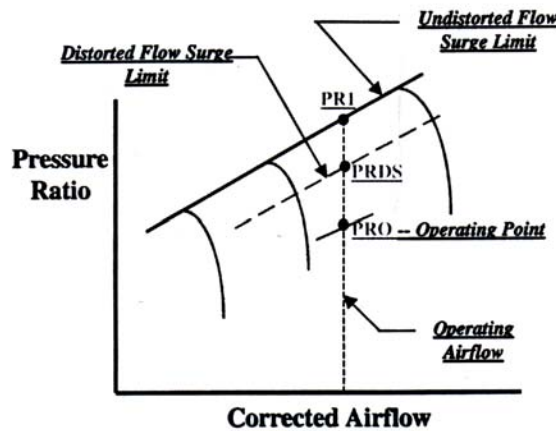


Figure 1-4: Compressor map showing the loss in surge limit caused by a distorted inlet flow [ARP-1420, 2002].

The long-term effects associated with inlet distortion are aeromechanical in nature and could result in the excitation of blade vibratory modes leading to high cycle fatigue. High cycle fatigue (HCF) is defined as “metal fatigue that results in cracking or fracture from a large number of stress cycles well below the yield strength of the material”. Several hundred incidents of varying severity have occurred in U.S. Air Force aircraft engines since the late 1960s [Air Force Scientific Advisory Board, 1992]. Most of these incidents have been attributed to HCF. Due to the high number of HCF related incidents, the Air Force declared the elimination of HCF as their number one priority in the 1980s. Previous research has shown total pressure distortion to be the dominant HCF driver in aero engines [Manwaring et al, 1997]. Since current modeling techniques allow for total pressure distortion magnitudes to be directly related to blade vibratory response, the prediction of downstream distortion patterns from an upstream

measurement would allow for the inference of the vibratory response of downstream blade rows to an inlet total pressure distortion. This provides the motivation for my research.

The goals of my research are as follows: (1) create a semi-empirical model in order to predict total pressure distortion transfer in fans and compressors; (2) extract the frequency components of the non-uniform pressure profiles to enable the prediction of blade response; and (3) use the combined pressure and blade response predictions as a tool to identify potential HCF problem areas. This work presents the development and subsequent testing of a modeling technique that is based on nonlinear Volterra theory. The emphasis of this research will be placed on the accurate prediction of the magnitude of the dominant frequency content associated with total pressure distortion transfer. The goal is to be able to make this prediction to within a 20% error at any point along the blade of the compressor. This error rate was chosen to coincide with the Integrated High Performance Turbine Engine Technology (IHPTET) program's goal of blade vibratory stress prediction to within 20% error anywhere on a blade.

2 Literature Review

The history of experimental and analytical research devoted to better understanding compressor performance to varying inlet conditions is extensive, dating back to the late 1950s. As will be shown in the subsequent section, most of this work has focused on the change in compressor performance as caused by non-uniform inlet flow, specifically the reduction in stall margin and pressure rise. More recently, the aeromechanical effects (blade vibratory response) of a compressor rotor to non-uniform flow have received a growing amount of attention.

Despite significant gains made to date, there still exists the need to further our understanding of compressor aeromechanical response to a non-uniform inlet flow. Many different modeling techniques have been developed in this area, with several of them discussed in this chapter. All techniques discussed in this chapter have had varied success coupled with certain limitations or assumptions that must be satisfied. Moreover, the application of nonlinear Volterra theory as an aerodynamic response modeling method will be introduced and reviewed.

2.1 Inlet Distortion Effects on Compressor Performance and Blade Response

In the mid 1970's Danforth [1975] realized that the effects caused by an inlet distortion on compressor stall margin and blade response can be dramatically different. He examined several mechanisms that have the potential to excite blade vibration including circumferential total pressure distortion. Through this examination, he discovered that a high-intensity narrow-sector distortion, despite being too small to affect surge margin, was capable of generating severe resonant response in rotor blades and stator vanes. Danforth also stated that the primary mechanism to instigate blade vibration was the

coupling of an aerodynamic forcing function – circumferential total pressure distortion being the primary one considered – with a natural mode of the blade. The severity of the response depends upon the effectiveness of energy input to the blades. These findings led Danforth to define a distortion index for blade vibration to be used as a design alert to potential vibratory problems.

Following the same school of thought as Danforth [1975], Longley and Greitzer [1992] summarized two different types of distortion indices, the “K” series and the $DC(\theta_{crit})$. Both of these classify the severity of the distortion as a function of the size of the total pressure region that is below the average inlet value. The two indices differ in that the “K” series defines the distortion using all of the distorted sectors while the $DC(\theta_{crit})$ indices uses only the sector with the strongest intensity.

Reid [1969] performed a series of experiments where he examined how a compressor’s performance varied with different inlet distortions. Here he defined the angle of spoiling, which is the angular width of the low total pressure region. Figure 2-1 illustrates how the surge delivery static pressure varies as a function of the angle of spoiling. It also shows that there is little change in the surge margin beyond a certain “critical angle”. Figure 2-1 also shows the effect of sub-dividing the total angle of spoiling into different numbers of equal sections. This figure showing the effect of sub-division also demonstrates that the greatest effect on peak pressure loss is when there is only one distorted section.

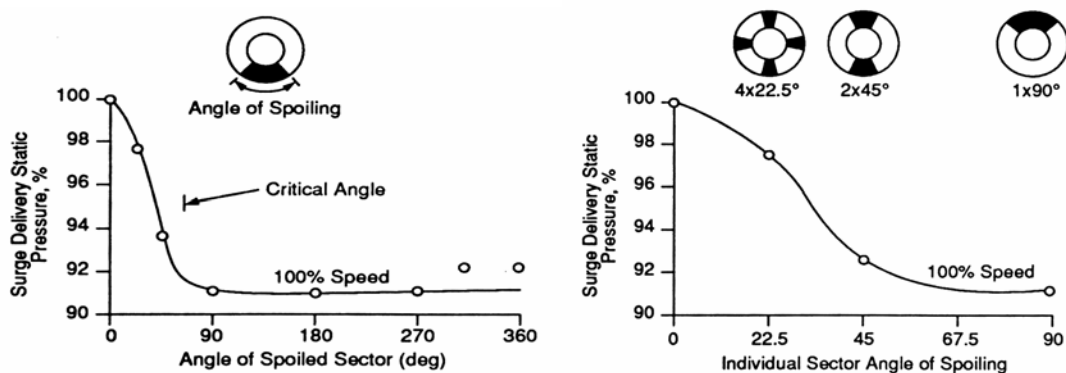


Figure 2-1: The effect on surge delivery static pressure of spoiled sector width and of sub-dividing the spoiled area [Reid, 1968].

The Campbell diagram, named for Wilfred Campbell [1924], is the primary tool used to indicate areas where resonance (blade vibration at its natural frequency) may occur. The Campbell diagram graphically displays the natural frequency of various modes of vibration of a blade overlaid on the forcing frequency or “# per-rev” lines of that compressor. The crossing of a natural frequency line by a “# per-rev” line indicates a critical speed for a compressor. The stiffening effect of centrifugal loading can significantly increase the natural frequencies of a blade as the rotational speed increases. Figure 2-2 from Manwaring et al. [1997] shows a Campbell diagram for a typical blade. Four natural frequency lines are shown: 1st Flexural, 2nd Flexural, 1st Torsional, and 3rd Flexural. The forcing frequency lines are the straight slanted lines. They are an indication of the number of distortions or defects per revolution of a blade, hence the name “# per rev”, and increase linearly with rotational speed. Figure 2-2 from Danforth [1975] shows that vibratory stress magnitude is directly related to the intensity of the distortion.

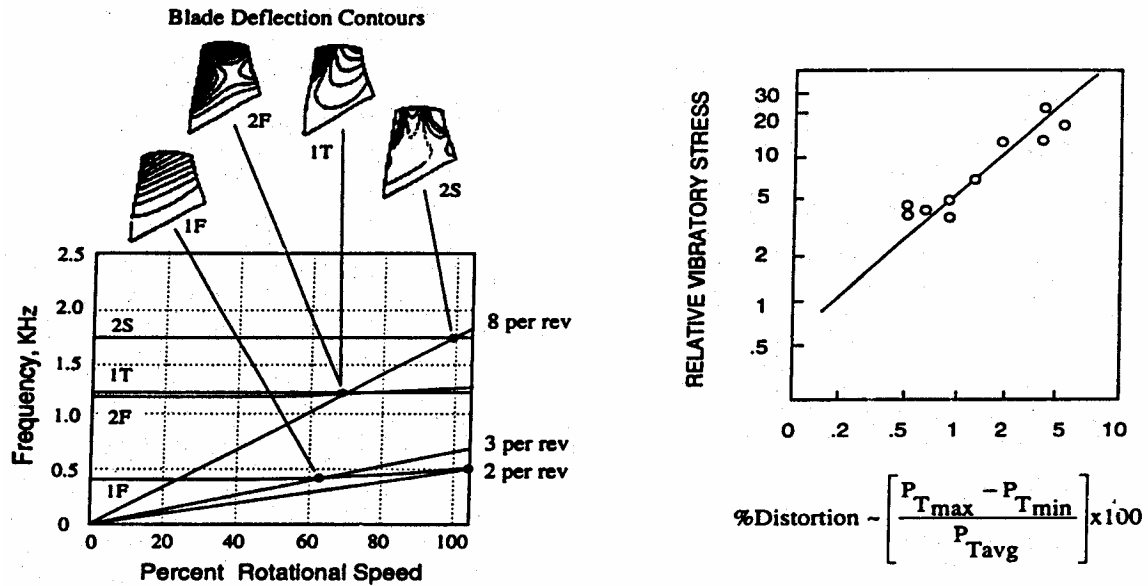


Figure 2-2: Campbell Diagram [Manwaring et al., 1997] and the variation of blade vibration amplitude with the intensity of the distortion [Danforth, 1975].

Peacock and Overli [1975] measured the unsteady normal force at mid span of a lightly loaded low speed compressor as the rotor passed through a steady circumferential distortion. Two different types of distortions were used: a square wave distortion created

by a screen of uniform porosity, and a sine wave distortion that was created by a screen of graduated porosity. It was shown in the results that the blade had a more violent response to the square wave than to the sine wave distortion. Suggested was a correlation between the time rate of change of the axial velocity and the normal blade coefficient.

Lecht and Weyer [1976] performed a similar experiment on a subsonic (LP) and a transonic (HP) compressor. The blade force measurements were taken at various locations around the circumference of the compressor relative to the spoiled, or low total pressure, area. Results indicated that the maximum blade loads were reached upon first exiting the low pressure or spoiled area. Minimum loads were experienced when the blade first entered the distorted section.

Datko and O'Hara [1987] tested a transonic compressor's response to seven different inlet total pressure non-uniformities created with distortion screens. The measured response to the various distortions was compared with two "clean" inlet configurations that were also part of the test. The first stage of the compressor was fitted with an integrally bladed disk (blisk). Of primary interest was the blisk's vibratory response to the various inlet distortions. The results indicated that the blisk did experience severe resonant stresses when exposed to inlet distortion. All major resonances were in the first three natural modes of vibration. A blisk is one solid piece of material that is formed into a complete compressor stage, as opposed to a conventional stage where the blades are individually attached to a solid central piece of metal. Because of the way it is made, a blisk has low mechanical damping, which contributes to its high level of vibratory response. The first stage of the compressor used for my research also contains a blisk.

Manwaring and Fleeter [1989, 1990] investigated the rotor blade row unsteady aerodynamics caused by an inlet distortion. In this study, they included the effects of steady loading and various aerodynamic forcing functions on the blade row. Gust amplified two-per-revolution inlet distortions were generated as the aerodynamic forcing function and the resultant blade surface pressures and the aerodynamic response of the rotor were examined. All

measurements were transformed into the frequency domain by means of Fourier decomposition. As is to be expected, the second harmonic was the dominant harmonic in all tests, with the amplitude of higher harmonics increasing with gust amplification.

Manwaring et al. [1997] performed a series of experiments on the low-aspect-ratio, transonic, first-stage blade of a two-stage fan. Two types of inlet flow distortions, a 3/rev and an 8/rev, were created with screens. The resultant unsteady blade loading was measured with on-blade pressure transducers and the vibratory response recorded with blade-mounted strain gages. This was the first time that all aspects of the forced response of a compressor stage were incorporated in an experiment. Blade resonance, the crossing of a natural frequency line by a “# per rev” line, was reached at three points. Results showed the distortions to be strongly vortical and while the steady flow matched modeling methods well, more understanding is needed of the unsteady flow to enable accurate prediction of the unsteady blade stresses associated with it.

Greitzer et al. [1994] examined the effect that a non-uniform inlet flow has on the aeromechanical excitation of a compressor and the stability of the overall compression system. Flutter, a self-excited aeromechanical instability, and forced response were investigated in the area of aeromechanical excitation. In Greitzer’s study, it was noted that several hundred incidents of varying severity had occurred in U.S. Air Force aircraft engines since the late 1960’s [Air Force Scientific Advisory Board, 1992]. Most of these incidents were attributed to high cycle fatigue (HCF). Greitzer et al. also stated that more work is needed in two areas: the prediction of aerodynamic forcing functions that can cause blade excitation possibly leading to HCF, and a better understanding of the stage—to—stage transfer of inlet distortions in multistage machines.

2.2 Aerodynamic Performance Modeling Techniques

The ability to accurately model a compressor’s performance degradation caused by distorted inlet flow is very important. An accurate model, when used in lieu of engine testing, is capable of reducing development time and hardware costs, resulting in large cost savings. Computational fluid dynamics (CFD) is capable of providing such an

ability at the expense of being very time consuming and computationally intensive. A simpler and faster modeling method capable of accurately predicting compressor performance would be of great value. Many modeling methods exist that meet the first criterion, most of them having been developed before the advent of CFD. However, as compressor performance margins increase, so do their expected life spans. For that reason, the second criterion is becoming more and more elusive. This section discusses various techniques, starting with parallel compressor theory, that have been developed to model a compressor's aerodynamic performance.

Pearson and McKenzie [1959] originally developed the parallel compressor theory. The parallel compressor model is based upon dividing the distorted compressor into two or more hypothetical compressors, or flow fields, operating in parallel. The operating point of the distorted compressor is equal to the averaged operating points of each of the individual hypothetical compressors. Parallel compressor theory relies on five critical assumptions, or restrictions: (1) the distorted compressor consists of two or more independently operating sub-compressors; (2) all sub-compressors have individually uniform inlet conditions and operate on the undistorted compressor characteristics; (3) no circumferential cross-flow exists between sub-compressors; (4) exit static pressure of all sub-compressors is equal; and (5) the entire compressor stalls when an individual compressor reaches the undistorted stall pressure ratio. Figure 2-3 provides an illustration depicting a parallel compressor model using two hypothetical flow fields.

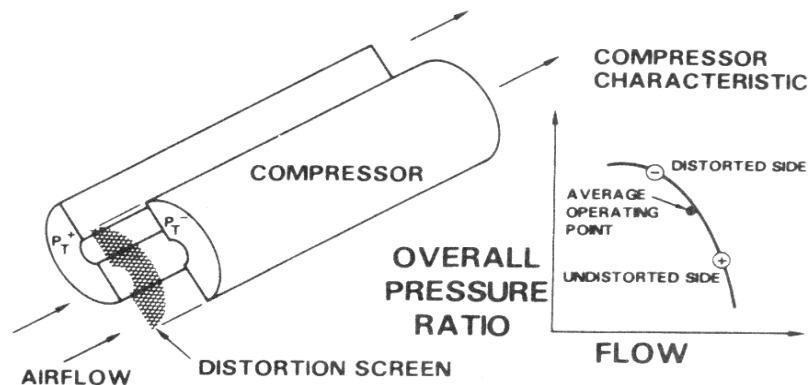


Figure 2-3: Pictorial representation of parallel compressor theory [Reid, 1969].

Many modeling techniques have been developed that concentrate on either reducing the number of assumptions required or improving the results obtained from the parallel compressor model. Roberts et al. [1968] found that the assumption of no circumferential cross-flow caused the predicted waveform to have a square-wave shape, which, especially in downstream stages, is not the case. As can be seen in Figure 2-4, the actual downstream flows vary appreciably from a square-wave.

Roberts et al. [1968] also varied rotor and stator chord lengths in order to investigate blade response time to a disturbance. These tests revealed that compressor rotor blades with longer chord lengths are more tolerant to distortion, suggesting that blade response to an inlet distortion is not immediate. This time lag in blade response to a distortion is more than likely due to downstream effects and the fact that a pressure disturbance takes a certain amount of time to travel through the blade passage. Roberts et al. introduced a reduced frequency parameter in order to define this time dependency.

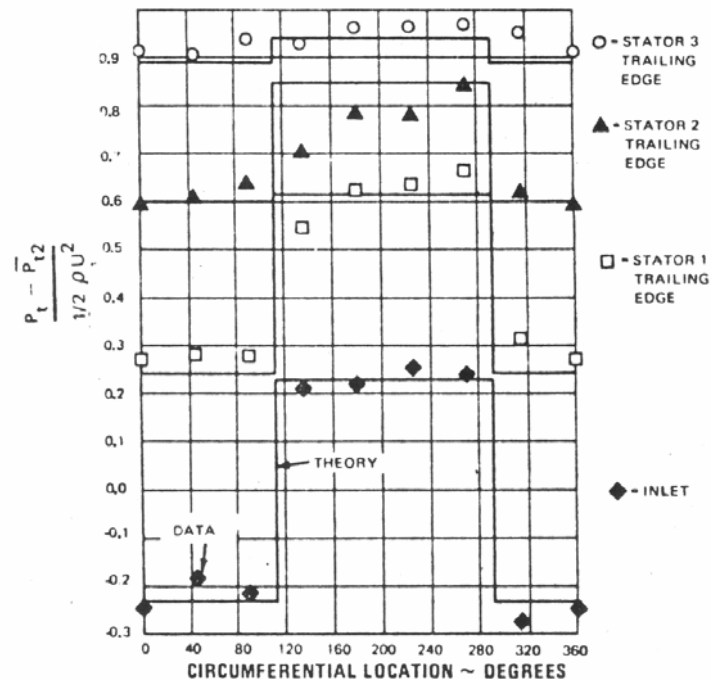


Figure 2-4: Deviation of flow from predicted square-wave pressure pattern [Roberts et al., 1968].

Adamczyk [1974] developed a model that improved upon the original parallel compressor theory. His model did not require exit circumferential static pressure to be

constant and also allowed for circumferential cross-flow to exist. In addition, Adamczyk's model could also handle large amplitude distortions, which the original parallel compressor model was unable to do. Adamczyk's problem was that there was no experimental data available to make a direct comparison with his model's predictions.

Significant improvements to parallel compressor theory were made by Mazzawy [1977] by replacing the original sub-compressors with pseudo-streamtubes. This method increased the circumferential resolution as well as reduced the number of restrictions from five to one. The only restriction required in Mazzawy's model was that the distortion's circumferential extent covered several blade passages. Mazzawy used a first-order decay equation with an empirically derived time constant to model blade response to distortion whereas original parallel compressor theory assumed the blade responded instantaneously. Figure 2-5 shows prediction results from Mazzawy's model and the original parallel compressor model as compared with experimental data. Mazzawy's model, represented by the solid line, does a better job of predicting compressor response than the original parallel compressor theory.

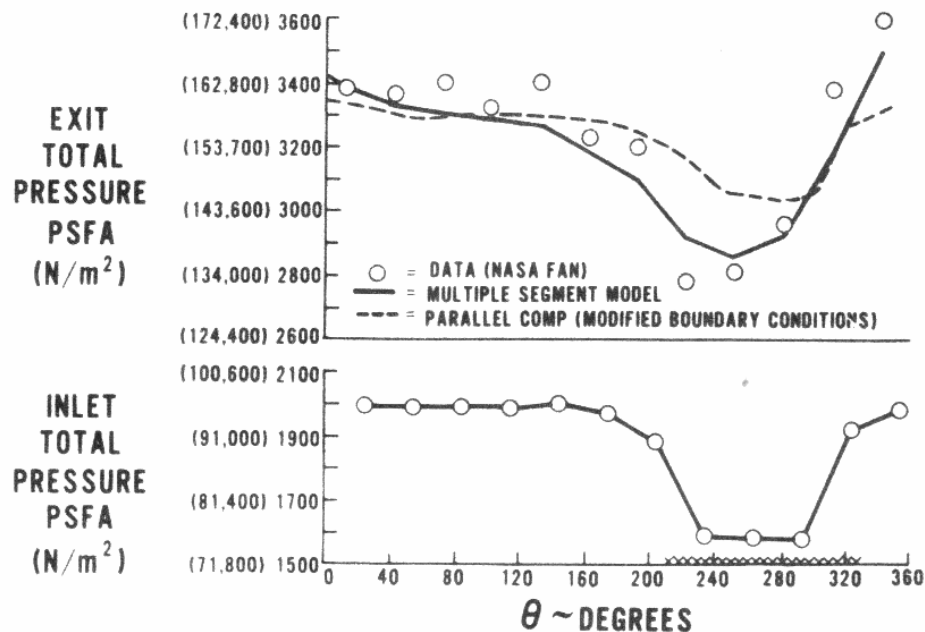


Figure 2-5: Multiple stream-tube model versus parallel compressor theory
[Mazzawy, 1977].

Melick [1973] developed yet another modification to parallel compressor theory by combining it with a time-dependent lift coefficient. His model was similar to a spring-mass-damper system with a second order equation describing the lift coefficient, with the two time constants being determined empirically. Lecht [1986] improved this approach when he added the concept of lift overshoot to the model. Lift overshoot occurs when an airfoil momentarily exceeds its maximum lift coefficient without stalling. One result of the approach used by Melick and Lecht was the definition of a time domain transfer function of exponential decay between steady state and the effective angle of attack. Figure 2-6 illustrates the comparison of the exponential decay function to the actual step input.

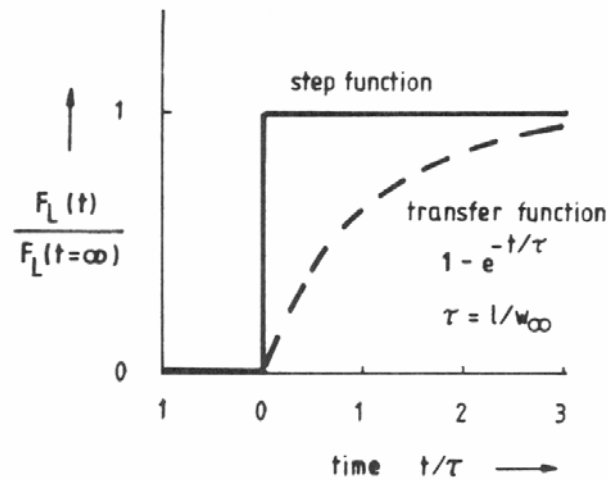


Figure 2-6: Exponential decay transfer function [Lecht, 1986].

Another technique used for compressor modeling uses an actuator disk in place of a compressor's blade row. Greitzer [1973] was the first to use this method and with it was able to include the circumferential velocities and the pressure rise caused on the flow by the compressor stage in the evaluation. With this method, Greitzer was the first to model compressor rotating stall and surge and therefore was able to mathematically describe an experimentally observed problem in turbomachinery.

Barr [1978], Henderson and Shen [1981], and Colpin and Kool [1978] also used the actuator disk modeling method. Barr and then later Henderson and Shen examined the effect of sinusoidal disturbances and found that the maximum distortion attenuation occurred when the ratio of blade spacing to distortion wavelength was one half. Colpin

and Kool derived a transfer function to model total enthalpy change over the disk. This derivation enabled the prediction of the exit total pressure, which was compared to experimental measurements, as shown in Figure 2-7.

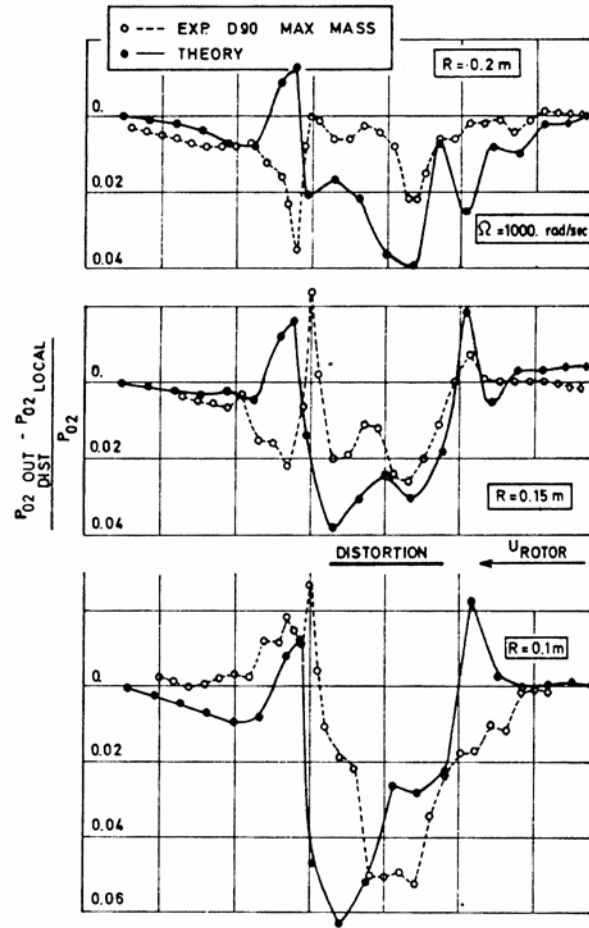


Figure 2-7: Actuator disk total exit pressure predictions compared with experimental measurements [Colpin and Kool, 1978].

The first nonlinear stall model using an actuator disk was proposed by Nagano and Takata [1970]. In their model, they used the non-linear equations of motion coupled with the blade row characteristics to obtain a finite difference solution using a digital computer. Sexton and O'Brien [1981] improved this method by introducing frequency response functions that were used with a semi-actuator disk model to predict the rotating stall behavior of an experimental compressor. The development of the frequency response functions used the quasi-steady total pressure loss as the forcing function and

the dynamic total pressure loss as the response function. Cousins and O'Brien [1985] used the same approach in the development of a post-stall compressor model. In this model an experimentally derived transfer function driven by the quasi-steady total pressure loss variations was used to calculate dynamic loss response.

Rabe et al. [1995] examined the effects on a transonic fan blisk as caused by various circumferential distortion patterns. Investigated were circumferential distortions of 2, 3, and 8 per revolution. Blade response was measured using high frequency pressure transducers mounted in the blade, enabling the investigation of the distribution along the chord of the blade's response. Manwaring et al. [1997] used this same test data to characterize the unsteady aerodynamic forcing function and the blade response as discussed in section 2.1. Hah et al. [1998] modeled the same experiments as Rabe and Manwaring by solving the Reynolds-averaged Navier-Stokes equations with a numerical solution. The predictions of Hah's model were then compared with the experimental data with good prediction results for uniform flow. There was a problem, however, predicting the unsteady blade pressure distributions that resulted from a non-uniform inlet flow. Rabe et al. [1999] went on to extend Hah's numerical procedure to generate a full annular solution with similar results.

Small [2001], Luedke [2001], and my work also use the data from Rabe et al. [1995]. Small [2001] used a frequency response function modeling technique entitled the "Tuned FRF Method" in which frequency response functions are "tuned" to the operating conditions and properties of the inlet flow field. Luedke [2001] created a model based on nonlinear Volterra theory, which is discussed more in depth in the next chapter. Small's, Luedke's, and my work are all designed to predict the transfer of an inlet pressure circumferential distortion. In Chapter 7, the results of Small's and Luedke's models will be compared with the results of my study.

Hale and O'Brien [1998] developed the Turbine Engine Analysis Compressor Code (TEACC). This method uses information calculated by a streamline curvature code regarding mass flow, blade forces, and shaft work. TEACC uses this information to solve the conservation equations, building a three-dimensional grid representing the full annulus of the compressor as shown in Figure 2-8. In this grid, the three-dimensional Euler equations allow the interaction of circumferential and radial control volumes with

one another. TEACC provides the ability to model distortion that is moving; however, TEACC's capabilities are limited to steady-state conditions [Davis et al., 2000].

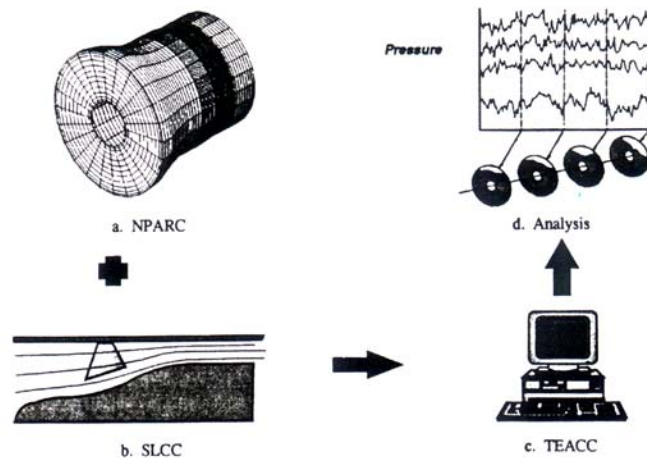


Figure 2-8: TEACC methodology [Davis et al., 2000]: (a) three-dimensional grid built from the conservation equations (b) streamline curvature code calculates mass flow, blade forces, and shaft work (c) digital computer combines a & b to solve the conservation equations and (d) model distortion in steady-state conditions.

2.3 Conclusions from Literature Review

Over the last 40 years there has been a great deal of work devoted to the understanding and modeling of compressor response to non-uniform flow. One has only to do a search for inlet distortion or high cycle fatigue in an Aerospace and High Technology database to see that there is a wealth of information about the two related subjects. While an understanding exists of a compressor's basic performance response to inlet distortion, more knowledge is needed in the areas of distortion transfer and aeromechanical response as it is related to high cycle fatigue. The preferred method to obtain this information is through numerical modeling, often in the area of Computational Fluid Dynamics (CFD) that is capable of providing accurate information in less time at a lesser cost than an actual test of the compressor in question.

CFD harnesses the calculating power of computers to solve complex three-dimensional equations describing a fluid flow. While CFD is capable of accurately predicting compressor response in uniform flow and advances continue to be made in the

area of non-uniform flow response prediction, more development is needed before it can be relied upon as a prediction tool in the design process. Drawbacks of CFD are its computational complexity and the large amount of time required to solve for each inlet condition. Solving for just one inlet condition with CFD could take hours to days. Solving for a number of inlet conditions, as would be required in the design process, could take months and cause significant delays in production.

The option most commonly exercised when developing a new compressor design uses the ever-growing database of knowledge gained through experience and a comprehensive testing program. Every company has its own database of information pertaining to every type of compressor rotor they have ever built. Subsequently, a new design dramatically different or outside of a statistical “comfort zone” offers quite a few unknowns and requires rigorous testing throughout the entire design process. Part of the testing procedure of a new rotor design involves creating various types of inlet pressure distortions with screens and measuring inlet and outlet total stage pressure as well as blade response, as was done in many of the experiments discussed in the previous section. Figure 2-9 shows some typical screen designs used as distortion generators. As can be imagined, the testing process can be time consuming and costly.

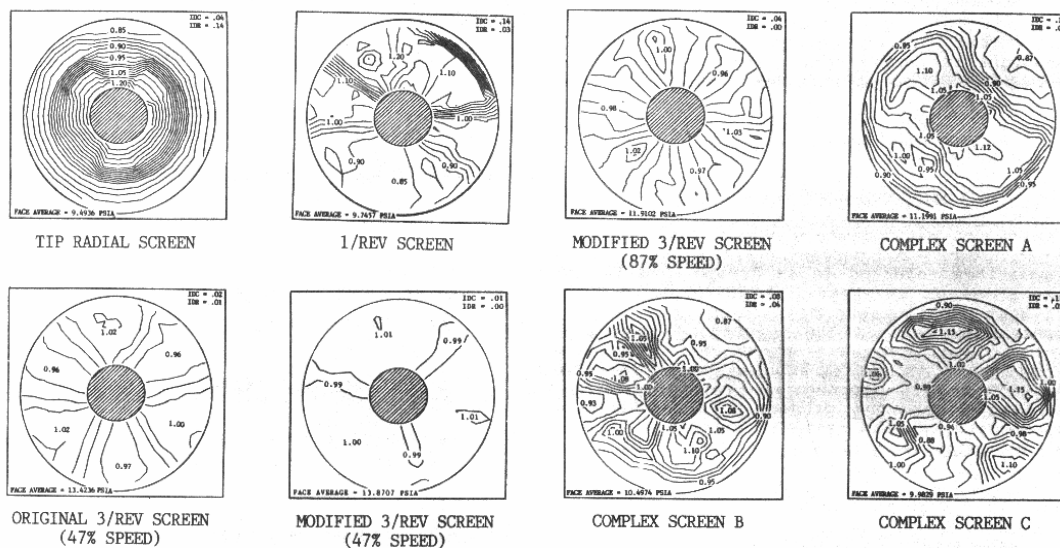


Figure 2-9: Distortion screen designs to generate total pressure non-uniformities [Datko et al., 1987].

In the rapidly changing world of high technology and high competition, every dollar saved without the sacrifice of quality or safety in the production of a better rotor is important and needed. For this reason, a modeling method that would be capable of accurately predicting the response of a rotor to varying inlet conditions in uniform and non-uniform flow would be of great benefit. It would provide an even greater benefit if this modeling method was simple to use and able to make predictions in minutes to a few hours as opposed to hours to a few days. While these goals are ambitious, it is not unrealistic to believe that as the power of computers continues to increase rapidly, such a modeling method or capability will one day exist. The use of nonlinear Volterra theory in aerodynamic response modeling offers some of these desired abilities. The next chapter discusses nonlinear Volterra theory, its development, and its history as an aerodynamic response modeling method.

3 Nonlinear Volterra Theory Modeling

The first section of this chapter will start with the development of nonlinear Volterra theory in the early 1900's and then jump to more recent times when it has started to be used in aerodynamic modeling. The second section explains in more detail the heart of Volterra theory, its kernels, and the chapter ends with a discussion of the system requirements necessary in order to use Volterra theory as a modeling method.

3.1 Nonlinear Volterra Theory

Vito Volterra, an Italian mathematician who lived from 1860 until 1931, developed nonlinear Volterra theory in the early 1900's [Volterra, V., 1930]. During that time he published papers on partial differential equations, but his most famous work was done on integral equations, which became known as integral equations of the Volterra type. Nonlinear Volterra theory states that any time-invariant nonlinear system can be modeled as an infinite sum of multidimensional convolution integrals of increasing order. The series is represented symbolically as shown in Equation 3.1.

$$y(t) = \int_0^{\infty} h_1(\tau_1)x(t-\tau_1)d\tau_1 + \int_0^{\infty} \int_0^{\infty} h_2(\tau_1, \tau_2)x(t-\tau_1)x(t-\tau_2)d\tau_1d\tau_2 + \dots$$
$$\int_0^{\infty} \dots \int_0^{\infty} h_n(\tau_1, \dots, \tau_n)x(t-\tau_1)\dots x(t-\tau_n)d\tau_1\dots d\tau_n$$

Equation 3-1

In the equation, $x(t)$ represents the mean-zero input into the system while $y(t)$ is the output, or system response. As can be seen in the above equation, both the input and output of the system are functions of time (t) and time lag (τ). Another way of describing this type of system is as a system “with memory”. The memory of a system is a measure of the time required for the system to completely recover from an impulse. Convolution is used to predict the exact response of the system to an input.

Each term in the Volterra series contains a kernel, denoted by the h terms in the equation, also known as the impulse response function of the system. The first term in

the series represents the linear response of the system. Each additional term represents the next successive response of the system, or the number of impulses that act upon the system before it recovers. The second term represents the way the system responds to two inputs, the only time requirement between these inputs being that the second one happens before the system has recovered from the first. Once the kernels of a system are known, the response of the system can be calculated for any arbitrary input.

A third order system is pictorially represented in Figure 3.1. Each of the first three terms in a Volterra series representation of this system would account for each order response within that system. The linear or first order term represents the mean response of the system. Each higher order term accounts for variations about that mean with the addition of all three responses being the system output.

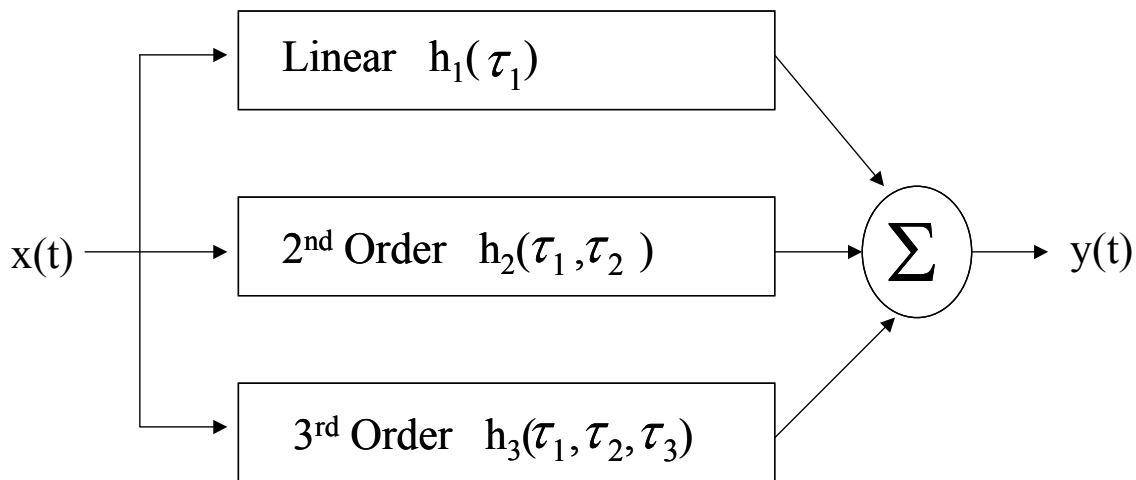


Figure 3-1: Third order system representation [Bendat, 1998].

In order to successfully use the Volterra series to model a nonlinear system, the system needs to be “weakly” nonlinear. This means that the higher order terms within the series quickly drop off to approximately zero so that their effects are negligible. Most causal systems fit within this description [Tromp and Jenkins, 1990]. A system is considered to be causal if the response of the system to any impulse does not depend on the future impulses. Restated, the response of the system at time (t) to a signal applied at time (τ) depends only on the amount of time between the two, ($t - \tau$). All known physical systems are causal.

Volterra theory has seen little use outside of the Electrical Engineering and Biological fields. Not until the last 15 years has Volterra theory started to be used in aerodynamic modeling. This is primarily due to the fact that in the past linear modeling methods provided acceptable accuracy and were much easier to use than nonlinear ones. As the performance of modern day compressors continues to increase as well as their expected life spans, linear methods are no longer adequate. In addition, with the advancement of computers, methods that were once too complex and time consuming to consider are now much more feasible.

Boyd et al. [1983] developed a method to measure the second-order Volterra kernel of a weakly nonlinear system. Boyd et al. defined a weakly nonlinear system similarly to what has been previously discussed, with the additional requirement that the nonlinearities that do exist must be subtle, less than 40 dB. Examples of this type of system are simple communication systems, some high quality transformers, and electro acoustic transducers. This method involves applying a multitone-probing signal to the system being analyzed and uses an interpolation method to estimate the second order response of the system, thereby providing a measurement of the second order kernel. While this is not an example of aerodynamic modeling, this work is referred to in future aerodynamic applications of Volterra theory.

A Volterra kernel identification method originally developed for use in electrical circuits was employed by Tromp and Jenkins [1990] to model nonlinear aerodynamic behavior over a 2-D airfoil. The procedure involved exciting the system with very specific inputs, recording the system response, and then calculating the kernel association with that response. Initially, an input was used employing a small angle of attack to insure linear system response. A pencil of functions (POF) method was then utilized to identify the system's linear kernel. After the linear kernel was known, the system was excited with another input in such a way that third order and above effects were negligible. Since the linear impulse response had just been solved for, the difference between the system's response to the second input and the previously calculated linear response was the second order kernel of the system. This method, despite being successful, is extremely limited by the input types that can be used and, obviously, could

not be used with wind-tunnel models or flights tests where the order of the system response is not known.

Silva [1993] identified the linear and second-order kernels of a NACA 64A010 rectangular wing undergoing pitch using a numerical kernel identification technique based on impulse responses. Airflow over the wing was modeled using a finite-difference computer program; the output from this program due to specific unit impulses was used to calculate the two kernels of the system. Silva [1997] continued his research by using digital filter techniques to identify linear and nonlinear aerodynamic impulse responses. In this paper Silva states that the aerodynamic impulse response function is the most fundamental and computationally efficient aerodynamic function that can be extracted from an aerodynamic system. He goes on to state that once the unit impulse response is identified, the output of the system to any input can be calculated via convolution. He also shows how the first two terms in a Volterra series can be used to calculate the system output using the earlier identified linear and second-order impulse response functions. As is the case in the other methods discussed so far, despite encouraging results, neither of these methods would be applicable with wind tunnel or flight tests.

In 1999 Patrick Reisenthel developed a method to identify Volterra kernels which uses “physically realizable inputs, is robust with respect to noise, and minimizes or eliminates the need for analytical assumptions”. Reisenthel [1999] states that the identification of impulse response functions from experimental data is a poorly posed problem. A poorly posed problem cannot be solved using straightforward methods, the result would be that the problem either has no solution whatsoever, or it has more than one. Neither of these alternatives is acceptable in that the one “unique” solution is what is desired. Reisenthel employed regularization methods developed in other fields such as radar detection, mathematical biology, and astronomy in order to overcome this difficulty and successfully used this method to model airflow over a wing. He goes on to show that once the kernels of the system are identified, the prediction of the system’s response to any novel maneuver is possible.

3.2 Volterra Kernels

The kernels of a system characterize the system's response to an impulse or a group of impulses. In the Volterra series representation, the h terms denote the linear and nonlinear kernels. The first term in the series represents the linear response of the system to an impulse at time τ_1 . τ_1 is a “dummy” variable that is used to represent time. The linear response of the system occurs at time t to an impulse that occurred at time τ_1 , $(t - \tau_1)$ representing the response of the system over time. This is why the Volterra series is sometimes referred to as a way to model a system with “memory”.

The second order kernel, $h(\tau_1, \tau_2)$, defines the system's response to two impulses occurring at different times, τ_1 and τ_2 . Even though these two impulses have subscripts one and two, that does not imply that there is a definite order in which they must take place. The only requirement regarding the times that these impulses occur is that the second one happens before the system has recovered from the first.

Taking this one step farther, the system's third order kernel $h(\tau_1, \tau_2, \tau_3)$ characterizes the way the system reacts to three unit impulses, each occurring at a separate time, but all three acting on the system before it has recovered from any one of them. The modeling methods used in this research will not go above a third order kernel for two reasons. The amount of data required to accurately define a fourth order kernel is not available and, the basis of this method is that the system is a weakly nonlinear system, meaning that the higher order kernels fall off to zero very quickly.

3.3 System Requirements for Volterra Series Modeling

The first requirement of a system to be able to use a Volterra series technique to model it is that the system must be physically realizable. A physically realizable system's input, output, and impulse response functions are all real valued functions occurring over time. Causality is also a requirement. To define a system as causal simply means that the system cannot respond before the input occurs, therefore, the impulse response functions, or kernels, of the system have a value of zero for $\tau < 0$. The last requirement is that the system be time-invariant. At first glance this may seem to be a contradiction to the first requirement of time dependent input, output, and response functions; it's not. A time-

invariant system is one whose properties do not change over time. Another way of looking at this requirement is that the basic system properties, the impulse response functions or kernels, do not change, hence the term time-invariant. These three requirements, although very important, are not difficult to meet as most real world systems satisfy all three.

4 Identification of Volterra Kernels

Generally stated, and reviewing from the previous chapter, the Volterra theory of nonlinear systems states that any physically realizable nonlinear system may be represented as a series of multidimensional integrals (see Equation 3.1). In the below equation $y(t)$ represents an aerodynamic quantity of interest (stage exit total pressure), $x(t)$ is the stage inlet total pressure, and $h(\tau)$ represents the system's impulse response functions (the kernels of the system).

$$y(t) = \int_0^{\infty} h_1(\tau_1)x(t-\tau_1)d\tau_1 + \int_0^{\infty} \int_0^{\infty} h_2(\tau_1, \tau_2)x(t-\tau_1)x(t-\tau_2)d\tau_1d\tau_2 + \dots$$
$$\int_0^{\infty} \dots \int_0^{\infty} h_n(\tau_1, \dots, \tau_n)x(t-\tau_1)\dots x(t-\tau_n)d\tau_1\dots d\tau_n$$

Equation 3.1

In order to facilitate the use of Volterra theory as a modeling method, the assumption is made that the value of the higher order kernels falls to zero very quickly [Tromp and Jenkins, 1990]. This is known as a weakly nonlinear system. Boyd et al. [1983] extends this definition even further by stating that the nonlinearities of the system must be subtle (less than 40 dB distortion). According to Silva [1993], for many aeroelastic and vibration analyses, these assumptions are appropriate.

This chapter starts by discussing the three basic categories of kernel identification methods used before 1999. A fourth category or method of kernel identification will then be explained. This fourth method was developed by Patrick Reisenthel [1999] and is used in my research. This technique is based upon expanding the unknown kernel into basis function space. The various basis functions used will be covered along with a more detailed look at the linear and higher order kernels and their identification using Reisenthel's extraction method.

4.1 Volterra Kernel Identification Methods

In the past, methods used to identify Volterra kernels typically fell into one of three categories: “direct” methods, “optimization” methods, and “active probing” or “measurement” methods. Reisenthel [1999] developed a fourth method, an “indirect” technique designed to identify the kernels of a system from unsteady aerodynamic data. The first three categories will be discussed in this section. The fourth method will be introduced with a more detailed explanation following in the next section.

“Direct” methods are very straightforward, therefore the name “direct”, and involve applying pulse or step inputs to the system. The system’s response to a single pulse or excitation is used to determine the linear kernel $h_1(\tau_1)$. Similarly, applying two pulses to the system enables the second order kernel, $h_2(\tau_1, \tau_2)$, to be constructed. This is the method used by Silva [1993, 1997] in his research as discussed in the previous chapter.

“Optimization” methods involve assuming the form of the kernel and then identifying the unknown coefficients through parameter identification. Optimization methods are typically done in either the time or Laplace domain. Tromp and Jenkins [1990] pencil of functions method falls into this category. Tromp and Jenkins research was done in the Laplace domain.

The third category of methods, “measurement”, requires very specific, predetermined excitation inputs be applied to the system in order to “probe” its structure. These methods can be either statistical or deterministic in nature, and, for the most part, have been developed in the electrical engineering field. One technique that falls into this category is that of kernel separation. Kernel separation can be done in the time and frequency domain and involves making repeated measurements with different excitation amplitudes. Boyd et al.’s [1983] multiple harmonic probing, done in the frequency domain, is an example of this type of method.

Reisenthel [1999] developed the fourth method of “indirect” kernel identification, where the unknown kernels are “extracted” from existing aerodynamic data not necessarily obtained with the goal of kernel identification. The goals for the development of this technique were as follows: the method must use physically realizable inputs, must

be applicable to existing data, and it should minimize or eliminate the need for any assumptions about the form of the kernels. Reisenthel successfully applied this technique to wind-tunnel data of a maneuvering aircraft and believes that the technique would also be useful for the identification of Volterra kernels in aeroelastic systems.

Indirect kernel identification is an inverse problem, where the goal is to solve for the transfer function that produces an already known output from the input that was introduced to the system in question. In its simplest form, this type of problem is an easy one and can be solved through basic division. However, when dealing with aerodynamic data, there are many more factors and unknowns to deal with and one finds that there is either no exact solution for the data in question or that there are multiple solutions which will produce the already known output. Neither one of these options is desirable, as the goal is to solve for the one unique solution to the problem in question. This is known as an ill-posed problem, and is a result of having to solve integral equations similar to those in inverse scattering problems. A straightforward attempt to solve these equations would result in nonsense; however, in recent years regularization methods have been invented that enable this difficulty to be overcome. These methods have been used successfully in radar detection, medical imaging, mathematical biology, astronomy, optics, geophysics and tomography [Hansen, 1998].

4.2 Indirect Extraction Technique

As previously mentioned, this kernel “extraction” technique is designed to identify the Volterra kernels of a system from arbitrary experimental data that was not necessarily obtained with the goal of kernel identification. The technique is based upon expanding the unknown kernel into basis function space.

As an example, consider the identification of the Volterra kernel of a linear system. Since this system is linear, it can be exactly described by the first term in a truncated Volterra series (see equation 4-1). Since this is a physically realizable system, the limits of integration are from $t = 0$ until $t = T$, the length of the sampling period.

$$y(t) = \int_0^T h_1(t - \tau_1) x(\tau_1) d\tau_1$$

Equation 4-1

The unknown kernel, $h_1(t - \tau_1)$, is next expanded in some basis function space, $\varepsilon_j(t)$. The kernel now becomes the summation of unknown coefficients multiplied by the basis function (see Equation 4-2), and the original equation representing the system now becomes Equation 4-3.

$$h_1(t) = \sum_{j=1}^N c_j \varepsilon_j(t)$$

Equation 4-2

$$y(t) = \sum_{j=1}^N c_j \int_0^T \varepsilon_j(t - \tau_1) x(\tau_1) d\tau_1$$

Equation 4-3

In Equation 4-2 and Equation 4-3 the subscript j varies from $j=1$ to $j=N$ with N representing the number of basis functions and, therefore, the number of coefficients that need to be solved for. The unknown coefficients, c_j , must satisfy Equation 4-3 at all times. Since there are N coefficients to solve for, there must be N realizations of Equation 4-3. Each realization will look like Equation 4-4.

$$y(t_i) = \sum_{j=1}^N c_j \int_0^{t_i} \varepsilon_j(t_i - \tau_1) x(\tau_1) d\tau_1$$

Equation 4-4

In Equation 4-4, all terms behind the integration sign, the basis function and the input, are known. Therefore, the only unknowns are the coefficients, c_j . Each realization of Equation 4-4 results in one row of a matrix. The matrix will be $[i \times j]$ in size, with i representing the number of data points and j the number of basis functions. Equation 4-4 can also be representing equivalently as Equation 4-5, with a_{ij} as the matrix formed through the integration process. The final result of this process is the formation of a matrix problem similar to Equation 4-6.

$$y(t_i) = \sum_{j=1}^N c_j a_{ij}$$

Equation 4-5

$$[A][C] = [Y]$$

Equation 4-6

In Equation 4-6, $A = [a_{ij}]$ and is known as the motion matrix, $Y = [y(t_1), y(t_2), \dots, y(t_n)]^T$ is the output total pressure, and $C = [c_1, c_2, \dots, c_j]^N$ is the solution vector. This same type of equation is also obtained in the nonlinear case as well. In the case of a second-order system, two terms of a truncated Volterra series would be used as in Equation 4-7. Using a similar expansion technique for the second-order kernel would produce Equation 4-8, which, when substituted back into the original equation, would yield Equation 4-9.

$$y(t) = \int_0^T h_1(t - \tau_1)x(\tau_1)d\tau_1 + \int_0^T \int_0^T h_2(t - \tau_1, t - \tau_2)x(\tau_1)x(\tau_2)d\tau_1d\tau_2$$

Equation 4-7

$$h_2(t, t') = \sum_{k=1}^{N_2} d_k \mu_k(t, t')$$

Equation 4-8

$$y(t_i) = \sum_{j=1}^N c_j \int_{i=0}^{i=T} \varepsilon_j(t_i - \tau_1)x(\tau_1)d\tau_1 + \sum_{k=1}^{N_2} d_k \int_{i=0}^{i=T} \int_{i=0}^{i=T} \mu_k(t - \tau_1, t - \tau_2)x(\tau_1)x(\tau_2)d\tau_1d\tau_2$$

Equation 4-9

Following the same school of thought as in the linear case, Equation 4-9 could be rewritten in the form of Equation 4-10, with a_{ij} and a_{ik} representing, respectively, the results of the integrations as shown in Equation 4-9. These integrals form the first and second-order motion matrices of the problem. The unknown solution vectors $[c_j]$ and $[d_k]$ are next in-lined, forming a linear system of equations, again similar to Equation 4-6.

This is a key point in the solution process; even though the original problem is nonlinear, its solution reduces to a linear matrix problem.

$$y(t_i) = \sum_{j=1}^N c_j a_{ij} + \sum_{k=1}^{N_2} d_k a_{ik}$$

Equation 4-10

Despite the fact that a nonlinear problem has now been reduced to a much simpler linear matrix problem, its solution is still not straightforward. As mentioned previously, the inverse problem of solving for the unknown coefficients is often an ill-posed problem. This is a result of the motion matrix, $[A]$ in Equation 4-6, being singular. Since the data used to solve for the kernels is obtained through experimentation, it contains a lot of noise. Solving for the kernels from the output measurements, $y(t)$, tends to amplify the noise. This results in either more than one set of kernels being able to satisfy the equation, or none at all. Neither result is better than the other, as the goal through all of this is to find the one unique solution to the problem at hand.

Both of these difficulties (no unique solution or no solution at all) are handled by considering the solution to Equation 4-5 in the least squares sense. The requirement being that the solution vector $[C]$ is able to solve the matrix equation approximately, as shown in Equation 4-11.

$$\sum_{n=1}^{Nds} [A^{T(n)}][A^{(n)}][C] = \sum_{n=1}^{Nds} [A^{T(n)}][Y^{(n)}]$$

Equation 4-11

Another way to write Equation 4-11 is $[M][C]=[B]$, where $[M]$ is equivalent to the motion matrix multiplied by its transpose, $[C]$ is the solution vector, and $[B]$ is the transpose of the motion matrix multiplied by the output total pressure measurements. Nds in Equation 4-11 represents the total number of data sets that are being used to calculate the kernel. Equation 4-11 still cannot be solved in a straightforward manner. The goal is to find the best solution possible for the equation in question. This is done by means of singular value decomposition (SVD).

The SVD procedure works in the following manner. If $[M]$ is nonsingular, it can be broken down as the product of an orthogonal matrix $[U]$, a square diagonal matrix $[S]$, and the transpose of an orthogonal matrix $[V]$ as shown in Equation 4-12. Because of this, the vector $[C]$ can be solved for as indicated in Equation 4-13. Now, if $[M]$ is singular, the values of the diagonal matrix $[S]$ are initially large, but drop off to zero at some point with no evident pattern or way to calculate when. Since solving for $[C]$ involves taking the inverse of $[S]$, the equation becomes unsolvable once the values of the diagonals fall to zero. Thus, in order to find a “good” solution to the problem, only the nonzero values of $[S]$ can be used. The key to all of this is to decide at what point the diagonal values of $[S]$ are considered to be zero, represented in Equation 4-13 by N . In other words, one has to decide on a noise floor. This is often done as a percentage of the largest value of $[S]$; one percent is a typical choice.

$$[M] = [U][S][V^T]$$

Equation 4-12

$$[C] = \sum_{i=1}^N \frac{1}{[S_i]} ([U_i^T][B])[V_i]$$

Equation 4-13

After the solution vector $[C]$ is calculated, it's simply a matter of multiplying it by the basis function(s) to solve for the kernel(s) of the system. Providing that there was enough information in the data used to calculate the kernel(s), the response of the system to any arbitrary input can now be accurately calculated using Equation 3-1.

4.3 Choice of Basis Functions

The choice of basis functions is based on the characteristics of the data that is being analyzed. According to Reisenhel [1999], any type of basis functions can be chosen as long as a complete set of values can be formed from them. In his research, Reisenhel chose an exponential decay function as the basis function. Exponential decay functions

are a good representation of the way a physically realizable system responds to an input, with the response of the system gradually recovering to zero output as time passes.

For my research, I also chose basis functions of exponential decay. Again, the linear kernel was assumed to take on the form of Equation 4.2. The linear basis function used by Reisenthel [1999] and also in my research is shown in Equation 4-14.

$$h_1(t) = \sum_{j=1}^N c_j \varepsilon_j(t)$$

Equation 4-2

$$\varepsilon_j(t) = e^{-t/\tau_1}$$

Equation 4-14

Following this same line of thinking, the second-order kernel is also one of exponential decay. However, it involves the response of the system to two impulses occurring at times τ_1 and τ_2 . Two different forms of the second order basis function were used in my research as shown in Equations 4-15 and 4-16. Equation 4-15 shows the initial form that was considered with Equation 4-16 being a more complicated form in which $H(t_n - t_m)$ represents the Heaviside step function. The Heaviside step function is basically an on/off switch. If the operation within the parenthesis yields a positive number, the value of the Heaviside step function is one and if that same operation is negative, the step function yields a value of zero. The two forms considered for the third-order basis function are the same as that of the second-order with the addition of one more time variable, t'' or t_3 . In all, three different models were created. The higher-order basis functions of Model 1 are in the form of Equation 4-15 and Model 2 uses Equation 4.16. Both Model 1 and 2 utilize the built-in Matlab convolution function as an integration method. Model 3 also uses the Heaviside step function, Equation 16, for its higher-order basis function, but utilizes numerical integration rather than the built-in Matlab convolution function. Models 1 and 2 both are third order, meaning that they calculate the first three kernels of the system being analyzed. Model 3, due to the dramatic increase in time required to perform numerical integration, is a second order model, calculating the first two kernels from the experimental data.

$$\mu_2(t, t') = e^{-\Delta/\tau_1} e^{-t/\tau_2}$$

Equation 4-15

$$\mu_2(t_1, t_2) = H(t_1 - t_2) e^{-(t_1 - t_2)/\tau_1} e^{-t_2/\tau_2} + H(t_2 - t_1) e^{-(t_2 - t_1)/\tau_1} e^{-t_1/\tau_2}$$

$$t_1 = t - \tau_1$$

$$t_2 = t - \tau_2$$

Equation 4-16

At this point, the question may have arisen as to what exactly does a kernel look like? Each kernel characterizes the way the system responds to a certain number of impulses occurring over time, so there is always at least one axis that is or is directly relatable to time. Figure 4-1 shows an example of a linear kernel of the test compressor as calculated from total pressure measurements taken at 9500rpm, RI3.

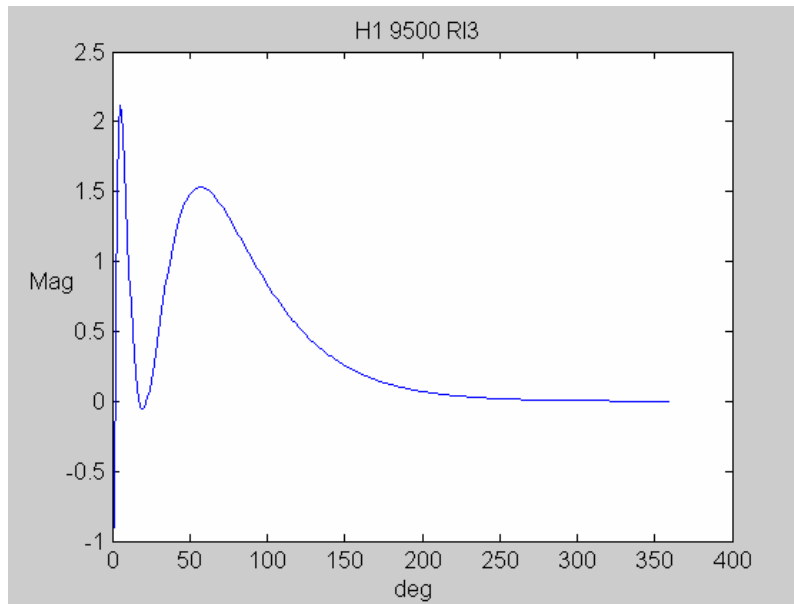


Figure 4-1: Linear kernel calculated from experimental data obtained at 9500rpm, RI3.

The x-axis in Figure 4-1 represents the circumferential location in degrees, which is directly relatable to time. The y-axis is the magnitude of the system response to an input. Notice that the system response is not unlike that of a spring-mass-damper, with the initial value being comparably large and then oscillating around zero until full recovery (zero response) at approximately 180 degrees later.

The second-order kernel is similar with the addition of another axis representing time, as shown in the contour plot in Figure 4-2. The particular kernel shown in Figure 4-2 was calculated under the same operating conditions as the linear kernel shown in Figure 4-1, 9500rpm RI3.

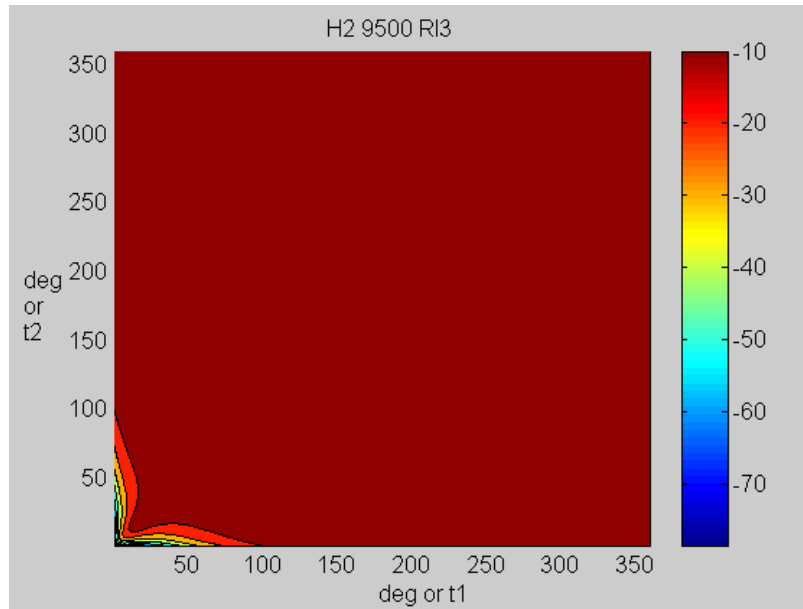


Figure 4-2: Second-order kernel calculated from experimental data obtained at 9500rpm, RI3.

The x and y-axes both represent circumferential location in relation to present location and are directly relatable to time. Notice that the second-order kernel is symmetric. This is due to the fact that the system does not differentiate between which impulse occurs first, just that there are two. For an impulse occurring at the time lag corresponding to one degree, there is a second impulse that could occur anywhere between 1 and 360 degrees. This is true regardless of whether the initial impulse occurs as t1 on the x-axis or t2 on the y-axis; the magnitude of the system response is the same. A three-dimensional view of the second-order kernel is shown in Figure 4-3.

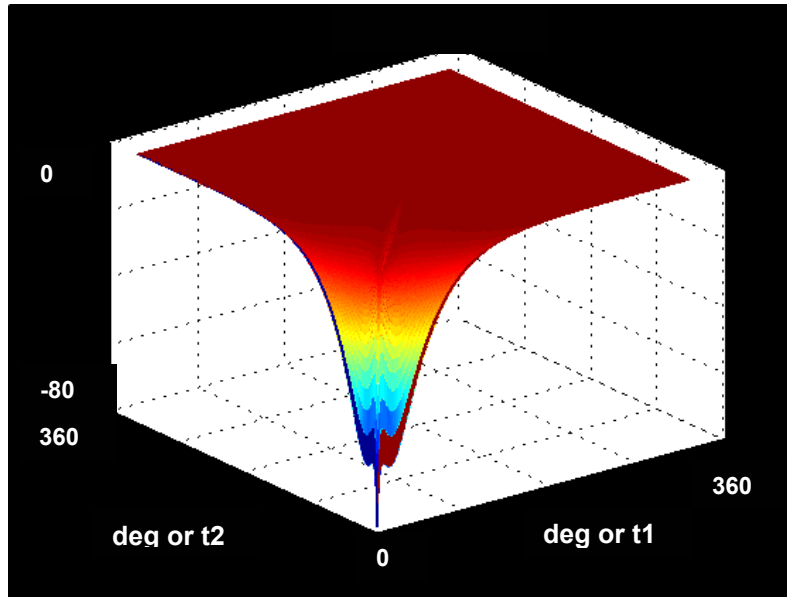


Figure 4-3: Three-dimensional view of the second-order kernel calculated from experimental data obtained at 9500rpm, RI3.

A plot of the third-order kernel is not possible as, similarly to the second-order kernel, it involves another axis representing time. The third-order kernel therefore has four dimensions, three corresponding to time and one to response magnitude. The third-order kernel represents the response of the system to three separate impulses occurring over time, with a certain magnitude associated with the response for every combination of times associated with each of the three impulses.

4.4 Number of Basis Functions

There is no exact way to calculate the number of basis functions that will be needed to adequately identify the kernels of a system. The only method is by trial and error. As the number of basis functions increases, the kernel will converge to its appropriate value. This is shown in Figure 4-4 where the linear kernel is shown with a varying number of basis functions used to calculate it. It can be seen that after 8 basis functions, the amount the kernel changes is not significant. Because of this, 10 basis functions were used to calculate the linear kernel.

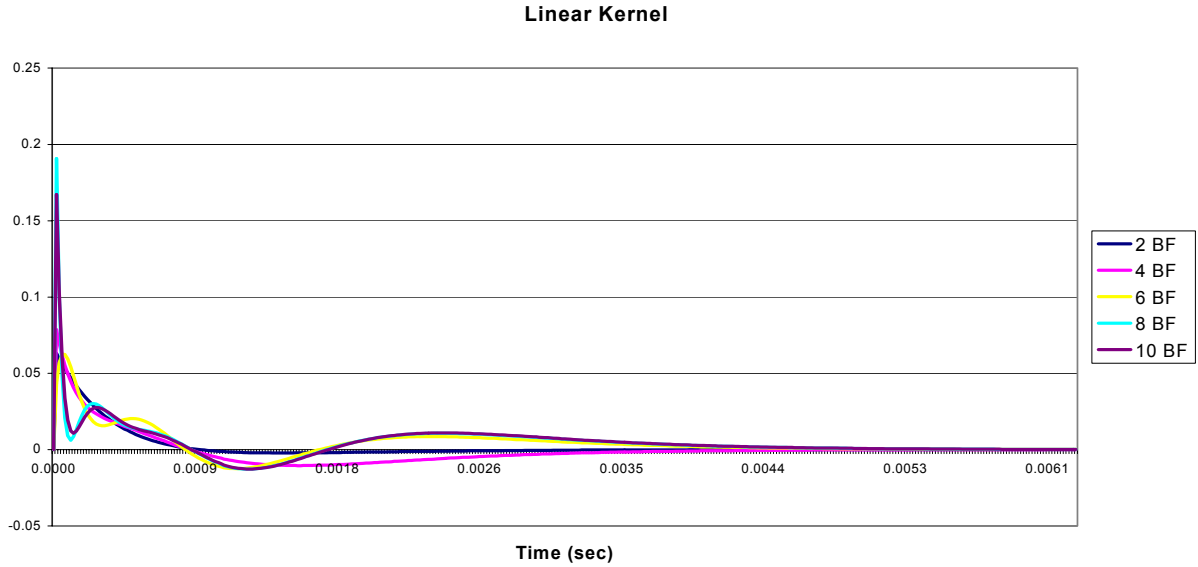


Figure 4-4: Convergence of the linear kernel as the number of basis functions increases.

Another thing to consider when choosing the number of basis functions is the amount of data that is available and will be needed to solve for the coefficients that make up the kernel. In the case of the linear kernel of the system, increasing the number of basis functions by 2 increases the number of equations to solve by 2 also. However, for higher-order kernels, the increase in the number of equations to solve is exponential. For example, 10 basis functions for a linear kernel would result in 10 equations to solve for 10 unknown coefficients. For a second-order kernel, 10 basis functions would result in 10×10 , or 100 equations and 100 unknowns while in the instance of a third-order kernel, one would generate $10 \times 10 \times 10$, or 1000 equations and 1000 unknowns by choosing 10 basis functions. This exponential increase in basis functions and resulting coefficients to solve for causes the amount of data available to rapidly become an issue. Therefore, both for the sake of time and especially the amount of available data, one does not want to use more basis functions than needed to solve for each kernel. These facts also prompted the decision to truncate my model at the third term, therefore assuming all fourth and higher-order terms to be insignificant.

5 Experimental Data

The data for this research was acquired from tests that were run on a two-stage transonic, low aspect ratio compressor at the Compressor Research Facility (CRF) at Wright-Patterson Air Force Base, OH. The compressor was operated at certain speeds under specific conditions known to cause rotor resonance in order to acquire aerodynamic and aeromechanical data. This chapter provides a summary of the “Experimental Procedure and Data Acquisition” of Matt Small’s thesis [Small, 2001] as an overview of the experimental methods applied.

5.1 Experimental Facility

The CRF is made up of three buildings: the test building, the electrical building, and the operations building. Office space, data acquisition, and control computers are housed in the test building. The electrical building contains transformers and power supplies for the drive motors, and the test building houses the test chamber, flow conditioners, and electrical drive motors.

Figure 5-1 shows a schematic of the test section where the two-stage compressor was operated. The test section draws atmospheric air into the facility via the test compressor. The air is then filtered and run through throttle valves in order to regulate the upstream pressure for the compressor being tested. Flow conditioners are also utilized in order to straighten the flow before it is introduced to the compressor bellmouth. The test chamber is 65 feet long and 20 feet in diameter. After exiting the test chamber, the flow passes through throttle valves used to regulate downstream pressure and control the compressor pressure ratio. The flow is then discharged to the atmosphere via a vertical flue after passing through venturis, which regulate the mass flow. The test article is capable of mass flows from 0 – 500 lbm/s.

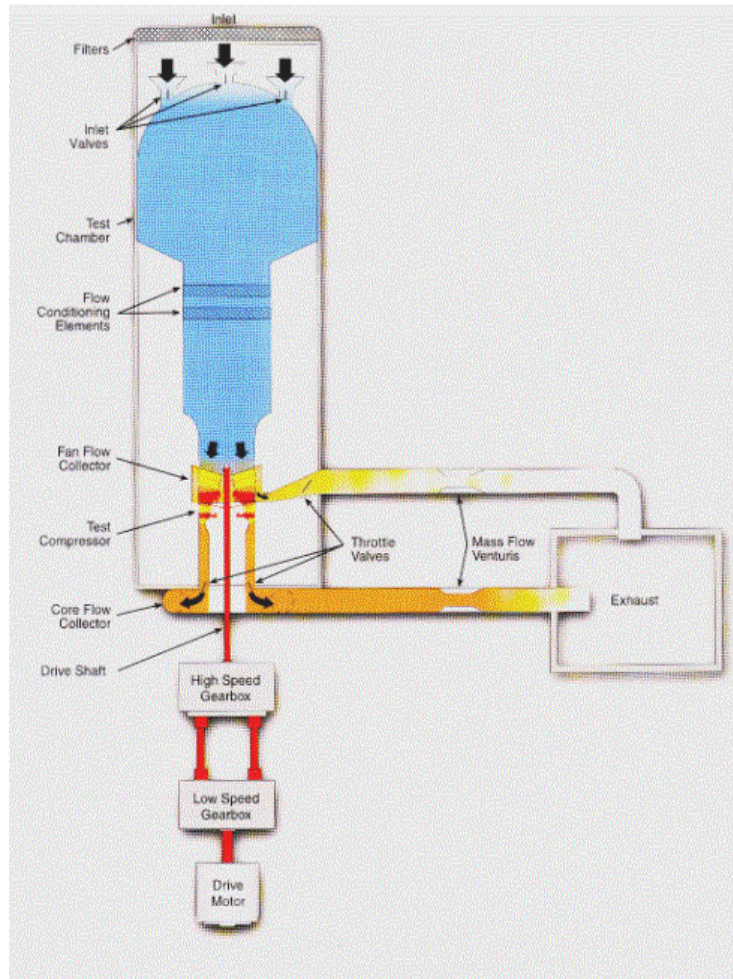


Figure 5-1: Test facility at the Compressor Research Facility, Wright-Patterson AFB [Morrow, 1993].

The speed of the test compressor is determined by the motor-gearbox combination. There are two 30,000 horsepower electric motors to choose from, as well as a high and low-speed gearbox. The CRF Variable Speed Drive control system sets test speed, controls any changes in speed, and also provides automatic safety coast-down modes.

The first stage rotor blisk (modern integrally bladed disk) used for this particular study is shown in Figure 5-2. The blisk consists of 16 low aspect ratio blades of modern design. At the design operating point, rotor relative velocities for inlet temperatures near 300K are supersonic above 45% span. Table 5-1 shows the geometric characteristics of this rotor. The second stage rotor consists of 40 blades mounted on a disk using a conventional dovetail arrangement (see Figure 5-3).

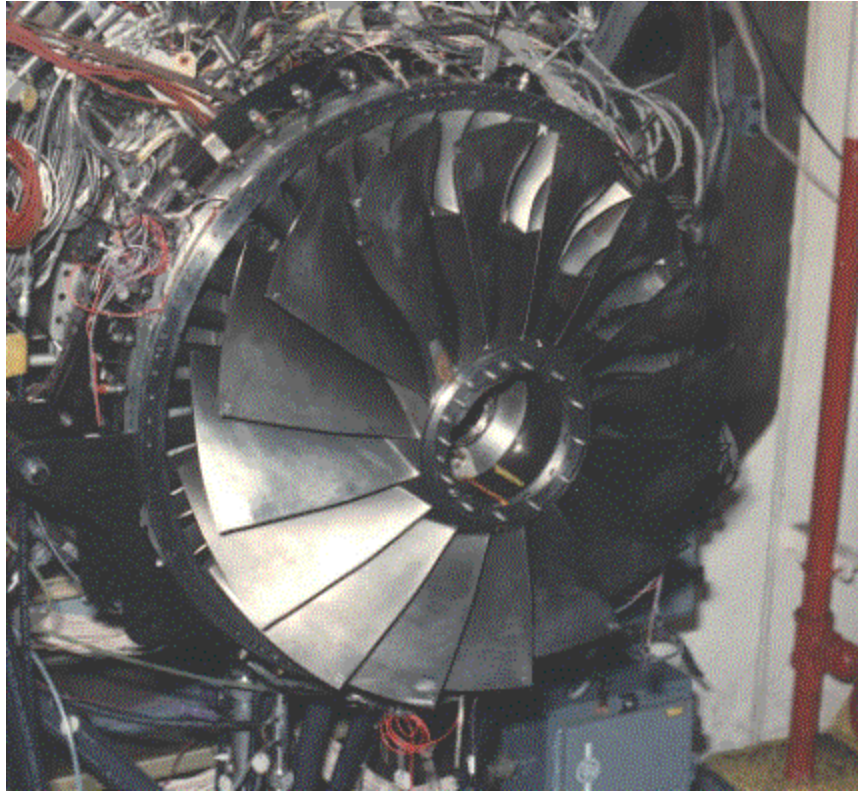


Figure 5-2: First stage blisk mounted on test rig [Morrow, 1993].

| Parameter | Value |
|-------------------------|-------|
| Average Aspect Ratio | 1.22 |
| Rotor Tip Radius (in.) | 13.87 |
| Inlet Radius Ratio | 0.33 |
| Average Radius Ratio | 0.47 |
| Average Tip Solidity | 1.50 |
| Maximum Thickness/Chord | 0.028 |

Table 5-1: First stage blisk geometry characteristics [Rabe et al., 1999].

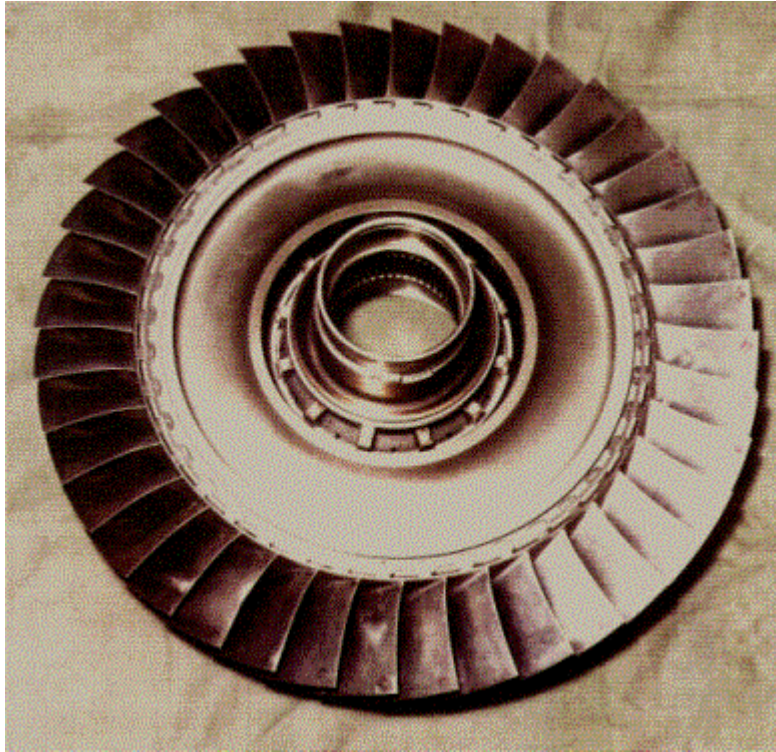


Figure 5-3: Second stage rotor [Morrow, 1993].

5.2 Experimental Procedure

The test setup used for these experiments is shown in Figure 5-4. A distortion generating device was installed downstream of the bellmouth and approximately 1.5 diameters in front of the leading edge of the first stage rotor. The entrance to the compressor was divided into five circumferential tubes of equal mass flow. Radial immersion probes, each one at the center of a circumferential tube and all of them approximately $\frac{1}{2}$ diameter in front of the first stage rotor, measured inlet total pressure. There were a total of eight groups or rakes of inlet total pressure probes equally spaced around the circumference. The radial position of each probe within a rake is shown in Table 5-2.

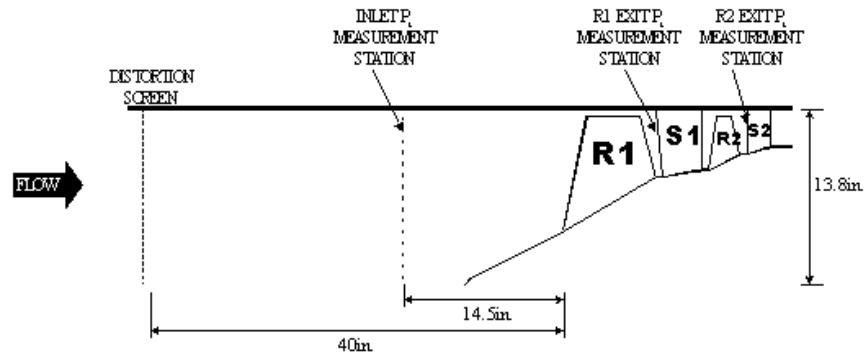


Figure 5-4: Experimental setup [Morrow, 1993].

| Immersion | Radial Distance from O.D. (in.) |
|-----------|---------------------------------|
| 1 | 0.74 |
| 2 | 2.31 |
| 3 | 4.11 |
| 4 | 6.33 |
| 5 | 9.57 |

Table 5-2: Radial locations of inlet total pressure probes [Morrow, 1993].

Total pressure was also measured between each stage via seven probes that were imbedded in three equally spaced stator vanes after each of the two stages (see Figure 5-5). The first and second stages probes' positions are shown in Tables 5-3 and 5-4.

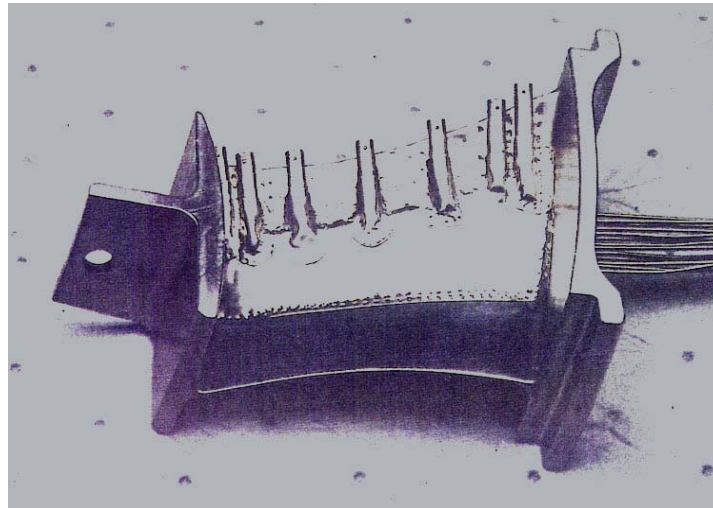


Figure 5-5: Instrumented stator vane [Morrow, 1993].

| Immersion | Radial Distance from O.D. (in.) | Axial Distance from R1 LE (in.) |
|-----------|---------------------------------|---------------------------------|
| 1 | 0.315 | 6.60 |

| | | |
|---|-------|------|
| 2 | 0.662 | 6.80 |
| 3 | 1.577 | 7.05 |
| 4 | 2.577 | 7.27 |
| 5 | 3.573 | 7.29 |
| 6 | 4.241 | 7.16 |
| 7 | 4.595 | 7.10 |

Table 5-3: First stage stator probe locations [Morrow, 1993].

| Immersion | Radial Distance from O.D. (in.) | Axial Distance from R2 LE (in.) |
|------------------|--|--|
| 1 | 0.271 | 13.07 |
| 2 | 0.479 | 13.12 |
| 3 | 0.903 | 13.22 |
| 4 | 1.479 | 13.30 |
| 5 | 2.011 | 13.30 |
| 6 | 2.430 | 13.26 |
| 7 | 2.650 | 13.22 |

Table 5-4: Second stage stator probe locations [Morrow, 1993].

The distortion-generating device referenced earlier in this section and depicted in Figure 5-4 that is mounted in front of the compressor inlet is a wire mesh screen of varying porosity. The distortion-generating screen is used to create downstream areas of reduced axial velocity. These areas of reduced axial velocity are also areas of reduced total pressure. The distortion screens used in these experiments were created to cause a circumferentially sinusoidal, steady state distortion. Specifically, 3 per rev and an 8 per rev distortion screens were used. Figure 5-6 depicts a 3 per rev distortion screen.

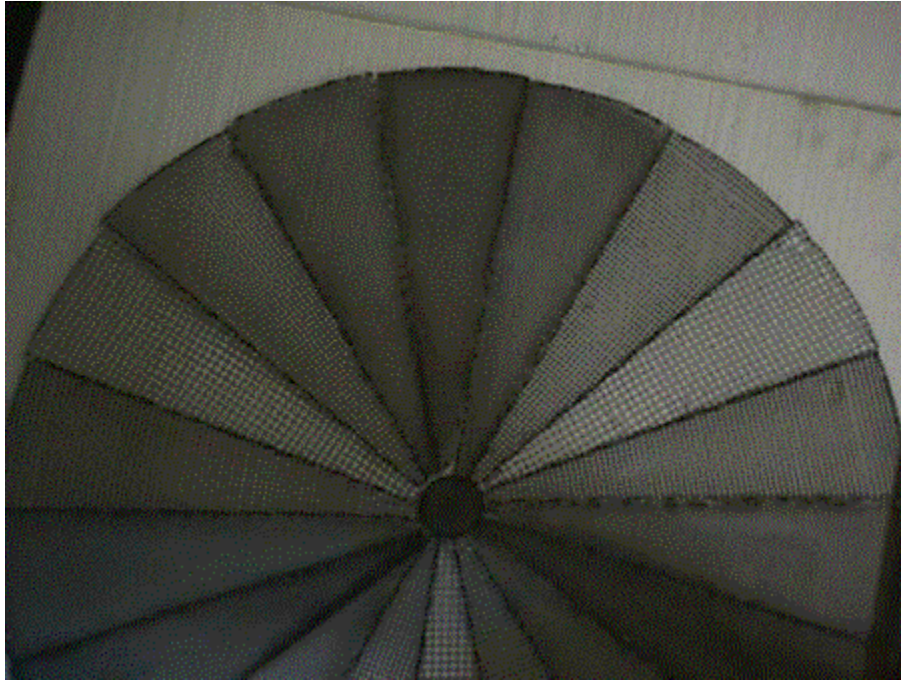


Figure 5-6: Example of a 3 per rev distortion screen [Morrow, 1993].

The distortion generating screens were mounted to a screen rotator for these experiments. The screen rotator consists of a backup screen supported by radial struts. A drive motor, mounted outside the flow field, causes the screen to rotate around the compressor centerline. By rotating the screen, high spatial circumferential data resolution is obtained with a relatively small number of probes. If a non-rotating screen were used, a probe would be required for each spatial position at which a measurement is desired. In other words, if a measurement was desired for each degree around the circumference, 360 probes would need to be mounted, one at each degree, around the compressor's inlet circumference. In order to have good spatial resolution circumferentially and radially, an unreasonably large number of probes would be required, which would complicate data acquisition and produce an unacceptable flow blockage.

With a rotating distortion screen, a single probe's data contains as much or more spatial resolution than would multiple probes used in conjunction with a static screen. Using a high sampling rate with a fixed probe accomplishes this by relating the time of each sample to the position of the screen at that point in time. In order to use this technique the assumption needs to be made that the screen is rotated slowly enough in

order for the data to be considered quasi-steady. Williams [1999] found that a rotation rate of 2 degrees per second is sufficient to make this assumption.

5.3 Data Reduction

The raw data reduction was carried out by Small as part of his M.S. thesis [Small, 2001]. This section summarizes the data reduction procedures from Small's thesis. For further details, the reader is referred to the original document.

Approximately 900 circumferential measurements or one every 0.35 – 0.45 degrees at each probe location were taken for this study. The raw data was then reduced to 360 equally spaced measurements by rounding each data point to the nearest degree (in spatial coordinates) and then averaging all the measurements at the same location or degree. Averaging the probe measurements actually served as a high frequency filter eliminating some of the high frequency noise content.

Streamline position, relative blade velocities, and shock Mach number were calculated by Small [2001] using a streamline curvature (SLC) method. SLC is an iterative solution technique that assumes steady, adiabatic, inviscid, and axisymmetric flow with negligible body forces. Small used SLC code written by Boyer [2001], who had made improvements to the code for transonic applications. Boyer's code calculated 19 axial streamline positions and followed them through each stage of the compressor. The five streamlines that correspond to the five inlet total pressure probes were chosen for this study. Figure 5-7 shows the streamline positions as they travel through the compressor.

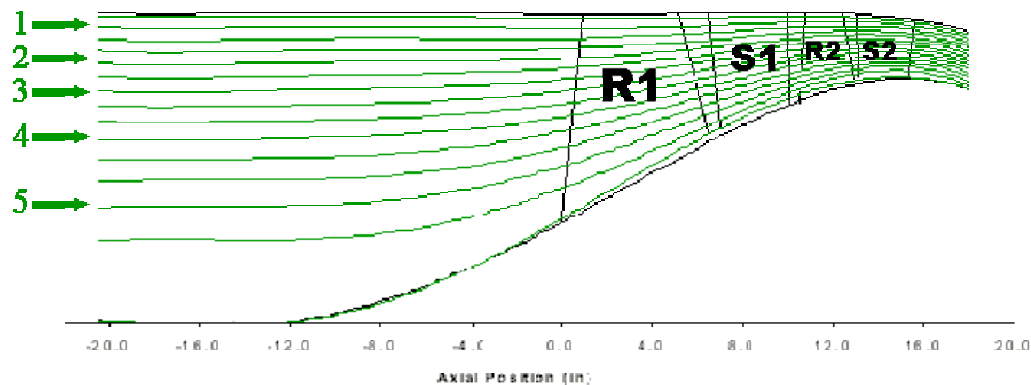


Figure 5-7: SLC computed streamline positions through the compressor [Small, 2001].

Volterra theory deals only with the dynamic component of data. Therefore, it was necessary to subtract the mean from each data set for my study. This has no negative impact on the outcome, as the variation in total pressure from the mean is what creates the distortion and, therefore, causes blade response, which can lead to HCF.

5.4 Data Characteristics

Circumferential total pressure measurements were collected for 11 different operating points of the test compressor. These 11 different operating points are made up of measurements taken at 3 different rotational speeds and 4 mass flow settings. The three speeds are 9100 rpm, 9500 rpm, and 13200 rpm, corresponding to 68.5%, 71.5%, and 99.3% respectively, of design speed. The four mass flow settings at each speed were normal operating line (NOL), near stall (NS), peak efficiency (PE), and wide-open discharge (WOD). The reason that there are 11 data sets as opposed to 12 is that at 13200 rpm, the data sets for mass flow settings of NS and PE were coincident.

A compressor characteristic map showing pressure ratio plotted as a function of corrected mass flow is shown for clean and distorted inlet conditions in Figure 5-8. As can be seen in the plot, a distorted inlet results in dramatically reduced mass flow at a given rotor speed. Also depicted in the plot is the drop in pressure ratio at a given mass flow setting when operating with a distorted inlet, thus resulting in decreased compressor performance.

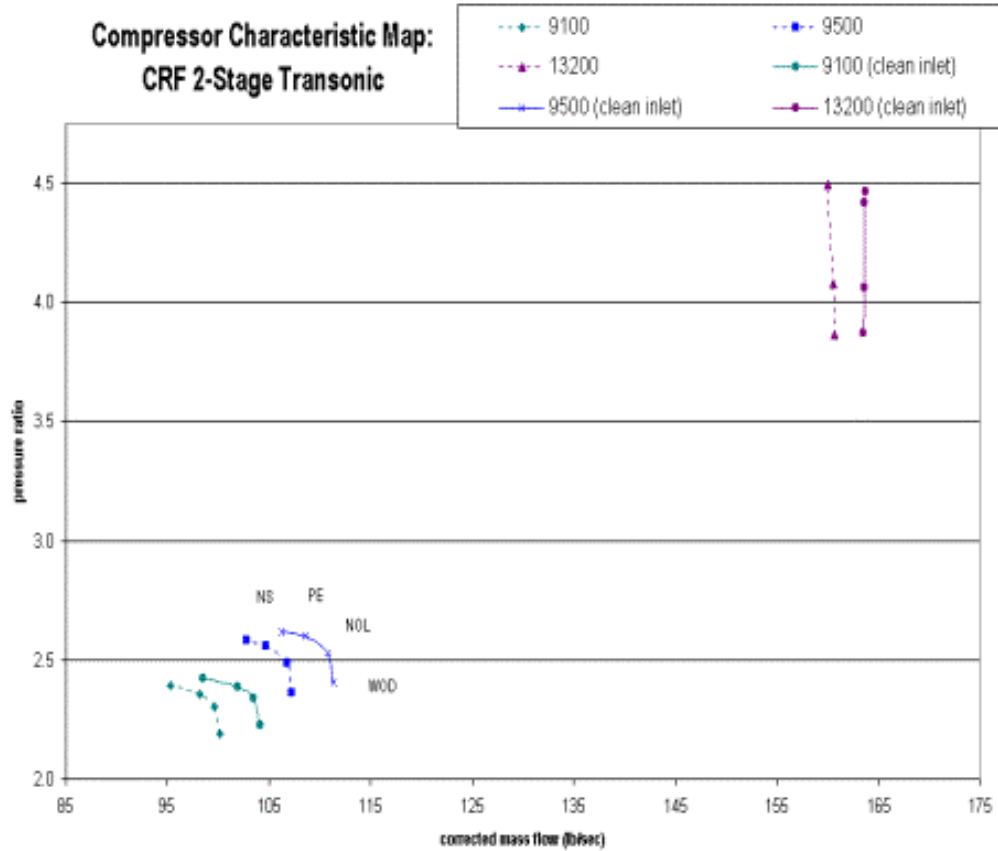


Figure 5-8: Compressor operating map, including clean and distorted inlet conditions [Small, 2001].

As mentioned earlier in this chapter, two different types of distortion-generation screens were used for these experiments, a 3/rev and an 8/rev. The 3/rev screen was used at 9100 rpm and the 8/rev screen was used at 9500 rpm and 13200 rpm. Figure 5-9 shows an example of a typical dataset plotted in the time domain. Since time can be directly related to blade position, the x-axis of this plot represents angular positions around the circumference of the compressor. This particular dataset was measured at 9100rpm, NOL mass flow, and mid-span on the blade. The 3/rev total pressure distortion is easily seen both before and after the first stage. Figure 5-10 portrays the first 15 harmonics of the frequency domain representation of the same dataset. Since a 3/rev distortion pattern was used in this case, there is dominant third harmonic excitation evident in the magnitude plot. The distortion screens used to generate the total pressure distortions for these experiments are designed to produce a frequency excitation at a

specific harmonic with very little secondary harmonic excitation. This can be seen in Figure 5-10 in that there is much less energy at the multiples of the dominant harmonic (the 6th, 9th, or 12th harmonics).

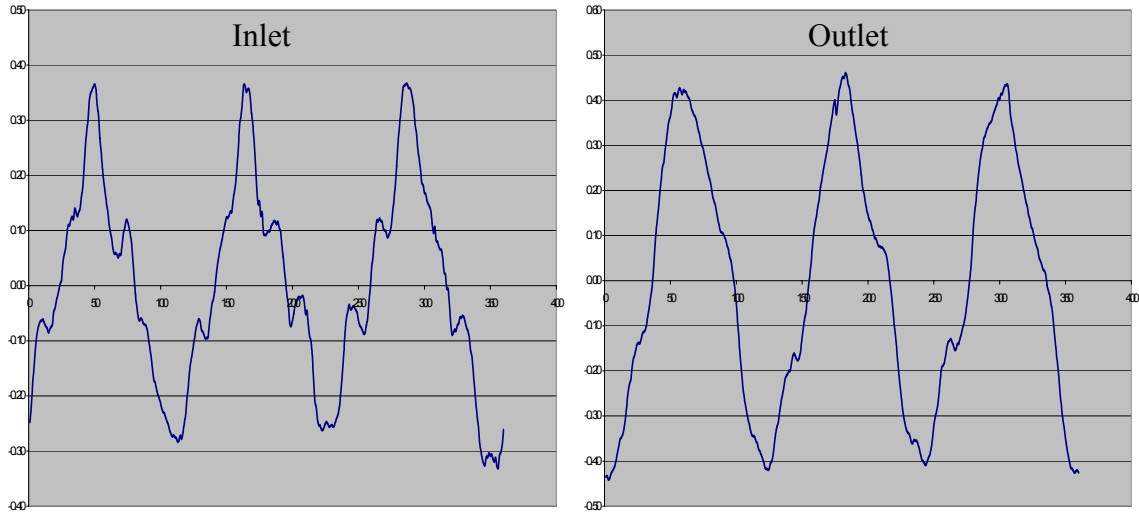


Figure 5-9: Time-series inlet and outlet dynamic total pressure profiles at 9100NOL RI3.

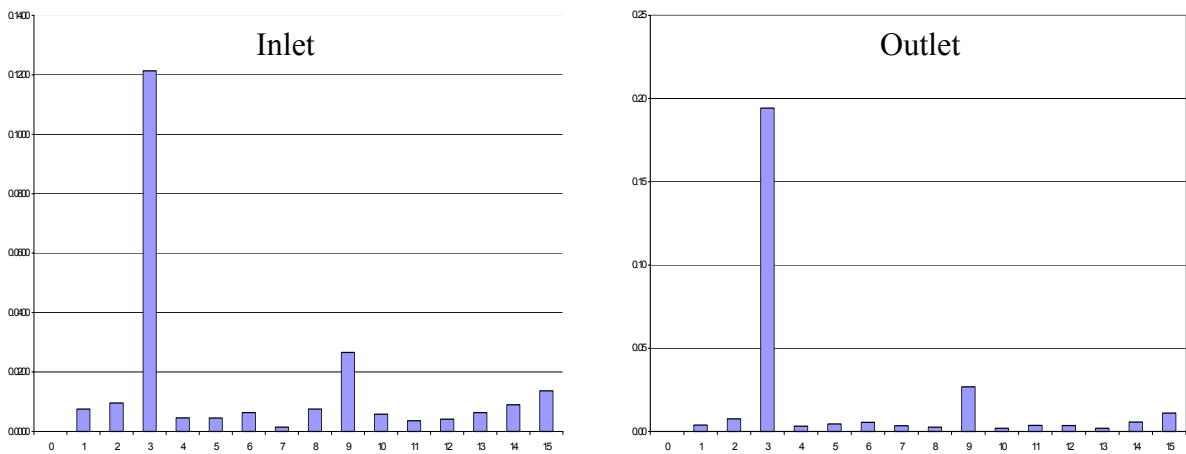


Figure 5-10: Frequency content of 9100 NOL RI3.

A time-series representation of a dataset resulting from an 8/rev distortion screen installed before rotor 1 is shown in Figure 5-11. These plots are of 9500 NOL, RI1 (near tip), before and after the first stage. Figure 5-12 illustrates the first 15 harmonics of the frequency content of the same dataset. The datasets measured at 13200 rpm are similar to the 9500 rpm datasets.

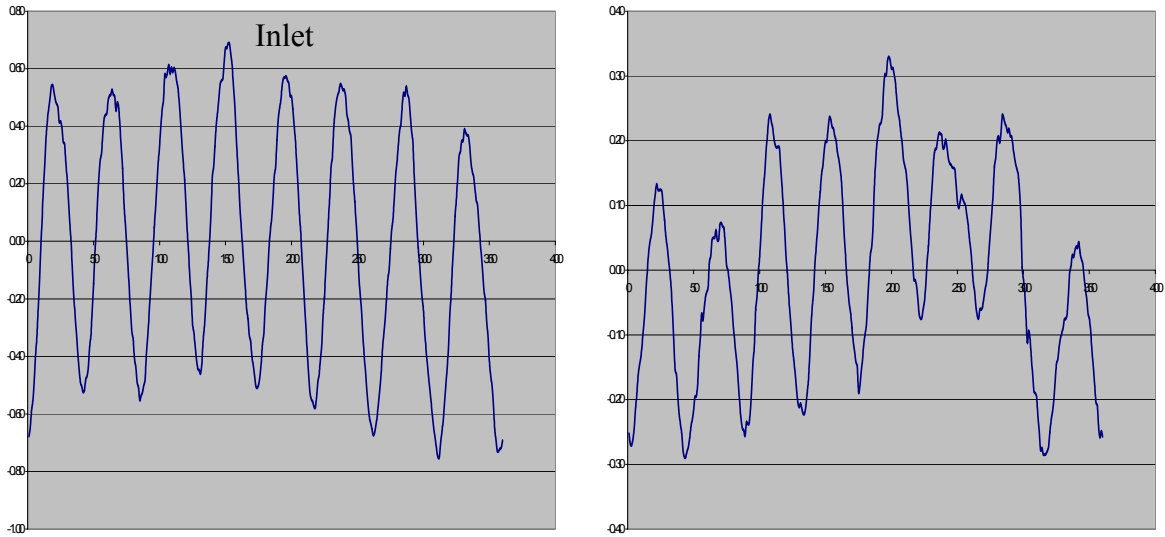


Figure 5-11: Time-series inlet and outlet dynamic total pressure profiles at 9500 NOL RI1.

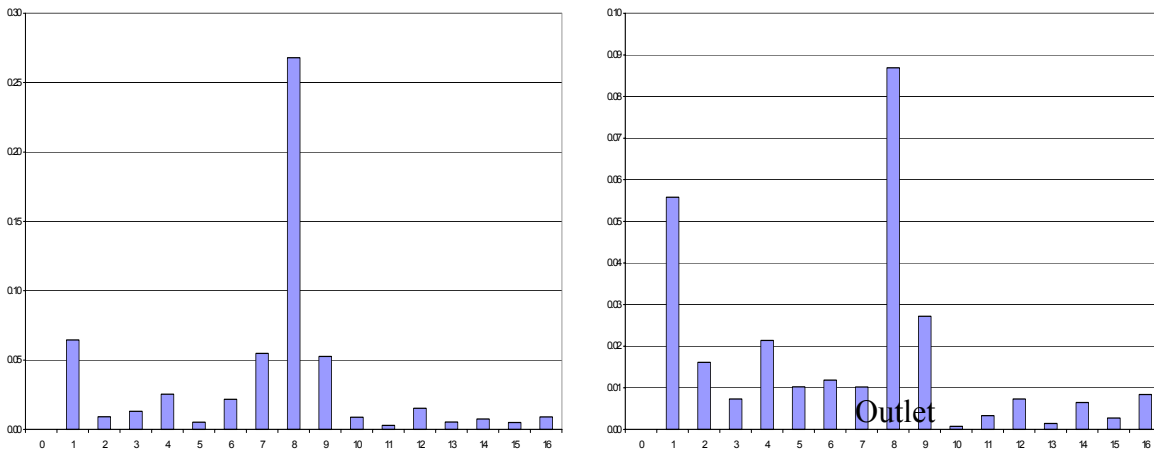


Figure 5-12: Frequency content of 9500 NOL RI1.

Also mentioned earlier in this chapter was that mean-zero data sets were used in my study. The mean value of each separate data set was subtracted out before any analysis was done in order to obtain the dataset's dynamic component. Figure 5-13 shows a plot of dynamic total pressure as a function of circumferential location for all

four mass flow settings at 9100 rpm mid-span. Perhaps surprisingly, mass flow setting has no impact whatsoever on dynamic pressure, as can be seen by the fact that the four plots are practically identical. With the exception of one mass flow setting each at 9500 rpm and 13200 rpm, this was true for all remaining data sets.

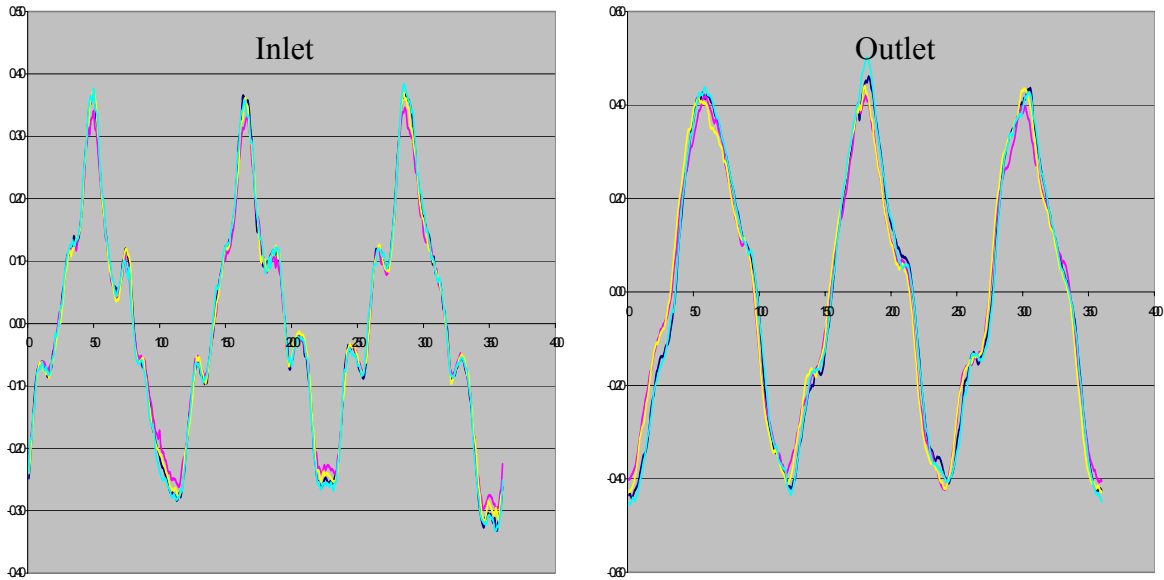


Figure 5-13: First stage dynamic total pressure at 9100 rpm, mid-span, inlet, and outlet.

It is also interesting to look at exactly what happens to the magnitude of the pressure distortion as it travels through the first stage in the test compressor. Figure 5-14 depicts the gain associated with the magnitude of the distortion (maximum total pressure – minimum total pressure) as it travels through the first stage as a function of position on the blade. Therefore, in order for the distortion to travel directly through the first stage with no change whatsoever to its magnitude, it would have a gain of 1, which is depicted by the red horizontal line.

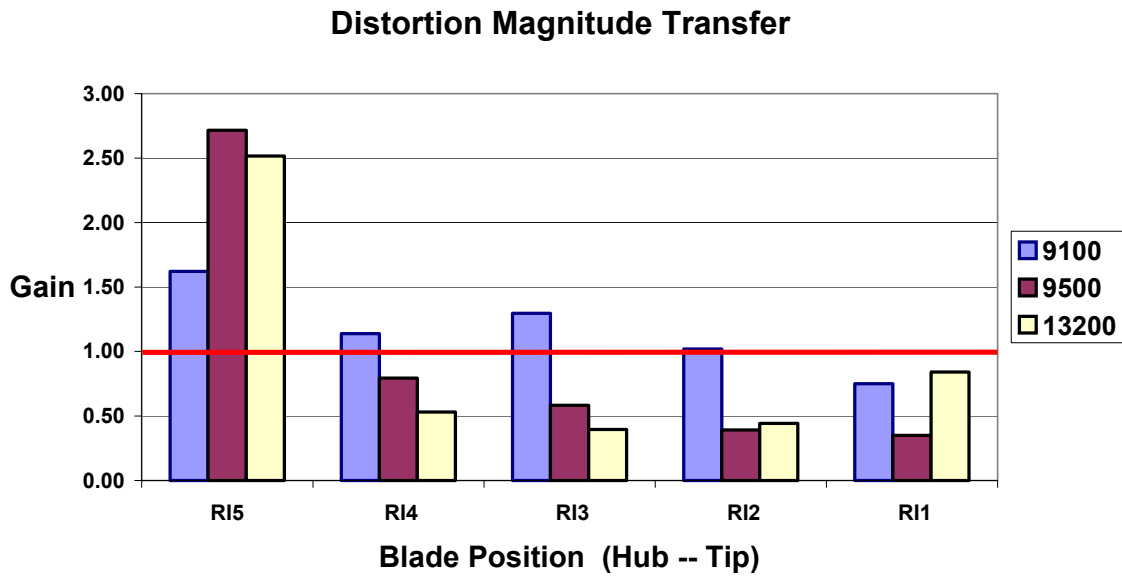


Figure 5-14: First stage distortion magnitude gain as a function of blade position and rotational speed.

As can be seen in Figure 5-14, the transfer of distortion is not only affected by rotational speed, but also radial blade position, with the distortion magnitude actually more than doubling at the hub at 9500 rpm and 13200 rpm. Also remember that each blade position corresponds to its own streamline as a result of the use of the SLC code. Due to the radial dependence of distortion, I chose to apply my compressor model along each individual streamline, calculating 5 separate transfer functions along the span of the blade.

6 Solution Technique

As opposed to airflow over a wing, where the wing in the relative plane is immobile with the air rushing over it, a compressor stage is spinning at a high and varied rate of speed with air rushing through it. This added another dimension and a definite challenge to creating a model. System identification, as well as the choice of non-dimensionalization and normalization parameters, was critical.

This chapter discusses just how the kernel indirect extraction technique as explained in Chapter 4 is used in conjunction with the experimental data as explained in Chapter 5 to create a model of the first stage of the ADLARF test compressor. Included are discussions of further data conditioning, the use of the resultant data sets to ensure that there is enough input to model the system and still allow an accurate assessment of its performance, and different model variations. The first section explains the system definition in order to remove radial dependence from the problem.

6.1 System Identification

An advantage of using Volterra theory to identify the impulse response function of a system is that the Volterra model essentially turns the system in question into a black box. Since the model is purely mathematical, all that it cares about is the inlet and outlet data. One could model any stage or even group of stages in a compressor without making any changes to the model other than altering the input statements to reflect the appropriate system identity.

In my research, I defined each stream tube as it travels through the first stage of the compressor as its own system. This system definition required that the modeling code be run five times – one for each stream tube – in order to predict the first stage exit conditions. The first stage was chosen to model because there is more data for the first stage and since the inlet air is drawn directly from the atmosphere, there were fewer unknowns and, therefore, assumptions to be made regarding inlet conditions. Additionally, if the model is capable of accurately modeling the first stage, the next stage

could be modeled just as accurately by using the outlet predictions from the first stage as the input data for the second.

6.2 Data Set Expansion

Reviewing, the data for my research consists of measurements at 3 rotational speeds, 4 compressor mass flows per rotational speed, 5 streamlines—or stream tubes—per mass flow setting, and 360 measurements—one per degree at the inlet and outlet—per stream tube. By deciding to treat each stream tube of data through the compressor as its own system, I reduced the amount of data available to solve for each kernel by a factor of 5. This, coupled with the fact that the amount of basis functions and resulting coefficients to solve for increase exponentially as the order of the equation increases, caused some concern that the amount of data available would be insufficient to adequately solve for the first three kernels of the system.

In order to ensure that there would be enough information to solve for the first three kernels of the system and still be able to test the model by predicting at an operating condition different from those used to solve for the kernels, more data was needed. There were three options available in order to obtain more data: (1) the original, unconditioned data sets could be used (2) more data could be collected either by myself or by CRF, or (3) data could be “created” by fitting a spline to the existing, conditioned data sets. Since the original data sets contained a measurement approximately every .35 degrees, the amount of information would be almost tripled by using the first option. However, this would also be adding more noise to the problem, which would make the answer less accurate. Collecting more measurements at other operating conditions was not feasible due to cost and time. Therefore, the third option was the one chosen.

A spline is a flexible ruler that is used to connect plotted data points. Once the spline is shaped so that it lines up with every data point, it is used to draw a line connecting them. Now, new data points can be read from the line that was just drawn. Rather than plotting points on graph paper, computer code was written that accomplished the same task. The type of spline code used was a cubic spline. This code works in essentially the same way as the flexible ruler, only more accurately. Rather than physically drawing a line between all the data points, the cubic spline code works with

two consecutive data points at a time. The code considers each group of two data points as a separate function and calculates an equation that will fit those two points. Since each function connects two adjacent data points, the end points of each line already match. By stopping here however, the result would be a jagged plot of little straight lines – not desirable. Since this is a cubic spline code, it is capable of doing three things. Therefore, not only are the end points of each line matched, the first and second derivatives of the end points are forced to match as well. This ensures that the final composite function of all the individual functions provides a smooth fit to all the data points. After calculating this composite function, any output can be calculated for any point between the initial and final data point. The number of data points per stream tube was doubled in this way, resulting in a data point every $\frac{1}{2}$ degree around the circumference of the compressor. Figure 6-1 shows an initial data set of 360 points as well as the data set after running it through the spline code, now consisting of 720 points. As can be seen, the final data set directly overlays the original, proving that the spline code worked properly.

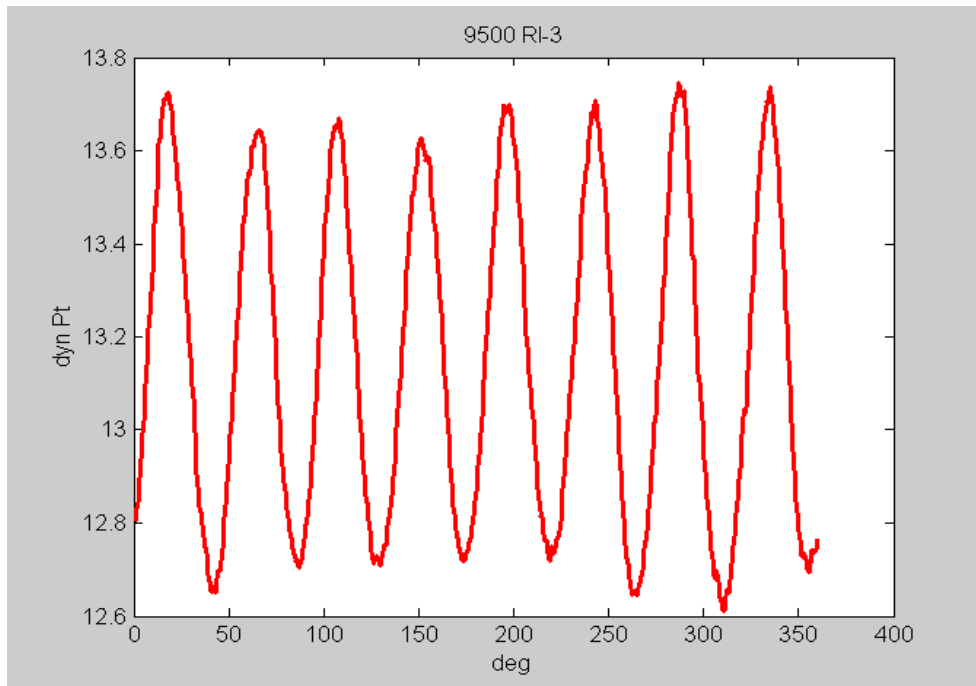


Figure 6-1: Data set before and after being run through spline code. Final data set of 720 points directly overlays the original, which consisted of 360 data points.

6.3 Data Conditioning

Since the Volterra theory is a strictly mathematical theory, it does not account for changes in compressor rotational speed. Therefore, without any type of data conditioning, the Volterra model would have very little hope of accurately predicting compressor response at different inlet conditions than those used to calculate the impulse response function. Due to this, physics-based parameters were used to non-dimensionalize the problem and also to deal with the matter of rotational speed dependence.

The time non-dimensionalization parameter was calculated by dividing the chord length by the inlet relative velocity to the blade (see Equation 6-1). The units of t_{nd} are (s); therefore, time was divided by this parameter in order to obtain a dimensionless time variable. Inlet relative velocity is used because it contains information pertaining to fluid axial and radial velocities at the specified inlet conditions. Chord length is also important since convection speed -- the speed at which total pressure distortions travel through the rotor -- is a function of this variable. Due to the fact that the relative blade velocities are quite large in relation to the chord length -- on the order of four magnitudes larger -- t_{nd} is a very small number. Dividing by t_{nd} stretches out the time variable, which is desirable due to the rapid changes in inlet and outlet total pressure that occur over small increments in time.

$$t_{nd} = \frac{Chord}{W_1}$$

Equation 6-1

Inlet and outlet total pressure measurements were also non-dimensionalized by dividing by p_{nd} (see Equation 6-2). This variable also includes information pertaining to fluid axial and radial velocities due to the inclusion of inlet relative velocity. In addition, the density of the air at the inlet, ρ_1 , is included and multiplication by $1/2$ is done due to convention.

$$p_{nd} = \frac{1}{2} \rho_1 W_1^2$$

Equation 6-2

Some of the Volterra models were also normalized with a non-dimensional work term (see Equation 6-3) [Cousins, 2002]. It was found that some of the models did not adequately account for rotational speed dependence. Multiplication by the non-dimensional work variable defined in Equation 6-3 helped to correct this deficiency. Non-dimensional work was calculated by dividing the stage work by the rotor speed squared, U^2 ($U = r\omega$). Normalizing the data sets with stage work was not necessary in all cases.

$$work_{nd} = \frac{work_{stage}}{U^2}$$

Equation 6-3

All non-dimensional and normalization parameters were calculated with respect to stage inlet conditions and location on the blade. This was necessary because of the system definition. Since there were five separate stream tubes (systems) that made up the first stage, it was required to calculate non-dimensionalization and normalization terms for each system.

6.4 Training and Prediction Data Sets

The data sets used in the indirect extraction technique to calculate the kernels of the system are called the training data sets. This is due to the fact that from these data sets, the model is “taught” the characteristics of the system. The fact that multiple data sets are used in order to calculate the kernels of the system is important since it is doubtful that just one data set could contain all the information necessary to accurately characterize the system. Another important point is that the Volterra model does not simply average all the input and response data sets before extracting the kernels. All the data sets create the boundary conditions that must be satisfied at all times by the basis coefficients, which combined with the basis functions create the system’s kernels.

The data sets available consist of measurements taken at three rotational speeds (9100, 9500, and 13200 rpm), four mass flows per speed (NOL, NS, PE, and WOD), and two different distortion patterns (3/rev and 8/rev). The 3/rev distortion pattern was used

at 9100 rpm and the 8/rev was used at the other two speeds. None of the speeds contains information of both distortion patterns. In order to capture as much information about the system as possible with these limited data sets, both distortion patterns should be used in kernel training. Also, in order to truly test the model once the kernels were calculated, one of the three speeds should not be used at all in kernel training. This third speed would be used in the prediction phase of the research as the novel data, meaning that the model would be predicting at a speed it had never seen before. Because of these initial parameters, in the final phase of research, the two speeds used in the kernel extraction phase were 9100 and 13200 rpm. All the data sets at these two speeds were used to calculate the kernels. Predictions were then made using the 9500 rpm data.

As alluded to in the previous paragraph, numerous tests were run through the various Volterra models created in order to gain an understanding of their capabilities and limitations. The next chapter will explain all tests that were run and discuss the results of each in detail.

6.5 Modeling Method Variations

As previous discussed in Chapter 4, more than one Volterra model was created in my research. Different forms of the higher-order basis functions were used, as well as different normalization methods. This was done in an effort to learn as much as possible about the capabilities and limitations of the kernel extraction method used in my research.

In addition to using multiple forms for basis functions, different integrations techniques were also employed. All computer code was written in Matlab, which has numerous built-in functions that were made use of as much as possible. Convolution is one of these functions. Matlab is capable of performing linear convolution in multiple dimensions. However, there is no built-in 2nd or 3rd order convolution function, which is necessary in calculating the higher-order kernels. In two of the methods developed (Model 1 and Model 2), squaring or cubing the input data sets and using the built-in, linear, convolution command addressed the lack of a higher-order convolution function. The problem with this approximation is that all the inputs, or impulses, are forced to occur at the same time, which isn't necessarily the case. The advantage of this approximation is seen in processing speed. The number of calculations necessary in this

method are a number of orders of magnitude less than if a calculation was done for every conceivable combination of impulse times. The cost of this approximation is, obviously, accuracy.

The second integration method utilized was that of numerical integration (Model 3). By using numerical integration rather than the built-in convolution function, every conceivable combination of impulses to the system could be evaluated, making this second integration method the more theoretically correct of the two. Being more theoretically correct should result in an increase in accuracy, with the cost of a dramatic increase in processing time. It is due to this increased processing time as well as a much greater demand for system memory that Model 3 is only a second-order model as opposed to Model's 1 and 2, which are third order. The next chapter discusses the various tests used to assess each model as well as each model's performance in these tests.

7 Prediction Results of Nonlinear Volterra Series Model

All of the discussion and background in the previous chapters leads up to this one final and important question. Does it work? The answer to that question is the focus of this chapter. As will be shown in the subsequent discussions, each model (Model 1, 2, and 3) was evaluated using the same tests. Initially, all three models performed similarly. However, as the tests became more difficult, differences began to materialize. These differences were in the form of prediction accuracy and also analysis speed.

The tests were performed in such a way that the level of difficulty steadily increased. This was done in an effort to fully understand the capabilities and limitations of this method of analysis as well as each individual model. Before the experimental data from the ADLARF tests were used, data sets were generated from simple functions. In these initial tests, the input waveform was kept constant while the output waveform was varied. In this way, different “systems” were created, each “system” having a different effect on the input. This type of evaluation is similar to the “measurement” kernel identification method as discussed in Chapter 4 and used by Boyd [1983] in his research. Whereas Boyd altered the input to a system in order to only elicit a certain type of response, I altered the “system” itself by changing the output data resulting from a constant input. Section 7.1 discusses these initial tests in more detail.

The remainder of testing done on each model was with the experimental data. Predictions were made in the time domain and then converted to the frequency domain with the output of each run including both. The prediction results were then cut and pasted into Excel spreadsheets, which is the primary method of presentation. Rather than showing all the time domain and frequency domain plots at each radial position for all three models, the following format will be followed. Plots will be shown of the predictions results for one of the three models in the time domain as well as the magnitude plots in the frequency domain. Results will be shown for each of the five radial positions. Any major differences between the three models will be included in the discussion of the plots and a table summarizing each model’s performance will be

included at the end of that particular section for the sake of comparison. Since prediction results are shown in the time and frequency domain, the models performance is assessed in both as well. The standard deviation of the prediction as compared with the experimental data is used in the time domain with a perfect prediction having a standard deviation of zero. In the frequency domain, the percent error of the magnitude of the dominant harmonic is used for performance assessment. An error of zero percent would represent a perfect prediction of the magnitude of the dominant harmonic.

7.1 Validation of Model

In order to initially test the model, data sets were generated using sine functions. Sine functions were chosen for two reasons. First, sine waves, being periodic, resemble a waveform caused by a non-uniform inlet pressure profile. Second, by using sine functions to generate data sets, the exact order of operation of the “system” is known. This enabled the calculation of each individual kernel to be evaluated separately based on the data sets that were used as input and output waveforms.

For all of the sine tests performed, the input waveform was $\sin(x)$ while the output waveform was some form of $\sin(x)$, such as $\sin^2(x)$, $\cos(x)$, or the combination of two sine waves. Over 10 different tests were run of varying difficulty. In all of the sine tests, the input and output waveforms were first used to calculate, or extract, the system’s kernels. Next, the same input waveform was used with the kernels just calculated to predict the system’s output. That prediction was then compared to the output waveform initially used in kernel extraction to assess how well the model was working. Since these tests were just reproducing the same waveform used in kernel extraction, they are not a true assessment of the model’s ability to fully define a system. However, the ability to reproduce the same data used in kernel extraction is an important and necessary step that a model must be able to do before any more difficult scenarios can be attempted. These sine tests were also a good first opportunity to evaluate the different higher-order forms of basis functions as well as methods of integration (Models 1, 2, and 3).

The Volterra models treat the system as if it were a black box, only being concerned with the input and output waveforms as they enter and leave the system. The models are only concerned with what must be done to the input waveform to make it look

like the output. Therefore, the models do not recognize these waveforms as sine waves or any type of function whatsoever, they just see an input vector that is changed in some way to end up looking like the output vector.

Results from three of the sine tests are shown in Figures 7-1, 2, and 3. These plots are just of the output waveforms; the input waveform for every sine test was $\sin(x)$. The figures shown have outputs in the form of $\sin^2(x)$, $\sin^3(x)$, and $\sin(x) + \sin(2x)$, respectively. All three models were tested with all of the various data sets generated with sine functions. There was no difference in performance between the models at this level of testing. Each model was able to exactly replicate the output data set that was used in the kernel calculation phase, as can be seen in the following figures.

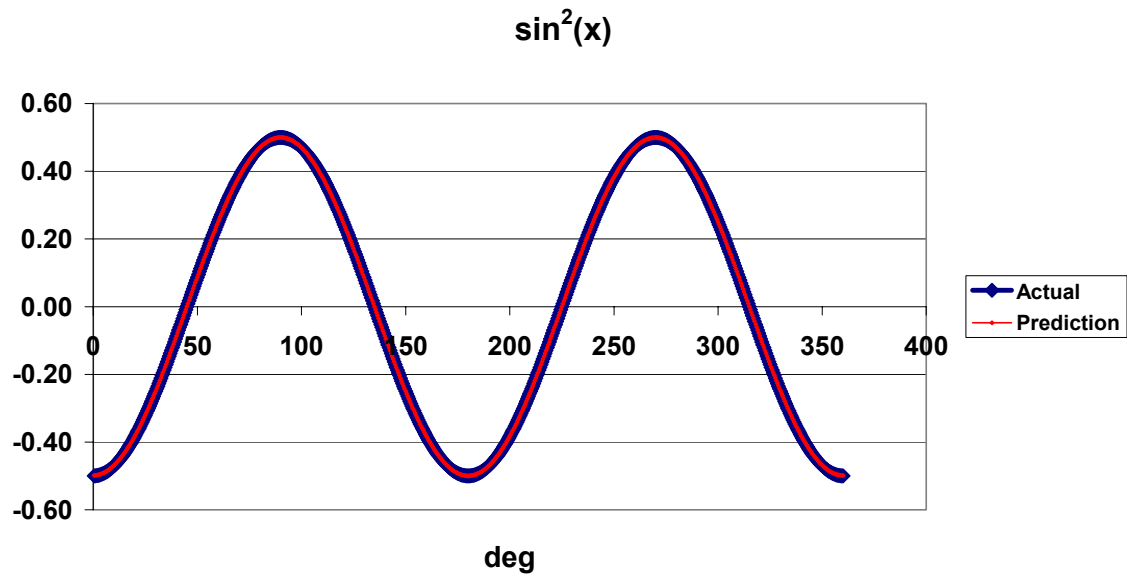


Figure 7-1: Prediction result from kernels calculated with input of $\sin(x)$ and output of $\sin^2(x)$. Prediction directly overlays the actual data set analytically calculated from sine squared.

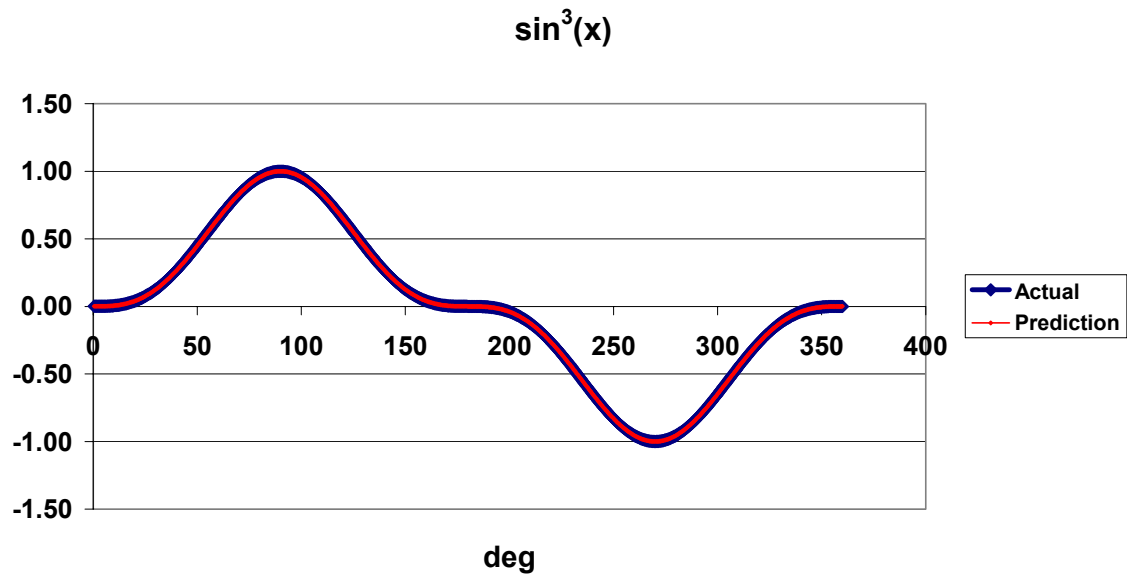


Figure 7-2: Prediction result from kernels calculated with input of $\sin(x)$ and output of $\sin^3(x)$. Prediction directly overlays the actual data set analytically calculated from sine cubed.

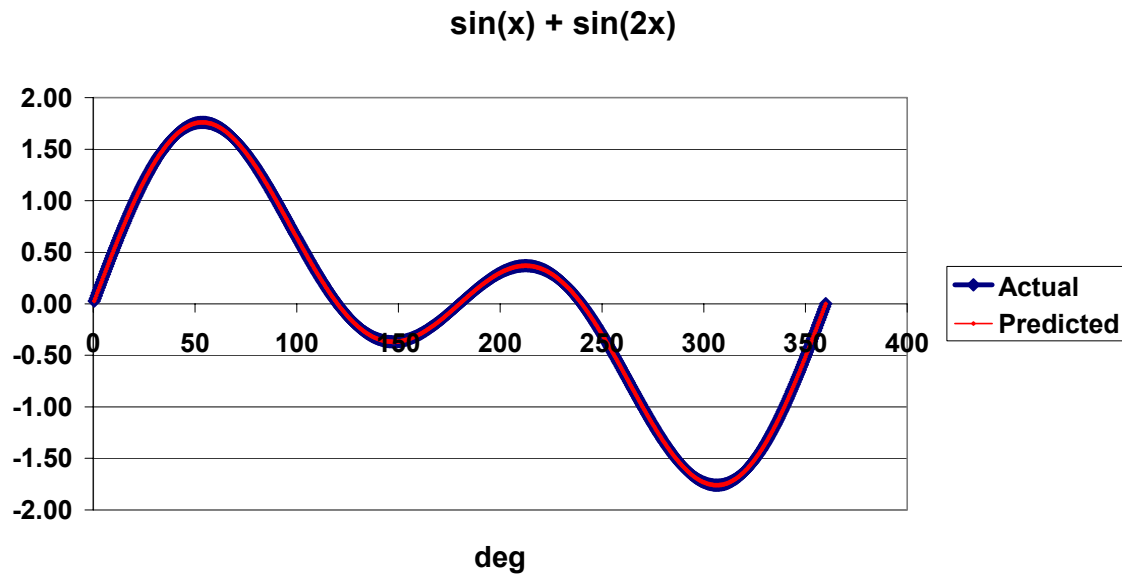


Figure 7-3: Prediction result from kernels calculated with input of $\sin(x)$ and output of $\sin(x) + \sin(2x)$. Prediction directly overlays the actual data set analytically calculated from the addition of $\sin(x)$ and $\sin(2x)$.

7.2 Same Speed Predictions

The next stage of testing involves predicting the variation in total output pressure of the compressor at the same rotational speed that the kernels were calculated. This particular stage has two parts. The first part is replication of the same data used in kernel calculation, similar to the sine tests. The input and output data sets corresponding to just one operating condition (9100NOL RI3, for example) were used for kernel calculation. The same input data set was then used in conjunction with the previously calculated kernels to predict the compressor's response. Each of the three models was tested under the same operating conditions (9100NOL, all 5 radial positions). Figures 7-4 through 7-8 show the time domain predictions at all five radial positions from Model 3. The corresponding magnitude plots in the frequency domain of those same predictions are shown in Figures 7-9 to 7-13.

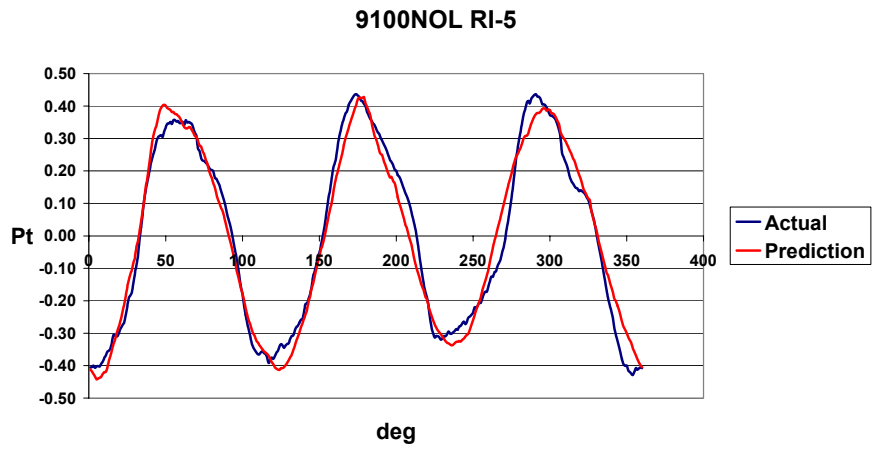


Figure 7-4: Time domain prediction obtained with Model 3 of the output variation in total pressure at 9100NOL, RI5 after calculating the system kernels with the same data.

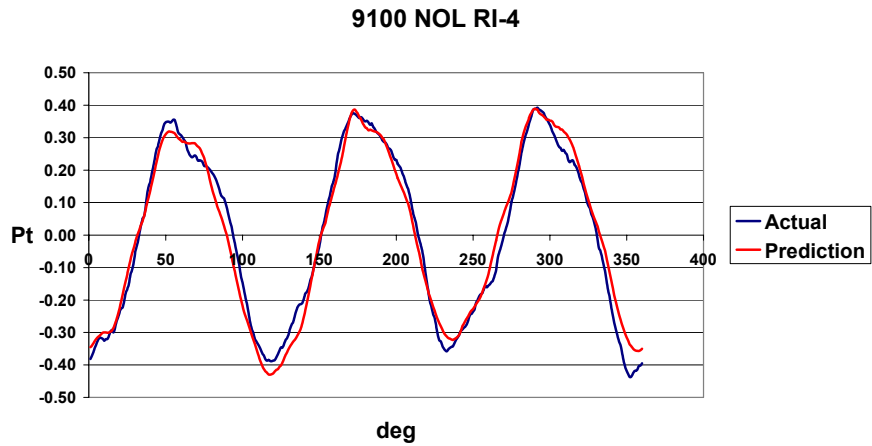


Figure 7-5: Time domain prediction obtained with Model 3 of the output variation in total pressure at 9100NOL, RI4 after calculating the system kernels with the same data.

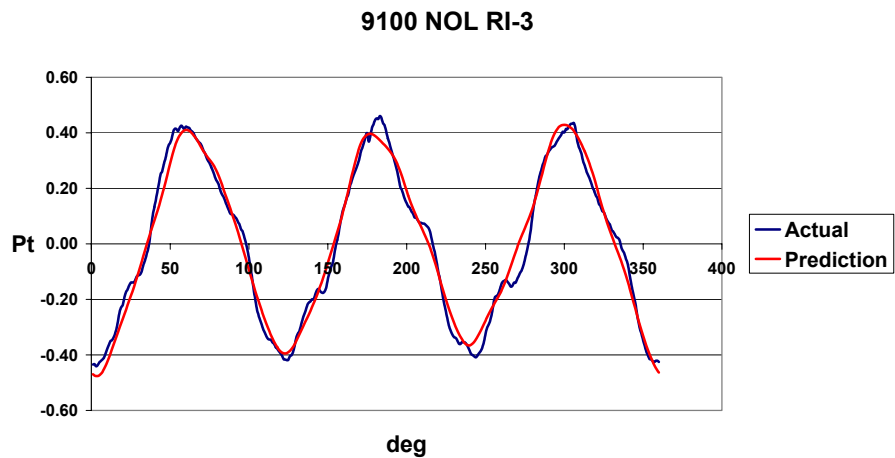


Figure 7-6: Time domain predictions obtained with Model 3 of the output variation in total pressure at 9100NOL, RI3 after calculating the system kernels with the same data.

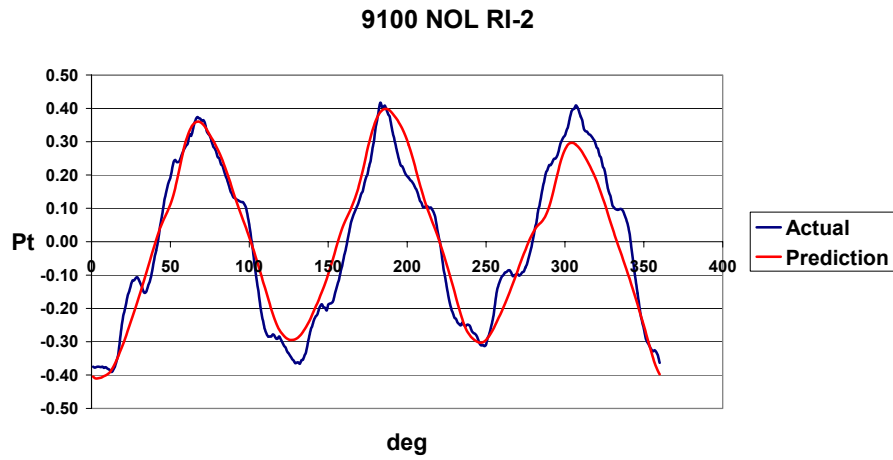


Figure 7-7: Time domain predictions obtained with Model 3 of the output variation in total pressure at 9100NOL, RI2 after calculating the system kernels with the same data.

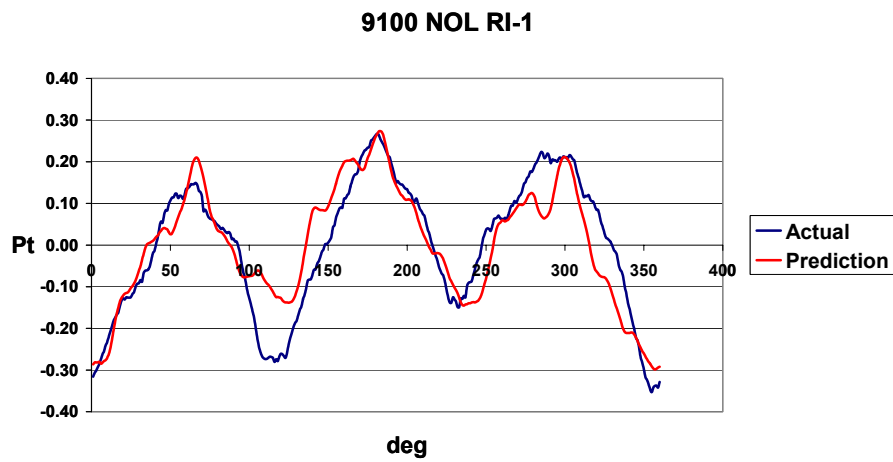


Figure 7-8: Time domain predictions obtained with Model 3 of the output variation in total pressure at 9100NOL, RI1(near tip) after calculating the system kernels with the same data.

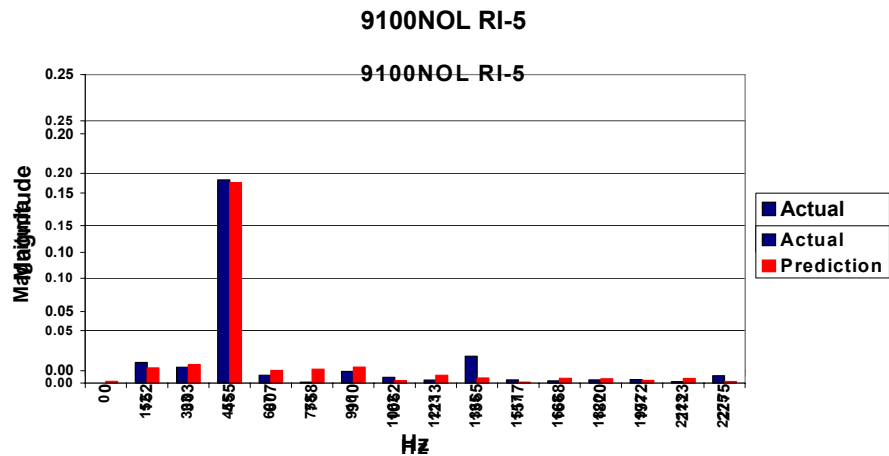


Figure 7-9: Magnitude plot in the frequency domain of the output variation in total pressure corresponding to the prediction shown in Figure 7-4 that was made with Model 3.

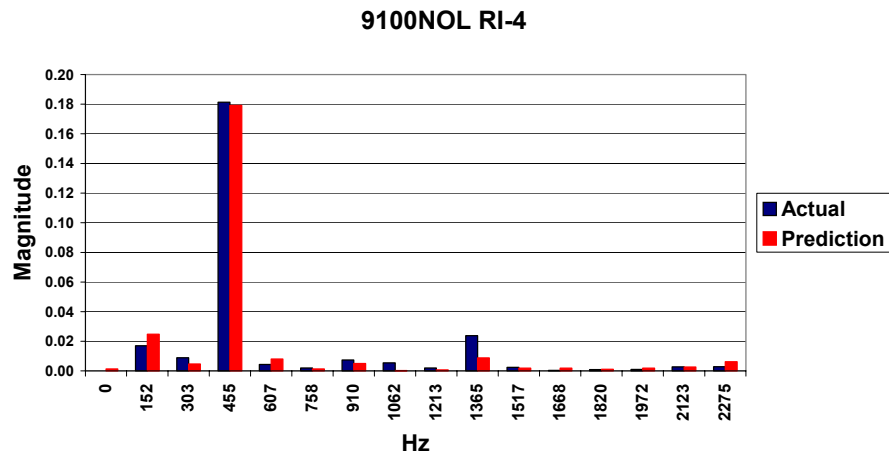


Figure 7-10: Magnitude plot in the frequency domain of the output variation in total pressure corresponding to the prediction shown in Figure 7-5 that was made with Model 3

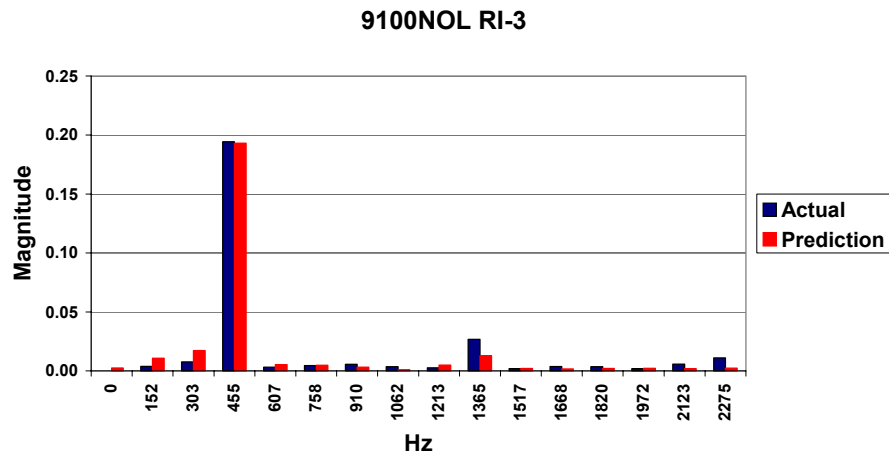


Figure 7-11: Magnitude plot in the frequency domain of the output variation in total pressure corresponding to the prediction shown in Figure 7-6 that was made with Model 3.

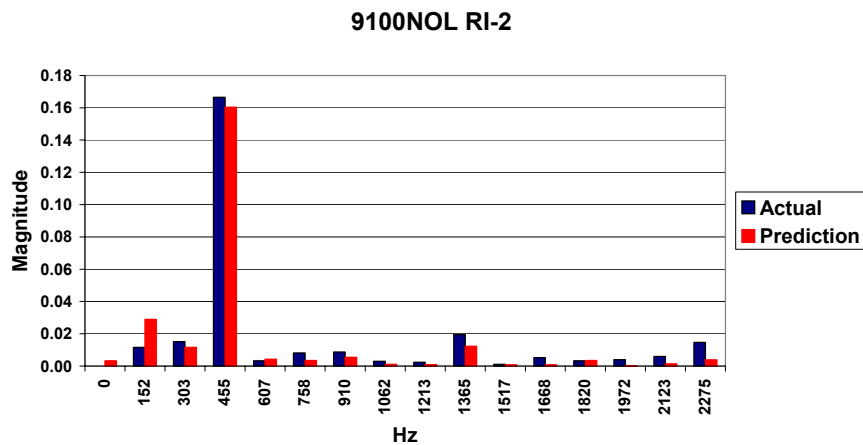


Figure 7-12: Magnitude plot in the frequency domain of the output variation in total pressure corresponding to the predictions shown in Figure 7-7 that was made with Model 3.

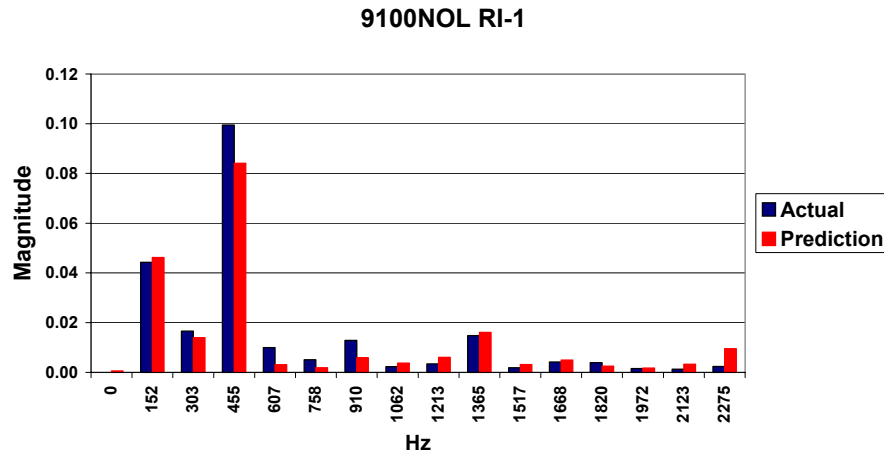


Figure 7-13: Magnitude plot in the frequency domain of the output variation in total pressure corresponding to the prediction shown in Figure 7-8 that was made with Model 3.

The first thing noticed when looking at the time domain plots is that there is an obvious 3 per rev distortion pattern, depicted by the 3 peaks and valleys in total pressure about the mean. There is not a dramatic difference in any one of the peaks or valleys, meaning that the areas of higher/lower density material on the screen are identical. This would cause the sinusoidal total pressure profiles seen in Figures 7-4 through 7-8. The 3 per rev distortion is also plainly seen in the frequency magnitude plots. The third harmonic, at 455 hertz, is obviously the dominant one. In the magnitude plots, the third harmonic is actually the fourth bar. This is because the first bar represents the zeroeth harmonic, or the magnitude associated with the average total pressure. Since all data sets were mean-zeroed, this value is zero. Any magnitude associated with the zeroeth harmonic as predicted by the model is an error.

As seen in Figures 7-4 through 7-8, the model does a good job of replicating the overall shape of the distorted pressure profile in the time domain at all radial locations with the exception of RI1, near tip. In the frequency domain, Figures 7-9 through 7-13, the model seems to do an even better job of accurately predicting the magnitude of the dominant harmonic associated with the distorted pressure profile. At 9100 rpm, a three per rev distortion screen was used to create the total pressure distortions. This is plainly evident when looking at both the time domain and frequency domain plots. In Figures 7-9 through 7-13, it can be seen that the frequency associated with the third harmonic is approximately 450 hz. It can also be seen in the magnitude plots (Figures 7-9 through 7-

13) that the distortion is strongest from the hub to the center of the blade with the magnitude decreasing to half the strength at the tip. In this test, the model is more accurate in that region as well. Despite the fact that this is coincidental, it is encouraging just the same.

Table 7-1 shows how each of the three models performed in this particular test. The best performer at each radial immersion is highlighted in blue in the frequency domain and red in the time domain. Since the goal of predicting total pressure distortion transfer is to help eliminate the incidence of high cycle fatigue, the prediction of the dominant harmonic in the frequency domain was chosen as the more important over the time domain prediction. The best performer in the frequency domain is highlighted in blue for this reason.

| domain | Model 1 | | Model 2 | | Model 3 | |
|-----------------|---------|---------|---------|---------|---------|---------|
| | time | freq | time | freq | time | freq |
| radial position | std | % error | std | % error | std | % error |
| RI5 - hub | 0.068 | -1.0% | 0.084 | -4.6% | 0.054 | -1.5% |
| RI4 | 0.051 | -1.0% | 0.042 | -0.6% | 0.044 | -1.1% |
| RI3 | 0.049 | 0.0% | 0.044 | 0.0% | 0.042 | -0.5% |
| RI2 | 0.068 | -1.8% | 0.064 | -2.4% | 0.066 | -4.2% |
| RI1 - tip | 0.077 | -15.0% | 0.082 | -16.0% | 0.074 | -16.0% |

Table 7-1: Prediction results when replicating the same data used in kernel calculation(9100NOL) in the time and frequency domain of each model. Best prediction is highlighted in blue in the frequency domain and red in the time domain.

All three models performed very well with there being little difference in the standard deviation of their predictions as well as the percent error of the dominant harmonic magnitude. Model 1, however, did have the lowest error rate. Model 1 also has the least complicated basis function of the three and subsequently, has the shortest run time. Since in this test only one data set was being evaluated at a time, run time wasn't as much of an issue, although there is a definite difference. Model 1 takes approximately 10 minutes to extract the kernels and then replicate or predict the output waveform, Model 3 being the most complicated needs approximately 2 hours, and Model 2 requires approximately 30 minutes.

The second level of testing done in this phase of analysis involves using three of the four data sets at the same rotational speed (different mass flows) for kernel calculation and then predicting the system response for the fourth mass flow. Remembering that mass flow variation at the same rotational speed has little impact on distortion transfer [Section 5.4]; this is still not a very difficult test. It is, however, a logical progression in assessing each model's capabilities before attempting prediction at an operating condition completely different from those used in kernel calculation. In these tests, data sets from 9500 NOL, NS and PE were used in the kernel calculation stage and then the compressor output was predicted at 9500WOD. The results of the predictions of Model 1 are shown in Figures 7-14 through 7-23 and are in the same format as before, 7-14 through 7-18 are in the time domain with 7-19 through 7-23 depicting the magnitude plots in the frequency domain of those same predictions. Once again, the input waveform is not shown in these plots, just the measured output and the model's prediction.

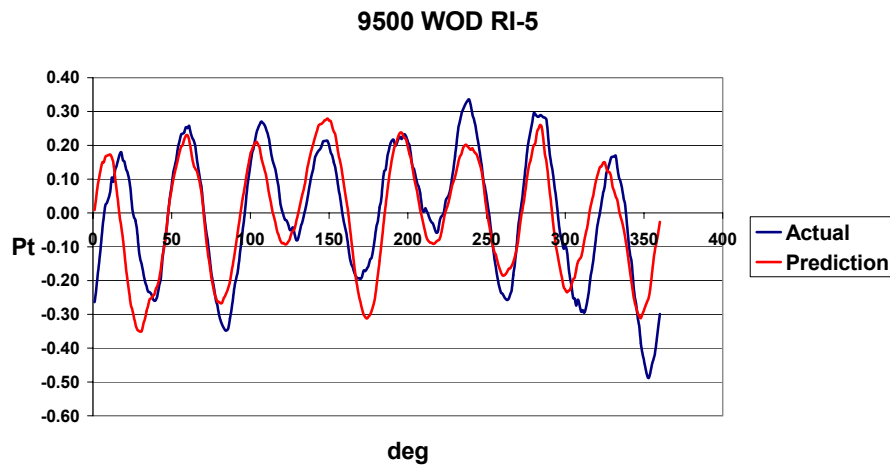


Figure 7-14: Prediction of Model 1 of the output variation in total pressure at 9500WOD, RI5 after calculating the system kernels with the other data sets at that same rotational speed.

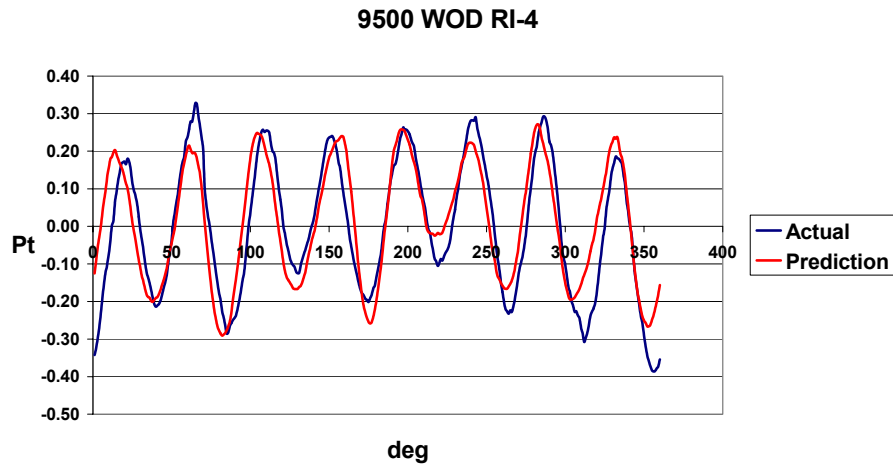


Figure 7-15: Prediction of Model 1 of the output variation in total pressure at 9500WOD, RI4 after calculating the system kernels with the other data sets at that same rotational speed.

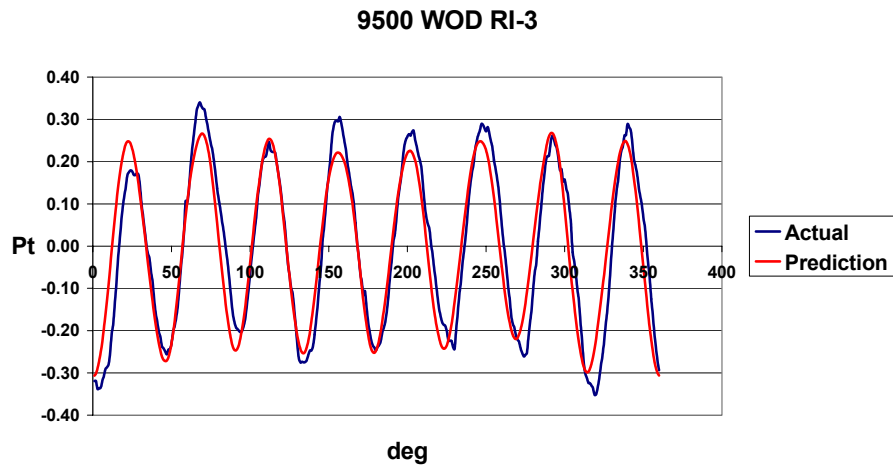


Figure 7-16: Prediction of Model 1 of the output variation in total pressure at 9500WOD, RI3 after calculating the system kernels with the other data sets at that same rotational speed.

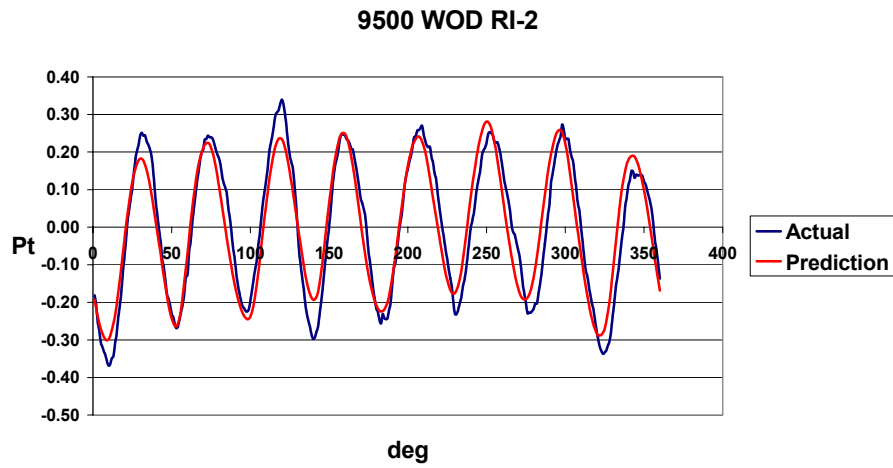


Figure 7-17: Prediction of Model 1 of the output variation in total pressure at 9500WOD, RI2 after calculating the system kernels with the other data sets at that same rotational speed.

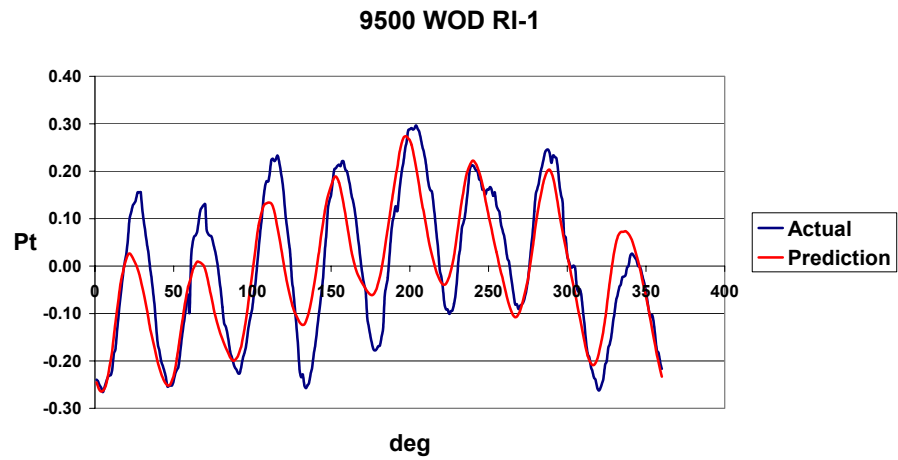


Figure 7-18: Prediction of Model 1 of the output variation in total pressure at 9500WOD, RI1 after calculating the system kernels with the other data sets at that same rotational speed.

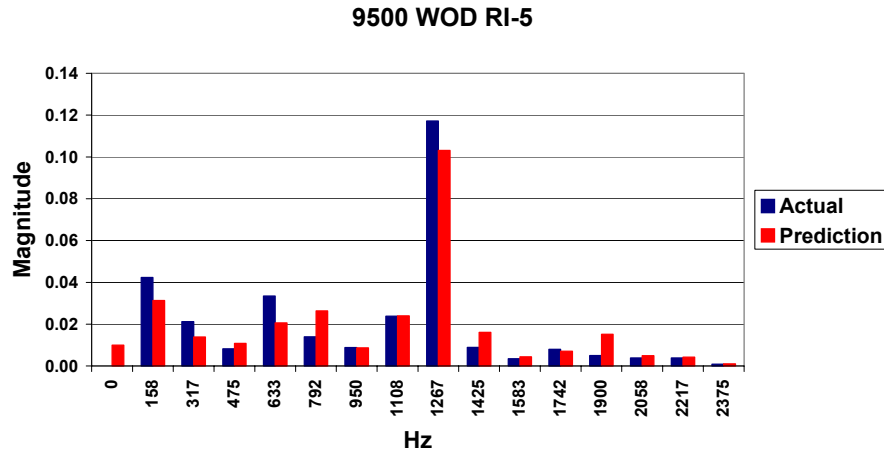


Figure 7-19: Magnitude plot in the frequency domain of the output variation in total pressure corresponding to Figure 7-14 that was made with Model 1.

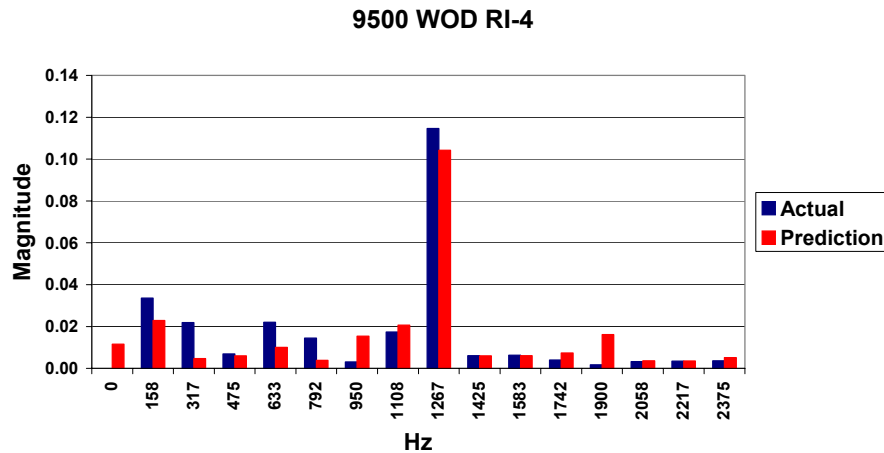


Figure 7-20: Magnitude plot in the frequency domain of the output variation in total pressure corresponding to Figure 7-15 that was made with Model 1.

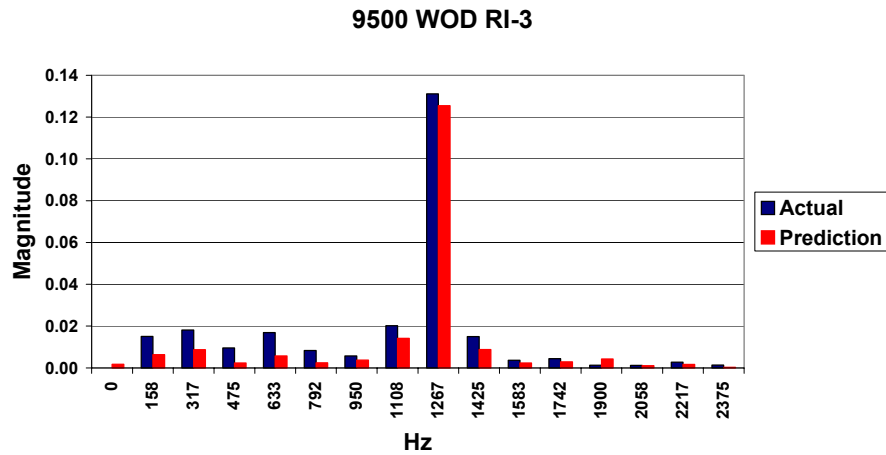


Figure 7-21: Magnitude plot in the frequency domain of the output variations in total pressure corresponding to the prediction shown in Figure 7-16 that was made with Model 1.

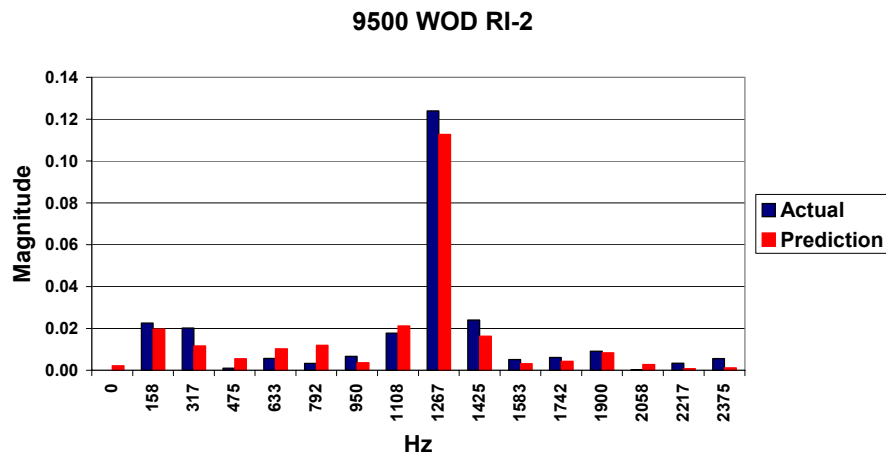


Figure 7-22: Magnitude plot in the frequency domain of the output variations in total pressure corresponding to the prediction shown in Figure 7-17 that was made with Model 1.

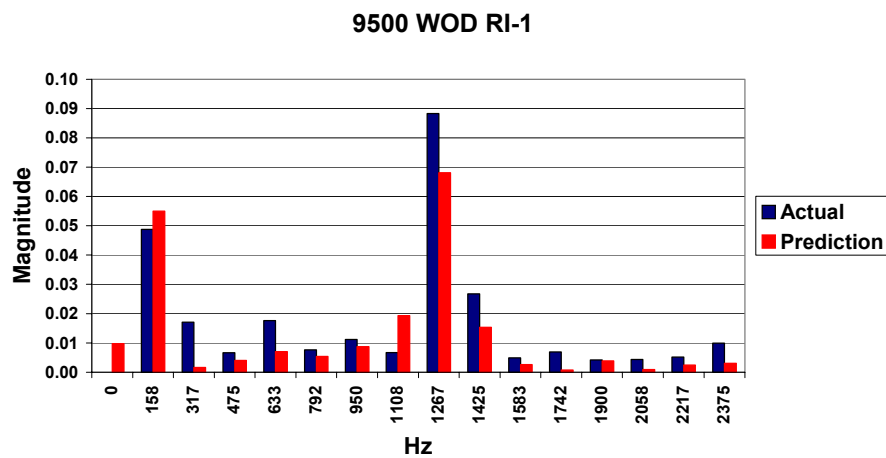


Figure 7-23: Magnitude plot in the frequency domain of the output variations in total pressure corresponding to the prediction shown in Figure 7-18 that was made with Model 1.

One of the first things noticed in these plots is that a different type of distortion screen was used at this rotational speed, an 8 per rev. This can be seen in both the time domain and the frequency domain plots. In the time domain, there are 8 peaks and valleys of total pressure variation about the mean corresponding with the 8 higher density areas in the distortion screen that was used. It can also be seen that there is not a dramatic difference in the magnitude of the peaks, meaning that the screen is made up of 8 identical and repeating sections of higher and lower density material. In the frequency domain plots, the 8 per rev distortion is obvious by the larger magnitude of the 8th harmonic, occurring at just under 1270 hertz.

Since the level of difficulty is not much greater in this test than the first series of tests (replication of the same waveform used in kernel calculation), the results also look quite good in the time domain as well as the frequency domain. It is difficult to see much difference in the time domain plots from the previous tests. The prediction of the magnitude of the dominant frequency is not quite as good as in the previous tests, but it is still very close to the actual data measurements. Table 7-2 shows the standard deviation of the prediction and the percent error of the magnitude of the dominant harmonic for each model. The format of Table 7-2 is identical to that of Table 7-1, with the best prediction highlighted in blue in the frequency domain and red in the time domain.

| domain | Model 1 | | Model 2 | | Model 3 | |
|-----------------|---------|---------|---------|---------|---------|---------|
| | time | freq | time | freq | time | freq |
| radial position | std | % error | std | % error | std | % error |
| RI5 - hub | 0.115 | -11.9% | 0.119 | -9.4% | 0.111 | -12.8% |
| RI4 | 0.092 | -9.6% | 0.094 | -8.7% | 0.091 | -7.8% |
| RI3 | 0.072 | -4.6% | 0.08 | -5.3% | 0.071 | -6.1% |
| RI2 | 0.064 | -8.9% | 0.07 | -12.9% | 0.06 | -6.5% |
| RI1 - tip | 0.079 | -22.7% | 0.081 | -20.5% | 0.078 | -23.9% |

Table 7-2: Prediction results of compressor output at 9500WOD from 9500NOL, NS, and PE in the time and frequency domain are shown.

Once again, the difference between the three models is not dramatic and any one of them could be used with confidence to predict the output pressure profile of an alternate mass flow at the same rotational speed. Nevertheless, Model 3 is the clear winner of the three in the time domain. The results are fairly evenly split in the frequency domain, however, which is the more important of the two when dealing with

high cycle fatigue. The very slight increase in accuracy in the time domain comes at a fairly high cost in processing time. Model 3 took approximately 4 hours to run, the other two models were finished in less than 45 minutes.

Realizing however, that the impact of mass flow on distortion is minimal, there really is not a need to predict distortion transfer at variable mass flow but constant rotational speed. Once data is measured at one mass flow at any rotational speed, the data in this study indicates that the variation in total pressure about the mean at any other mass flow would be the same [Section 5.4].

7.3 Different Speed Predictions

The final and true test of the Volterra models is to predict the compressor response to an input at operating conditions completely different from those that were used during kernel extraction. For these tests and as discussed in section 6.4, all data sets at 9100rpm and 13200rpm were used for kernel extraction. By using these data sets, the kernels will contain information pertaining to the response of the compressor stage to a 3 per rev and an 8 per rev distortion as well as two rotational speeds, 9100 and 13200rpm. Predictions were then made using the input waveforms measured at 9500rpm, NOL mass flow using the previously calculated kernels. Figures 7-24 through 7-33 show the predictions of Model 2 as compared to the measured output data.

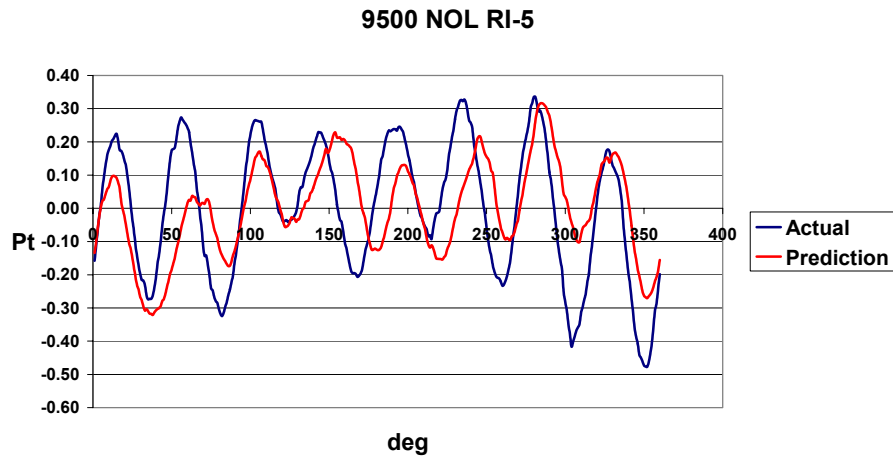


Figure 7-24: Prediction of Model 2 of the output variation in total pressure at 9500NOL, RI5 after calculating the system kernels with the data sets from the other two rotational speeds.

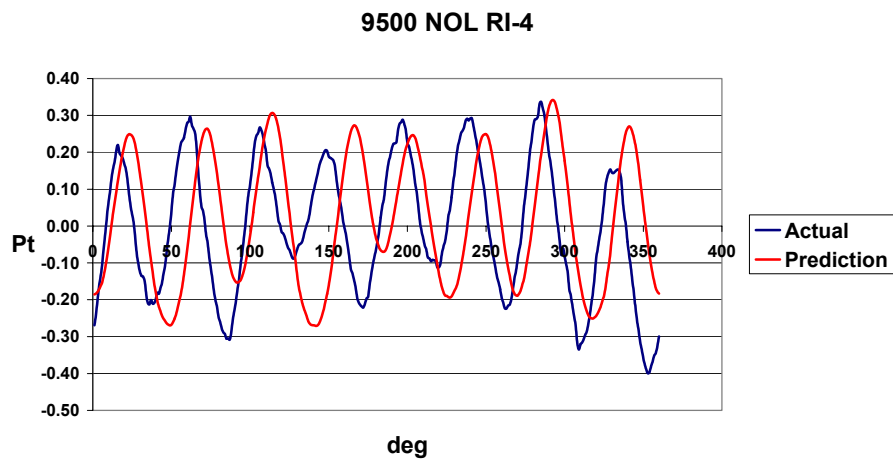


Figure 7-25: Prediction of Model 2 of the output variation in total pressure at 9500NOL, RI4 after calculating the system kernels with the data sets from the other two rotational speeds.

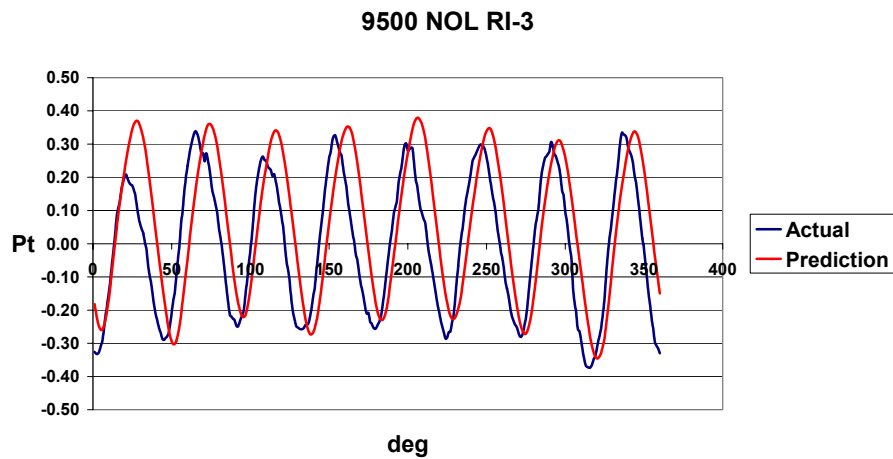


Figure 7-26: Prediction of Model 2 of the output variation in total pressure at 9500NOL, RI3 after calculating the system kernels with the data sets from the other two rotational speeds.

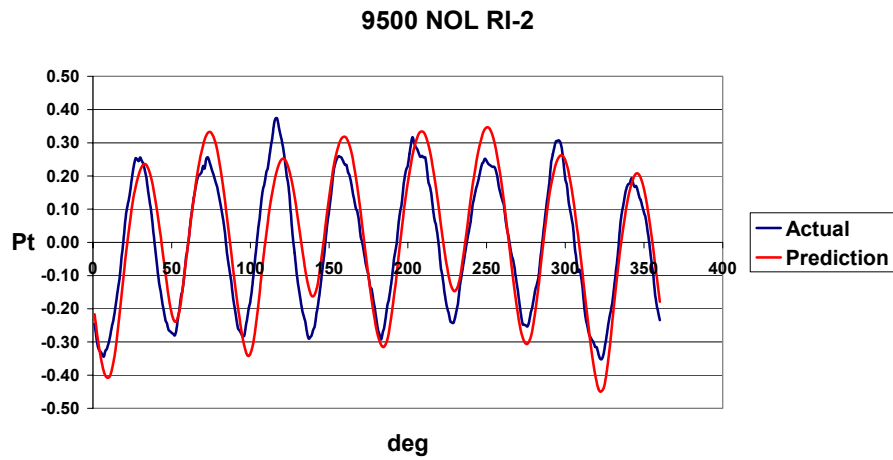


Figure 7-27: Prediction of Model 2 of the output variation in total pressure at 9500NOL, RI2 after calculating the system kernels with the data sets from the other two rotational speeds.

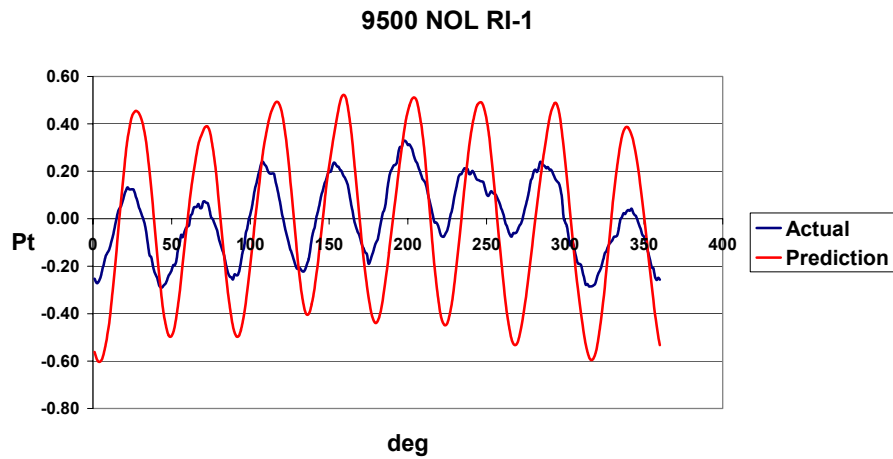


Figure 7-28: Prediction of Model 2 of the output variation in total pressure at 9500NOL, RI2 after calculating the system kernels with the data sets from the other two rotational speeds.

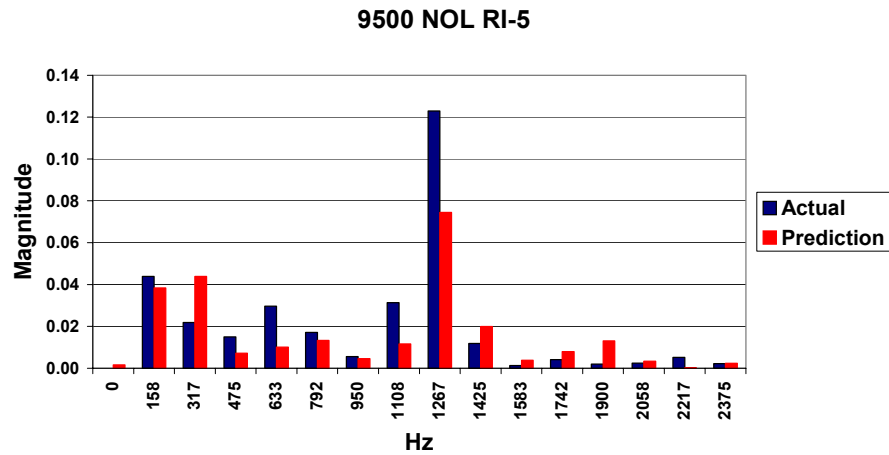


Figure 7-29: Magnitude plot in the frequency domain of the output variation in total pressure corresponding to the prediction shown in Figure 7-24 that was made with Model 2.

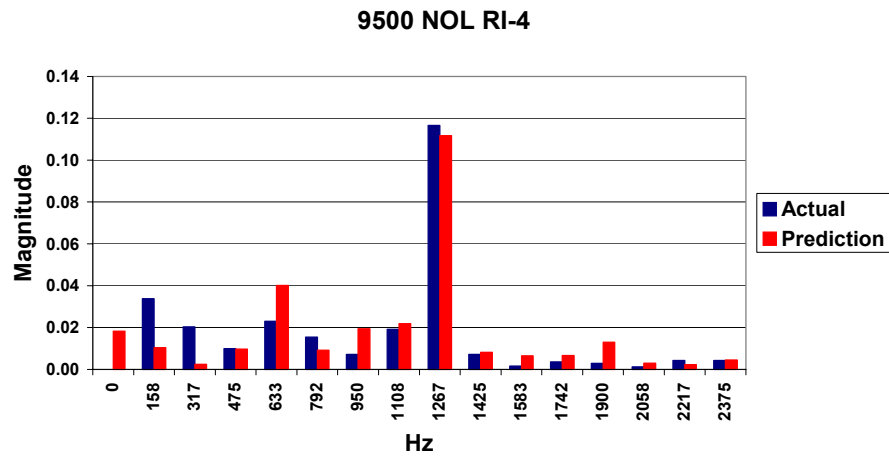


Figure 7-30: Magnitude plot in the frequency domain of the output variation in total pressure corresponding to the prediction shown in Figure 7-25 that was made with Model 2.

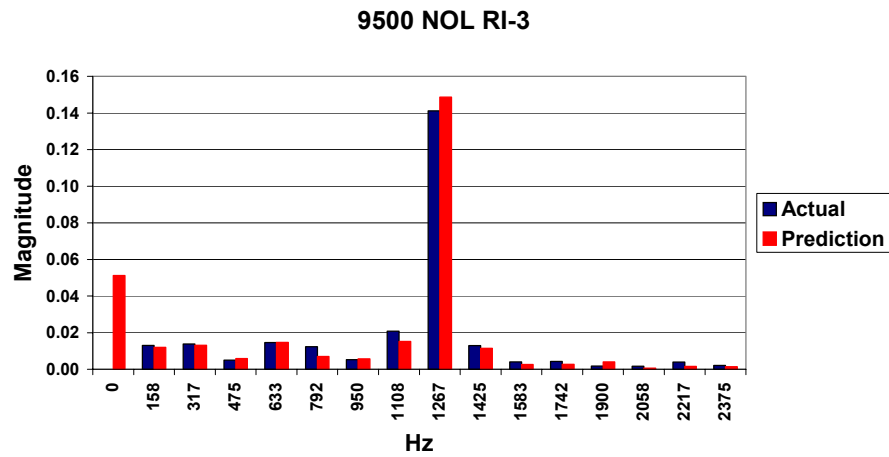


Figure 7-31: Magnitude plot in the frequency domain of the output variation in total pressure corresponding to the prediction shown in Figure 7-25 that was made with Model 2.

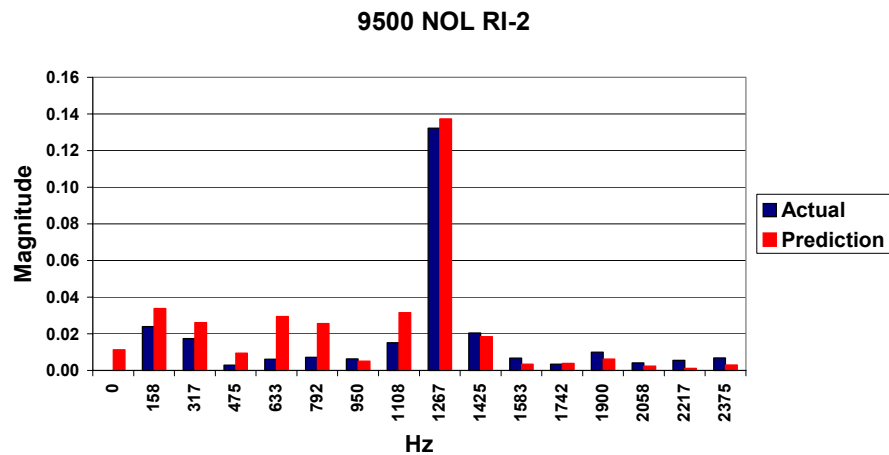


Figure 7-32: Magnitude plot in the frequency domain of the output variation in total pressure corresponding to the prediction shown in Figure 7-26 that was made with Model 2.

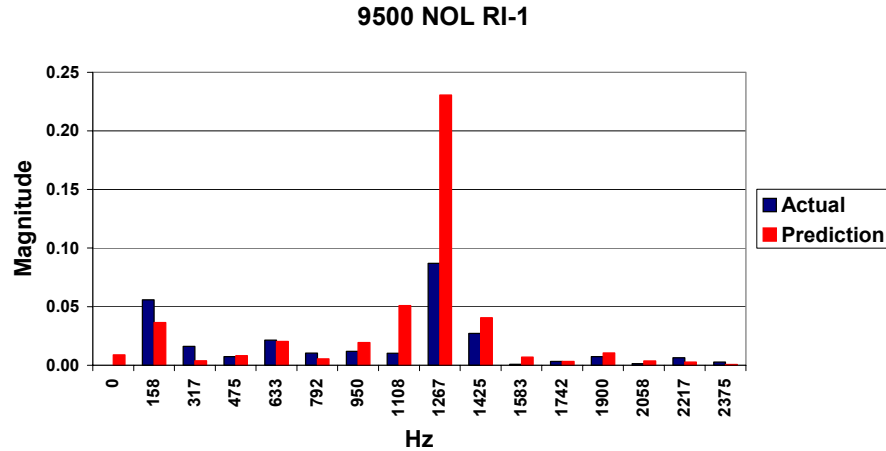


Figure 7-33: Magnitude plot in the frequency domain of the output variation in total pressure corresponding to the prediction shown in Figure 7-27 that was made with Model 2.

The predictions of all three models were not as accurate in these tests, which was suspected due to the increased difficulty. Prediction results also varied dramatically dependent on radial location. All three models were much more accurate at the three interior points of the blade than at the hub and tip where performance was not near as good. It was also revealed in these tests that Models 1 and 3 did not account for the rotational speed dependence adequately. Normalizing the input and output data sets with a non-dimensional work term as discussed in Section 6.3 helped to correct this deficiency [Cousins, 2002].

An example of the impact of normalizing the data sets with non-dimensional stage work within Model 1 is shown in Figures 7-34 through 7-37. Figures 7-34 and 35 show the prediction of output variation in total pressure at 9500rpm, NOL mass flow, RI3 (mid-span) in the time domain and also the magnitude value in the frequency domain. Figures 7-36 and 37 show the prediction results at the same operating condition after normalizing the data sets with non-dimensional stage work.

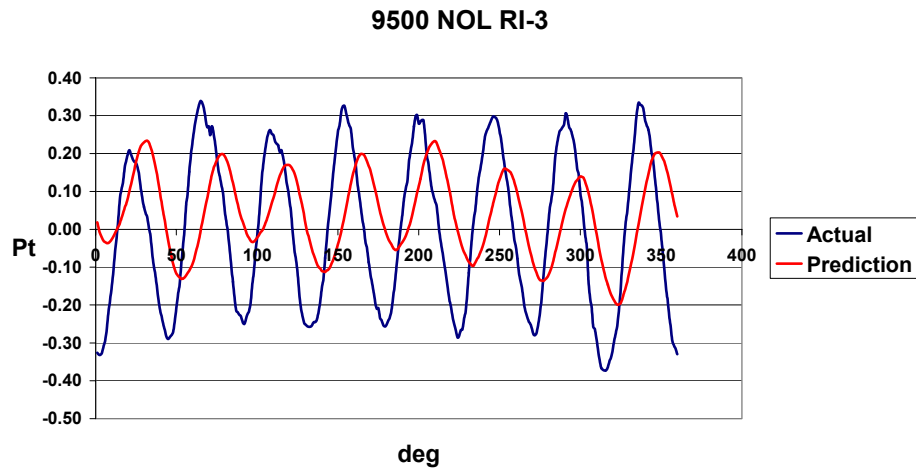


Figure 7-34: Prediction of Model 1 of the output variation in total pressure at 9500NOL RI3, after calculating the system kernels with the data sets measured at 9100 and 13200rpm.

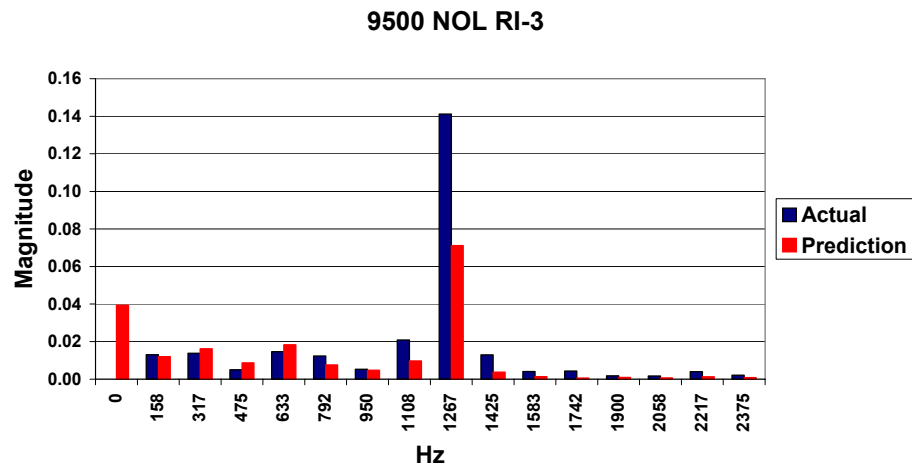


Figure 7-35: Magnitude plot in the frequency domain of the output total pressure prediction show in Figure 7-34.

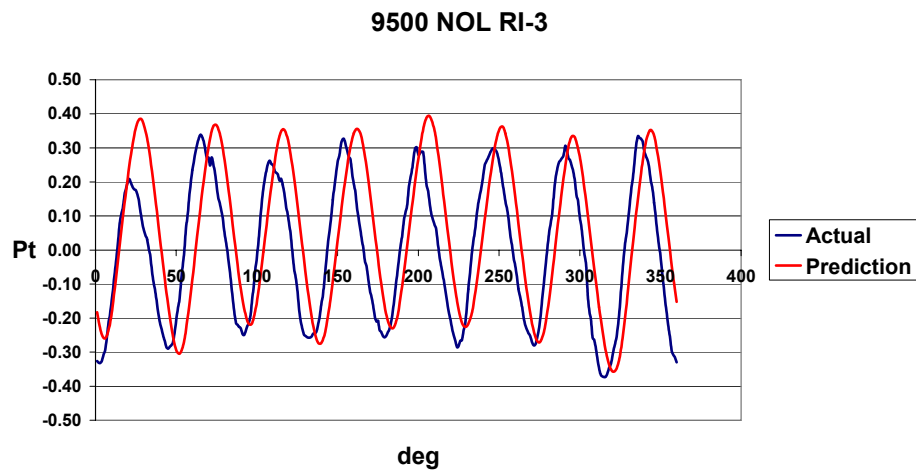


Figure 7-36: Same scenario as in Figure 7-34, only data sets were further normalized with the non-dimensional stage work.

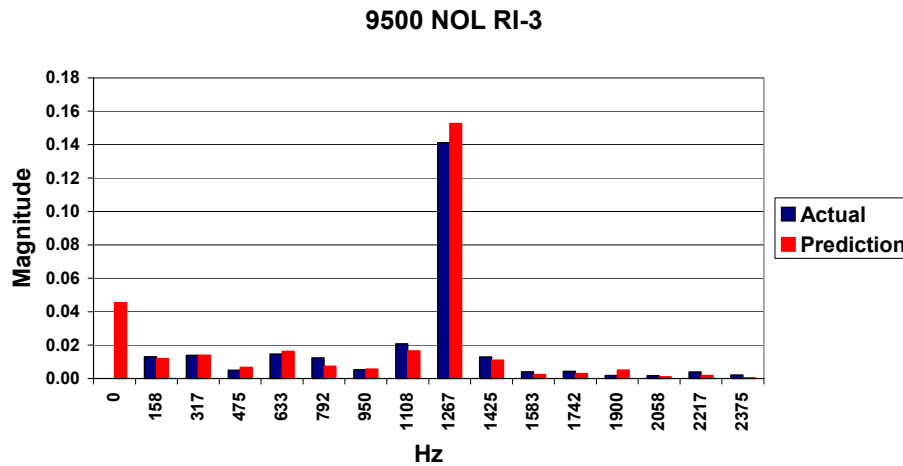


Figure 7-37: Magnitude plot in the frequency domain of the output total pressure prediction shown in Figure 7-36.

As shown in the preceding figures, the prediction accuracy of Model 1 is dramatically improved by taking the stage work into account. When normalizing the data sets, the input and output data sets were divided by the stage work term as defined in Section 6.3 within the code at the same time the data sets were mean-zeroed and non-dimensionalized. This was done to both the input and output waveforms used in the kernel extraction phase and the input waveform used in the prediction phase. The prediction was then multiplied by this work term as well as the non-dimensional term to obtain the final, dimensional, prediction. The improvement results were not as dramatic with Model 3, but the final predictions were still more accurate with work normalization than without. Table 7-3 shows the prediction results numerically of each model and is in the same format as Tables 7-1 and 2. The prediction results of Models 1 and 3 as shown in the table have been work normalized.

| domain | Model 1 | | Model 2 | | Model 3 | |
|-----------------|---------|---------|---------|---------|---------|---------|
| | time | freq | time | freq | time | freq |
| radial position | std | % error | std | % error | std | % error |
| RI5 - hub | 0.155 | -42.3% | 0.171 | -39.0% | 0.201 | -90.2% |
| RI4 | 0.153 | -4.3% | 0.227 | -4.3% | 0.152 | -47.9% |
| RI3 | 0.176 | 8.5% | 0.167 | 5.7% | 0.241 | 12.8% |
| RI2 | 0.077 | 3.8% | 0.091 | 3.8% | 0.297 | 25.0% |
| RI1 - tip | 0.289 | 177.0% | 0.253 | 164.4% | 0.429 | 141.4% |

Table 7-3: Prediction results made at 9500NOL after kernel calculation with 9100 and 13200-rpm data.

Despite the fact that the models are evenly split when comparing time domain predictions, Model 2 is the best of the three by a slim margin over Model 1 after

considering the frequency domain results. Even though predictions are not very good at the hub and tip, results at the interior points of the blade are a different matter, with less than 6% error of the dominant frequency magnitude as predicted by Models 1 and 2. This low error rate is especially significant since the models were predicting compressor response to an input measured at a rotational speed that was not at all included in kernel calculation.

In order to further assess Volterra modeling, one more test scenario was created. The goal of this test was to see if the Volterra models were capable of predicting distortion transfer at a frequency that was not included in the training data sets. The best option for this type of scenario would be to use data for kernel calculation and prediction that was collected at the same rotational speed, but with two different types of distortions, therefore two different dominant frequencies. One of the distortion types could be used in kernel training and the other in the prediction phase. Unfortunately, none of the rotational speeds included in the data had been exposed to two types of distortions. Two of the speeds, however, were very close to one another, 9100 and 9500rpm. Therefore, the 9100rpm data sets were used for kernel training and compressor response was predicted at 9500rpm. Rather than showing time and frequency domain plots of all the predictions along the span of the blade, Table 7-4 summarizes the standard deviation of the prediction in the time domain and percent error of the magnitude of the dominant frequency harmonic as predicted by Model 2.

| domain | Model 2 | |
|-----------------|---------|---------|
| | time | freq |
| radial position | std | % error |
| RI5 - hub | 0.221 | -64.2% |
| RI4 | 0.229 | -0.9% |
| RI3 | 0.111 | 16.3% |
| RI2 | 0.882 | 76.2% |
| RI1 - tip | 0.876 | 273.6% |

Table 7-4: Summary of results obtained with Model 2 when predicting compressor output at 9500NOL after calculating the kernels with 9100rpm data.

The results shown in Table 7-4 indicate that the Volterra model is not able to accurately predict distortion transfer at a frequency not included in the initial kernel calculation phase. While it would be very nice if the predictions obtained in this test were more accurate, it is logical that they are not. This is not the same as predicting at a different rotational speed. Differences in rotational speed are accounted for through the non-dimensional and normalization parameters that are used within the code. There are no such parameters to deal with variations in excitation frequency. Therefore, the frequency of concern must be included in the data sets used for kernel calculation. This is especially challenging when creating distortions with screens, as a screen is designed to contain energy at specific frequencies and have very little energy anywhere else. Because of this, distortion screen selection to generate data sets for kernel training is critical.

All of the models created were coded in Matlab with the final prediction results cut and pasted into Excel. This was done solely due to the ease of data storage and display that Excel offers. The actual output of the Matlab code presented the prediction results in a manner very similar to what has been shown. An example of what the output looked like is shown in Figure 7-38.

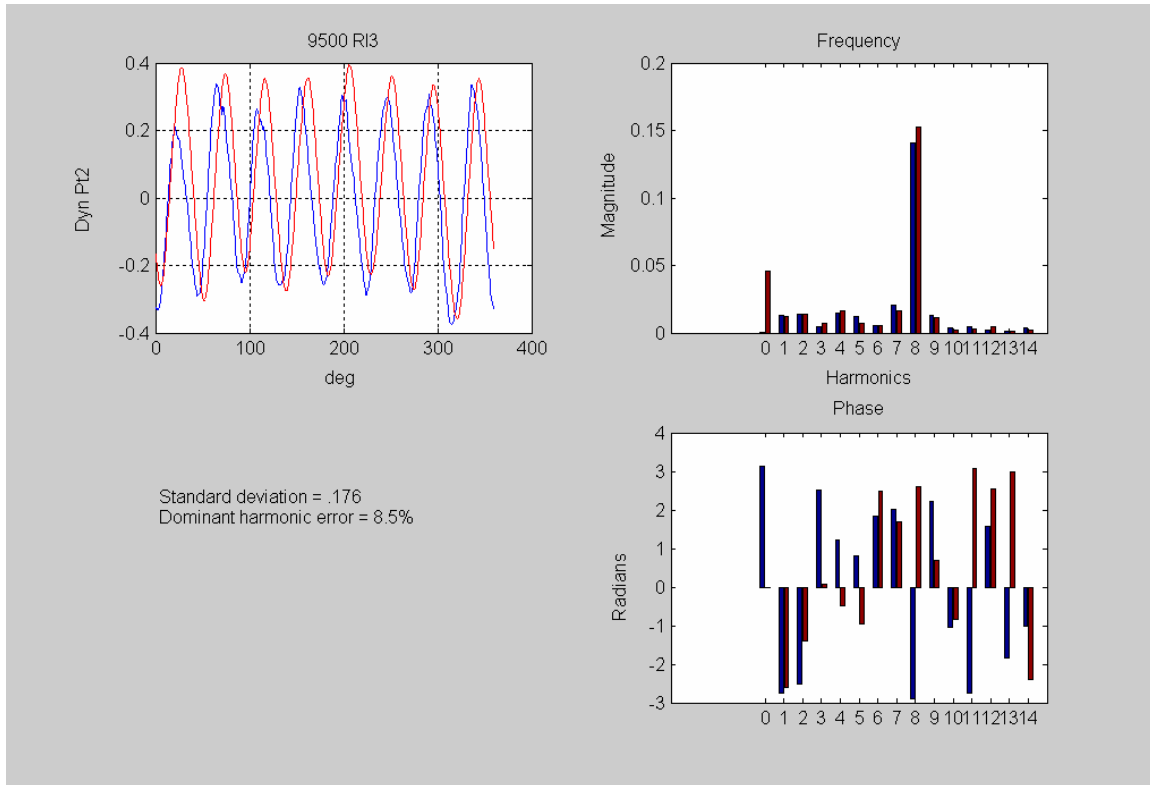


Figure 7-38: Example of the output in Matlab of a prediction of the variation in total pressure at 9500rpm, NOL mass flow, RI3 (mid span). Blue coloring corresponds to the actual experimental data and red the prediction.

7.4 Higher-Order Effects

In this section, the influence that each of the higher order kernels has on the final prediction will be examined. The highest order of operation that any of the three Volterra models is capable of analyzing is third order. One reason for truncating the Volterra series after the third term is the extremely large number of coefficients that would be required to solve for if more terms were used. A fourth order model with 10 basis functions per order would require solving for $10 + 10^2 + 10^3 + 10^4$ (11,110) coefficients. This would more than likely require a great deal more data than is currently available. Besides, the whole idea of using Volterra theory in system modeling is that the system is “weakly” non-linear, meaning that the higher order impulse response functions, or kernels, fall off to zero very rapidly.

Within the code, all of the coefficients that make up each separate kernel are calculated concurrently. However, once the coefficients are known each individual

kernel is calculated separately. The first, second, and third-order kernels are then used to separately calculate the first, second, and third-order terms associated with the final response prediction. The final prediction is the summation of these three terms. Figure 7-39 shows each of the three terms plotted separately and the final summed prediction of compressor response at 9500rpm, NOL mass flow. In this particular scenario, the kernels were calculated with the same waveform that is being predicted, part of the same tests that were discussed in the beginning of section 7.2.

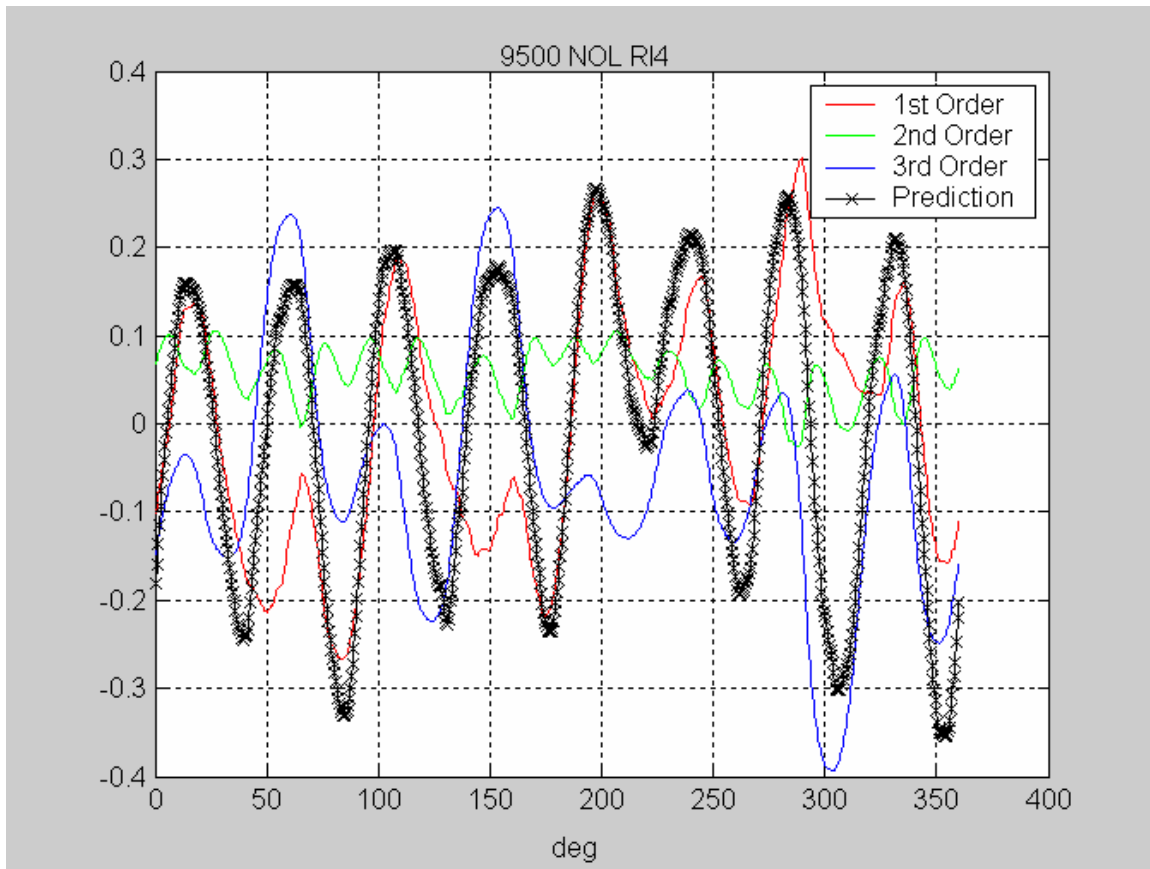


Figure 7-39: Graphical display of the 1st, 2nd, and 3rd order terms and their combination to form the final response prediction using Model 2.

In Figure 7-39 it can be seen that each term or “sub” prediction is independent of the other two and that when added together, their sum forms the final response prediction. The significance of each order of operation is also evident by the influence of each “sub” prediction. This particular case is primarily a 1st and 3rd order operation with the second order effects just wavering between 0 and 0.1.

7.5 Comparison with Previous Models

As discussed in Chapters 2 and 5, my research data has been used for two previous projects at Virginia Tech with the goal of all three being distortion transfer prediction in an axial compressor. Matt Small [2001] used a “tuned” frequency response function (FRF) modeling method and Jon Luedke [2001] created the first Volterra series models, prompting the interest in that same modeling method for my work. An advantage to all of us using the same data is that direct comparison of modeling methods/results is easily accomplished. As Luedke compared his results to Small at the end of his research, I will also compare my results with those of Luedke and Small in this section.

In Small’s, Luedke’s, and my research, the models all initially “learn” about the system they are representing using experimental data (the kernel training phase in my work). In Table 7-5, prediction results of the tuned FRF [Small, 2001], Volt 33 [Luedke, 2001], Volt 33 Rad [Luedke, 2001], and Model 2 are compared with the percent error of the dominant frequency magnitude as the means of comparison. The operating condition that is being predicted by all three is 9500PE. Model 2 and the FRF model both used all data sets at 9100 and 13200rpm in the initial training phase, while the Volt 33 model used the following: 9100PE, 9100WOD, 9500NOL, and 9500NS. Even though the mass flow is different, it is worth noting that the Volt 33 models in this particular case are predicting compressor response at a rotational speed that is also used in model training. Model 2 and Volt 33 Rad are streamline specific, the other two use data and make predictions along the entire span of the blade. Model 2 and Volt 33 Rad must be run five separate times in order to predict compressor response along the entire span of the blade.

| radial position | FRF | Volt 33 | Volt 33 Rad | Model 2 |
|-----------------|---------------|---------------|---------------|--------------|
| R15 - hub | -52.7% | -87.9% | -37.2% | -39.0% |
| R14 | -40.1% | -52.4% | -40.6% | -4.3% |
| R13 | -13.6% | -34.2% | -8.7% | 5.7% |
| R12 | -47.6% | -12.0% | -25.3% | 3.8% |
| R11 - tip | -7.6% | 27.6% | 161.0% | 164.4% |
| Avg error | 32.3% | 42.8% | 54.6% | 43.4% |
| w/o hub & tip | 33.8% | 32.9% | 24.9% | 4.6% |

Table 7-5: Comparison of Model 2 with previous modeling methods. The percent error of the dominant frequency magnitude is shown.

In Table 7-5, all predictions at individual radial positions that are within the acceptable error rate of 20% are highlighted in red and the best, or lowest, average percent error is highlighted in blue. Model 2 is more consistently accurate at the interior radial positions on the blade. The tuned FRF method has the lowest average error, although it is still greater than the 20% cut-off with two of its individual predictions within that same cut-off. The final average error was calculated by only considering prediction performance at the three interior blade positions. Model 2 has the best results in this category with less than 5% average error at the three interior points along the blade.

8 Summary and Conclusions

The transfer of circumferential total pressure distortion in a transonic axial compressor has been investigated. A semi-empirical modeling method has been developed, using nonlinear Volterra theory, in order to predict the transfer of circumferential total pressure distortion. This modeling method is based on calculating, or extracting, the 1st, 2nd, and 3rd order impulse response functions (kernels) from experimental data. It has been shown in this study that modeling methods using nonlinear Volterra theory are capable of predicting the transfer of total pressure distortion in axial compressors and fans – with limitations.

Properly identifying the Volterra kernels is essential; once the kernels of a system are known, the output for any arbitrary input can be accurately calculated. The solution method presented is based on expanding the unknown kernels into basis function space. The basis functions are multiplied by the input to the system, forming what is known as the motion matrix. Now a matrix problem has been formed where the system output is equal to the motion matrix multiplied by some unknown coefficients. The coefficients are solved for in a least squares sense using a regularization technique called singular value decomposition.

In the work presented, three different models were created using various forms of higher order basis functions and/or integration methods. The best of the three models was able to predict the dominant frequency magnitude associated with total pressure distortion transfer to within a 5% error rate along the interior points of the blade. These predictions were done at operating conditions that the model had not previously seen before, which is especially significant. Also of importance is the fact that the largest magnitude associated with distortion transfer is at the mid-span of the blade, where the prediction is the most accurate. Prediction results at the hub and tip, however, proved to be unreliable. This can be explained by referring to the distortion magnitude transfer plot, Figure 5-14, as shown below.

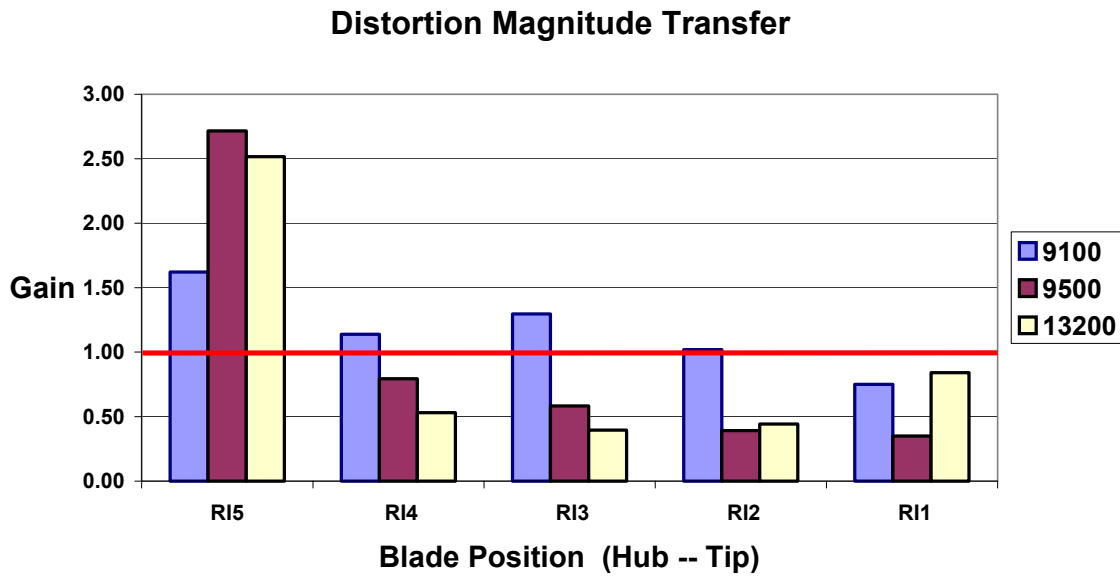


Figure 5-14. First stage distortion magnitude gain as a function of blade position and rotational speed.

In the above plot, distortion transfer at the interior points of the blade (RI4, 3, and 2) follows a trend. The distortion transfer at 9100 is larger than that at 9500, which is larger than the distortion transfer at 13200. This is most certainly true at RI4 and 3 and very close to being true at RI2. This trend, however, is not followed at the hub and tip of the blade, with the distortion transfer either being much larger (hub) or smaller (tip) at 9500rpm than at the other two rotational speeds. Data at two rotational speeds was used in kernel calculation, 9100 and 13200rpm. System response was then predicted at 9500rpm, which at these two points on the blade is very atypical when compared to distortion transfer at the other two speeds. This explains why the model is not capable of accurately predicting distortion transfer at the hub and tip. If Figure 5-14 did not have any information pertaining to distortion transfer at 9500rpm, one would expect the gain associated with 9500rpm to fall somewhere between the gain associated with 9100 and 13200rpm. That is exactly what happens on the interior points of the blade, consequently resulting in good model performance. At the other two points on the blade this does not happen, resulting in an under-prediction at the hub and an over-prediction at the tip.

The frequency range of interest must be included in the training data sets. In other words, if one is interested in the transfer of a 4 per rev distortion and that coincides with a frequency of 500hz; the data sets used for kernel training must have some

frequency content at 500hz. Otherwise, the model will have no idea how the system responds to energy contained at that particular frequency and will, subsequently, be unable to accurately predict system response. As discussed in Chapter 7, this presents a challenge when testing with distortion screens as screens are designed to have significant energy at a specific frequency and very little anywhere else.

Finally, the speed of prediction should be between the speeds used for kernel calculation. The data sets used for kernel training should be considered as the limits of known performance with all predictions done within these limits. Although this is not a linear process, an analogy can be made to interpolation as opposed to extrapolation.

The goals of this particular study were initially discussed in Chapter 1 and will be re-iterated here: (1) create a semi-empirical model capable of accurately predicting total pressure distortion transfer in fans and compressors, (2) extract the frequency components of non-uniform pressure profiles to enable the prediction of blade response, and (3) use the combined pressure and blade response predictions as a tool to identify potential HCF problem areas. The first goal has definitely been attained with the limitations as discussed in this chapter. The frequency components associated with total pressure distortion have also been extracted, although this research did not include actually applying these frequencies to a blade model in order to predict blade response/stress. This work is part of another study at Virginia Tech being carried out by Rob Wallace for his Masters thesis. Part of the third goal has also been attained in that this study has shown that total pressure distortion is definitely transferred through an axial compressor stage and that the accurate identification of the dominant frequency magnitude associated with that distortion can be accomplished at mid-span conditions via Volterra modeling.

9 Recommendations

This study has shown that Volterra modeling is capable of accurately predicting total pressure distortion transfer in axial compressors and fans within specific limitations at mid-span conditions. While promising, this study was done with limited data and therefore, more research and testing of this modeling method should be done before even considering its use in industry.

The next step in testing should be the use of a total pressure distortion generator that produces wide-band frequency content. Use a distortion generator that has significant frequency content within the first 8 – 12 harmonics to generate data sets when testing a compressor. Collect data at two rotational speeds, the lower and upper limit in the range of operation, using this distortion generator. Use these data sets in the kernel-training phase of the model. After the kernels have been calculated, predict compressor response using data that was collected using a specific per rev distortion screen, such as the 3 or 8 per rev used in this study. If the prediction results are similar to those obtained in this study, the usefulness of Volterra modeling will be even greater.

The models created in this study are semi-empirical models, meaning that rather than being purely mathematical, the physics of the flow was considered and incorporated as non-dimensional parameters. Quantities such as velocity and pressure were non-dimensionalized by relevant physical parameters, such as U^2 and dynamic pressure, $\frac{1}{2} \rho W^2$, in order to bring some physics and fluid dynamics into the math model. Thought should be given to incorporating even more physics-based parameters into the models to better account for phenomena associated with transonic flow, such as shocks.

Also, this study revealed the strong radial dependence of total pressure distortion transfer. As a result of this finding, the models created were streamline specific, calculating the impulse response functions as functions of time for one point along the span of the blade. The next step to better understand the way in which a compressor stage responds to an impulse is to develop a model that calculates the impulse response functions as a function of time and radial position. In other words, adding a radial dimension to the impulse response functions so that they could be used to calculate the

system response along the entire span of the blade, rather than at just one point, for example $y(r,t) = \int h(r,t)x(t-\tau)d\tau + \dots$ where, perhaps $h(r,t) = f(r)h(t)$.

More testing is needed to further understand compressor response at the hub and tip of the blade. What was observed in this study could have been a result of boundary layer or secondary flow effects. Another thought is that the model at the tip should account for the tip gap between the end of the blade and the outer wall of the compressor. Whatever the cause for the unusual gain associated with distortion transfer at these two blade locations, more data is needed before it can be fully understood.

10 Postscript

While it has been shown that Volterra modeling is capable of predicting total pressure distortion transfer, the dominant driver in HCF, the question remains as to the usefulness of this type of modeling. Does Volterra modeling actually have an application in industry and, if so, what is it? First, before that question can be confidently answered in the positive or negative, more testing must be done utilizing data collected under many different operating conditions. The data used for this study, besides being very informative and useful in the development of this model, is limited to 12 different operating conditions that, after examination, can essentially be reduced down to 3 data sets (one for each rotational speed) at each radial location on the blade. This is not enough information to truly test any modeling method. All of this being said, Volterra modeling has shown definite potential in its ability to accurately predict the magnitude associated with the dominant frequency of a total pressure distortion.

The usefulness of Volterra modeling is not as a replacement for CFD analysis, as CFD gives a much more detailed breakdown of the entire flow field. The potential of Volterra modeling is as a quick assessment tool to ascertain if a more detailed analysis is even necessary. Typically, mid-span conditions are used for quick assessment, which is where the Volterra model is the most accurate. In addition, the largest frequency magnitude associated with total pressure distortion is at the mid-span of the blade, also good for Volterra modeling. An analysis of an axial compressor stage could be done with a Volterra model using a typical desktop computer in as little as 30 minutes to an hour, depending on the number of data sets used in kernel training. Also, after the kernels are calculated defining a certain compressor stage, they could be saved and any future predictions of total pressure distortion transfer could be done just utilizing the prediction phase of the model, further reducing processing time. The prediction phase of the Volterra model runs in as little as 10 minutes on a 1 Ghz desktop computer. If the Volterra model predicts a substantial transfer of the frequency of interest, then a more detailed analysis could be done with CFD. However, if the energy contained at the

frequency of interest were small, further analysis would not be necessary producing a potential savings of days to weeks in analysis time.

11 Works Cited

Adamczyk, J.J., "Unsteady Fluid Dynamic Response of an Isolated Rotor with Distorted Inflow," AIAA Paper No. 74-49.

Barr, L.C., "The Unsteady Response of an Axial Flow Turbomachinery Rotor to Inlet Flow Distortions," The Pennsylvania State University Applied Research Laboratory, TM 78-253.

Bendat, J.S., *Nonlinear Systems Techniques and Applications*, John Wiley & Sons, Inc., New York, 1998.

Boyd, S., Tang, Y.S., Chua, L.O., "Measuring Volterra Kernels", *IEEE Transactions on Circuits and Systems*, vol. 30, no. 8, Aug. 1983, pp. 571-577.

Boyer, K.E., "An Improved Streamline Curvature Approach for Off-Design Analysis of Transonic Compression Systems," Ph.D. Dissertation, Virginia Polytechnic Institute and State University (Blacksburg, VA, 2001).

Campbell, Wilfred, "Protection of Turbine Disk Wheels from Axial Vibration," *Proceedings of the Cleveland Spring Meeting*, ASME, May 1924.

Colpin, J., Kool, P., "Experimental Study of an Axial Compressor Rotor Transfer Function with Non-Uniform Inlet Flow," ASME Paper No. 78-GT-69, Gas Turbine Conference and Products Show, April 9-13, 1978, London, England.

Cousins, W.T., private communication, 2002.

Cousins, W.T., O'Brien, W.F., "Axial-Flow Compressor Stage Post-Stall Analysis," AIAA Paper No. 85-1349, 1985.

Danforth, C.D., "Distortion-Induced Vibration in Fan and Compressor Blading," *Journal of Aircraft*, vol. 12, no. 4, pp. 216-225, April 1975.

Datko Jr., J.T., O'Hara, J.A., "The Aeromechanical Response of an Advanced Transonic Compressor to Inlet Distortion," ASME 87-GT-189, 1987.

Davis, M., Hale, A., Beale, D., "An Argument for Enhancement of the Current Inlet Distortion Ground Test Practice for Aircraft Gas Turbine Engines," ASME 2000-GT-0505, 2000.

Greitzer, E.M., "Upstream Attenuation and Quasi-Steady Rotor Lift Fluctuations in Asymmetric Flows in Axial Compressors," ASME 73-GT-30, 1973.

Greitzer, E.M., Tan, C.S., Wisler, D.C., Adamczyk, J.J., Stazisar, A.J., "Unsteady Flows in Turbomachines: Where's the Beef?," *ASME Unsteady Flows in Aeropropulsions*, 1994, pp. 1-11.

Hah, C., Rabe, D.C., Sullivan, T.J., Wadia, A.R., "Effects of Inlet Distortion on the Flow Field in a Transonic Compressor Rotor," *ASME Journal of Turbomachinery*, Vol. 120, April 1998, pp. 233-246.

Hale, A.A., O'Brien, W.F., *A 3-D Turbine Engine Analysis Compressor Code (TEACC) for Steady-State Inlet Distortion*. Ph.D. Dissertation, Virginia Polytechnic Institute and State University (Blacksburg, Virginia, 1996.).

Hamed, A., Numbers, K., "Inlet Distortion Considerations for High Cycle Fatigue in Gas Turbine Engine," AIAA Paper 97-3364, AIAA 33rd Joint Propulsion Conference and Exhibit, July 6-9, 1997, Seattle, WA.

Hansen, P.C., *Rank-Deficient and Discrete Ill-Posed Problems*, SIAM, Philadelphia, 1998.

Henderson, R.E., Shen, I.C., "The Influence of Unsteady Rotor Response on a Distorted Flow Field," ASME Paper No. 81-GT-185, International Gas Turbine Conference and Products Show, March 9-12, 1981, Houston, Texas.

Jenkins, J., Tromp, J., "A Volterra Kernel Identification Scheme Applied to Aerodynamic Reactions," AIAA 90-2803, August 1990.

Lecht, M., "Improvement of the Parallel Compressor Model by Consideration of Unsteady Blade Aerodynamics," AGARD CP-400, 1986.

Lecht, M., Weyer, H. B., "On the Unsteady Aerodynamic Rotor Blade Loading in a Transonic Axial Flow Compressor with Unsteady State Inlet Distortion," IUTAM Symposium on Aeroelasticity in Turbomachines, October 18-23, 1976, Paris.

Luedke, J., private communication, 2002.

Luedke, J., "Use of Nonlinear Volterra Theory in Predicting the Propagation of Non-uniform Flow Through an Axial Compressor," M.S. Thesis, Virginia Polytechnic Institute and State University (Blacksburg, Virginia, 2001.).

Longley, J.P., Greitzer, E.M., "Inlet Distortion Effects in Aircraft Propulsion System Integration," *Steady and Transient Performance Prediction of Gas Turbine Engines*, AGARD LS-183, May 1992.

Manwaring, S.R., Fleeter, S., "Inlet Distortion Generated Periodic Aerodynamic Rotor Response," ASME 89-GT-299, 1989.

Manwaring, S.R., Fleeter, S., "Forcing Function Effects on Rotor Periodic Aerodynamic Response," *Transactions of the ASME*, vol. 113, April 1991, pp. 312-319.

Manwaring, S.R., Rabe, D.C., Lorence, C.B., Wadia, A.R., "Inlet Distortion Generated Forced Response of a Low Aspect-Ratio Transonic Fan," *ASME Journal of Turbomachinery*, vol. 119, October 1997, pp. 665-676.

Mazzawy, R.S., "Multiple Segment Parallel Compressor Model for Circumferential Flow Distortion," *ASME Journal of Engineering for Power*, April, 1977.

Melick, H.C., "Analysis of Inlet Flow Distortion and Turbulence Effects on Compressor Stability," NASA CR 114577, 1973.

Morrow, P., "Detailed Test Plan for the Augmented Damping of Low Aspect Ratio Fans (ADLARF)," USAF Technology Branch Turbine Engine Division, WPAFB, March 1993.

Nagano, S., Takata, H., "Nonlinear Analysis of Rotating Stall," Institute of Space and Aeronautical Science, University of Tokyo, Report No. 449, 1970.

Peacock, R.E., Overli, J., "Dynamic Internal Flows in Compressors with Pressure Maldistributed Inlet Conditions," AGARD CP-177, 46th P.E.P. Conference of AGARD, 1975, Monterey, CA.

Pearson, H., McKenzie, A., "Wakes in Axial Compressors." *Journal of the Royal Aeronautical Society*, vol. 63, July 1959.

Press, W.H., Flannery, B.P., Teukolsky, S.A., Vetterling, W.T., *Numerical Recipes in C – The Art of Scientific Computing*, Cambridge University Press, Cambridge, 1988.

Rabe, D., Bolcs, A., and Russler, P., "Influence of Inlet Distortion on Transonic Compressor Blade Loading," AIAA 95-2461, Presented at the 31st Joint Propulsion Conference and Exhibit, July 1995, San Diego, CA.

Rabe, D., Williams, C., and Hah, C., "Inlet Flow Distortion and Unsteady Blade Response in a Transonic Axial Compressor Rotor," ISABE 99-7297, 1999.

Reid, C., "The Response of Axial Flow Compressors to Intake Flow Distortion." ASME Paper No. 69-GT-29, 1969.

Reisenthel, P.H., "Application of Nonlinear Indicial Modeling to the Prediction of a Dynamically Stalling Wing," AIAA 96-2493, June 1996.

Reisenthel, P.H., "Development of a Nonlinear Indicial Model for Maneuvering Fighter Aircraft," AIAA 96-0896, 1996.

Reisenthel, P.H., "A Nonlinear Volterra Kernel Identification System for Aeroelastic Applications," NEAR TR 547, June 1999.

Reisenthel, P.H., "Prediction of Unsteady Aerodynamic Forces Via Nonlinear Kernel Identification," Langley International Forum on Aeroelasticity and Structural Dynamics, Williamsburg, VA, June 1999.

Reisenthel, P.H. and Bettencourt, M.T., "Data-Based Aerodynamic Modeling Using Nonlinear Indicial Theory," AIAA 99-0763, Jan. 1999.

Reisenthel, P.H. and Bettencourt, M.T., "Extraction of Nonlinear Indicial and Critical State Responses from Experimental Data," AIAA 99-0761, Jan. 1999.

Roberts, F., Plourde, G.A., Smakula, F. "Insights into Axial compressor Response to Distortion," AIAA Paper No. 68-565, 1968.

Rugh, W.J., *Nonlinear System Theory -- The Volterra/Wiener Approach*, The Johns Hopkins University Press, Baltimore, 1981.

Sexton, M.R., O'Brien, W.F., "A Model for Dynamic Loss Response in Axial-Flow Compressors," ASME 81-GT-154, 1981.

Silva, W.A., "Identification of Linear and Nonlinear Aerodynamic Impulse Responses Using Digital Filter Techniques," AIAA 97-3712, Aug. 1997.

Silva, W.A., "Extension of a Nonlinear Systems Theory to General-Frequency Unsteady Transonic Aerodynamic Responses," AIAA 93-1590, Apr. 1993.

Small, M., "Improved Methods for Predicting the Effects of Inlet Flow Distortion on the Performance of Axial Flow Compressor," M.S. Thesis, Virginia Polytechnic Institute and State University (Blacksburg, Virginia, 2001.).

Tromp, J.C., and Jenkins, J.E., "A Volterra Kernel Identification Scheme Applied to Aerodynamic Reactions," AIAA 90-2803, Aug. 1990.

Volterra, V., *Theory of Functionals and of Integral and Integro-Differential Equations*, Blackie & Sons Ltd., London, 1930.

Williams, C., "Turbine Engine Research Center Inlet Distortion Measurement," 4th National Turbine Engine High Cycle Fatigue Conference, 1999, Monterey, CA.

Wu, C.H., "A General Through-Flow Theory of Fluid Flow with Subsonic or Supersonic Velocity in Turbomachines or Arbitrary Hub and Casing Shapes," NACA TN 2302, 1951.

Part B: Modal Response of a Transonic Fan Blade to Periodic Inlet Pressure Distortion

Robert M. Wallace

Table of Contents

| | | |
|------------|--|------------|
| 1 | Introduction | 116 |
| 2 | Literature Review | 120 |
| 2.1 | Inlet Pressure Distortion Effects on Compressor Performance and Blade Response | 120 |
| 2.2 | Research Focused on Testing and Modeling Resonant Vibratory Response with Computer Modeling | 124 |
| 2.3 | Literature Review Conclusion | 127 |
| 3 | Experimental Data Conditioning and Collection | 129 |
| 3.1 | Experimental Facility | 129 |
| 3.2 | Experimental Procedure | 133 |
| 3.3 | Data Characteristics | 135 |
| 3.4 | Raw Data Reduction and Manipulation | 136 |
| 4 | Finite Element Model Development | 140 |
| 4.1 | Choosing the Correct Modeling Method | 140 |
| 4.2 | Model Properties and Constraints | 142 |
| 4.3 | Rotational Effects | 144 |
| 4.4 | Finite Element Model Summary | 146 |
| 5 | Analysis and Results | 147 |
| 5.1 | Finite Element Generated Eigenvectors | 147 |
| 5.2 | Generalized Forcing Function | 153 |
| 5.3 | Fast Fourier Transform of the Generalized Forcing Function | 159 |
| 5.4 | Sensitivity Analysis | 162 |
| 5.5 | Checking Modal Force Results with Strain Gage Data | 164 |
| 6 | Summary and Conclusions | 171 |
| 7 | Recommendations for Future Work | 174 |

References

Table of Figures

| | |
|---|-----|
| Figure 1-1: The AV-8B Harrier on take off is an example of hot exhaust gases mixing with cooler atmospheric air [www.globalsecurity.com]. | 117 |
| Figure 1-2: Compressor map showing the loss in surge limit caused by a distorted inlet flow [ARP-1420, 2002]. | 117 |
| Figure 1-3: Examples of typical screens used to produce pressure distortions during testing [Eddy, 2001]. | 119 |
| Figure 2-1: The effects of spoiled sector width on surge delivery static pressure [Reid, 1968]. | 121 |
| Figure 2-2: Campbell Diagram [Manwaring et al., 1997]. | 125 |
| Figure 2-3: Sample of curve veering [Kenyon, 1999]. | 126 |
| Figure 3-1: Test facility at the Compressor Research Facility, Wright-Patterson AFB [Morrow, 1993]. | 130 |
| Figure 3-2: First stage blisk mounted on the test rig [Morrow, 1993]. | 131 |
| Figure 3-3: Second stage rotor [Morrow, 1993]. | 132 |
| Figure 3-4: Cross section of the experimental setup [Morrow, 1993]. | 134 |
| Figure 3-5: An example of a 3-per-rev distortion screen [Morrow, 1993]. | 134 |
| Figure 3-6: Experimental 3-per-rev total pressure distortion. | 137 |
| Figure 3-7: Total pressure 3-per-rev model. | 138 |
| Figure 4-1: The 5568-element model used for analysis. | 142 |
| Figure 5-1: Single degree of freedom model. | 149 |
| Figure 5-2: Multiple degree of freedom model. | 149 |
| Figure 5-3: ADLARF 1st stage compressor Campbell diagram. | 153 |
| Figure 5-4: 1st Mode - Modal force as a function of distortion level. | 155 |
| Figure 5-5: 2nd Mode - Modal force as a function of distortion level. | 155 |
| Figure 5-6: 3rd Mode - Modal force as a function of distortion level. | 156 |

| | |
|--|-----|
| Figure 5-7: Modal force comparison at the 80% distortion level. | 156 |
| Figure 5-8: Modal force comparison at the 100% distortion level. | 157 |
| Figure 5-9: Modal force comparison at the 120% distortion level. | 157 |
| Figure 5-10: Harmonic content present in the 1st mode. | 160 |
| Figure 5-11: Harmonic content present in the 2nd mode..... | 160 |
| Figure 5-12: Harmonic content present in the 3rd mode. | 161 |
| Figure 5-13: 3rd Engine order pressure distortion sensitivity..... | 163 |
| Figure 5-14: 6th Engine order pressure distortion sensitivity. | 163 |
| Figure 5-15: Side view of the test compressor showing strain gage location [Kenyon, 1999]. | 165 |
| Figure 5-16: Blade root stress in the x-direction. | 167 |
| Figure 5-17: Blade root stress in the y-direction. | 168 |
| Figure 5-18: Blade root stress in the z-direction. | 169 |

Table of Tables

| | |
|---|-----|
| Table 3-1: First stage blisk geometry characteristics [Rabe et al, 1999]. | 132 |
| Table 3-2: Radial locations of the inlet total pressure probes [Morrow, 1993]... | 133 |
| Table 4-1: First stage rotor FE model material properties..... | 143 |
| Table 5-1: Eigenvector RMS error calculation results..... | 152 |
| Table 5-2: Modal force summary. | 162 |
| Table 5-3: Sensitivity factor summary..... | 164 |
| Table 5-4: Mean rotor stress calculation and comparison at wide open discharge | 170 |

1 Introduction

The assumption that the airflow at the inlet of axial turbomachinery is uniform has widely been accepted historically. In the early years of turbomachinery design, this assumption was acceptable and more useful than it is today for a number of reasons. As the performance of modern aircraft and their engines increase, the rotating blades of the engine are required to withstand more loading and in varying directions, both sometimes changing very rapidly, pushing ever closer to the material strength and fatigue limits.

High G maneuvers, such as aggressive turning, often cause the inlet flow to be non-uniform as it must enter the engine at a sharp angle to the axis of rotation as the aircraft turns. In addition, traveling in the wake of other aircraft and firing wing-mounted weapons can cause disturbances in the airflow. Vertical take-off and landing (VTOL) aircraft present yet another scenario for ingesting a non-uniform flow as exhaust gases are often mixed with cooler atmospheric air as they wash off the ground and are pulled back into the engine (see Figure 1-1). These disturbances, be it a change in total pressure or total temperature, are referred to as inlet distortions. These distortions by the nature of their source can be highly unpredictable and often changing throughout an aircraft's flight envelope.

A second source of inlet distortions can be the result of the engine's nacelle design or other obstructions related to the aircraft structure. As an example, a support strut, an S-shaped inlet duct, or the engine inlet's proximity to other exterior features of the aircraft can cause a non-uniform flow to enter the engine. Distortion caused by objects in a fixed location related to the engine's inlet presents a more static or constant disruption in the airflow. These quasi-static distortion patterns can be modeled and studied much more easily and are the focus of this research.

Inlet distortions can cause many problem areas to arise, from short-term performance degradation to long-term structural degradation. Short-term effects include loss of pressure rise and a reduction in mass flow, which can ultimately lead to a reduction of stall margin. These short-term effects have been studied a great deal and are often the result of the dynamic inlet distortions mentioned above (see Figure 1-2).



Figure 1-1: The AV-8B Harrier on take off is an example of hot exhaust gases mixing with cooler atmospheric air [www.globalsecurity.com].

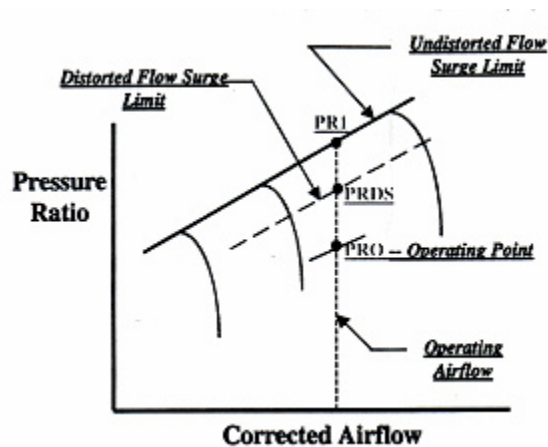


Figure 1-2: Compressor map showing the loss in surge limit caused by a distorted inlet flow [ARP-1420, 2002].

The long-term effects, however, are caused by repeated exposure to the dynamic inlet distortions or, more likely, the result of operating in the presence of a quasi-static distortion pattern.

By definition, all turbomachines are mechanical devices that transfer power by rotating blades around an axle or spindle, as the word *turbo* comes from the Latin

meaning “to rotate.” It is this fundamental mode of operation that makes all distortions appear periodic in nature as seen by the fan or compressor blades of a gas turbine as they sweep past the section of distorted airflow. For example, if a single strut spanning the entire diameter of the inlet is partially blocking the airflow, then a change in the total pressure as seen by the fan blades will occur twice per revolution. Divide this by the time it takes to complete one revolution, and what was a constant pressure distortion in the stationary frame of reference becomes a time-dependent impulse in the rotating frame of reference at a certain frequency determined by the speed of rotation.

This periodic change in total pressure causes varying blade loading. If the frequency at which the blade load changes coincides with one of the natural frequencies of the blade, a very dangerous situation can occur, leading to rapid blade failure due to high cycle fatigue. High cycle fatigue (HCF) is defined as metal fatigue that results in cracking or fracture from a large number of stress cycles well below the yield strength of the material, and is associated with fatigue lives greater than about 10^4 to 10^5 cycles. At first inspection this may seem like a very high number of cycles for a lower limit. However consider the single strut mentioned above. If the blade is subjected to this excitation at 10,000 RPM, not an uncommon operational speed for today’s engines, then each blade will be cycled 10^5 times in just five minutes as it is excited twice per revolution. Doubling the number of excitations per revolution reduces the time by one-half, and so forth. Now, assume this excitation at approximately 333 Hz coincides with one of the natural frequencies of the blade. This means that the blade loading changes concurrently with blade deflection in a way that amplifies blade bending to the point of catastrophic failure. This type of blade failure can take place in a much shorter time period, on the order of seconds under the right conditions.

The risk of catastrophic failure occurring so quickly has lead to much time, energy, and money spent on testing varying distortion patterns placed at the inlet (see Figure 1-3) as previous research has shown that total pressure distortion is a dominant HCF driver [Manwaring et al, 1997].

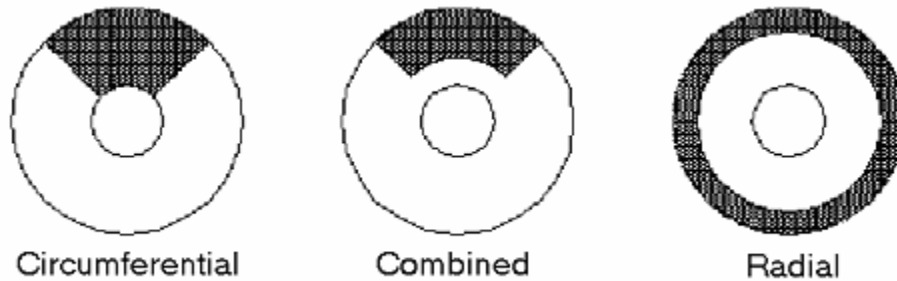


Figure 1-3: Examples of typical screens used to produce pressure distortions during testing [Eddy, 2001].

If a mathematical model representing the blade and how it responds to total pressure distortion could be developed, much time and money could be saved by partially eliminating such extensive testing. This provides the motivation for my research.

The goals of my research are as follows: (1) create an accurate finite element (FE) model of the ADLARF fan blade for eigenvector extraction; (2) identify dominant engine order modal force magnitudes based on coupling computational fluid dynamics (CFD)-generated total pressure distortion and FE generated eigenvectors; and (3) determine the relationship between the magnitude of the modal force and the total pressure distortion level used to drive the system. The modal force represents the magnitude of the generalized forcing function used to drive a model of the ADLARF fan blade for a given mode. If a relationship between the level of total pressure distortion present and the response of the fan blade can be identified through the use of a simplified model, perhaps large savings from multiple resources can be realized.

2 Literature Review

The idea of non-uniform inlet conditions leading to reduced compressor performance is not new and has been the subject of many experimental and analytical studies dating back to the 1950s. Most of this work has been concentrated around reductions in compressor performance in the form of reduced stall margins and pressure rise. This included many studies measuring, predicting and indexing various inlet distortions and will be discussed in this chapter. In recent years, a separate yet very much related area has been studied. The effects of blade response caused by forced vibration due to non-uniform inlet distortions has been studied with emphasis on compressor blade life due in part to HCF. The forced vibrations have lead to studying aeromechanical effects known as blade vibratory response. Studying blade vibratory response experimentally has proved difficult due to the speed at which the blade operates. Recent developments in computer modeling and computational ability have opened the door to CFD and finite element modeling (FEM) as viable analytical methods to accurately recreate and study blade vibratory response.

Despite significant gains made to date in understanding the effects of non-uniform inlet conditions, the need to further our understanding is ever present and even more so in the relatively new area of compressor aeromechanical response. A variety of modeling techniques, along with their successes and limitations, will be discussed in this chapter. Finally an introduction to a new attempt in modeling the aeromechanical effects and predicting blade vibratory response will be presented.

2.1 Inlet Pressure Distortion Effects on Compressor Performance and Blade Response

While many types of inlet distortions can occur, total pressure distortions are the focus of this research and therefore a timeline of studies on this topic will be presented. Reid [1969] performed a series of experiments using different inlet distortions and studied how

this affected the compressor's performance. His major contribution to the area of inlet distortion studies comes from his work to define what is known as the angle of spoiling. The spoiling angle is defined as the angular width of the low total pressure region. Using a varying spoiling angle Reid was able to show how the surge delivery static pressure varies accordingly, Figure 2-1 presents his findings. Notice how the area labeled "critical angle" defines a point in the spoiling angle range where little change in surge margin is present. Beyond this critical angle the surge delivery static pressure remains relatively constant. In addition, Reid was able to show that sub-dividing the area of spoiled flow has less effect on the peak pressure loss than one larger distorted sector does.

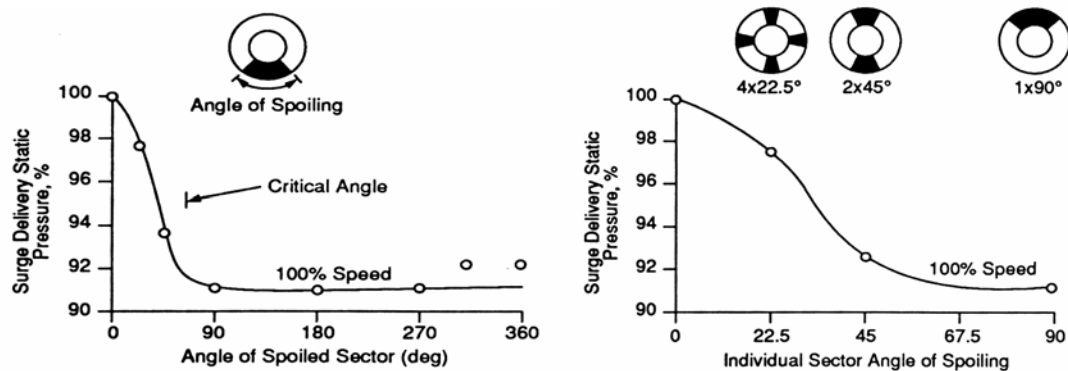


Figure 2-1: The effects of spoiled sector width on surge delivery static pressure [Reid, 1968].

Later, Danforth [1975] studied the effects of an inlet distortion on compressor stall margin and blade response. He examined several mechanisms that have the potential to reduce compressor stall margin and induce forced blade vibrations and concluded that the effects can be extremely different. While Reid showed large areas of distorted flow can adversely affect the static delivery pressure, Danforth showed that small regions of distorted flow that would be insignificant in Reid's study could generate large vibratory responses in both rotor and stator blades. In addition, Danforth noted that coupling a circumferential total pressure distortion that appears periodic to the passing blades can create severe blade vibrations if present at or near the natural frequency of the blade. The severity of the blade vibrations is directly related to the energy input which

led Danforth to create a distortion index. This index has been used as an alert for potential problems that exist in a blade design in the area of forced blade vibratory response.

Along the same time as Danforth, Peacock and Overli [1975] also used circumferential distortion to study the unsteady normal force at mid span of a lightly loaded low speed compressor. They used two different screen types to create the inlet distortions needed for their experiment. The first screen consisted of a sine wave distortion pattern where the screen porosity gradually changes over the circumference of the inlet. The second screen was comprised of sections of uniform screen porosity effectively creating a square wave input as seen by the passing rotor blades. As can be imagined, the results showed a more violent blade response to the square wave as the time rate of change in axial velocity was much greater than that of the sine wave. A correlation between the time rate of change in the axial velocity of the incoming air and the normal blade coefficient was theorized.

A year later Lecht and Weyer [1976] published their findings on a similar experiment conducted on both a subsonic and transonic compressor. Lecht and Weyer increased the number of blade force measurement locations taken relative to the low total pressure area. The results indicated that the blade experienced the maximum and minimum loads immediately after exiting and entering the spoiled area, respectively.

In the late 80s Datko and O'Hara [1987] continued testing a transonic compressor's response to seven different inlet total pressure distortion screens. To create a baseline case in which to compare the measured response with, two inlet configurations were tested with a "clean" designation, meaning no distortion screens were used. In addition, Datko and O'Hara used a compressor containing a blisk. The word blisk comes from the combination of the words "bladed disk" and indicates the blades are not fitted with traditional dovetail joints and instead are part of a monolithic piece of metal combining the hub and blades. The lack of dovetail joints greatly increases the strength of the rotor/blade system at the expense of severely reducing the mechanical damping present. As expected, the blisk underwent severe resonant stresses when exposed to inlet distortions. The major resonant stresses occurred at the first three natural modes of

vibration where large deflections are common. The first stage compressor blade used for my research is also a blisk and the first three natural modes are studied.

In the progression of studies, Manwaring and Fleeter [1989,1990] introduced unsteady inlet flow conditions to the testing of a compressor rotor blade row. Steady loading was used while varying aerodynamic forcing functions were included in the distortion placed on the blade row. A steady 2-per-rev inlet distortion was placed in the flow while an unsteady simulated wind gust amplified the distortions. Measurements were taken to study the aerodynamic response, as well as the blade surface pressures. To better examine the forcing function as seen by the blades, the results were transferred to the frequency domain using Fourier decomposition. Not surprisingly, the 2-per-rev signal also known as the 2nd engine order, or 2nd harmonic, contained the largest magnitude and therefore was dominant. Higher harmonics of the 2nd harmonic were present and gained magnitude with increasing gust magnitudes.

Later, Greitzer et al. [1994] further studied the effect that non-uniform inlet conditions have on both the aeromechanical excitation of a compressor and the overall stability of the compressor system. In addition to the forced response previously mentioned, Greitzer et al. examined flutter, a self excited aeromechanical instability. Possibly as part of the motivation to study these effects, it was noted that several hundred engine failures since the late 1960's had occurred in U.S. Air Force aircraft engines and mostly were attributed to high cycle fatigue (HCF) [Air Force Scientific Advisory Board, 1992]. Greitzer et al. suggested much work was needed for a better understanding of the stage-to-stage transfer of inlet distortions in multistage compressors, a research focus here at Virginia Tech. Ryman [2003] showed Volterra modeling is capable of predicting total pressure distortion transfer through compressor stages, the dominant driver of HCF, with limitations and requires further study. Secondly, Greitzer et al. also recommended further work in predicting the aerodynamic forcing functions that can cause blade excitation that can lead to HCF, which is related to my research in an attempt to model vibratory blade response to aerodynamic forcing functions.

2.2 Research Focused on Testing and Modeling Resonant Vibratory Response with Computer Modeling

Most recently and directly related to my research, Manwaring [1997] examined a low-aspect-ratio, transonic, first stage blade of a two stage fan with a series of experiments with the goal of characterizing aspects of distortion in order to create models to predict its effects. Manwaring tested two types of inlet flow distortions, a 3-per-rev and an 8-per-rev, using distortion screens. By mounting on-blade pressure transducers along with strain gages mounted at three positions on the blade, vibratory response was recorded for the unsteady blade loading. Special attention was shown to the areas of operation where the blade undergoes resonance, caused by exciting the blade near its natural frequency. Manwaring was able to test at these areas by constructing a Campbell diagram which identifies areas of probable vibratory problems. Wilfred Campbell [1924] developed a diagram that shows the natural frequency of a blade for various modes with multiple per-rev lines superimposed. Figure 2-2 shows Manwaring's Campbell Diagram with four blade modes lines and three per-rev lines, the 2-, 3-, and 8-per-rev. As can be seen in the diagram, the centrifugal force placed on the blade during operation increases the natural frequency at which the mode occurs by artificially stiffening the blade. Anywhere a mode line crosses a per-rev line, severe vibratory response is almost guaranteed as the distortion pattern and operation speed excited the blade at resonance.

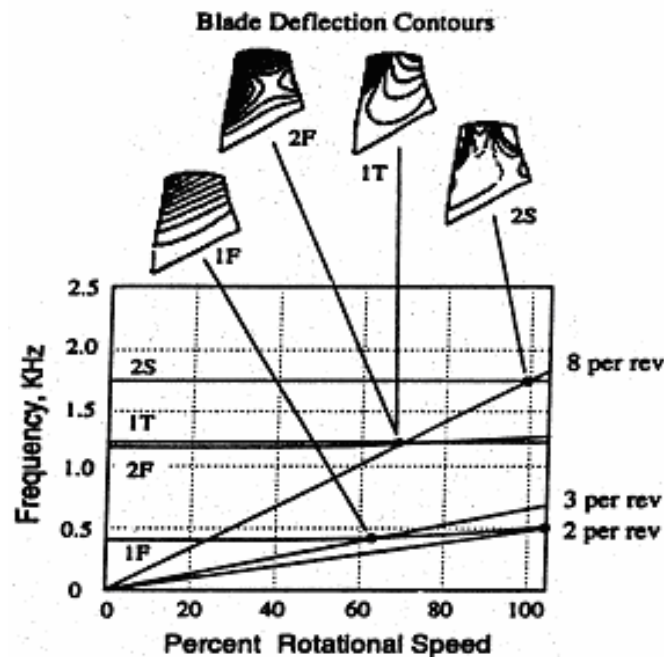


Figure 2-2: Campbell Diagram [Manwaring et al., 1997].

Hah et al. [1998] used Reynolds-averaged Navier-Stokes CFD code to model the same experiment studied by Manwaring. The inlet distortion pattern was modeled and used to predict the blade pressure profiles on both the pressure and suction side of the blade. Upon comparison, Hah's numerical solution successfully predicted the flow field to that found in the experiments. The pressure field generated by Hah's CFD was used in my research and in part made my research possible.

Using modal analysis to predict stresses in the blade due to vibratory response requires that the correct eigenvector must be used in calculations. This requires the correct mode shape used in modeling to match the actual mode being excited during engine operation and testing. This may seem trivial with the graphical display of a Campbell diagram to help the researcher determine which mode shape is present; however, what happens when two mode lines converge or cross has been a topic of debate.

Kenyon [1999] investigated a phenomenon called curve veering using computational and experimental techniques. Upon first inspection it appears that mode

lines simply cross with no special occurrences taking place. However, mathematical models have shown that when eigenvalues converge, the mode lines do not cross and instead the eigenvalues “repel” each other while abruptly swapping mode shapes. Kenyon showed through use of finite element modeling that a compressor blade over a range of speeds demonstrates that the interacting modes veer away from each other rather than cross while switching their respective eigenvalues. In his study, however, the interaction was not abrupt and took place over a large range of the compressor operating range. Figure 2-3 is a close up of converging mode lines from a finite element model over a short operational range, the dark solid portion of both lines indicating where the modes swap.

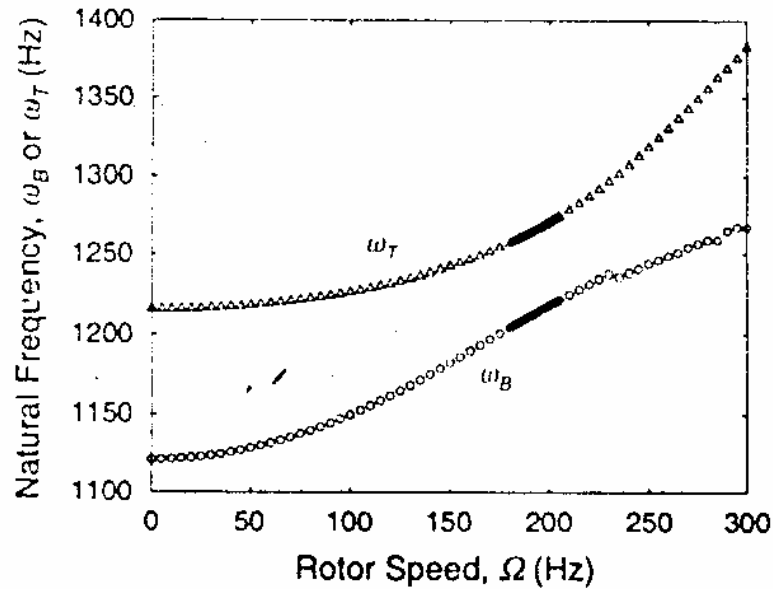


Figure 2-3: Sample of curve veering [Kenyon, 1999].

During the interaction phase the modes become mixed, exhibiting characteristics of both converging mode shapes simultaneously. This result has been validated experimentally by strain gages placed on the blade at mode specific locations. Kenyon concluded that fully determining how the exchange of mode shapes occurs during curve veering is essential in accurately predicting and measuring blade resonant response.

Another aspect studied to better predict blade vibratory response has been the effects of blade-to-blade variations that cause changing blade resonant frequencies known as mistuning. Large finite element models have been used in limited mistuning research, as the computations become too cumbersome with large model sizes. Cyclic symmetry can be used to reduce the finite element model size but using symmetry inherently makes blade variation around the rotor impossible since symmetry mirrors a single blade model around an axis to create the entire rotor. One attempt by Ottarsson et al. [1995] used variations in the calculations for a symmetric finite element model to effectively create a mistuning while keeping the model size much smaller and lessening the computational intensity.

Griffin [1988] experimentally researched mistuning for a low-speed bladed disk assembly through the use of strain gages. He defined the tuned-disk frequency as the frequency at which the entire bladed disk assembly would vibrate if all the blades were tuned. From his studies he found that the blades whose resonant frequency matched the tuned-disk frequency had the largest stress amplitudes.

Kenyon [1999] investigated blade response to inlet total pressure distortions on a blisk by measuring dynamic strain gage output coupled with a reduced-order analytical model to predict the blade resonant stress variations with respect to mistuning. He determined that blade structural mistuning and mechanical coupling had a relatively small effect in measured stress variations when compared to the effects of unsteady aerodynamic coupling. Experimental results were compared with results from the reduced-order model, and both agreed that unsteady aerodynamic coupling played a major role in the mistuned response of the blisk with a rough correlation of blade-to-blade stress amplitude variations.

2.3 Literature Review Conclusion

Over the course of gas turbine and compressor technology development a great deal of time and effort has been spent examining and understanding the effects of inlet distortion on a wide variety of operational parameters. The first area of concentration dealt with performance loss due to reduced stall margin and a loss in pressure rise. Many

experiments using many different techniques over the years have been tried to theorize, categorize, and summarize the cause and effect of varying total pressure inlet distortions with only an extremely small number of them discussed here.

In comparison to compressor performance studies, experiments and modeling of fluid-structure interaction and vibratory blade response are relatively new. The progress of computing power has led the way to make CFD and FEM viable options in place of extensive testing. While physical testing will likely never be eliminated from the design process, computer modeling will become more and more important and realizing the many ways to exploit the capabilities of the computer in distortion studies will be as important as the modeling itself. This research is an attempt to move distortion and vibratory blade response in a new direction by utilizing CFD results to excite blade response through the use of modal and harmonic analysis. While complete fluid-structure interaction codes exist, it is computationally expensive and possibly unneeded if it can be shown that results from manually adjoining CFD and FEM can produce promising results for “small” deflections as validated by experimental results.

With an ever-increasing push to cut cost while decreasing design, test, production and implementation time, it's likely inlet distortion studies on performance loss and structure life will never end. This research is just one attempt at reducing experimental testing time by using modal analysis to predict stress variation magnitudes induced from an aerodynamically forced vibratory response.

3 Experimental Data Conditioning and Collection

All data used during this research was provided by the USAF Compressor Research Facility (CRF) at Wright-Patterson Air Force Base in Dayton, Ohio. The data was acquired from tests that were run on a two-stage transonic, low aspect ratio compressor while operated at certain speeds and conditions known to produce rotor resonance. Many operating speeds were used to collect aerodynamic and aeromechanical data however only a small portion of the data collected will be the focus of this research, to be discussed later in greater detail. This chapter provides a partial summary of the “experimental procedure and data acquisition” of [Small, 2001] as an overview of the experimental facility, set up and procedure, and the characteristics of the data collected. Lastly, the reduction and manipulation of only the data related to the focus of this research will be discussed.

3.1 Experimental Facility

The CRF is comprised of three main buildings: the test building, the operations building and the electrical building. The test building houses the test chamber, flow conditioners, and the electric drive motors, while the electrical building houses the power supplies and transformers necessary to operate the drive motors. A schematic of the test section is shown in Figure 3-1. All experiment controls, data acquisition devices and test monitoring equipment are located in the operations building.

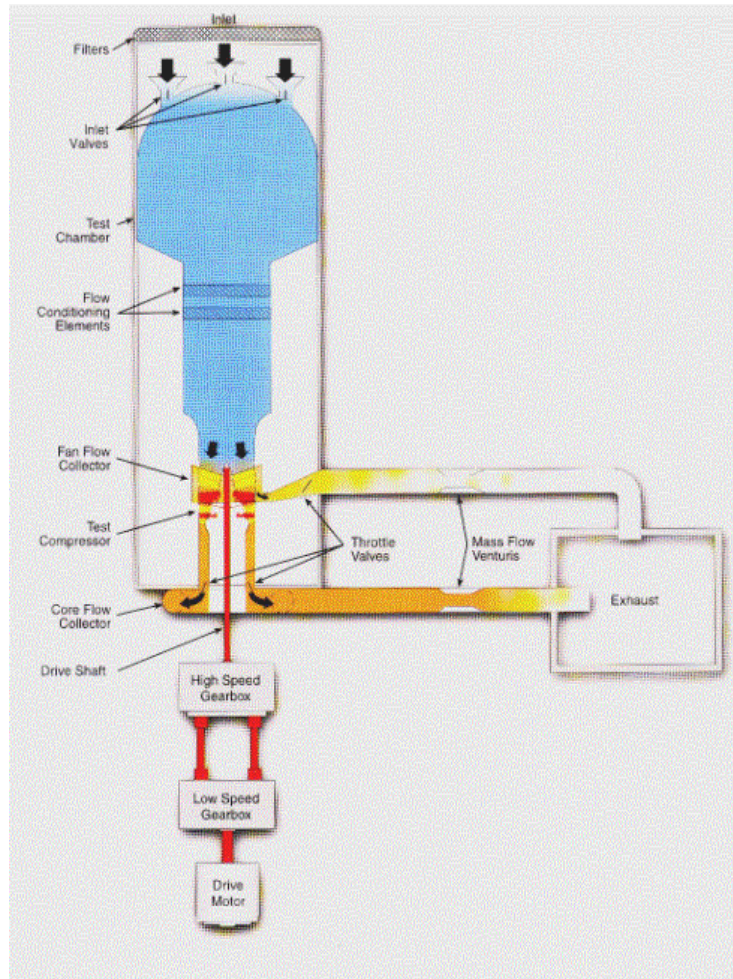


Figure 3-1: Test facility at the Compressor Research Facility, Wright-Patterson AFB [Morrow, 1993].

The test section uses the test compressor to draw atmospheric air through a number of devices used to regulate and control the airflow before entering the actual compressor bellmouth intake. Throttle valves are used to regulate the upstream pressure while flow conditioners are used to ensure the flow is straightened. The test chamber upstream of the compressor is 65 feet long and 20 feet in diameter. Once the air has passed through the test compressor it again passes through more valves to regulate downstream pressure, which ultimately controls the compressor pressure ratio. The flow is then discharged through a vertical flue back into the atmosphere. Venturis located just before the exit allows regulation of the mass flow through the test chamber and is capable of providing mass flow rates from 0-500lbm/s.

Two 30,000 horsepower electric motors and two gearboxes, one high and one low-speed, are available to choose from to control the test compressor speed. The speed is determined by the combination of the motor and gearbox selected for the test. The CRF uses a system called the Variable Speed Drive Control to set test speeds, control any changes in speed during a test, as well as provide safe automatic coast-down modes.

Data taken from the first stage in this two-stage compressor is the focus of this research. A picture of the first stage can be seen in Figure 3-2. The first stage is of modern design, called a rotor 'blisk' (contraction of blade and disk) and is made of a monolithic piece of titanium alloy. This means there is no dovetail joints present at the blade-disk interface therefore making the structure stronger by eliminating seams. This design feature should be noted, as it will become very important later.

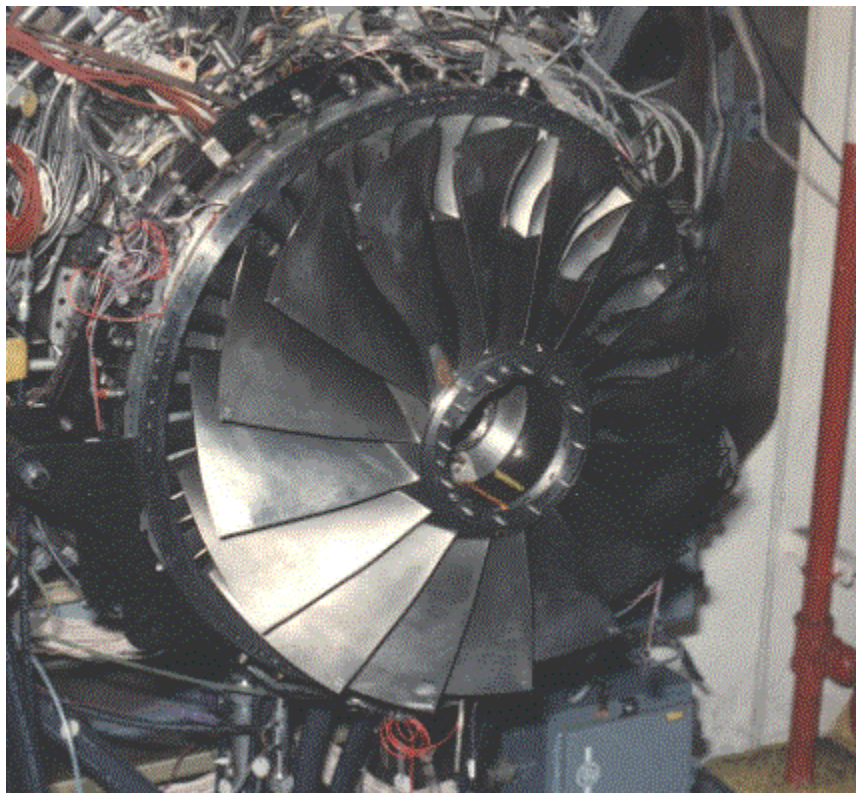


Figure 3-2: First stage blisk mounted on the test rig [Morrow, 1993].

Notice there are 16 low aspect ratio blades of modern design so the inlet conditions are temperatures near 300K and are supersonic about 45% span when operated

at the operation design point. The second stage of the compressor is of traditional design with 40 blades mounted to the disk using the dovetail joints mentioned above; see Figure 3-3. Table 3-1 shows the geometric characteristics of only the first stage.

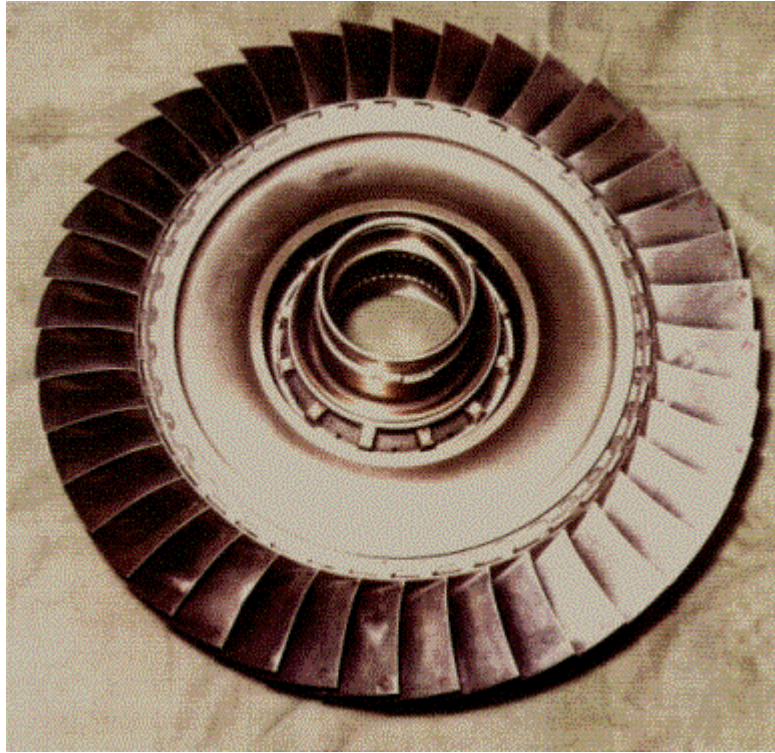


Figure 3-3: Second stage rotor [Morrow, 1993].

Table 3-1: First stage blisk geometry characteristics [Rabe et al, 1999].

| Parameter | Value |
|-------------------------|-------|
| Average Aspect Ratio | 1.22 |
| Rotor Tip Radius (in.) | 13.87 |
| Inlet Radius Ratio | 0.33 |
| Average Radius Ratio | 0.47 |
| Average Tip Solidity | 1.50 |
| Maximum Thickness/Chord | 0.028 |

3.2 Experimental Procedure

To collect data on aerodynamic and aeromechanical effects of pressure distortion, devices capable of generating distortions in the airflow are needed. Distortion screens, as discussed earlier, were used for this purpose and were located downstream of the bellmouth but approximately 1.5 engine diameters in front of the leading edge of the first stage rotor. To measure the pressure distortions caused by the screens, pressure probes were inserted at five radial immersions. The location of the probes was determined by dividing the frontal area of the compressor into five equal annuli with respect to mass flow [SAE, 1999]. Each probe was positioned in the center of its annulus at approximately $\frac{1}{2}$ diameter in front of the first stage rotor. A total of eight groups of probes, called rakes, were positioned around the circumference of the compressor equally spaced apart. The radial position of each probe within a rake is shown in Table 3-2 as measured from the outside diameter inward. A cross section of the experimental setup is shown in Figure 3-4. Total pressure was also measured between each stage by stator vane-mounted probes imbedded at three locations equally spaced around the circumference; however this data is not relevant to the focus of this research and is therefore not included.

Table 3-2: Radial locations of the inlet total pressure probes [Morrow, 1993].

| Immersion | Radial Distance from O.D. (in). |
|------------------|--|
| 1 | 0.74 |
| 2 | 2.31 |
| 3 | 4.11 |
| 4 | 6.33 |
| 5 | 9.57 |

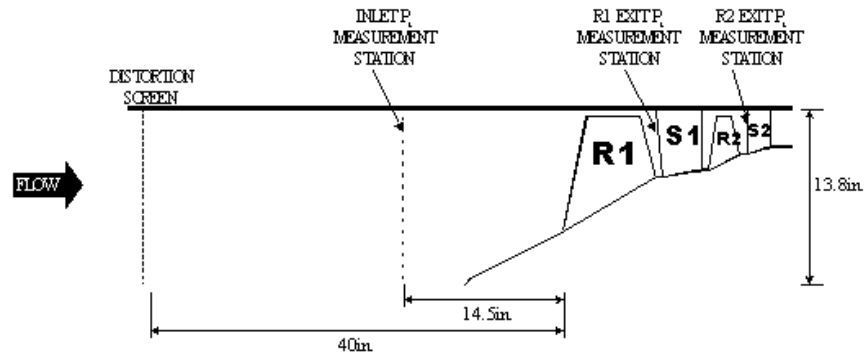


Figure 3-4: Cross section of the experimental setup [Morrow, 1993].

A distortion screen used to create total pressure distortions, as mentioned earlier, is shown in Figure 3-5. The screen is constructed of several sections of wire mesh with varying porosity. The idea behind the screen was to gradually vary the distortion level while moving in the circumferential direction and therefore create a smooth, steady state, sinusoidal pressure distortion. The screens succeed in causing total pressure distortions by reducing the axial momentum of the air as it passes through the screen and therefore reducing the dynamic pressure, a component of total pressure, as seen by the rotor blades. During testing two screens were used, a 3 per rev and an 8 per rev screen. Figure 3-5 is that of a 3 per rev distortion screen.

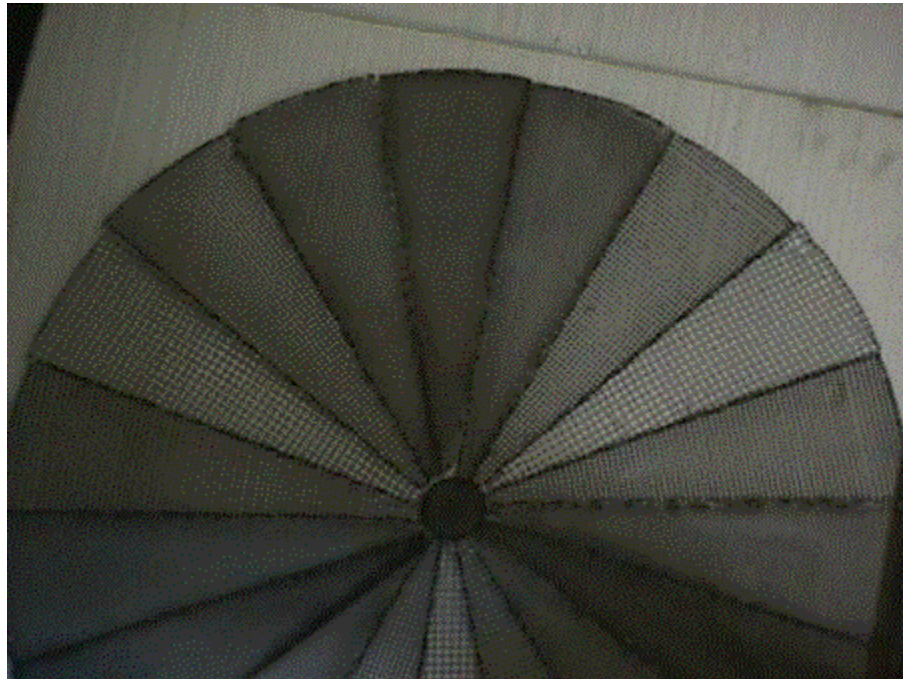


Figure 3-5: An example of a 3-per-rev distortion screen [Morrow, 1993].

To obtain a high resolution of circumferential pressure data while keeping the number of probes needed reasonable, the screens were rotated. Each distortion screen was mounted on a screen rotator comprised of support struts to which the distortion screens were attached and an external drive motor. The motor is located outside the flow field to prevent unwanted airflow blockage. If the screens had not been rotated, it would have been essential to mount a pressure probe at every location data was desired. This scenario, while possible, is certainly not desirable due to the sheer number of probes required as well as the increased flow blockage caused by the extra probes.

Using the rotating screen method, a single probe's data could contain a full 360 degree sweep of the pressure distortion. To resolve the data spatially the position of the screen must be related to the time at which the sample was taken. A sample rate high enough with respect to the rotation speed of the screen is required to ensure the high spatial resolution desired. However, it must be recognized that the distortion screens are designed to create steady state pressure distortions and therefore the speed at which they are rotated must be considered. If the screens are rotated too quickly, a rotational component is added to the distortion that is undesirable regardless of increasing the sampling rate. A study by Williams [1999] determined that a rotation speed of 2 degrees per second is sufficiently slow enough to consider the distorted flow quasi-steady.

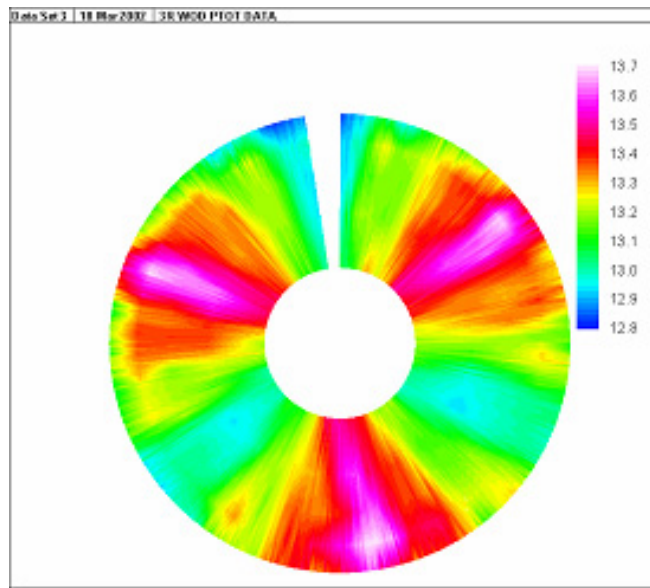
3.3 Data Characteristics

The total data set consists of circumferential total pressure measurements collected for 11 different operating points of the test compressor. The 11 operating points are comprised of 4 different mass flow settings at 3 different rotational speeds. The four mass flow settings are as follows: Normal Operating Line (NOL), Near Stall (NS), Peak Efficiency (PE), and Wide-Open Discharge (WOD). The three test speeds are 9100 rpm, 9500 rpm, and 13200 rpm which corresponds to 68.5%, 71.5%, and 99.3% respectively, of design speed. (Note: There are only 11 operating points instead of 12 because NS and PE are coincident at 13200rpm).

As mentioned earlier, two distortion screens were used during testing, a 3-per-rev and an 8-per-rev, however both screens were not used for all operating points. The 3-per-rev screen was used at 9100 rpm only while the 8-per-rev screen was used at 9500 rpm and 13200 rpm. As noted before, only a small portion of the data was used for this research focus, that being the 3-per-rev distortion screen operated at 9100 rpm and WOD only. In addition, this data was filtered to a pure 3-per-rev signal that will be discussed in greater detail in the next section.

3.4 Raw Data Reduction and Manipulation

A pure 3-per-rev distortion pattern is almost impossible to create in the test chamber due to all the mounting hardware and probes. The seams where the various wire mesh pieces are joined together on the distortion screen along with the struts to which the distortion screen is attached and the pressure probes and rakes all add unwanted distortions to the flow. For this research focus it is desired to have the purest 3-per-rev pressure distortion possible to isolate the blade response as a result of only the given pressure distortion. Gary Ostdiek at CRF used a curve fit of the data to remove unwanted distortion. The data were taken at 5 different radii and with a point taken about every half degree. The data were then arranged in a spreadsheet with the curve fit divided into 50 radii by 448 circumferential points in an array. Figures 3-6 and 3-7 show the pressure profile before and after the unwanted distortion was removed from the original 3 per rev data, respectively. A sample from Immersion 3 (mid-span) shows the total pressure with unwanted frequency content in Figure 3-6 and again in Figure 3-7 with the unwanted frequency content removed. The numbers on the right side of the legend indicate total pressure in psi in both figures.



Experimental Total Pressure at Immersion 3 (mid-span)

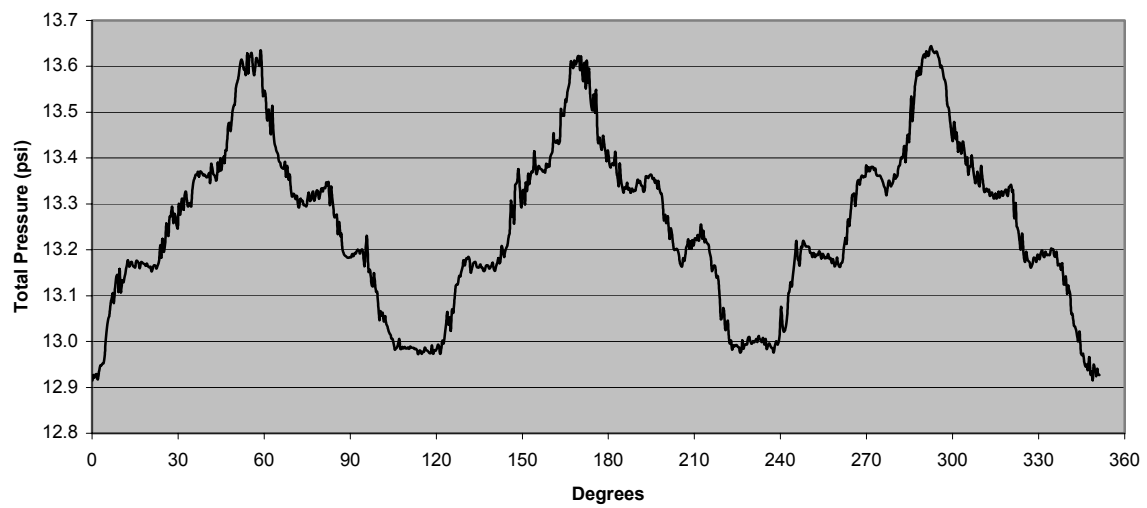
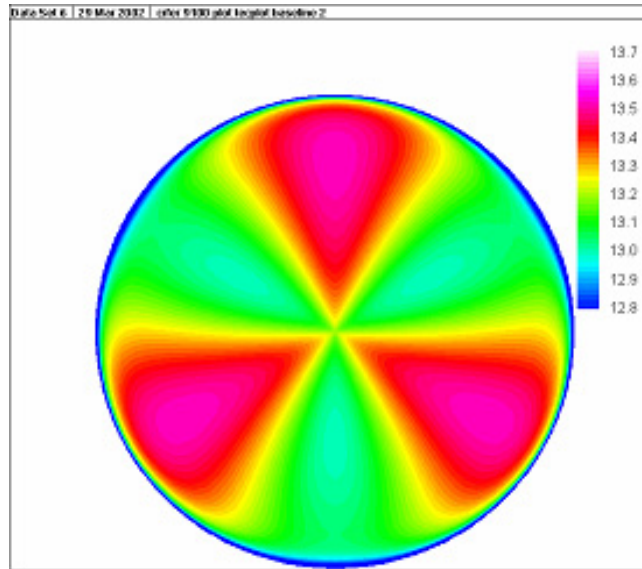


Figure 3-6: Experimental 3-per-rev total pressure distortion.



Model Total Pressure at Immersion 3 (mid-span)

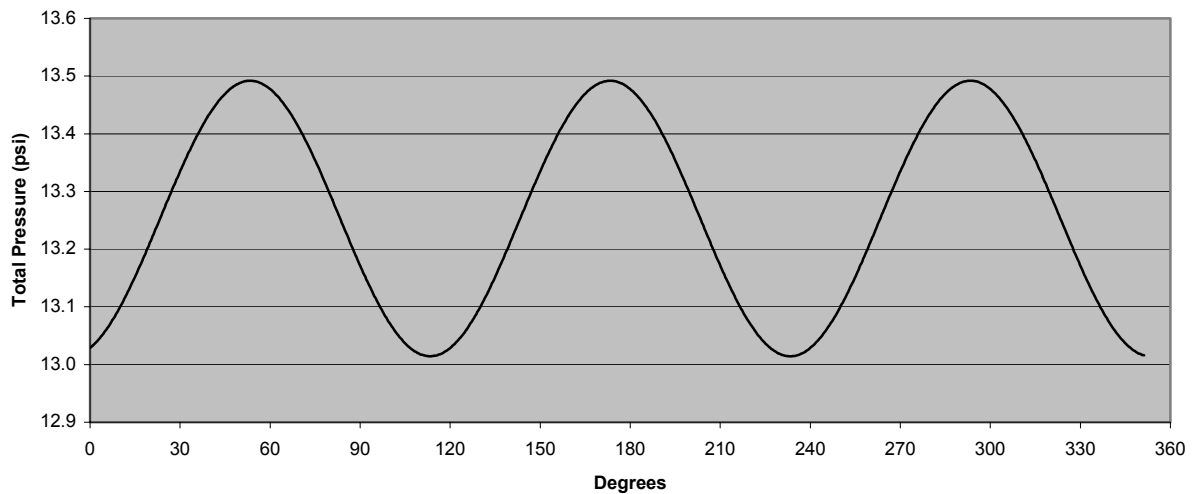


Figure 3-7: Total pressure 3-per-rev model.

After the pressure profile was modified it was then sent to Dr. Hah at the NASA-Glenn Research Center for further development. Dr. Hah used the pressure profile as the inlet conditions for a single blade passage CFD model of the first rotor stage. From this model he was able to create a blade surface pressure profile for both the pressure and suction sides of the blade. Since the inlet distortion is assumed steady state and each sinusoid was identical to the other two in the 3-per-rev distortion, only 1/3 of the

distortion profile was needed as the results could be duplicated around the remaining 2/3 of the circumference.

A 64 by 29 element grid in the streamwise and spanwise direction, respectively, was used to describe the blade surface on both sides and data was collected for 3 different cases. The 3 cases consisted of a 3-per-rev distortion with 80%, 100%, and 120% of the original pressure distortion magnitude. Before running each case through the CFD code the level of distortion was simply multiplied by either 0.8 or 1.2 to change only the magnitude but not the pattern. It is important to understand that the three cases are not independent experimental results from changing the actual distortion screen porosity or any other parameter. Only one case was actually tested experimentally, the 100% case; all other cases are just an amplification or attenuation of the resulting distortion level measured experimentally for the 100% case. However, due to the possible non-linearity of the calculated blade surface pressures, it can not be assumed that the blade surface pressure profile generated will simply be a constant multiple across the entire face equal to that of the inlet pressure profile. For example, the blade surface pressure profile for the 80% case cannot be assumed to be 80% of the value found for the 100% case at any grid point on the blade

I was supplied six data files from Dr. Hah at this point, one for each distortion level on each side of the blade as well as the CFD grid point locations. Upon receiving the data, some reformatting and manipulation was required due to varying reference methods used to describe the data. Multiple coordinate systems were used and nodal numbering schemes had to be resolved to one single system so that data could be applied to the FE model created using the grid points supplied.

4 Finite Element Model Development

A finite element (FE) model was developed for the first stage rotor blade using the CFD grid points as the nodal coordinates in the model. Before this method of describing the geometry was chosen, other methods were considered and attempted in order to weigh the pros and cons associated with each. In an ideal situation, a parametric model describing the exact blade geometry would have been desired, however at the date this blade was designed such models were not prevalent and therefore one was not made. In fact, no data containing the exact blade geometry could be located for this research, leaving only pre-existing finite element models to be used. At some point a NASTRAN model was developed for vibrations analysis but the mesh density was very coarse and did not match the grid points used for CFD and therefore was not used.

4.1 Choosing the Correct Modeling Method

In preliminary model development and testing a solid model was created by using a limited number of points measured from a scale drawing and interpolating the curved surfaces between them. This method proved to be accurate to solve for the natural frequencies of the blade as compared with frequencies measured experimentally. However, natural frequency is largely dependent on material properties and the general geometry of the object being tested for low order modes like the ones here, with slight changes in the geometry affecting the solution very little, and is therefore not a conclusive way to test whether the interpolated blade curvatures were those of the actual blade.

A second attempt to create a solid model was executed using a slightly different method. An approximate solid model could be developed by importing the CFD grid points into ANSYS® and using them to more accurately describe the blade geometry. Many attempts were made to create splines through the many points in the streamwise direction. Splines were also used to create the leading and trailing edge of the blade.

Using the splines as borders, many areas were created to describe the surfaces in small strips. By selecting and adding the relevant areas, a volume can be created (picture selecting the sides of a cube as areas that describe the boundaries of the volume created by them). Adding all of the volumes together creates a single volume and a solid model that describes the entire blade is created. However, remember that the initial step employed the grid points to define the geometry, and as a result the curvature of the blade is still approximated, albeit much better, but not exact nonetheless. Splines do not always follow the path desired and areas are not easily created on curved surfaces unless a process called 'skinning' is used. Even then the area created does not always adjoin the splines picked as the borders used to describe the area. Therefore, when attempting to create a volume from areas with discontinuities between them, obvious problems arise. In the end, the attempt to create a solid model in this fashion was abandoned due to numerous problems that prevented a continuous solid from ever being created.

The advantage of starting the analysis with a solid model allows the user to define and refine the mesh type and density applied to the model during analysis. Refining a mesh in FE analysis becomes very important as it allows the convergence of a solution by continually making the mesh more refined until the value in question no longer changes, in this case the natural frequency. However, since the true natural frequency of the blade was already known from experimental tests, this allowed one more and final option for developing a model.

The third model again used the CFD grid points as nodal locations in 3D space to describe the blade geometry. Instead of attempting to back out an accurate solid model, the nodes created were simply connected to create elements directly. At this point a rectangular element was chosen and a small code was written to read in the node locations of each of the nodes defining the 8 corners of the cube, create the element and then proceed to the next node. After this was finished, a complete FE model was created with a fixed mesh density. In order for this model to be used, the natural frequency solution as found by ANSYS would have to be close to the actual natural frequency with the given mesh density since no refinement was possible without additional extensive work to subdivide the elements. To accurately model bending with the element type used, ANSYS suggests at least a thickness of three elements in the primary direction of

bending. Since CFD only needs surface nodes to evaluate the flow around the blade, two rows of internal nodes had to be created using TECPLOT® to interpolate between the two surfaces. Initially only 3 rows of elements were created and the model was tested. The natural frequency found was within 2.3% of the experimental value and therefore the model was considered valid. It should be pointed out that the blade surfaces have been discretized by the flat element surfaces but this is of no consequence in the vibration analysis since the natural frequencies were found to agree. This may not be the case if the model were used for other types of analysis. The final FE model used for this analysis is shown in Figure 4-1. A black dot has been placed at the leading edge tip in both views as a point of reference.

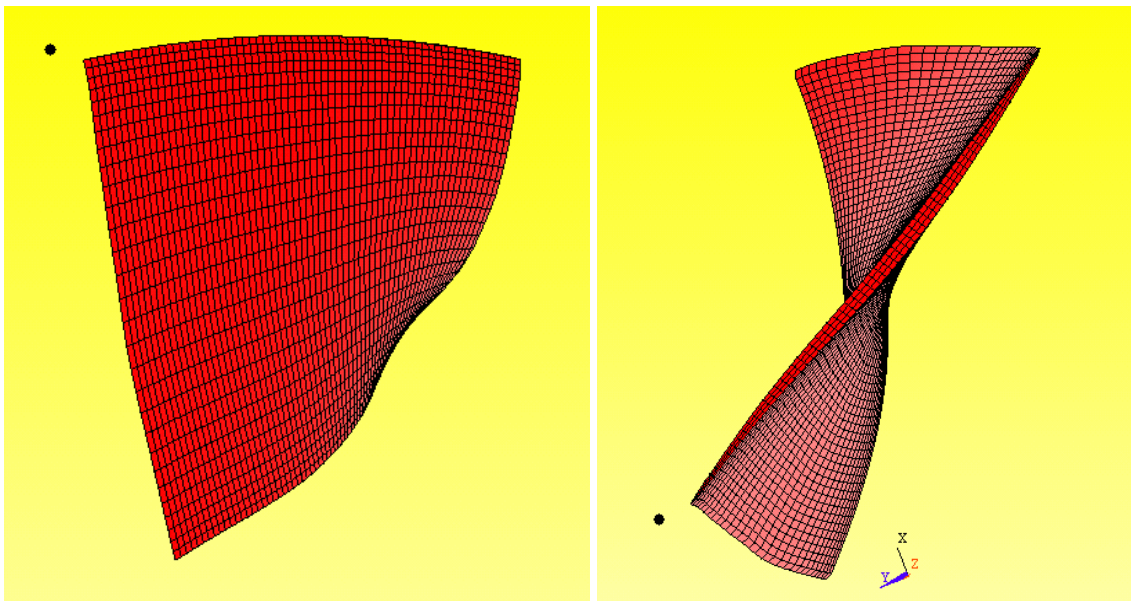


Figure 4-1: The 5568-element model used for analysis.

4.2 Model Properties and Constraints

As mentioned previously, the blades are not connected to the hub with a dovetail configuration on the first rotor stage. Thus, there is virtually no damping provided by the ‘hub’, which allows for it to be eliminated from the model and the blade to be assumed constrained as a cantilevered beam. In theory, all 16 blades are identical and therefore

should possess the same natural frequency. In reality, however, this is not the case due to mistuning. For this research it is assumed that all the blades are identical. Therefore for it is assumed that response is equal allowing only one blade analysis to speak for the group. The material properties used in the FE model are detailed in Table 4-1.

Table 4-1: First stage rotor FE model material properties.

| | Titanium Alloy (Ti-6-4) | Pure Titanium (Ti) | Percent Difference |
|------------------------------------|--------------------------------|---------------------------|---------------------------|
| Density (ρ) | 0.161 lbm/in ³ | 0.175 lbm/in ³ | +8.2 % |
| Modulus of Elasticity (E) | 16.5x10 ⁶ psi | 14.8x10 ⁶ psi | - 10.3 % |

The exact material properties were still unknown to the author at the time model creation started and therefore the values for pure titanium were used, as opposed to the titanium alloy actually present. The difference in material density and modulus of elasticity is also shown in Table 4-1. The pure titanium material properties were used throughout the entire analysis since the model validation phase, which included original MATLAB® code to verify the numbers ANSYS calculated on a much simpler two-element beam, used pure titanium. To change the material properties midway through the analysis would have required resolving all the initial steps leading up to the present calculation. Furthermore, the non-exact material property values gave extremely good natural frequency results. The process was repeated once the material used, titanium alloy Ti-6-4, became known. An unintentional positive outcome of this result is that it is shown that a small amount of approximation in material properties can be used without adversely affecting the solution's accuracy.

4.3 Rotational Effects

To accurately model the state of the rotor blade during operation, the blade must be rotated around a point equal to the distance of the engine's center of rotation at the correct speed. The model was therefore set to simulate 9100rpm throughout the analysis. Spinning an object can have two main effects: the object becomes artificially stiffened in certain directions due to the centrifugal forces pulling on the mass; and, the object's shape will change if portions of the mass are not aligned along a line drawn between the center of rotation and the object's center of mass. The rotor blade is subjected to both of these effects, which introduces another difficulty in modeling not yet discussed.

Compressor blade designers design the blade shape for the intended operation point keeping in mind the blade shape changes as a result of centrifugal forces. The shape of the blade at the design operation point is known as the "hot geometry," while the shape of the blade sitting stationary is known as the "cold geometry." The cold geometry must be determined in a way so that the blade will assume the intended geometry at the design point. This change in blade geometry is known as "untwist." The blade will continue to untwist as the speed at which the engine is operated increases.

For CFD analysis the hot geometry is all that is needed since the blade shape alone determines how the fluid flows around it. This presents a potential problem in using the CFD grid points to define the blade used in vibration analysis. While the natural frequencies were used to compare and validate the model, the mode shape is the end result desired. The natural frequency only indicates the point within the frequency spectrum that excites the object, however it says nothing about how the object moves once excited. The mode shape contains information on how the object moves, giving the direction and relative magnitude of any given point in relation to any other point within the object. All magnitudes are relative, as no absolute magnitude of deflection is known until the magnitude of the force exciting the object is defined. It now becomes apparent that if the shape of the blade before excited is different at different states ("hot" versus "cold") then it is possible the mode shapes will differ greatly for the same mode on two related, but different blade shapes.

The problem arises when considering the centrifugal stiffening and untwisting of the blade simultaneously. Using the hot geometry grid points from the CFD calculations gives the correct blade shape without using centrifugal force induced untwist. This alone would not be an issue if the centrifugal stiffening were not a concern. However, it is, and so this does become a concern. Ideally, the cold geometry would be desired so it could be spun at the correct operational speed and therefore introduce the artificial stiffening and untwist simultaneously as it occurs in reality. Again, due to the age of the design, computer models were not available that describe the cold geometry. Only later were hot geometry models generated for CFD calculations, and therefore a way to handle the obstacles had to be determined.

Since the natural frequency increases with increasing stiffness, the rotational speed directly determines the amount of stiffening that occurs and consequently the natural frequency. Knowing that all the data being considered was taken at 9100rpm means a possible solution was to increase the stiffness in the material property definition until the hot geometry had the correct natural frequency while sitting stationary. The amount to increase the stiffness would have to be determined by a trial and error approach and it was decided to explore other options before attempting this solution.

I decided to calculate and compare the mode shapes for the hot geometry stationary with the hot geometry spun at 9100rpm. While it is true that the hot geometry spun at 9100 rpm gives an incorrect blade shape, the degree of untwist should be approximately equal to that the blade undergoes while untwisting from the cold to the hot geometry. If the difference in mode shape turned out to be minimal between the hot geometry spun and unspun, then it could be argued the difference would be very similar between the cold and hot geometry. In addition, ANSYS is a linear finite element code, which means small deflection theory must be assumed. This means that the blade deflection due to untwist must already be assumed to be very small. If this assumption were not found to be correct, then the entire blade model would be invalid as ANSYS would be incapable of accurately calculating a solution, as the blade would untwist too much for a linear code solution. However, the test showed a maximum difference in mode shapes of less than 1% using a root-mean-square calculation to sum the differences between each node of the model. Therefore it was decided that mode shapes from the hot

geometry spun at 9100 rpm could be used. This means that while the blade shape would be slightly incorrect, the natural frequency and the mode shape will be approximately correct as the centrifugal stiffening and untwist plays a very small role in changing the mode shapes for the case being considered.

4.4 Finite Element Model Summary

The finite element model used for all analysis was constructed from the CFD grid points that described the hot geometry. This geometry was constrained only along the base of the model for zero displacement and rotation in all directions where it attaches to the “hub”, and was spun at 9100 rpm. It consisted of 5568 Solid 45 “brick” elements with a 3-element thickness in the direction of primary bending. The material properties used were those of pure titanium and titanium alloy Ti-6-4 as given in Table 4-1 with a damping ratio of 0.0083 as determined by CFD calculations [Breard, 2002].

5 Analysis and Results

The main research goal of developing a model representing the blade and how it responds to total pressure distortion and therefore saving much time and money by partially eliminating such extensive testing is the driving factor for determining the analysis methods. Remember the three main goals: (1) create an accurate finite element (FE) model of the ADLARF fan blade for eigenvector extraction; (2) identify dominant engine order modal force magnitudes based on coupling computational fluid dynamics (CFD) generated total pressure distortion and FE generated eigenvectors; and (3) determine the relationship between the magnitude of the modal force and the total pressure distortion level used to drive the system. The modal force represents the generalized force used to drive the FE model of the ADLARF fan blade at a given mode. Goal (1) was addressed in the previous chapter under Finite Element Model Development. The remaining goals will be addressed now.

5.1 Finite Element Generated Eigenvectors

The first step in determining and analyzing the reaction of the blade is to identify the way in which it naturally deflects under free vibration. Free vibration occurs when an object is given an impulse to excite the system but not continuously applied in any constant or changing rate. Experimentally, free vibration is often tested by suspending the object from a string or bungee chord, then striking it with a hammer and measuring the response with an accelerometer or a laser vibrometer. In the case of the compressor blade, one side is attached to the “hub” and is constrained from motion in all directions and therefore a shaker rig could be employed to test free vibration under these constraints. A shaker rig allows the object to be securely fixed to a moving platform that undergoes a frequency sweep, record the response over the range tested and determine the natural frequency, or eigenvalue, of the object by referencing the frequency at which the largest deflections occurred.

However, determining the mode shape, or eigenvector, experimentally is much more difficult. To accurately describe the eigenvector one needs to know the magnitude and direction that each “point” on the object moves. The word point is used in quotations to underline the fact that no discrete points exist on an object. Therefore, experimentally testing for eigenvectors would require numerous accelerometers, which would ultimately change the system with their added mass, or a scanning laser vibrometer that is capable of quickly scanning the entire surface of the blade as it deflects while being excited at any given frequency. Again, in the case of the compressor blade, the rotating nature of its operation introduces difficulty in experimental tests. Ways to use a scanning laser vibrometer in such an environment have been researched, but are not presently being used at CRF for this purpose. This is where the advantages of a finite element model can be realized.

In a FE model, mass and stiffness matrices are constructed and the equations of motion and therefore the eigenvectors can be solved for directly. The motion of the “points” on the object mentioned previously become the nodes present in the model. These nodes also represent the mass in the system. A finite element model divides the entire mass of each element and distributes it to the nodes at the corners. In this case, the solid 45 brick element is a rectangular shape and therefore has 8 nodes that make up the 8 corners of the brick. Therefore the mass of any given brick element is divided by 8 and assigned to each of its nodes. Most nodes (except those on the exterior blade corners) are connected to multiple brick elements and therefore receive an additional contribution to their mass as well.

Simplifying the situation for the sake of explanation, each node can be thought of as a single degree of freedom system consisting of a mass, spring, and damper and only allowed to deflect in one direction. The familiar diagram associated with this system is shown in Figure 5-1. The entire blade, however, is comprised of many nodes and must be evaluated as a multiple degree of freedom system where the motion of each mass affects all others in the system. A diagram showing a simple multiple degree of freedom system is given in Figure 5-2. In reality even one node on the blade contains more than one degree of freedom as it is allowed to deflect in all three directions, X, Y, and Z.

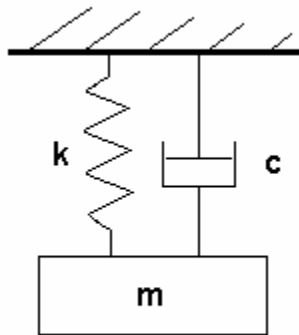


Figure 5-1: Single degree of freedom model.

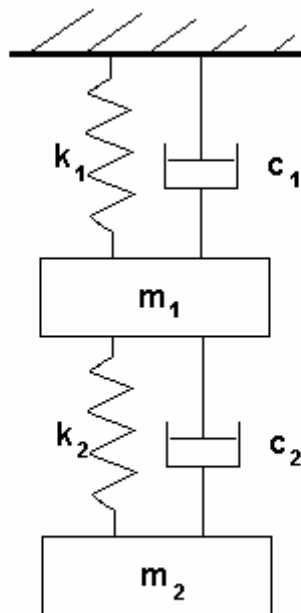


Figure 5-2: Multiple degree of freedom model.

The equation of motion for a single degree of freedom model is given by

$$m\ddot{x} + c\dot{x} + kx = F(t)$$

Equation 5-1

where m , c , k represent the mass, damping, and stiffness of the system, respectively. Realizing that the natural frequency, ω_n , is equal to the square root of the stiffness divided by the mass and introducing ζ as the damping ratio then the equation can be rewritten as

$$\ddot{x} + 2\zeta\omega_n\dot{x} + \omega_n^2x = F(t)$$

Equation 5-2

For modal analysis the same equations of motion apply and for multiple degrees of freedom they take on a matrix form. The nomenclature for the force acting on the system has been changed to represent a periodically changing force representative of the total pressure inlet distortion. In addition, most damped systems are analyzed in modal analysis as undamped. Damping is applied after the solution to find the natural frequency and therefore the damping has been removed from Equation 5-3.

$$M\ddot{x} + Kx = f e^{i\omega t}$$

Equation 5-3

The variables for the mass and stiffness become capital M and K to denote they are of matrix form. Here x is a vector containing all the modes of the system.

$$x = \sum_j \eta_j(t) \tilde{\Phi}_j$$

Equation 5-4

Substituting and premultiplying by $\tilde{\Phi}_i^T$ gives

$$\sum_j \ddot{\eta}_j(t) \Phi_i^T M \Phi_j + \sum_j \eta_j(t) \Phi_i^T K \Phi_j = \Phi_i^T \mathbf{f} e^{i\omega t}$$

Equation 5-5

Where

$$\Phi_i^T M \Phi_j = \begin{cases} 0 & \rightarrow i \neq j \\ 1 & \rightarrow i = j \end{cases} \quad \text{and} \quad \Phi_i^T K \Phi_j = \begin{cases} 0 & \rightarrow i \neq j \\ \omega_i^2 & \rightarrow i = j \end{cases}$$

Equation 5-6

Which then reduces to

$$\ddot{\eta}_j + \omega_i^2 \eta_j = \Phi_i^T \mathbf{f} e^{i\omega t}$$

Equation 5-7

Finally, solving in matrix form for the generalized force becomes

$$[I] \{\ddot{\eta}_i\} + \begin{bmatrix} \omega_i^2 & & \\ & \ddots & \\ & & \end{bmatrix} \{\eta\} = \{\Phi_i^T \mathbf{f}\} e^{i\omega t}$$

Equation 5-8

So that the total modal force, F_j , is the projection of the force on the mode shape.

$$F_j = \Phi_i^T \mathbf{f}$$

Equation 5-9

Using ANSYS to solve the equations of motion for the finite element model allow the first three modes shapes to be solved and the resulting eigenvectors to be output to a file. Now each node on the model has a direction and relative magnitude associated with it for each mode. The first three modes solved for are 1st flexural, 2nd flexural, and 1st torsional and were mass normalized. A table showing the error associated with each mode from testing the hot geometry spun and unspun was constructed as shown in Table 5-1.

Table 5-1: Eigenvector RMS error calculation results.

| Mode | Average RMS Error (%) |
|------|-----------------------|
| 1 | 0.238 |
| 2 | 0.356 |
| 3 | 0.929 |

A Campbell Diagram is often constructed and implemented to identify problem areas of engine operation. One is presented in Figure 5-3. The diagram is constructed by testing the blade, either experimentally or using FEM, to determine the natural frequency over the entire range of operation by evaluating the system at incremental steps and plotting those points at their respective speed of rotation. Connect the points and the three solid lines are created, each showing how the natural frequency increases for each mode. Next, the “per-rev” lines are added, in this case from one to eight. A per-rev line indicates how many excitations a blade will encounter by traveling one circumferential distance. Knowing the data being analyzed was taken at 9100rpm with a 3-per-rev distortion screen used, we can see a problem area is likely to exist because this 3-per-rev source of excitement occurs at 435 Hz while operated at 8700rpm which coincides with the first natural frequency associated with the 1st flexural mode. This area is highlighted by a red circle on the diagram. In fact, a Campbell Diagram similar to this one was constructed before the experimental testing took place to target problem areas as operation at these points is extremely dangerous and destructive. As a result, the data was taken at 9100rpm where the excitation occurs at 455 Hz and therefore still excites the first mode greatly, but not enough to induce deflections large enough to be destructive. The first mode shape is therefore of greatest concern with the largest deflection and modal force expected. From Table 5-1 it is reassuring to see the first mode has the least amount of error, as it will be the most important.

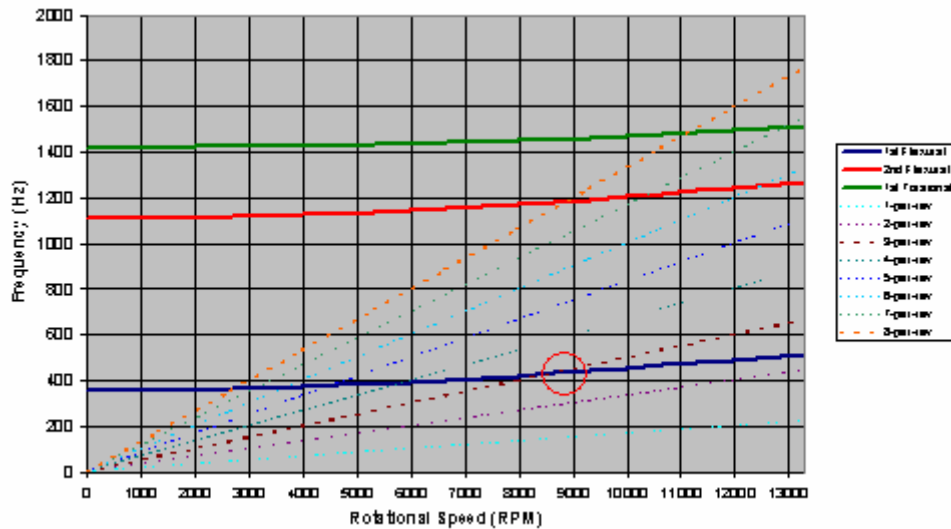


Figure 5-3: ADLARF 1st stage compressor Campbell diagram.

5.2 Generalized Forcing Function

Using modal analysis to determine the generalized forcing function, it is required to know how much of the pressure on the blade surface contributes to moving the blade in the same direction as the mode shape. The total pressure data as received from Dr. Hah only consisted of total pressure magnitudes at the given time steps. However, pressure can only act normal to a surface, so normal vectors had to be determined along both blade faces at each nodal location. Tecplot was used for this step and the normal vectors were associated with the pressure magnitudes using nodal coordinates. Normal vectors for the leading and trailing edge of the blade were eliminated since determining a normal for an edge is an ill-posed problem and as a result the eigenvector data from all nodes along the leading and trailing edge were not used.

Now that the mode shape and total pressure directions were known in 3-dimensional space acting through each of the nodes on the blade, a projection of the force due to pressure in the direction of the eigenvector could be determined. This requires an inner product to be taken. An inner product consists of multiplying each x, y, z component of the pressure with the matching component in the eigenvector and then summing the results from each component.

$$\sum (E_i P_i + E_j P_j + E_k P_k) = \frac{1}{\sqrt{m}} * P$$

Equation 5-10

After each component has been summed for every node, the resulting values are summed together on both blade surfaces for the solution. Finally, to acquire a force instead of a pressure, the elemental area of the pressure and suction side were averaged and multiplied through as shown below.

$$GFF = \frac{1}{\sqrt{m}} * PA = \frac{1}{\sqrt{m}} * F$$

Equation 5-11

The solution is a single value indicating the relative magnitude of the generalized force on the blade for the time step evaluated. To show how this changes with time, the inner product is repeated and plotted for each time step. As mentioned previously, only 1/3 of the distortion pattern was used in the CFD calculations so the generalized forcing function results were conditioned to represent a full annulus. This included copying the results twice and adding them tip to tail effectively expanding the results around the full annulus. Second, to give a spatial representation, the time steps were converted to an angular position from 0 to 360 degrees. Lastly, the time steps were arbitrarily assigned during the CFD calculations so conversion to angular positions did not result in all the peaks of the sinusoidal pressure distortion being aligned, therefore the data from different simulations were phase locked for a more physical representation and to make result comparisons easier. The inner product and results conditioning were done with Excel and the results are shown below in Figure 5-4 through Figure 5-9.

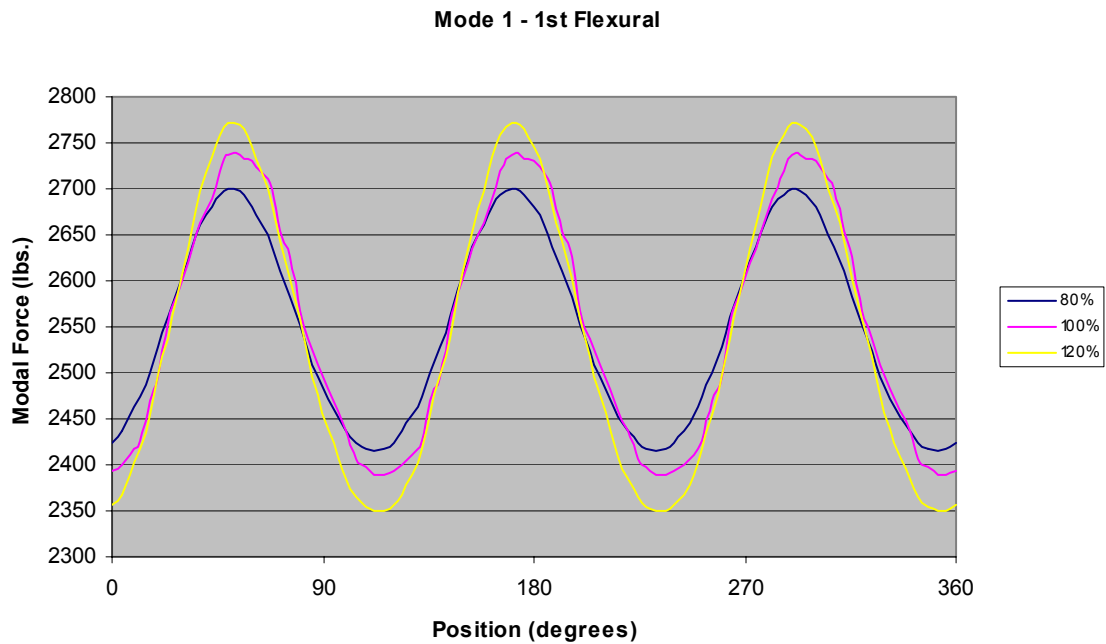


Figure 5-4: 1st Mode - Modal force as a function of distortion level.

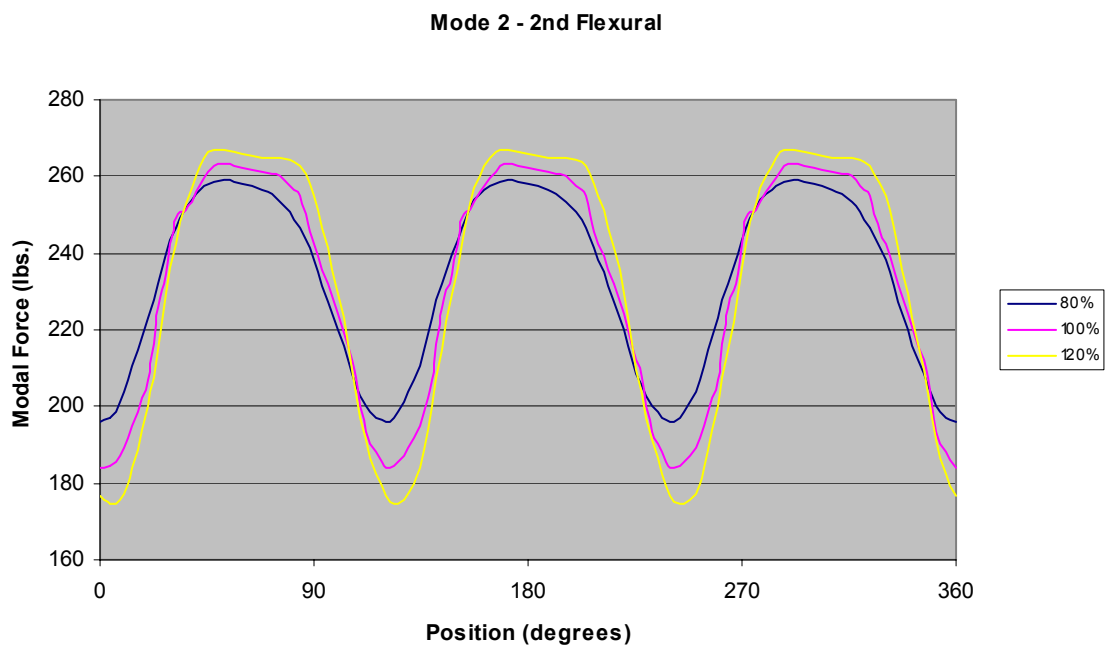


Figure 5-5: 2nd Mode - Modal force as a function of distortion level.



Figure 5-6: 3rd Mode - Modal force as a function of distortion level.

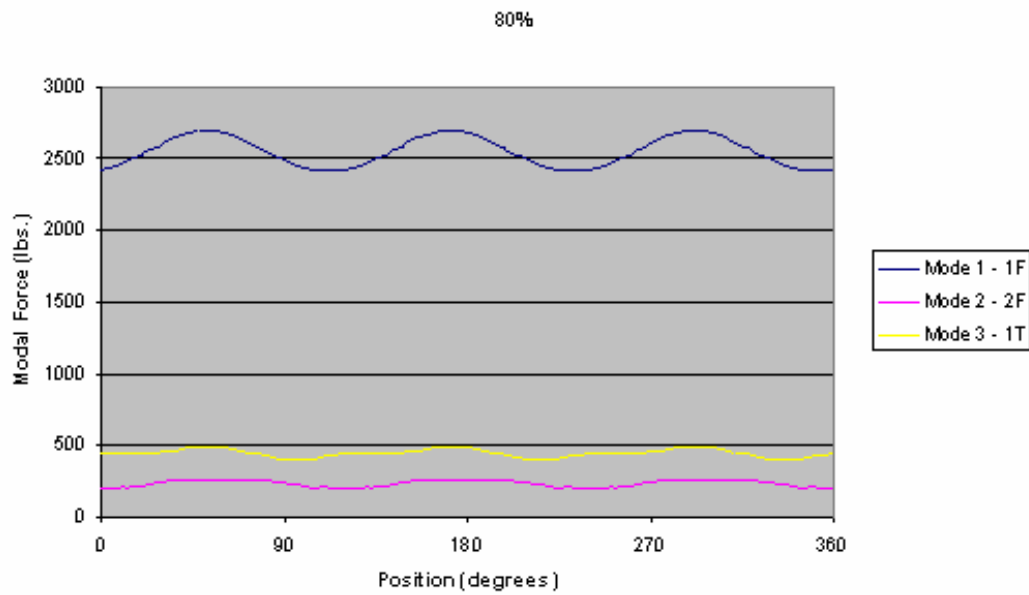


Figure 5-7: Modal force comparison at the 80% distortion level.

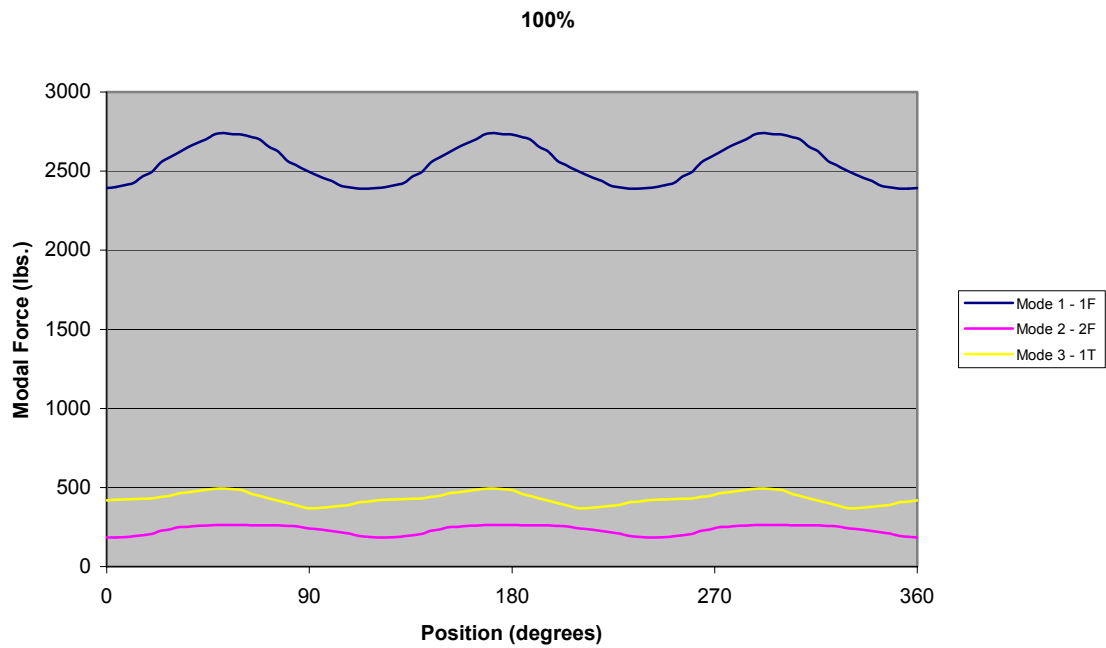


Figure 5-8: Modal force comparison at the 100% distortion level.

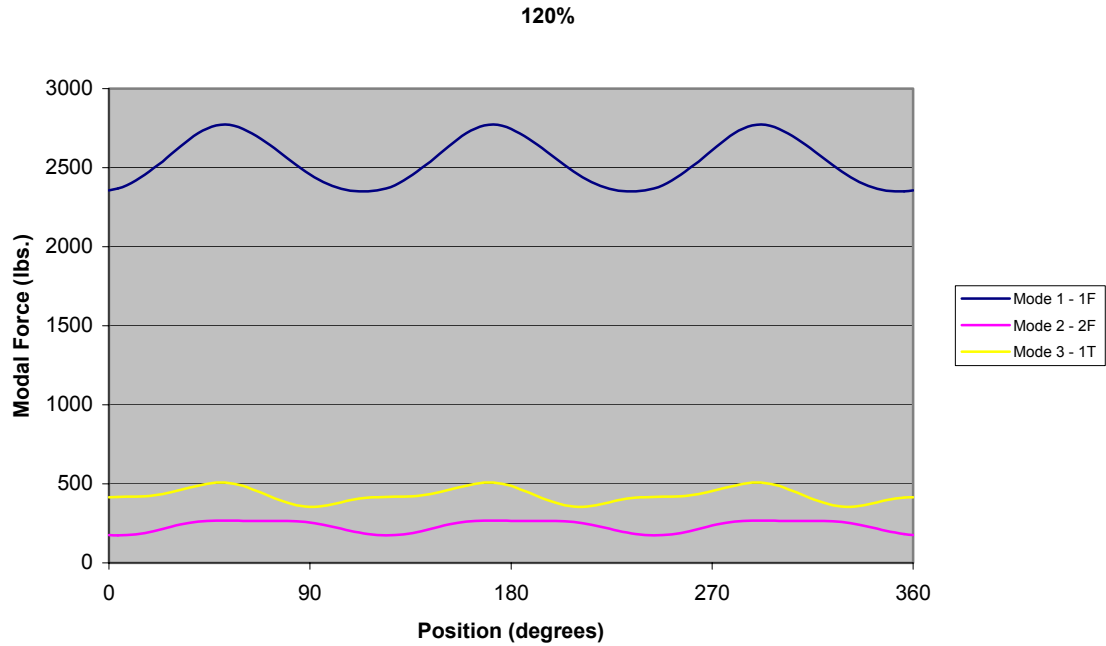


Figure 5-9: Modal force comparison at the 120% distortion level.

The results have been divided and displayed with respect to the two main categories in which to analyze the data, first by mode and second by inlet distortion level. When inspecting the plots arranged by mode, two things should be noted. First, the average value at which the generalized forcing function oscillates about, and second, the amplitude of the forcing function. The average value indicates the baseline loading the blade undergoes while under the 3-per-rev distortion pattern with respect to its contribution towards exciting that particular mode. The amplitude of the oscillation shows how much the loading changes as a result of the sinusoidal excitation. It is important to remember that the only thing changing between the separate modal plots are the eigenvectors associated with that mode; the pressure vectors used in the inner product remain the same throughout the analyses. As expected, the amplitude for each mode changes with the distortion level present and the shape of the sinusoidal generalized forcing function changes in accordance with the mode shape.

The second set of plots holds the distortion level constant for each plot while each of the three modes is plotted for each distortion level. These plots are a better indication of the difference in average blade loading caused by the 3-per-rev pressure distortion with respect to the contribution towards each mode. To better understand the idea of the same distortion pattern and level contributing different amounts to the three mode shapes, consider an example of a diving board.

Like a diving board, the compressor blade being studying is essentially a flat plate cantilevered on one end. Consider a person standing on the end of the diving board, and for now, think of the pressure loading on the blade only acting through one point as a single force. The person's weight will cause the board to deflect a finite amount dependant on the geometry and material properties of the diving board. Now consider the person jumping up and down on the board in such a way that their feet never lose contact with the board surface and every time their weight is exerted back on the board, the board is already moving downward, so the force they exert is always in the same direction of motion. It's easy to see in this way that the average deflection of the board as well as the amplitude of the oscillations could be large. This is exactly the scenario the blade will experience during the 1st mode, called 1st flexural. Now, to understand why the average deflection of the 2nd and 3rd mode is much less, you need to superimpose the

motion of the person jumping on the board onto a picture of the board deflecting in a different manner. Choosing the 3rd mode, called 1st torsional, the board will be twisted as if someone at the end of the board grasps both sides and applies a torque clockwise, and then counterclockwise over and over again. How much of the energy applied by the person jumping on the board helps this torque accomplish its deflection mode of twisting the board? When twisted, half of the board is moving downward while the other half is moving upward, so part of the energy exerted by the jumping person helps the side going downward, yet opposes the side going upward. If the blade were symmetric like a diving board, the effect would cause each side to cancel the other side out, however the blade is not symmetric and therefore a nonzero contribution exists. However, as expected, the 1st mode generalized forcing function is many times higher than the 2nd and 3rd mode since the oscillating pressure on the blade coincides with the natural motion of the blade in 1st flexural.

5.3 Fast Fourier Transform of the Generalized Forcing Function

A Fast Fourier Transform (FFT) was conducted on the generalized forcing function in order to determine the harmonic decomposition of the function. The modal force amplitudes have been plotted and appear in Figure 5-10 through Figure 5-12.

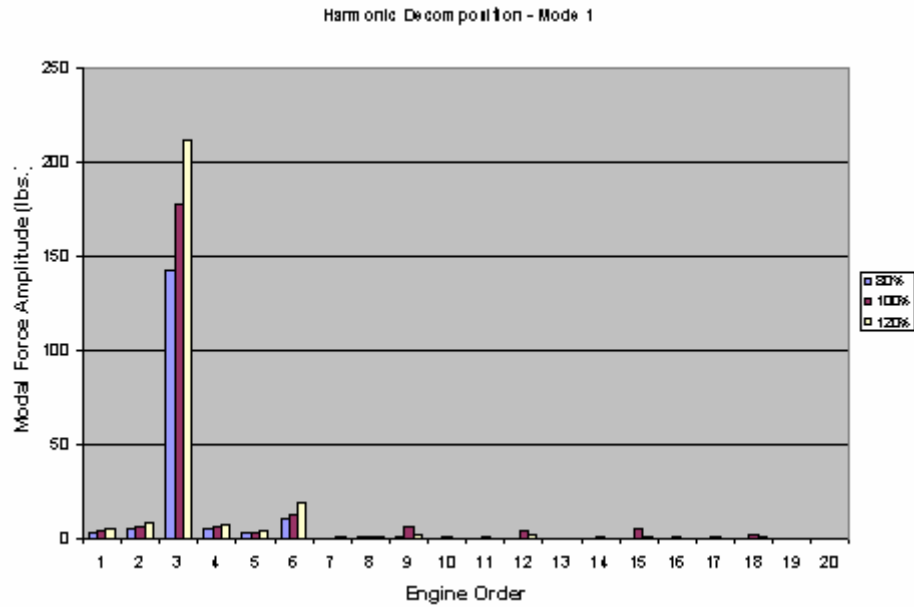


Figure 5-10: Harmonic content present in the 1st mode.

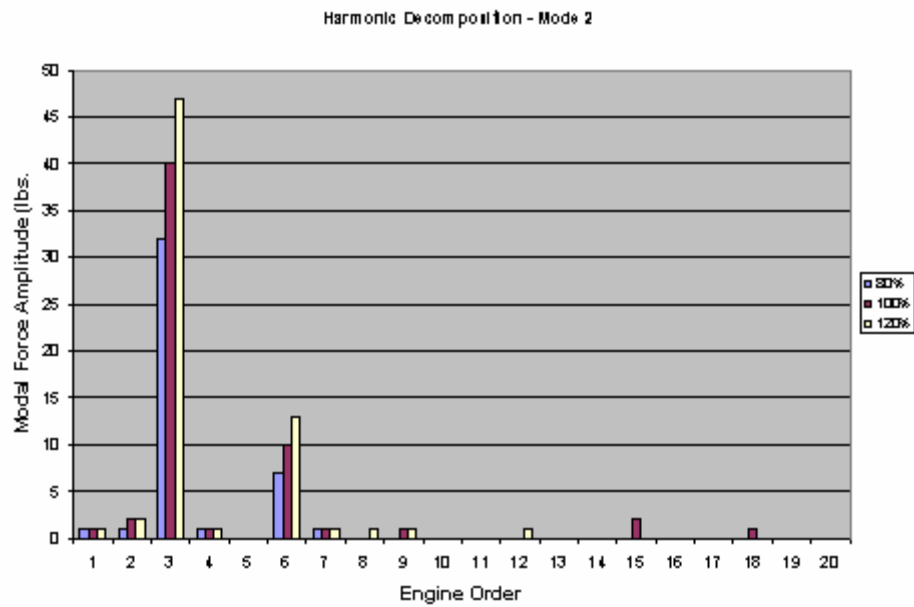


Figure 5-11: Harmonic content present in the 2nd mode.

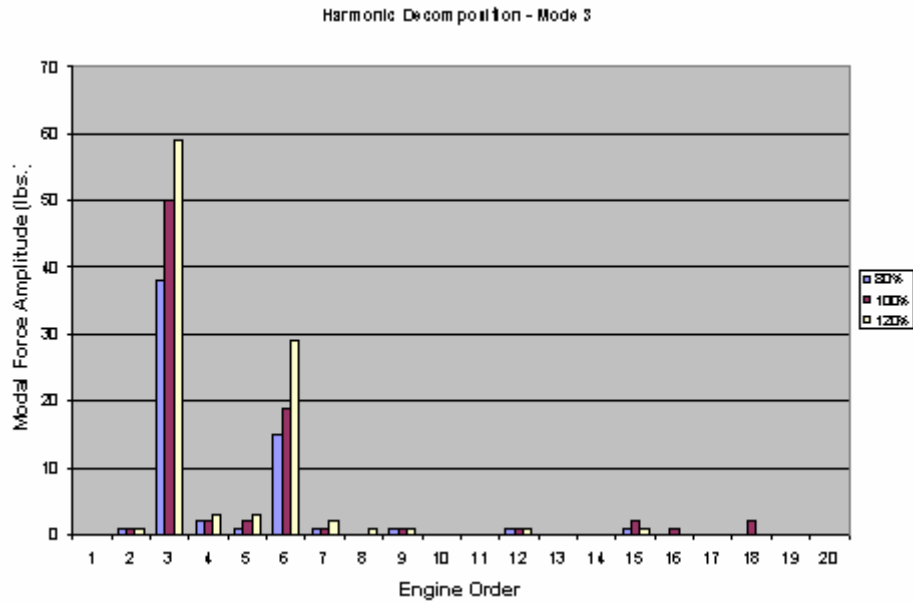


Figure 5-12: Harmonic content present in the 3rd mode.

The x-axis is labeled as Engine Order to denote the number of excitations per revolution and therefore it is no surprise again to see the highest modal force is present at the 3rd engine order. The zero engine order represents a DC offset, which corresponds to the average baseline blade loading discussed earlier. This value is so much larger than the oscillation magnitudes that it has been eliminated to make better use of plot scale. In addition, the amplitude of the oscillations is of greater importance than the baseline blade loading as this is the driver of high cycle fatigue. The modal force results from the FFT indicate how much of the amplitude present in the sinusoidal forcing function is a result of the various engine orders. The second highest modal force amplitude present was the 6th engine order, a harmonic of the 3rd engine order. In the 3rd mode this 6th engine order response was quite high and can actually be seen as a smaller extra “peak” or area where the sinusoid plateaus between the major trough and peak of the sinusoid in Figure 5-6.

A table summarizing the modal force amplitude of the 3rd engine order and the 6th engine order has been included as Table 5-2 for each mode and distortion level. The first mode has been highlighted as it had the highest modal force.

Table 5-2: Modal force summary.

| Mode | 3rd EO (lbs) | 6th EO (lbs) | Level |
|-------------|--------------------------------|--------------------------------|--------------|
| 1 | 142 | 10 | 80% |
| 1 | 177 | 13 | 100% |
| 1 | 211 | 19 | 120% |
| 2 | 32 | 7 | 80% |
| 2 | 40 | 10 | 100% |
| 2 | 47 | 13 | 120% |
| 3 | 38 | 15 | 80% |
| 3 | 50 | 19 | 100% |
| 3 | 59 | 29 | 120% |

5.4 Sensitivity Analysis

In an attempt to easily determine the relationship between the level of inlet pressure distortion and the modal force amplitude of the various modes tested, a sensitivity plot was developed. A plot for the 3rd and 6th engine order have been included as Figure 5-13 and Figure 5-14, respectively.

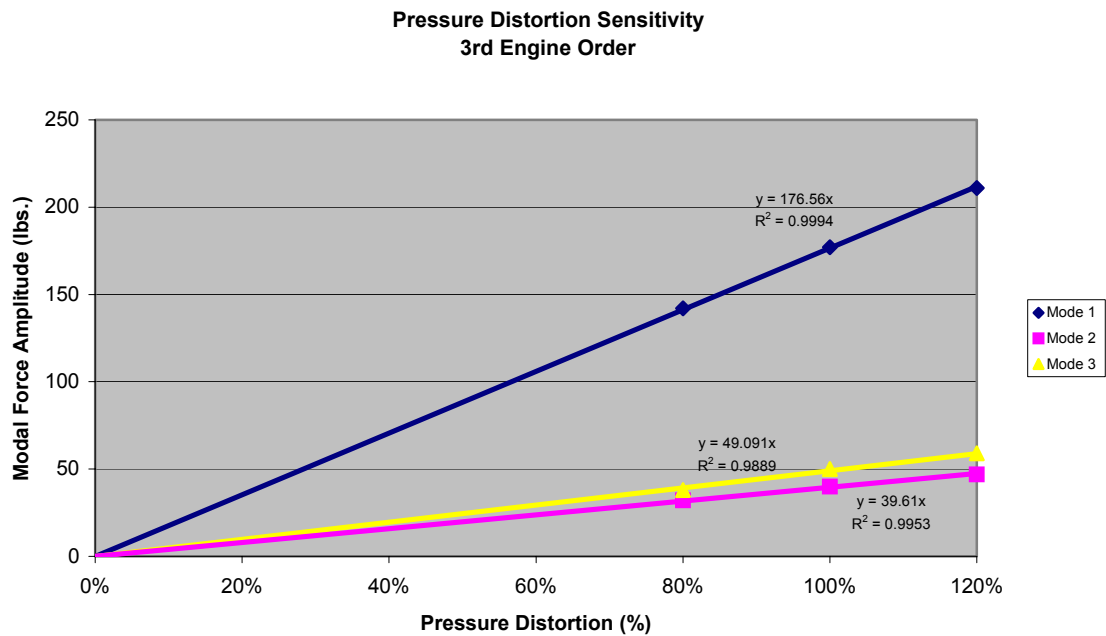


Figure 5-13: 3rd Engine order pressure distortion sensitivity.

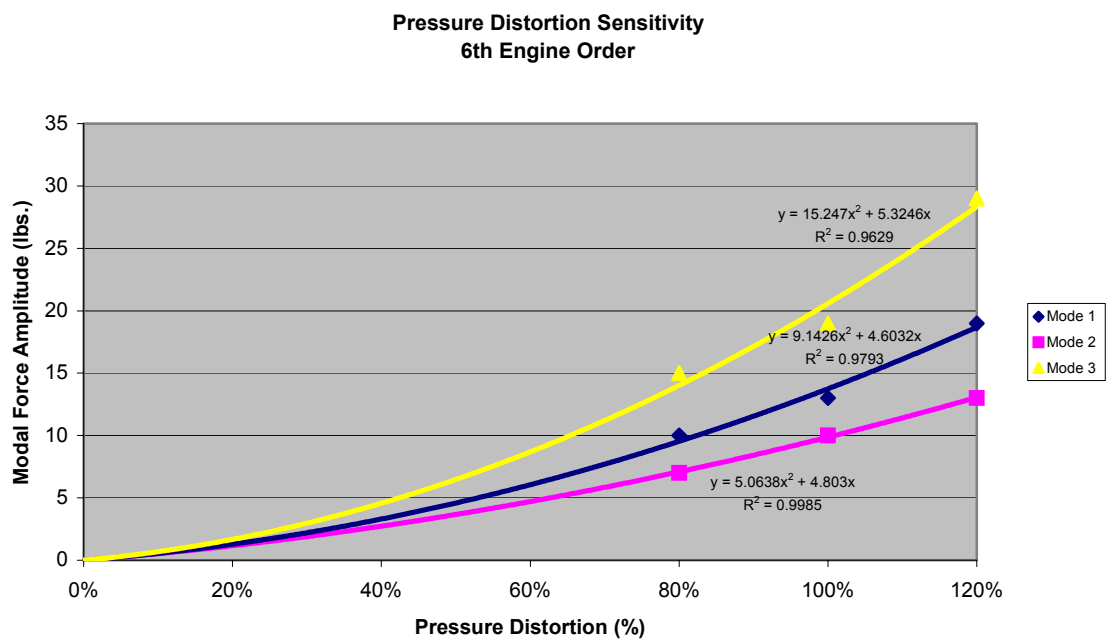


Figure 5-14: 6th Engine order pressure distortion sensitivity.

In Figure 5-13 it can be seen that the relationship between the modal force amplitude and the pressure distortion level appears to be very linear. A best fit line has been added with the equation and R^2 value included. The equation was forced through zero in the assumption that there should be no force present in the absence of any pressure distortion. The slope of the line indicates the sensitivity factor. The sensitivity factor indicates the gain in modal force as a function of percent gain in total pressure distortion. For example, for the 1st mode a 20% increase in total pressure distortion results in a $176.6 \times 20\% = 35.3$ gain in modal force. The 6th engine order sensitivity factor plot was made to see the relationship between pressure distortion and modal force for an engine order that was a harmonic of the engine order being directly excited by the distortion screen. From Figure 5-14 it appears that the relationship may be parabolic as the R^2 values are still relatively high with the equations being forced through zero once again. It is important to realize that the pressure distortion amplitudes are nonlinear for these harmonics and the sensitivity depends on the pressure distortion amplitude. However, for both plots the available data is limited with only three data points and adding a forth by forcing it through zero. It is often dangerous and possibly misleading to extrapolate over a large area as is done here but for the data points available, the R^2 value seem to indicate a good fit, especially in the linear case for the 3rd engine order. A sensitivity factor summary is shown in Table 5-3.

Table 5-3: Sensitivity factor summary.

| | Mode 1 | Mode 2 | Mode 3 |
|--------------------------|---------------|---------------|---------------|
| 3rd EO | 176.6(x) | 39.6(x) | 49.1(x) |
| 6th EO | 30.5(x) + 5.3 | 10.1(x) + 4.8 | 18.3(x) + 4.6 |

5.5 Checking Modal Force Results with Strain Gage Data

During initial testing of the ADLARF compressor at the CRF, three strain gages were placed at various locations on the suction side of the fan blade to measure response of strain and therefore stresses present. Twenty seconds of recorded data for resonant

operation at 8100 rpm and 9100 rpm were sampled at a rate of 2.5 kHz [Kenyon, 1999]. A diagram showing the location of the three strain gages is shown in Figure 5-15.

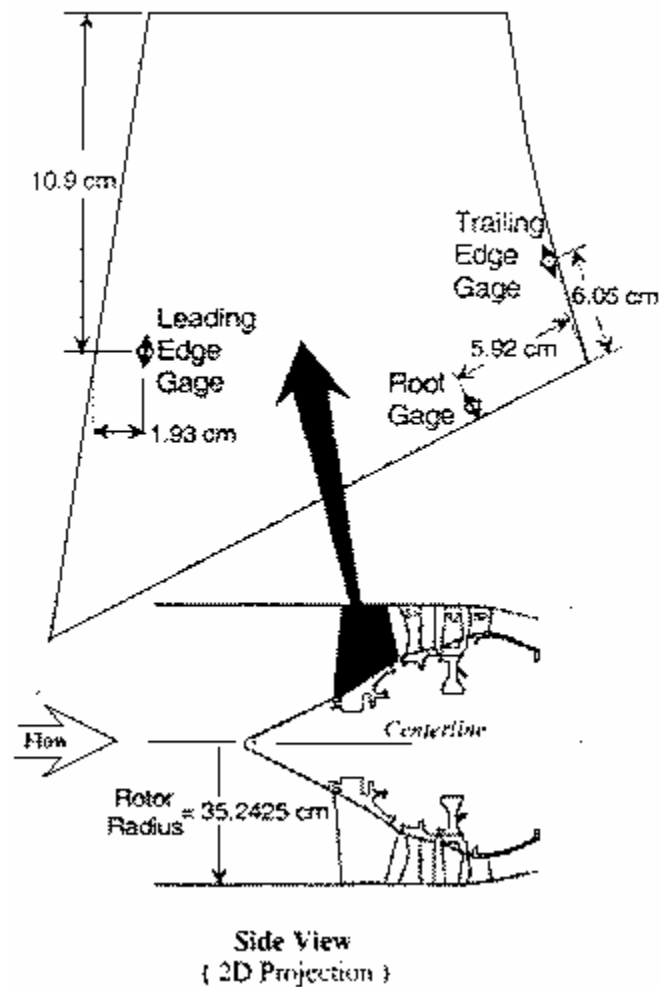


Figure 5-15: Side view of the test compressor showing strain gage location [Kenyon, 1999].

The Root Gage was located 5.92 cm from the trailing edge of the blade, which corresponds to Node 47 along the base of the blade. The strain gage however covers a small area just above the blade root and so the Node 177 located 2 elemental rows, approximately $\frac{1}{4}$ inches, above the root was chosen to compare stresses with experimental values found. The blade root was not aligned with any of the three axes in

Ansys and therefore a direct output from one of Ansys' predetermined directions aligned with the coordinate system was not possible. A vector describing the direction and location of the strain gage had to be determined as components in the x, y, and z directions. Again, Tecplot was employed to find this vector by outputting a vector normal to a slice through the blade at the strain gage location. This resulted in a unit vector of -0.551769, -0.057844, and 0.831988 in the x,y, and z directions, respectively. These vectors were then multiplied by stresses found in the way described in the following section.

In order to apply the generalized forcing function onto the FE model in Ansys, a point had to be chosen and then the appropriate force had to be determined. Any point will work equally well as the force changes depending on the location chosen. A point was arbitrarily chosen, Node 1887, which is one node back from the leading edge tip on the suction side of the blade. At this location the magnitude of the eigenvector was 45.000. To find the correct force to apply, the generalized force is simply divided by the displacement for the mode of interest. In this case the 1st mode is used since this is the mode being excited in the experimental stress data used for comparison. The equation and solution appear below.

$$\tilde{\Phi}_1^T \tilde{f}_1 = \tilde{\Phi}_2^T \tilde{f}_2$$

Equation 5-12

$$F_1 = \tilde{\Phi}_2^T \tilde{f}_2$$

let $x_2 = \tilde{\Phi}_2$ at a chosen point,

and let f_2 be a point force so that,

$$F_1 = x_2 f_2$$

$$\therefore f_2 = \frac{F_1}{x_2}$$

$$f_2 = \frac{177lbs.}{45} = 3.933lbs.$$

The variables f_1 and Φ_1 represent the total modal force and the eigenvector respectively, while f_2 and Φ_2 represent the modal force and eigenvector at a specific point. The force of 3.933 lbs. was applied at Node 1887 along the direction of eigenvector and was varied harmonically. The harmonic variance of the force is used so that the maximum stress can be determined as the force oscillates from zero to its maximum while slowly increasing in frequency. As the frequency at which the force is applied sweeps past the natural frequency of the blade, the deflection, strain and stress all reach their maximums. A plot showing the maximum stress present at the strain gage location in the x, y, and z directions are shown below in Figure 5-16 through Figure 5-18, respectively.

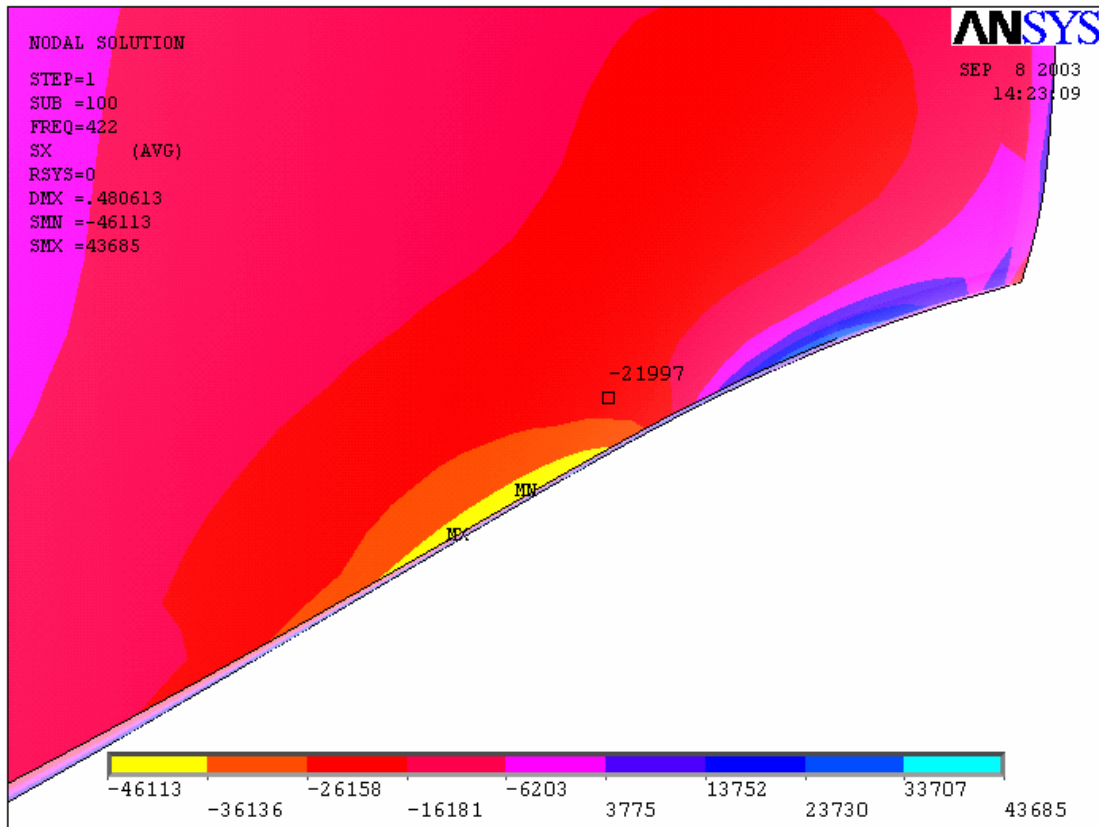


Figure 5-16: Blade root stress in the x-direction.

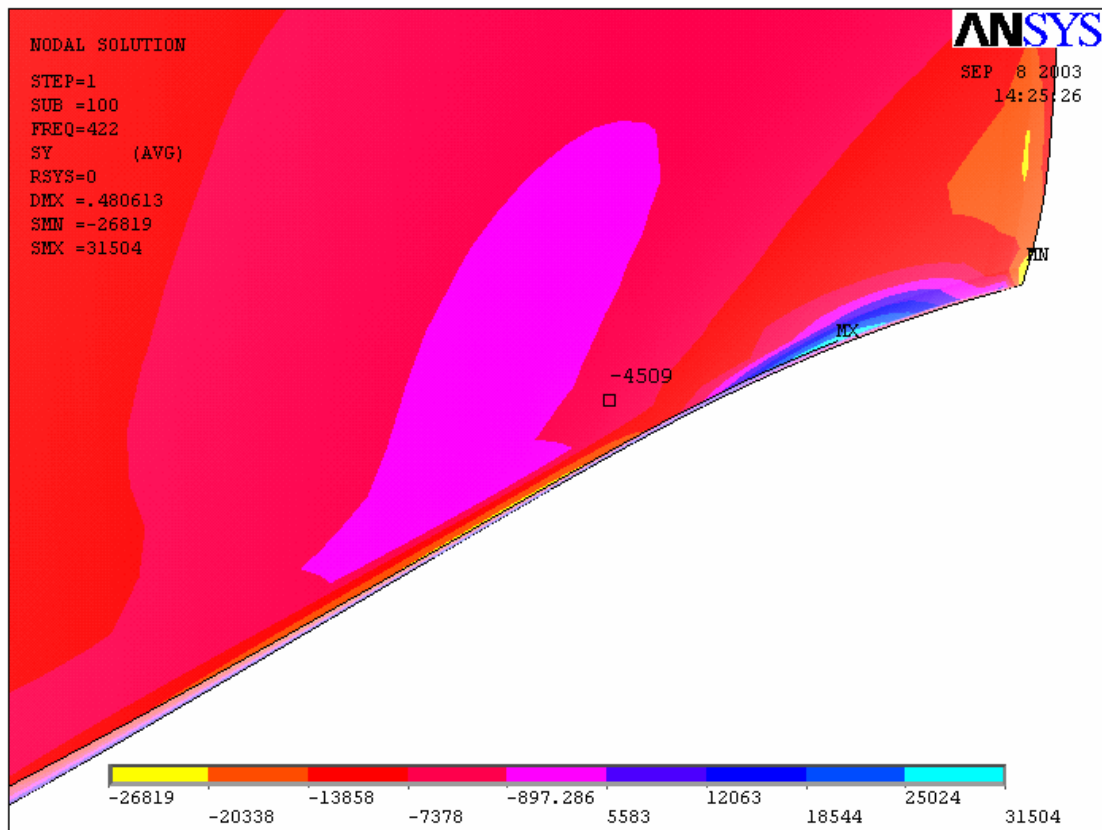


Figure 5-17: Blade root stress in the y-direction

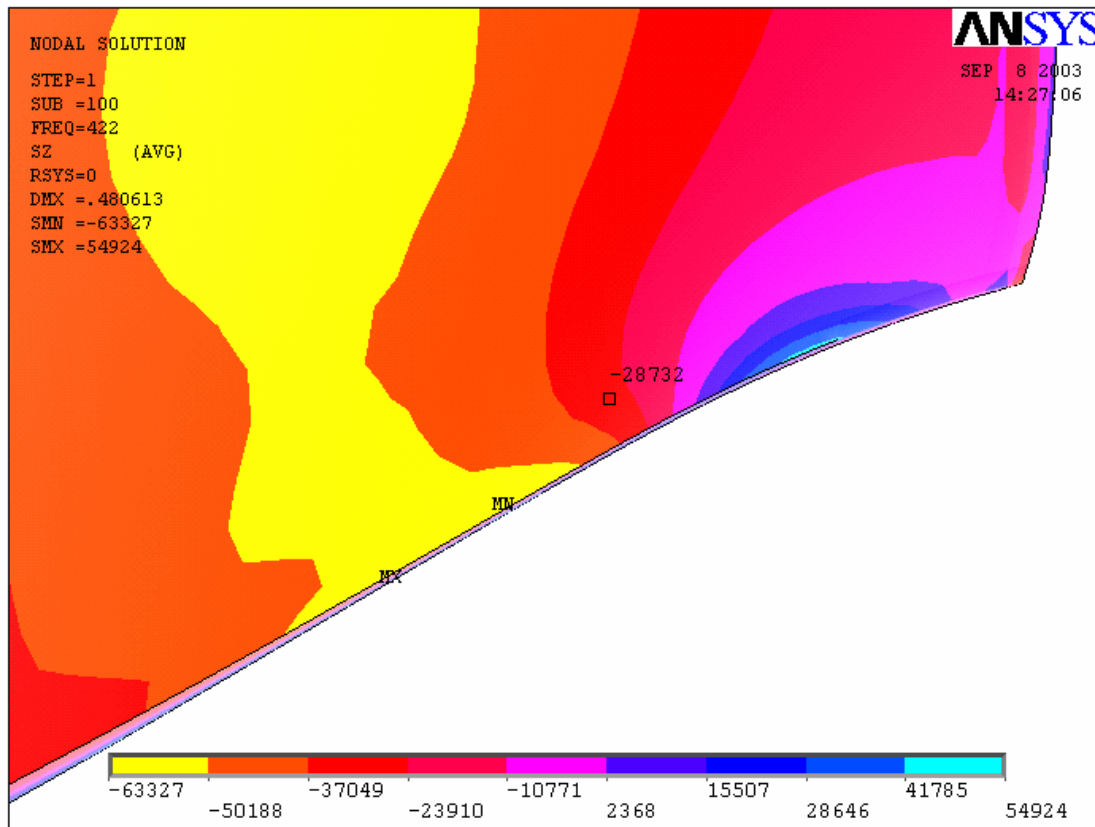


Figure 5-18: Blade root stress in the z-direction.

The rotor mean resonant stress found experimentally was 145,335 kPa [Kenyon, 1999]. The stress found using the FE model for the harmonic analysis resulted in a stress of -21997, -4509, and -28732 psi for pure titanium and -19740, -4069, and -25764 for Ti-6-4 in the x, y, and z direction, respectively. Once the stresses have been multiplied by the unit vector describing the strain gage orientation, the results must be doubled to be consistent with the experimental results as reported by Kenyon to represent the total stress magnitude from the minimum to maximum (peak-to-peak). Table 5-4 shows the calculation of the individual contributions from each principle stress direction and summarizes the results.

Table 5-4: Mean rotor stress calculation and comparison at wide open discharge.

| | FEM Stress (psi) (Ti-6-4) | Strain Gage Unit Vector | Contribution to Strain Gage (psi) |
|--|--------------------------------------|------------------------------------|--|
| x | -19740 | -0.551769 | 10891.9 |
| y | -4069.6 | -0.057844 | 235.4 |
| z | -25763.6 | 0.831998 | -21435 |
| Total | | | -10307.7 |
| Experimental Stress Results | FEM Stress Results | Percent Difference | |
| 21,132 psi | 20,615 psi (Ti-6-4) | -2.51 % | |
| | 23,013 psi (Ti) | +8.18 % | |
| 145,335 kPa | 141,783 kPa (Ti-6-4) | -2.51 % | |
| | 158,274 kPa (Ti) | +8.18 % | |

The results have been reported in both English and metric units since my work was done in English units and the experimental values were published in metric. The results show an agreement around 2.5%, this is an extremely good result and indicates that the simple model was able to accurately predict blade root stress using relatively inexpensive computations. In addition, the experimentally found blade root stress varied up to 21% of the mean near stall with a standard deviation of 9.8% at wide-open discharge [Kenyon, 1999]. Given this uncertainty in the experimental results, the FE stress result of 2.51% from the mean stress is well within one standard deviation.

6 Summary and Conclusions

The ability of modal analysis to accurately predict blade loading in a transonic axial compressor has been investigated. A method and parametric model has been developed using modal analysis with a harmonically varying excitation to predict the strain and stress in a finite element model. This method is based on calculating and extracting the eigenvectors associated with a finite element model and combining them with a known pressure profile created with computational fluid dynamics on the same blade grid. An inner product was taken between the pressure profile and three different mode shapes: 1st Flexural, 2nd Flexural, and 1st Torsional. These mode shapes represent the first three modes associated with the three lowest natural frequencies present in the compressor blade under the operating conditions. The lowest order mode shapes contain the largest amount of energy resulting in large deflections and therefore inducing the highest strain and stress leading to possible high cycle fatigue.

Second, a generalized forcing function was computed as the inner product was calculated over time. The forcing function was plotted for all three modes over time to visually inspect and compare how each mode was excited by the single 3-per-rev distortion pattern. As expected the first mode showed the highest average modal force and amplitude. A Fast Fourier Transform was taken of the generalized forcing function to decompose the sinusoidal signal into harmonic components and investigate their contribution to the entire signal. As expected the 3rd engine order returned the highest magnitude while a harmonic at the 6th engine order was second highest contributing a significant portion for the 3rd mode – 1st Torsional.

A sensitivity factor was developed to show the gain in modal force as a function of percent gain in total pressure distortion. A linear relationship appears to exist for the 3rd engine order which each mode having a different sensitivity. The 1st mode has the highest gain in modal force for a given increase in total pressure distortion level followed by the 3rd mode and last the 2nd mode. The 6th engine order appears to have a parabolic relationship indicating the gain in modal force increases at an increasing rate as the level of the total pressure distortion increases.

To verify the accuracy of the modal analysis and to predict the strain and stress in the compressor blade, a harmonic analysis was conducted. Using the modal force calculated, a point force was determined on an arbitrarily picked node on the finite element model. This point force was placed on the blade node acting in the same direction as given by the 1st mode eigenvector and varied harmonically from zero to its maximum magnitude. This harmonic sweep was conducted over the frequency range known to contain the natural frequency of the blade associated with the first mode in an attempt to acquire the maximum strain and stress. Without the harmonic sweep, the exact natural frequency would need to be known in order to apply the force at the identical frequency. A node on the FE model was chosen that coincided with location of the rotor blade root strain gage in which stress was sampled and compared with the experimentally found value. The strain gage orientation required a stress to be calculated using components of the stress in all of the x, y, and z directions. This was done and the stress was found to be within 2.51% of the experimental value.

The model contained a few approximations and assumptions that strengthen the argument of this approach to accurately model and predict blade loading. The preliminary model used the density and modulus of elasticity of pure titanium instead of the actual titanium alloy, Ti-4-6, used in the blade. The difference resulted in a modulus of elasticity deficit of 10.3% with a gain in density of 8.2% in the model. Despite these deviations in material properties from Ti-6-4, the model still predicted blade root stress to within 8.18% found experimentally. The only available blade geometry was that used in the CFD calculations. This hot geometry was in the form of a finite element grid with a density of 64 by 29 elements, in the streamwise and spanwise direction, respectively. An internal element thickness of 3 elements was added along the primary axis of bending for accuracy in accordance with Ansys element definition suggestions. A cold geometry would have been preferred so the proper artificial stiffening due to centrifugal force and blade geometry at engine operation speed due to untwist could have been achieved simultaneously. As a result, the hot geometry was tested to see if the correct eigenvectors could be extracted and was found that it could. The maximum RMS error of 0.9289% was found and considered to be minimal, therefore allowing the eigenvectors to be extracted from the hot geometry while spinning at 9100 rpm. This allowed

approximately the correct eigenvalues and eigenvectors to be present in the model simultaneously.

The goals of this particular study were introduced in Chapter 1 and will be reiterated here: (1) create an accurate finite element (FE) model of the ADLARF fan blade for eigenvector extraction; (2) identify dominant engine order modal force magnitudes based on coupling computational fluid dynamics (CFD) generated total pressure distortion and FE generated eigenvectors; and (3) determine the relationship between the magnitude of the modal force and the total pressure distortion level used to drive the system. The goals have been achieved here for the 1st mode – 1st Flexural conditions as dictated by the available data. Many approximations and assumptions were taken along the way and go to show the ability of modal analysis to accurately predict the blade loading to within 2.51% despite these assumptions and approximations. This result is extremely good and falls within one standard deviation of the experimentally found blade root stress. This study is in conjunction with previous studies conducted by Jon Ludke and John Ryman at Virginia Tech to determine if pressure distortions continue through multiple stages of an axial compressor. Their studies show that the pressure distortions do in fact travel downstream and underline the importance of developing a method to predict blade loading as the possible problems associated with high cycle fatigue can not be assumed to be limited to the first stage rotor. This study has shown one possible method by developing a parametric model to determine blade loading sensitivity to varying total pressure distortions and predicting the strain and stress at the blade root as a result of forced vibration.

7 Recommendations for Future Work

This study has shown that it is possible to accurately predict the root strain and stress present in an axial compressor blade through modal analysis. While the results appear promising, the study was conducted with limited data taken at only one distortion pattern and one engine operation speed. More research should be conducted using additional compressor blades, inlet distortion patterns, and engine operation speeds before a complete picture of the ability of modal analysis to accurately predict the strain and stress can be commented upon and implemented in industry to partially eliminate the arduous task of testing.

The next step in testing should be the use of total temperature distortions at the inlet. Since temperature and pressure are directly related through the Ideal Gas Law it is believed that modal analysis could be used to analyze the effect of total temperature change in the same way total pressure was tested. There has been much discussion in the industry lately as to whether total temperature distortion can produce excitations capable of inducing high cycle fatigue. This study may introduce one of many avenues to investigate this topic of debate.

In addition, if further testing proves promising using this parametric method of testing blade loading to inlet distortions that are quasi-steady state, perhaps a method of introducing unsteady inlet distortions could be investigated. Studies by Jon Ludke and John Ryman at Virginia Tech have shown that total pressure distortions pass through multiple rotor rows in an axial compressor. As a result, perhaps this method can be combined with their studies to predict blade loading on rotor blades farther downstream. Ultimately the model developed here may be expanded to study many other systems where forced vibrations are present and if the application continues to be successful could reach areas of interest far outside the realm of turbomachinery.

References

ANSYS, v.61, www.ansys.com .

Bielawa, R. L., “Rotary Wing Structural Dynamics and Aeroelasticity,” AIAA Education Series, 1992.

Boyer, K.E., “An Improved Streamline Curvature Approach for Off-Design Analysis of Transonic Compression Systems,” Ph.D. Dissertation, Virginia Polytechnic Institute and State University (Blacksburg, VA, 2001).

Breard, Imregun, Sayma, Vahdati, “An Integrated Time Domain Aerolasticity Model for the Prediction of Fan Forced Response Due to Inlet Distortion,” *Journal of Engineering for Gas Turbine and Power*, Vol. 124, January 2002, pp. 196.

Campbell, Wilfred, “Protection of Turbine Disk Wheels from Axial Vibration,” *Proceedings of the Cleveland Spring Meeting*, ASME, May 1924.

Carnegie, W., “Vibrations of Rotating Cantilever Blading: Theoretical Approaches to the Frequency Problem Based on Energy Methods,” *Journal of Mechanical Engineering Science*, Vol. 1, No. 3, 1959, pp. 235-240.

Carta, F.O., “Aeroelasticity and Unsteady Aerodynamics,” *The Aerothermodynamics of Aircraft Gas Turbines Engines*, AFAPL-TR-78-52, pp.22-10--22-11.

Cramer, K.B., O’Brien, W.F., “Design of a Total Distortion Generator for Aircraft Engine Testing,” M.S. Thesis, Virginia Polytechnic Institute and State University (Blacksburg, VA, 2002).

Colpin, J., Kool, P., “Experimental Study of an Axial Compressor Rotor Transfer Function with Non-Uniform Inlet Flow,” ASME Paper No. 78-GT-69, Gas Turbine Conference and Products Show, April 9-13, 1978, London, England.

Danforth, C.D., “Distortion-Induced Vibration in Fan and Compressor Blading,” *Journal of Aircraft*, vol. 12, no. 4, pp. 216-225, April 1975.

Datko Jr., J.T., O’Hara, J.A., “The Aeromechanical Response of an Advanced Transonic Compressor to Inlet Distortion,” ASME 87-GT-189, 1987.

Davis, M., Hale, A., Beale, D., “An Argument for Enhancement of the Current Inlet Distortion Ground Test Practice for Aircraft Gas Turbine Engines,” ASME 2000-GT-0505, 2000.

Dhar, V.B., "A Simple Finite Element for the Dynamic Analysis of Rotating Composite Beams," M.S. Thesis, Virginia Polytechnic Institute and State University (Blacksburg, VA, 1990).

Fleeter, S., Jay, R.L., Bennett, W.A., "Rotor Wake Generated Unsteady Aerodynamic Response of a Compressor Stator," ASME 78-GT-112, 1978.

Greitzer, E.M., "Upstream Attenuation and Quasi-Steady Rotor Lift Fluctuations in Asymmetric Flows in Axial Compressors," ASME 73-GT-30, 1973.

Greitzer, E.M., Tan, C.S., Wisler, D.C., Adamczyk, J.J., Stazisar, A.J., "Unsteady Flows in Turbomachines: Where's the Beef?," *ASME Unsteady Flows in Aeropropulsions*, 1994, pp. 1-11.

Hah, C., Rabe, D.C., Sullivan, T.J., Wadia, A.R., "Effects of Inlet Distortion on the Flow Field in a Transonic Compressor Rotor," *ASME Journal of Turbomachinery*, Vol. 120, April 1998, pp. 233-246.

Hamed, A., Numbers, K., "Inlet Distortion Considerations for High Cycle Fatigue in Gas Turbine Engine," AIAA Paper 97-3364, AIAA 33rd Joint Propulsion Conference and Exhibit, July 6-9, 1997, Seattle, WA.

Inman, D.J., "Engineering Vibration," 2nd Ed., New Jersey, Prentice Hall, Inc., 2001.

Kenyon, J.A., private communication, 2003

Kenyon, J.A., "Investigation of Curve Veering Using Computational and Experimental Techniques," AIAA-99-1383.

Kenyon, J.A., Fleeter, S., Rabe, D.C., "Aerodynamic Effects on Blade Vibratory Stress Variations," *Journal of Propulsion and Power*, Vol. 15, No. 5, September-October 1999, pp. 675-680.

Lecht, M., "Improvement of the Parallel Compressor Model by Consideration of Unsteady Blade Aerodynamics," AGARD CP-400, 1986.

Lecht, M., Weyer, H. B., "On the Unsteady Aerodynamic Rotor Blade Loading in a Transonic Axial Flow Compressor with Unsteady State Inlet Distortion," IUTAM Symposium on Aeroelasticity in Turbomachines, October 18-23, 1976, Paris.

Longley, J.P., Greitzer, E.M., "Inlet Distortion Effects in Aircraft Propulsion System Integration," *Steady and Transient Performance Prediction of Gas Turbine Engines*, AGARD LS-183, May 1992.

Manwaring, S.R., Fleeter, S., "Inlet Distortion Generated Periodic Aerodynamic Rotor Response," ASME 89-GT-299, 1989.

Manwaring, S.R., Fleeter, S., "Forcing Function Effects on Rotor Periodic Aerodynamic Response," *Transactions of the ASME*, vol. 113, April 1991, pp. 312-319.

Manwaring, S.R., Rabe, D.C., Lorence, C.B., Wadia, A.R., "Inlet Distortion Generated Forced Response of a Low Aspect-Ratio Transonic Fan," *ASME Journal of Turbomachinery*, vol. 119, October 1997, pp. 665-676.

Matlab, v.6.1, www.mathworks.com .

Mazzawy, R.S., "Multiple Segment Parallel Compressor Model for Circumferential Flow Distortion," *ASME Journal of Engineering for Power*, April, 1977.

Morrow, P., "Detailed Test Plan for the Augmented Damping of Low Aspect Ratio Fans (ADLARF)," USAF Technology Branch Turbine Engine Division, WPAFB, March 1993.

Peacock, R.E., Overli, J., "Dynamic Internal Flows in Compressors with Pressure Maldistributed Inlet Conditions," AGARD CP-177, 46th P.E.P. Conference of AGARD, 1975, Monterey, CA.

Rabe, D., Bolcs, A., and Russler, P., "Influence of Inlet Distortion on Transonic Compressor Blade Loading," AIAA 95-2461, Presented at the 31st Joint Propulsion Conference and Exhibit, July 1995, San Diego, CA.

Rabe, D., Williams, C., and Hah, C., "Inlet Flow Distortion and Unsteady Blade Response in a Transonic Axial Compressor Rotor," ISABE 99-7297, 1999.

Reid, C., "The Response of Axial Flow Compressors to Intake Flow Distortion." ASME Paper No. 69-GT-29, 1969.

Roberts, F., Plourde, G.A., Smakula, F. "Insights into Axial compressor Response to Distortion," AIAA Paper No. 68-565, 1968.

Ryman, J.F., private communication, 2003

Ryman, J.F., O'Brien, W.F., "Prediction of Inlet Distortion Transfer Through the Blade Rows in a Transonic Axial Compressor," M.S. Thesis, Virginia Polytechnic Institute and State University (Blacksburg, Virginia, 2003.).

SAE Aerospace Information Report – 1419, *Inlet Total-Pressure-Distortion considerations for Gas-Turbine Engines*, (Warrendale, PA, Rev. A, 1999).

Sexton, M.R., O'Brien, W.F., "A Model for Dynamic Loss Response in Axial-Flow Compressors," ASME 81-GT-154, 1981.

Silva, W.A., "Identification of Linear and Nonlinear Aerodynamic Impulse Responses Using Digital Filter Techniques," AIAA 97-3712, Aug. 1997.

Silva, W.A., "Extension of a Nonlinear Systems Theory to General-Frequency Unsteady Transonic Aerodynamic Responses," AIAA 93-1590, Apr. 1993.

Small, M., "Improved Methods for Predicting the Effects of Inlet Flow Distortion on the Performance of Axial Flow Compressor," M.S. Thesis, Virginia Polytechnic Institute and State University (Blacksburg, Virginia, 2001.).

Tecplot, www.tecplot.com .

Thomson, W.T., "Theory of Vibration with Application," Prentice Hall, Inc. 1981.

Williams, C., "Turbine Engine Research Center Inlet Distortion Measurement," 4th National Turbine Engine High Cycle Fatigue Conference, 1999, Monterey, CA.